Final Report Submitted to
the **California Department of Transportation**
under Contract No: **RTA-59A0496**

VERIFICATION OF COMPUTER ANALYSIS MODELS FOR SUSPENSION BRIDGES

by

Masanobu Shinozuka, Distinguished Professor and Chair

and

Debasis Karmakar, Graduate Student

Samit Ray Chaudhuri, Postdoctoral Scholar

Ho Lee, Assistant Researcher

Department of Civil and Environmental Engineering

University of California, Irvine

Report No: CA/UCI-VTB-2009

August 2009

VERIFICATION OF COMPUTER ANALYSIS MODELS FOR SUSPENSION BRIDGES

Final Report Submitted to the **Caltrans** under
Contract No: **RTA-59A0496**

by

Masanobu Shinozuka, Distinguished Professor and Chair

and

Debasis Karmakar, Graduate Student

Samit Ray Chaudhuri, Postdoctoral Scholar

Ho Lee, Assistant Researcher

Department of Civil and Environmental Engineering
University of California, Irvine

Report No: CA/UCI-VTB-2009

August 2009

STATE OF CALIFORNIA · DEPARTMENT OF TRASPORTATION

TECHNICAL REPORT DOCUMENTAION PAGE

TR0003 (REV. 9/99)

1. REPORT NUMBER	2. GOVERNMENT ASSOCIATION NUMBER	3. RECIPIENT'S CATALOG NUMBER
CA/UCI-VTB-2009		

4. TITLE AND SUBTITLE	5. REPORT DATE
VERIFICATION OF COMPUTER ANALYSIS MODELS FOR SUSPENSION BRIDGES	August 2009
	6. PERFORMING ORGANIZATION CODE UC Irvine

7. AUTHOR	8. PERFORMING ORGANIZATION REPORT NO.
Masanobu Shinozuka, Debasis Karmakar, Samit Ray Chaudhuri, and Ho Lee	

9. PERFORMING ORGANIZATION NAME AND ADDRESS	10. WORK UNIT NUMBER
Department of Civil and Environmental Engineering The Henry Samueli School of Engineering University of California, Irvine Irvine, CA 92697-2175	11. CONTRACT OR GRANT NUMBER RTA-59A0496

12. SPONSORING AGENCY AND ADDRESS	13. TYPE OF REPORT AND PERIOD COVERED
California Department of Transportation (Caltrans) Division of Research and Innovation 1227 O Street, MS-83 Sacramento, CA 95814	Final Report
	14. SPONSORING AGENT CODE

15. SUPPLEMENTARY NOTES

16. ABSTRACT

The Vincent Thomas Bridge, connecting Terminal Island with San Pedro, serves both Los Angeles and Long Beach ports, two busiest ports in the west coast of USA. The bridge carries an overwhelming number of traffic with an Annual Average Daily Traffic (AADT) volume of 45,500, many of which are cargo trucks. Based on the recent finding that the main span of the Vincent Thomas Bridge crosses directly over the Palos Verdes fault, which has the capacity to produce a devastating earthquake, the bridge underwent a major retrofit in spring 2000, mainly using visco-elastic dampers. This study focuses on performance evaluation of the retrofitted bridge under seismic, wind and traffic loads. A member-based detailed three-dimensional Finite Element (FE) as well as panel-based simplified models of the bridge are developed. In order to show the appropriateness of these models, eigenproperties of the bridge models are evaluated and compared with the system identification results obtained using ambient vibration. In addition, model validation is also performed by simulating and comparing with the measured dynamic response during two recent earthquakes. FE model is also updated using a sensitivity-based parameter updating method. Effect of spatial variability of ground motions on seismic displacement and force demands is investigated. To record actual wind velocity and direction, three anemometers are installed at three different locations of the bridge. Response of the bridge is computed under wind velocity. Finally, analysis of the bridge under traffic load is also carried out.

17. KEYWORDS	18. DISTRIBUTION STATEMENT
Suspension Bridge, System Identification, Retrofit, Fragility Curve, Earthquake, Wind, Traffic	No restrictions.

19. SECURITY CLASSIFICATION (*of this report*)	20. NUMBER OF PAGES	21. COST OF REPORT CHARGED
Unclassified	178	

DISCLAIMER: The contents of this report reflect the views of the authors who are responsible for the facts and the accuracy of the data presented herein. The contents do not necessarily reflect the official views or policies of the STATE OF CALIFORNIA or the Federal Highway Administration. This report does not constitute a standard, specification or regulation.

The United States Government does not endorse products or manufacturers. Trade and manufacturers' names appear in this report only because they are considered essential to the object of the document.

SUMMARY

The Vincent Thomas Bridge, connecting Terminal Island with San Pedro, serves both Los Angeles and Long Beach ports, two busiest ports in the west coast of USA. The bridge carries an overwhelming number of traffic with an Annual Average Daily Traffic (AADT) volume of 45,500, many of which are cargo trucks. Based on the recent finding that the main span of the Vincent Thomas Bridge crosses directly over the Palos Verdes fault, which has the capacity to produce a devastating earthquake, the bridge underwent a major retrofit in spring 2000, mainly using visco-elastic dampers.

This study focuses on performance evaluation of the retrofitted bridge under seismic, wind and traffic loads. A member-based detailed three-dimensional Finite Element (FE) as well as panel-based simplified models of the bridge are developed. In order to show the appropriateness of these models, eigenproperties of the bridge models are evaluated and compared with the system identification results obtained using ambient vibration. In addition, model validation is also performed by simulating and comparing with the measured dynamic response during two recent earthquakes. Tornado diagram and first order second moment (FOSM) methods are applied for evaluating the sensitivity of different parameters on the eigenproperties of the FE models. The study indicates that the mass density of deck slab and elastic modulus of bottom chord are very important parameters to control eigenproperties of the models. FE model is also updated using a sensitivity-based parameter updating method.

Considering a set of strong ground motions in the Los Angeles area, nonlinear time history analyses are performed using the FE models developed and seismic fragility curves are derived comparing the ductility demand with the ductility capacity at critical

tower sections. Effect of spatial variability of ground motions on seismic displacement and force demands is also investigated. To generate spatially correlated nonstationary acceleration time histories compatible with design spectrum at each location. A new algorithm is developed involving evolutionary power spectral density function (PSDF) and with the aid of spectral representation method. It has been found that, in some locations on the bridge deck, the response is higher when the spatially variable ground motion is considered as opposed to the uniform ground motion time histories having the highest ground displacement.

To record actual wind velocity and direction, three anemometers are installed at three different locations of the bridge. The fluctuating component of the wind velocity measured at these three locations are found to be non-Gaussian. They are used for simulation of fluctuating component of wind velocity throughout the span and along the tower on the basis of three different simulation methods (i) newly developed non-Gaussian conditional method, (ii) Gaussian conditional method, and (iii) Gaussian unconditional method. Response of the bridge is computed under wind velocity using these three different methods. It is observed that the non-Gaussian conditional simulation technique yields higher response than both Gaussian conditional and Gaussian non-conditional techniques. Finally, analysis of the bridge under traffic load is also carried out and a critical evaluation of shear force in deck shear connectors is performed.

ACKNOWLEDGEMENT

The research presented in this report was sponsored by the California Department of Transportation (Caltrans) with Dr. Li-Hong Sheng as the project manager. The authors are indebted to Caltrans for its support of this project and to Dr. Li-Hong Sheng for his helpful comments and suggestions.

TABLE OF CONTENTS

LIST OF FIGURES

LIST OF TABLES

CHAPTER 1

INTRODUCTION

1.1 Background

Throughout the history of suspension bridges, their tendency to vibrate under different dynamic loadings such as wind, earthquake, and traffic loads has been a matter of concern. The failure of the Tacoma Narrows bridge in 1940 has pointed out that the suspension bridges are vulnerable to wind loading (Rannie 1941). It is now widely accepted that the wind-induced vibration of suspension bridges may be significant and should be taken into consideration. Similar conclusions have also been drawn for other dynamic loadings. As a prerequisite to the investigation of aerodynamic stability, traffic impact, soil-structure interaction and earthquake resistant design of suspension bridges, it is necessary to know certain dynamic characteristics such as the natural frequencies and the possible modes of vibration. Several investigations have been taken place in recent years to determine the vibrational properties of suspension bridges. However, the complexity of a suspension bridge structure makes the determination of vibrational characteristics difficult.

With the advent of computers, non-conventional structures like suspension bridges are analyzed with the finite element (FE) analysis technique. There are several commercially available finite element software packages that are used by practicing

engineers as well as researchers, which can evaluate the response of a suspension bridge from operational traffic, wind and earthquake loads taking into account both material and geometric non-linear behavior.

In addition to analytical modeling and response analysis of suspension bridges, field tests are also very important from the analysis and design point of view. Field test results not only give experimental data but also help us to understand the behavior of the structure and to calibrate the analytical model. To perform field tests, it is necessary to measure, input loadings such as wind velocity at different pints and earthquake ground acceleration at different support locations, and output responses such as acceleration, velocity and displacement time history at different points of the bridge.

For predicting response of long span suspension bridges under random wind, the most widely used method is the frequency domain analysis. In theory, the frequency domain solution is accurate, when the load-response relationship is linear. Although the structural elements in a suspension bridge generally behave in a linear elastic fashion under normal loading, the overall load-displacement relationship exhibits geometrical nonlinearity, particularly when it is subjected to high wind. Therefore, in this case, a frequency domain analysis may not be appropriate. One way in which the limitation of the frequency domain analysis can be overcome is the use of Monte Carlo simulation technique. One of the most important components of the Monte Carlo simulation method is the generation of sample functions of stochastic processes, fields, or waves those are involved in the problem. For buffeting analysis, wind velocity fluctuation in the horizontal and vertical directions needed to be digitally simulated and fed into the equation of motion. Since the length of a modern suspension bridge generally exceeds 1

km, the simulated sample functions must accurately describe the probabilistic characteristics not only in terms of temporal variation but also in spatial distribution. Similarly for seismic response, critical members of the bridge may undergo significant nonlinear deformation and a simple response spectrum method for analyzing such response may not be adequate. In addition, there may be significant variation of ground motion from one support of the bridge to the other.

1.2 Literature Survey

Theoretical and practical treatises on the vibrational characteristics and the dynamic analysis of suspension bridges, have been developed by many authors, especially after the disastrous collapse of the Tacoma Narrows Bridge in 1940 (Rennie 1941). Bleich et al., 1950 studied the free vertical and torsional vibration by solving a forth order linearized differential equation. In addition, an approximate method of the Rayleigh-Ritz type solution was suggested. However, the procedure is applicable only for calculating the lowest few modes due to the great level of complexity and redundancy of higher modes of suspension bridges. Steinman, 1959 introduced a number of simplified formulas for estimating the natural frequencies and the associated mode shapes of vibration, both vertical and torsional, of suspension bridges. Japanese researchers (Konishi et al 1965; Konishi and Yamada 1969; Yamada and Takemiya 1969, 1970; Yamada and Goto 1972; and Yamada et al. 1979) performed extensive studies to investigate the vertical and lateral vibration as well as the tower-pier system of a three-span suspension bridge by using a lumped-mass system interconnected by spring elements. In their analysis for the

suspended structure, they assumed simple harmonic excitations and applied it separately to each supporting point. They reported that there was a fairly significant contribution from the higher modes to the bending response and a large number of modes should be included to accurately determine the dynamic response of suspension bridges.

The geometrically nonlinear behavior of suspension bridges was considered (Tezcan and Cherry 1969) due to large deflection and presented an iterative technique for the nonlinear static analysis by using tangent stiffness matrices. These matrices are incorporated in obtaining the free-vibrational modes of the structure. In their analysis, the bridge was modeled as a three-dimensional lumped mass system. They calculated the response of the bridge considering three orthogonal components of uniform ground motion and pointed out that the longitudinal motion of the deck as well as the vertical motion of the tower were small and therefore could be neglected.

Major advances in studying the dynamic characteristics of suspension bridges have been achieved through the use of finite element method and linearized deflection theory (Abdel-Ghaffar 1976, 1977, 1978a, 1978b, 1979, 1980 and 1982). Natural frequencies, mode shapes, and energy capacities of the different structural components for vertical, torsional, and lateral vibrations were investigated. Several examples were presented and the applicability of the proposed methods was illustrated by comparing the results obtained from analyzing the Vincent-Thomas bridge (Los Angeles Harbor) with the results of full-scale ambient vibration tests (Abdel-Ghaffar 1976, 1978 and Abdel-Ghaffar and Housner 1977). Some researchers (Abdel-Ghaffar and Rubin 1983a and Abdel-Ghaffar and Rubin 1983b) studied the effect of large amplitude nonlinear free coupled vertical-torsional vibrations of suspension bridges using a continuum approach

where approximate solutions of the nonlinear coupled equations were conducted. Nonlinearities due to large deflections of cables, the axial stretching of stiffening structure, and the nonlinear curvature of the stiffening structure were considered. It was mentioned that the importance of geometric nonlinearities arises only for very high amplitude vibration. Also, they studied using two-dimensional models the directional vertical, torsional, and lateral earthquake response, in both time and frequency domains, of long-span suspension bridges subjected to multiple-input excitations (Abdel-Ghaffar and Rubin 1982; Abdel-Ghaffar and Rubin 1983c and Abdel-Ghaffar et al. 1983). In addition, they considered a simplified model for the tower-pier system and investigated the longitudinal vibration response taking into account the flexibility and damping characteristics of the underlying and surrounding soil. They applied their procedure to the tower-pier system of the Golden Gate bridge (San Francisco) and different soil conditions were used.

The vertical response of suspension bridges has been studied to seismic excitations using a stochastic approach (Dumanoglu and Severn 1990). They applied their method to three suspension bridges using one set of earthquake records and a filtered white noise as well. They pointed out that the accuracy of that approach, in comparison to the time-history approach, depends upon the magnitudes of the fundamental period of the bridge under consideration. They reported that, for long-span suspension bridges like the Bosporus (in Turkey) and Humber (in England) bridges, the response results of the stochastic approach should be cautiously assessed, especially when the earthquake records are not zero-padded.

Some researchers (Lin and Imbsen 1990; Ketchum and Seim 1991 and Ketchum and Heledermon 1991) carried out an investigation on the Golden Gate bridge by developing an elaborate 3-D finite element model. The lower wind-bracing system of the bridge was considered to carry a light train. They incorporated different elements types and performed a nonlinear static analysis to determine the stiffness of the bridge in its dead-load state and used this matrix in the solution for the natural frequencies and mode shapes. Their model is verified by comparing its results with those obtained from previous studies (Abdel-Ghaffer and Scanlan 1985a and Abdel-Ghaffer and Scanlan 1985b). They reported that most of the lowest modes involving vibration of cables and torsional motion of the deck are not relevant to the earthquake performance of the bridge.

A 3D finite element model was proposed for the Vincent-Thomas bridge (Niazy et al. 1991). They considered geometrical nonlinearities in suspension bridges, and an iterative nonlinear static analysis technique was adopted. The stiffening truss, tower and cable-bent elements, were modeled as 3-D frame elements and cable elements were modeled as 3-D truss elements. In their study, 50 lowest natural frequencies and the corresponding mode shapes of the bridge model were determined in its dead-load configuration. However, in their modeling they did not consider the actual mass distribution over the length of the bridge. They considered uniform mass distribution over the center span and the side spans. Initial shape of the cable is one of the important parameters in the analysis of suspension bridges. A non-linear shape-finding analysis was used for a self-anchored suspension bridge named Yongjong Grand Bridge (Kim et al., 2002). The shape-finding analysis determines the coordinates of the main cable and

initial tension of main cable and hangers, which satisfies the design parameters at the initial equilibrium state under full dead loads.

Several models and expressions have been proposed (Davenport 1968) in relation to spatial variation of wind velocity fluctuation. For a more complete bibliography, the reader is referred to Simiu and Scanlan (1996). The analytical work by Beliveau et al., 1977 combined the effect of buffeting and self-excited forces. They used a two degrees of freedom mathematical model. Even though simulation techniques have been reported since 1970 (Shinozuka and Jan 1972), some earlier studies assumed uniformly distributed wind velocity fluctuations for the nonlinear time history analysis of cable-supported bridges (Arzoumanidis 1980). In past decades, a number of researchers reported on efficient methods for generating spatially correlated wind velocity fluctuations (Li and Kareem 1993; Shinozuka and Deodatis 1996; Deodatis 1996; Facchini 1996; Yang et al. 1997; Paola 1998; Paola and Gullo 2001). As a result of improvements in simulation techniques as well as computational speed, the time-domain approach has been utilized more frequently in recent buffeting analyses of long-span cable-supported bridges to take aerodynamic and/or geometric nonlinearity into consideration (Aas-Jakobsen and Strømmen 1998, 2001; Minh et al. 1999; Ding and Lee 2000; Chen et al. 2000; Chen and Kareem 2001; Lin et al. 2001). Kareem's group, in particular, has reported extensively on the line of time domain analysis framework for use in predicting aerodynamic nonlinear responses by incorporating frequency dependent parameters of unsteady aerodynamic forces by utilizing a rational function approximation technique (Chen and Kareem 2001). This technique is also readily available for the structure-originated nonlinearity in buffeting analysis. However, only a few studies utilized a nonlinear analysis procedure

for estimating buffeting response using structural nonlinearity, which is potentially involved in long-span cable-supported bridges, has been taken into consideration (Ding and Lee 2000; Lin et al. 2001).

The spatial variation of earthquake ground motions may have significant effect on the response of long span suspension bridges. Abdel-Ghaffar and Rubin (1982) and Abdel-Ghaffar and Nazmy (1988) studied response of suspension and cable-stayed bridges under multiple support excitations. Zerva (1990) and Harichandran and Wang (1990) examined the effect of spatial variable ground motions on different types of bridge models. Harichandran et al. (1996) studied the response of long-span bridges to spatially varying ground motion. Deodatis et al. (2000) and Kim and Feng (2003) investigated the effect of spatial variability of ground motions on fragility curves for bridges. Lou and Zerva (2005) analyzed the effects of spatially variable ground motions on the seismic response of a skewed, multi-span, RC highway bridge. Most of the aforementioned studies dealt with simple FE models of the bridge, as a result response of critical members could not be evaluated. In the present analysis a panel based detailed 3D FE model of a long span suspension bridge is utilized.

In this study, an iterative algorithm is proposed to generate spatially variable, design spectrum compatible acceleration time histories at different support locations of the bridge. The proposed algorithm is used to generate synthetic ground motions at six different points on the ground surface. For generating non-stationary accelerograms, previously researchers used time dependent envelope function on top of simulated stationary ground motions (Deodatis 1996). In this study by using evolutionary power spectral density function from the mother accelerogram, a new algorithm has been

proposed to simulate spatial variable ground motions. In the simulated acceleration time histories the temporal variations of the frequency content are same as the mother accelerogram. Mukherjee and Gupta (2002) proposed a new wavelet based approach to simulate spectrum compatible time histories. But they only considered one design spectrum and simulated one accelrogram from a single mother acceleration time history. Sarkar and Gupta (2006) developed a wavelet based approach to simulate spatially correlated and spectrum compatible accelerogram.

So far in a broad sense two approaches have been introduced by researchers regarding conditional simulation. The two approaches are based on "kriging" (Krige, 1966) (linear estimation theory applied to random functions) and conditional probability density function. Vanmarcke and Fenton (1991) applied conditional simulation of to simulate Fourier coefficients using kriging technique. Kameda and Morikawa (1992 and 1994), used an analytical framework based on spectral representation method, derived joint probability density functions of Fourier coefficients obtained from the expansion of conditioned random processes into Fourier series. They calculated conditional expectations and variances of the conditioned random processes and considered their first-passage probabilities. Hoshiya (1994) considered a conditional random field as a sum of its kriging estimate and the error. He simulated the kriging estimate and the error separately and combined them to get the Gaussian conditionally simulated field. In all the above studies the investigators considered Gaussian processes and Gaussian random fields.

Sometimes the assumption of Gaussian wind loading is not correct. In those cases, conditional simulation of non-Gaussian wind velocity field should be used. Elishakoff et

al. (1994) combined the conditional simulation technique of Gaussian random fields by Hoshiya (1994) and the iterative procedure for unconditional simulation of non-Gaussian random fields by Yamazaki and Shinozuka (1988), to conditionally simulate time-independent non-Gaussian random fields. Gurley and Kareem (1998) developed a procedure for conditional simulation of multivariate non-Gaussian velocity/pressure fields. For mapping the Gaussian process to non-Gaussian process and vice versa, they used modified Hermite transformation using Hermite polynomial function.

For buffeting analysis of long span cable supported bridges Chen (2001), Kim (2004) used time domain analysis to consider the effect of non-linearity in the structure. Also they only considered the wind forces on the deck only. They neglected the coupling effect of wind forces on tower and cable. Sun (1999) considered the coupling effect of the aeroelastic forces on the bridge deck, towers and cables. But they did not consider a 3D detailed finite element (FE) model of the bridge. Recently, He (2008) considered a detailed 3D model for buffeting analysis.

1.3 Objectives and Scope

The main purpose of this research is to evaluate the performance of a long span suspension bridge under seismic, wind, and traffic loads. A member-based detailed three-dimensional Finite Element (FE) as well as panel-based simplified models of the bridge are developed. In order to show the appropriateness of these models, eigenproperties of the bridge models are evaluated and compared with the system identification results obtained using ambient vibration. In addition, model validation is also performed by

simulating the dynamic response during the 1994 Northridge earthquake and 2008 Chino Hills earthquake and comparing with the measured response. Tornado diagram and first order second moment (FOSM) methods are applied for evaluating the sensitivity of different parameters on the eigenproperties of the FE models. This kind of study will be very helpful in selecting parameters and their variability ranges for FE model updating of suspension bridges.

Considering a set of strong ground motions in the Los Angeles area, nonlinear time history analyses are performed and the ductility demands of critical sections of the tower are presented in terms of fragility curves. Effect of spatial variability of ground motions on seismic displacement demand and seismic force demand is investigated. To generate spatially correlated design spectrum compatible nonstationary acceleration time histories, a newly developed algorithm using evolutionary power spectral density function (PSDF) and spectral representation method is used.

To simulate the wind velocity field accurately for the bridge site, measurement of the wind velocity is needed at the bridge location. For colleting actual wind data i.e. wind velocity and direction, three anemometers have been installed at three different locations of the bridge, so that the wind velocity field can be simulated in both horizontal and vertical directions. The measured wind velocity fluctuation data have been used for conditional simulation of wind velocity fluctuation field.

Finally, response of Vincent Thomas Bridge under conditionally simulated wind velocity field is also presented in this study. A new simulation technique for conditional simulation of non-Gaussian wind velocity fluctuation field is proposed and used for

buffeting analysis of the bridge under simulated wind load. Analysis of the Vincent Thomas bridge under traffic load is also carried out in this study.

1.4 Dissertation Outline

The dissertation contains the following chapters

Chapter 2 summarizes the finite element (FE) modeling of the before and after retrofitting of the bridge.

Chapter 3 presents the system Identification results obtained from response of the bridge and compared with modal parameters obtained from analytical model. A sensitivity analysis is also carried out.

Chapter 4 proposes a new methodology to simulate spectrum compatible spatial variable ground motions. Response variability due to spatial variation in ground motion is also assessed.

Chapter 5 describes the wind sensors installation in the bridge and data collection.

Chapter 6 proposes a new methodology to conditionally simulate non-Gaussian wind velocity fluctuation profiles using the data collected by anemometers at the bridge site. Wind buffeting analysis also carried out using the simulated wind velocity fluctuation profile.

Chapter 7 describes the traffic load analysis.

CHAPTER 2

FINITE ELEMENT MODELING OF VINCENT THOMAS BRIDGE

2.1 Background

With the advent of high-speed computer, major advances in studying the dynamic characteristics of suspension bridges have been achieved through the use of finite element method. In addition, effort has also been given for developing simplified models that can predict response consistent with detailed model. In recent years, several commercially available finite element software packages have been used by practicing engineers as well as researchers to evaluate the response of a suspension bridge from operational traffic, wind and earthquake loads taking into account both material and geometric non-linear behavior. This chapter focuses on numerical modeling of the Vincent Thomas Bridge. A member-based detailed three-dimensional Finite Element (FE) as well as a panel-based simplified model of the Vincent Thomas bridge have been developed for before and after retrofit of the bridge.

2.2 Calculation of Dead Weight

The dead load along the length of the bridge has been calculated. Table 1 shows the calculated dead load of the different components of the bridge. It has been found that the weight per unit length of the bridge in the center span is very close to the design value of

7.2 kip/ft indicated in the design drawing. The dead load calculation is also compared with the values reported by Abdel-Ghaffer, 1976 shown in Table 2.1.

2.3 Calculation of the Initial Shape of the Cable

Initial shape of the cable is one of the important parameters in the modeling of suspension bridges. Initial shapes of the cables of Vincent Thomas Bridge have been calculated using non-linear shape-finding analysis and subsequently used in the FE model. The shape-finding analysis determines the coordinates of the main cable and initial tension of main cable and hangers, which satisfies the design parameters at the initial equilibrium state under full dead loads. Details of the analysis methodology and software are described in Kim et al., 2002. The shape of the initial cable profile in the form of preliminary and final configurations are tabulated in Table 2.2 and the initial cable profile is plotted in Figure 2.1.

2.4 Panel-Based Simple Model

For simplified panel-based modeling, the girders and diaphragms are considered as equivalent 3D frame elements. The cable and suspender are modeled as 3D truss element. Also as in the case of detailed model, truss and cable bent were modeled with frame elements. Dampers are also included in the simplified model only at the tower and girder connections. . FE modeling is done with SUCOT (Kim, 1993) and SAP 2000 V10 (Computer and Structures, 2002). Area of the stiffening girder is set equal to the sum of the area of top chord, bottom chord and web.

Table 2.1 Calculated dead load (kip/ft) along the length of bridge

	Different components	Present study		Abdel-Ghaffer, 1976
		Center span	Side span	
Bridge floor	Curb	0.066	0.066	
	Bracket	0.019	0.019	
	Crash barrier	0.413	0.413	
	Sub total	0.498	0.498	0.203
	Grating	0.036	0.036	
	Railing	0.0414	0.0414	
	Fence	0.131	0.131	
	Sub total	0.208	0.208	0.199
	Lightweight concrete	2.521	2.521	2.592
	Reinforcement steel	0.173	0.173	0.173
	Stringers	0.544	0.544	0.682
	Bracings	0.154	0.154	
	Sub total	3.392	3.392	3.447
	Floor Truss	0.41	0.41	
	Inspection walkway	0.098	0.098	
	Inspection rail	0.052	0.052	
	Wind shoe	0.008	0.008	
	Sub total	0.568	0.568	0.613
Stiffening truss	Top chord	0.313	0.313	0.315
	Bottom chord	0.307	0.291	0.302
	Gusset plate, splice	0.234	0.234	0.124
	Web (diagonal)	0.162	0.166	0.142
	Post (vertical)	0.055	0.055	0.053
	Strut, rivet, bolt etc	0.007	0.007	0.007
	Sub total	1.078	1.066	0.943
Lateral system	K-truss	0.161	0.154	0.159
	Sub total	0.161	0.154	0.159
Cable	Cable	0.971	0.971	1.025
	Suspenders	0.066	0.065	0.054
	Sub total	1.037	1.036	1.079
	Cable and suspender weight	1.037	1.036	1.079
	Suspended structure weight	5.905	5.886	5.564
	Total weight	6.942	6.922	7.170

For SI: 1 kip/ft = 14.593 kN/m

Table 2.2 Calculated nodal coordinates of the cable-only system

X (ft)	Y (ft)		Z (ft)		Remark
	Preliminary configuration	Final configuration	Preliminary configuration	Final configuration	
1256.500	29.5833	29.5833	163.1400	163.1400	Cable bent
1221.840	29.7626	29.7628	172.5984	172.6094	
1190.780	29.9295	29.9297	181.5906	181.6075	
1159.720	30.1039	30.1042	191.0963	191.1143	
1128.660	30.2867	30.2869	201.1168	201.1324	
1097.600	30.4782	30.4784	211.6536	211.6664	
1066.540	30.6787	30.6787	222.7081	222.7190	
1035.480	30.8882	30.8882	234.2820	234.2919	
1004.420	31.1069	31.1069	246.3771	246.3866	
973.360	31.3349	31.3349	258.9949	259.0050	
942.300	31.5722	31.5723	272.1375	272.1489	
911.240	31.8188	31.8190	285.8068	285.8202	
880.180	32.0749	32.0751	300.0048	300.0211	
849.120	32.3404	32.3407	314.7336	314.7525	
818.060	32.6154	32.6157	329.9955	330.0132	
787.000	32.8998	32.9000	345.7927	345.8045	
750.000	33.2500	33.2500	365.2600	365.2600	Tower
714.380	32.9474	32.9482	351.2700	351.3089	
683.320	32.6931	32.6946	339.6119	339.6821	
652.260	32.4485	32.4505	328.4872	328.5843	
621.200	32.2136	32.2161	317.8940	318.0124	
590.140	31.9885	31.9913	307.8302	307.9643	
559.080	31.7732	31.7762	298.2938	298.4394	
528.020	31.5678	31.5710	289.2832	289.4360	
496.960	31.3723	31.3756	280.7965	280.9516	
465.900	31.1870	31.1901	272.8323	272.9846	
434.840	31.0117	31.0147	265.3889	265.5335	
403.780	30.8468	30.8495	258.4649	258.5980	
372.720	30.6922	30.6946	252.0591	252.1778	
341.660	30.5482	30.5502	246.1702	246.2718	
310.600	30.4149	30.4165	240.7971	240.8811	
279.540	30.2925	30.2937	235.9389	236.0069	
248.480	30.1812	30.1821	231.5945	231.6482	
217.420	30.0812	30.0819	227.7631	227.8042	

Table 2.2 Calculated nodal coordinates of the cable-only system (contd.)

X (ft)	Y (ft)		Z (ft)		Remark
	Preliminary configuration	Final configuration	Preliminary configuration	Final configuration	
186.360	29.9930	29.9934	224.4441	224.4743	
155.300	29.9168	29.9170	221.6367	221.6577	
124.240	29.8531	29.8531	219.3405	219.3539	
93.180	29.8024	29.8023	217.5550	217.5626	
62.120	29.7655	29.7653	216.2799	216.2833	
31.060	29.7429	29.7427	215.5150	215.5158	
0.000	29.7353	29.7350	215.2600	215.2600	Center

For SI: 1 ft = 0.3048 m

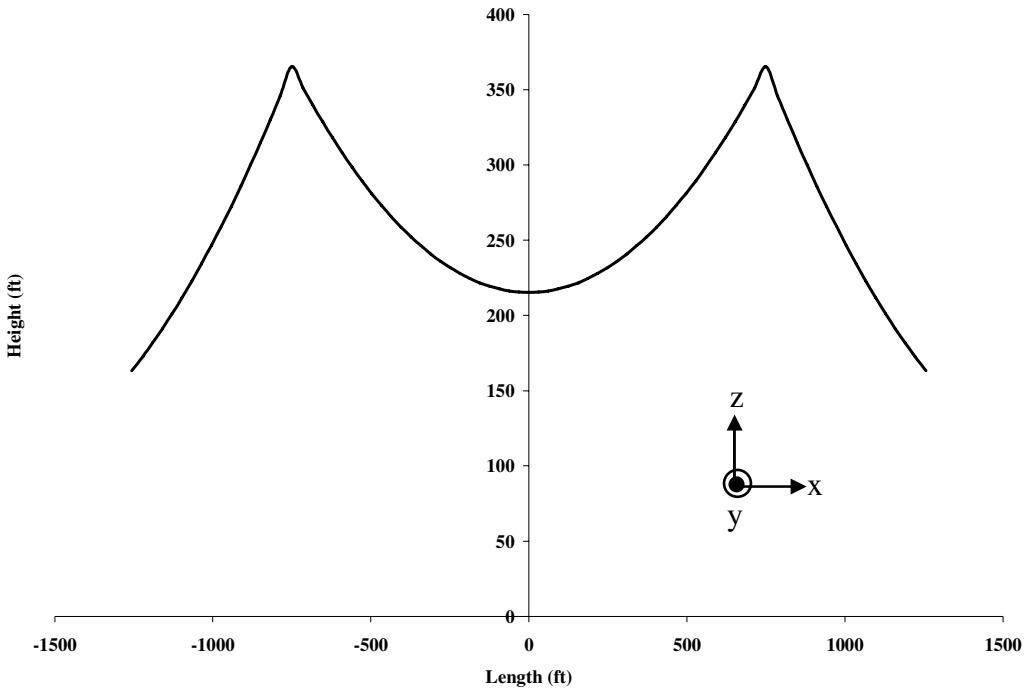

Figure 2.1 The shape of the initial cable profile under dead load

Calculations of other cross-sectional properties of girder (moment of inertia and torsional constant) are given as follows:

2.4.1 Moment of Inertia (Iz)

Moment of inertia of various members is computed from the equations in the table below and their values are given following the table.

Chord	Slab	Stringer
$I_y = A \times (e/2)^2 \times 2$	$Iy = \frac{bh^3}{12}$	$Iy = \sum_{i=1}^{4} A_i d_i^{\,2}$

Chord:

side span $= 55.56 in^2 \times 29.585^2 \times 2ea \times 2(both) = 194{,}520 in^2 ft^2$

center span $= 53.78 in^2 \times 29.585^2 \times 2ea \times 2(both) = 188{,}288 in^2 ft^2$

Slab:

Figure 2.2 shows the cross section of the deck.

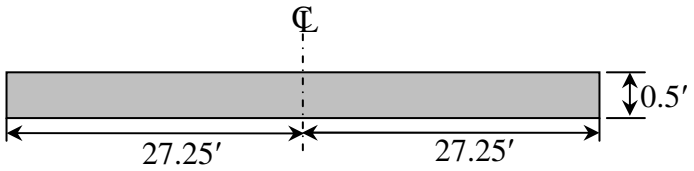

Figure 2.2 Cross section of deck

$$Iy = \frac{bh^3}{12} = \frac{54.5^3 \times 0.5}{12} = 6744.9\, ft^4$$

For equilibrant steel section: $Iy = \frac{6744.9}{15} = 449.7\, ft^4$

Stringer:

Figure 2.3 shows the location of stingers in one side of the deck.

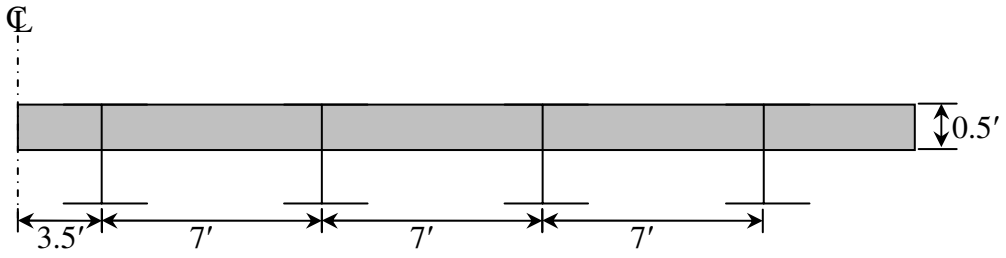

Figure 2.3 Location of stringers in one side of the deck

For one side:

$$Iz = \sum_{i=1}^{4} A_i d_i^{\,2} = 0.1389(3.5^2 + 10.5^2 + 17.5^2 + 24.5^2) = 142.93\,ft^4$$

So, for one stiffening girder $Iz = \frac{449.7}{2} + 142.93 = 367.78\,ft^4$

From (Abdel-Ghaffer, 1976),

slab + stringers : (105,000+ 290)sq. in. sq. ft./144/2=$365.59\,ft^4$

2.4.2 Torsional Constant (J)

Figure 2.4 shows commonly used lateral bracing systems and stiffening girders for suspension bridges.

$$J_i = 2\beta_i b_i d_i \;;\; \beta_i = \frac{b_i d_i \mu_{vi} \mu_{hi}}{b_i^{\,2} \times \mu_{vi} + d_i^{\,2} \times \mu_{hi}}$$

$$web: A_d = 0.117\,ft^2; k-truss: A_d = 0.115\,ft^2, Av = 0.132\,ft^2$$

b = 59.17´, d=15´ $G = \frac{E}{2(1+\mu)} \Rightarrow \mu = 0.25 \therefore \frac{E}{G} = 2.5$

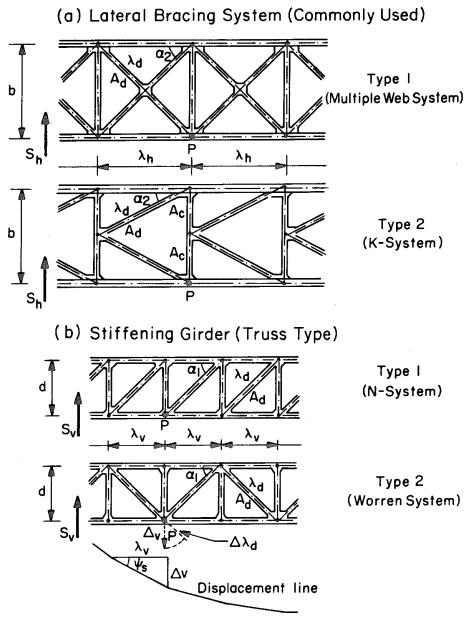

Figure 2.4 Commonly used lateral bracing systems and stiffening girders (Abdel-Ghaffer 1976)

To calculate the torsional constant of the suspension bridge girder two coefficients are used. Here, μ_h is the coefficient for horizontal K-type system and μ_V is for vertical Worren type web system. Figure 2.5 shows the horizontal K-type system and Figure 2.6 shows the for vertical Worren type web system. The procedure to calculate those two coefficients are shown below.

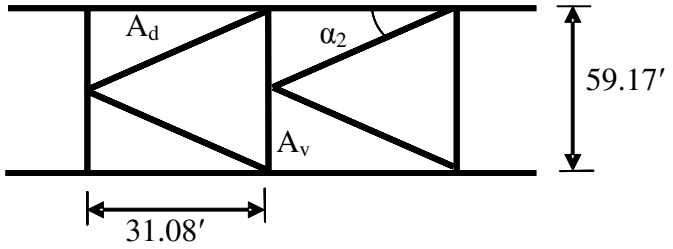

Figure 2.5 Horizontal system (K-type)

$$\alpha_2 = \tan^{-1}(\frac{59.17/2}{31.08}) = 43.6°$$

$$\mu_{h} = \frac{E}{G}(\frac{2 \times A_d \times A_v \times \sin^2 \alpha_2 \times \cos \alpha_2}{A_v + A_d \times \sin^3 \alpha_2})$$

$$= 2.5 \times (\frac{2 \times 0.114 \times 0.082 \times \sin^2 43.6° \times \cos 43.6°}{0.082 + 0.114 \times \sin^3 43.6°})$$

$$= 0.134$$

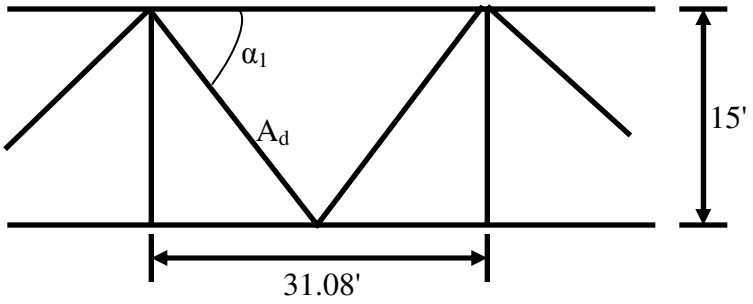

Figure 2.6 Vertical web system (Worren type)

$$\alpha_1 = \tan^{-1}(\frac{15}{31.08/2}) = 44°$$

$$\mu_v = \frac{E}{G} \times A_d \times \sin^2 \alpha_1 \times \cos \alpha_1 = 2.5 \times 0.137 \times \sin^2 44° \times \cos 44° = 0.119$$

$$\beta_i = \frac{b_i d_i \mu_{vi} \mu_{hi}}{{b_i}^2 \times \mu_{vi} + {d_i}^2 \times \mu_{hi}} = \frac{59.17 \times 15 \times 0.119 \times 0.134}{59.17^2 \times 0.119 + 15^2 \times 0.134} = 0.032$$

$$J_i = 2\beta_i b_i d_i = 2 \times 0.032 \times 59.17 \times 15 = 56.416 ft^4$$

The sectional properties computed in this section (Section 1) are summarized in Table 2.3 below for each panel.

Table 2.3 Calculated sectional properties of panels

Panel No.	Area	Torsional Constant	Iz	Iy
	ft^2	ft^4	ft^4	ft^4
1	0.958	24.342	369.010	39.367
2	0.931	23.021	369.010	39.367
3	0.911	22.944	369.010	38.234
4	0.941	21.304	369.010	41.676
5	0.972	21.304	369.010	43.398
6	0.902	16.515	369.010	43.398
7	0.972	21.304	369.010	43.398
8	0.938	19.141	369.010	43.398
9	0.938	19.141	369.010	43.398
10	0.938	19.141	369.010	43.398
11	0.972	21.304	369.010	43.398
12	1.010	23.308	369.010	43.398
13	0.979	23.308	369.010	41.676
14	0.948	24.704	369.010	38.234
15	0.968	24.797	369.010	39.367
16	0.968	24.797	369.010	39.367
17	0.866	19.188	369.010	39.367
18	0.866	19.188	369.010	39.367
19	0.846	19.141	369.010	38.234
20	0.811	16.523	369.010	38.234
21	0.811	16.523	369.010	38.234
22	0.841	16.523	369.010	39.957
23	0.824	15.034	369.010	39.957
24	0.824	15.034	369.010	39.957
25	0.824	15.034	369.010	39.957
26	0.824	15.034	369.010	39.957
27	0.855	15.034	369.010	41.680
28	0.907	19.141	369.010	41.680
29	0.907	19.141	369.010	41.680
30	0.968	19.141	369.010	45.117
31	0.968	19.141	369.010	45.117
32	0.968	19.141	369.010	45.117
33	0.968	19.141	369.010	45.117
34	0.916	15.034	369.010	45.117
35	0.916	15.034	369.010	45.117

Table 2.3 Calculated sectional properties of panels (contd.)

Panel No.	Area	Torsional Constant	Iz	Iy
	ft^2	ft^4	ft^4	ft^4
36	0.916	15.034	369.010	45.117
37	0.916	15.034	369.010	45.117
38	0.916	15.034	369.010	45.117
39	0.916	15.034	369.010	45.117
40	0.916	15.034	369.010	45.117
37	0.916	15.034	369.010	45.117
41	0.916	15.034	369.010	45.117
42	0.916	15.034	369.010	45.117
43	0.916	15.034	369.010	45.117
44	0.916	15.034	369.010	45.117
45	0.916	15.034	369.010	45.117
46	0.916	15.034	369.010	45.117
47	0.916	15.034	369.010	45.117
48	0.968	19.141	369.010	45.117
49	0.968	19.141	369.010	45.117
50	0.968	19.141	369.010	45.117
51	0.907	19.141	369.010	41.680
52	0.907	19.141	369.010	41.680
53	0.907	19.141	369.010	41.680
54	0.824	15.034	369.010	39.957
55	0.824	15.034	369.010	39.957
56	0.824	15.034	369.010	39.957
57	0.824	15.034	369.010	39.957
58	0.841	16.523	369.010	39.957
59	0.811	16.523	369.010	38.234
60	0.811	16.523	369.010	38.234
61	0.846	19.141	369.010	38.234
62	0.866	19.188	369.010	39.367
63	0.866	19.188	369.010	39.367
64	0.968	24.797	369.010	39.367
65	0.968	24.797	369.010	39.367
66	0.948	24.704	369.010	38.234
67	0.979	23.308	369.010	41.676
68	1.010	23.308	369.010	43.398
69	0.972	21.304	369.010	43.398

Table 2.3 Calculated sectional properties of panels (contd.)

Panel No.	Area	Torsional Constant	Iz	Iy
	ft^2	ft^4	ft^4	ft^4
70	0.938	19.141	369.010	43.398
71	0.938	19.141	369.010	43.398
72	0.938	19.141	369.010	43.398
73	0.972	21.304	369.010	43.398
74	0.902	16.515	369.010	43.398
75	0.972	21.304	369.010	43.398
76	0.941	21.304	369.010	41.676
77	0.911	22.944	369.010	38.234
78	0.931	23.021	369.010	39.367
79	0.958	24.342	369.010	39.367
80	0.958	24.342	369.010	39.367

For SI: 1 ft = 0.3048 m

Calculation of tower cross-sectional properties:

For thin walled closed sections the torsional constant is given by the following formula

(Bredt's formula): $$J = \frac{4A^2}{\oint \frac{ds}{t}}$$

Different sections of the tower is shown in Figure 2.7 and a typical plan view of the tower section is shown in Figure 2.8. Table 2.4 and 2.5 show the calculated sectional properties of the tower section at different heights for before and after retrofit models respectively.

2.5 Member-Based Detail Model

Finite Element modeling of the detailed structure is done with the help of SAP 2000 V10 (Computer and Structures, 2002). The cables and suspenders are modeled as 3D elastic truss elements. The chords, vertical members and the diagonal members in the stiffening

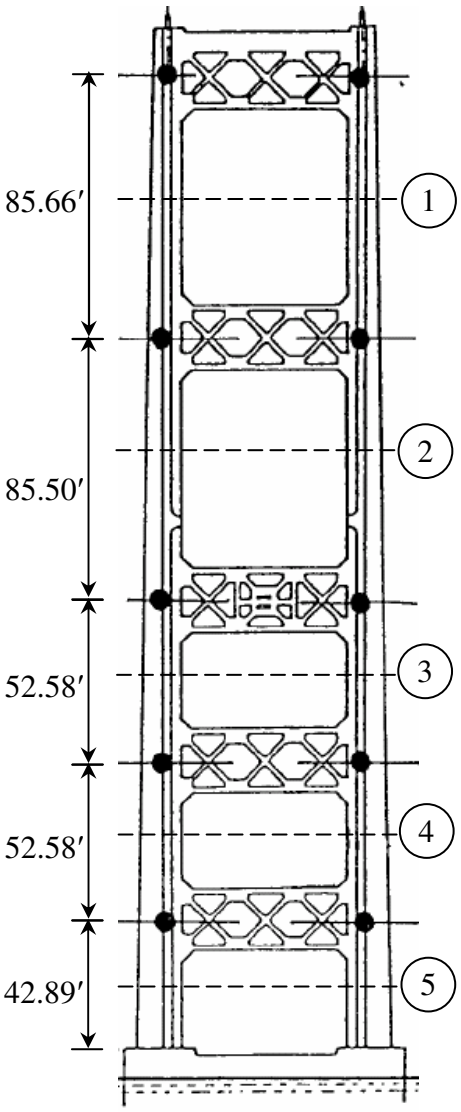

Figure 2.7 Different sections of the tower

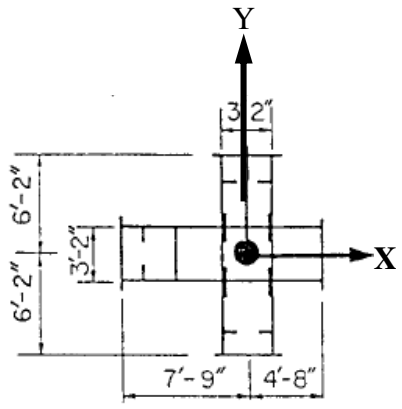

Figure 2.8 Typical tower cross-section

Table 2.4 Calculated sectional properties of the tower sections (before retrofit)

Section No.	Area	Ix	Iy	Torsional Constant
	ft^2	ft^4	ft^4	ft^4
1	3.18	20.42	21.07	17.81
2	4.35	42.75	48.25	25.69
3	4.92	57.64	65.06	26.89
4	4.93	60.32	65.86	29.14
5	5.47	76.11	90.37	34.20

For SI: 1 ft = 0.3048 m

Table 2.5 Calculated sectional properties of the tower sections (after retrofit)

Section No.	Area	Ix	Iy	Torsional Constant
	ft^2	ft^4	ft^4	ft^4
1	3.66	23.48	24.23	23.55
2	5.00	49.16	55.49	33.98
3	5.66	66.29	74.82	35.57
4	5.67	69.37	75.74	38.54
5	6.29	87.53	103.93	45.23

For SI: 1 ft = 0.3048 m

girder are modeled as 3D truss elements. Also members in the diaphragm are modeled as truss elements. The tower, the cable bent leg, and strut members are modeled as frame elements. The reinforced-concrete deck is modeled as shell element and the supporting stringers are modeled as beam elements.

Hydraulic, viscous dampers between tower and the suspended structure are also modeled according to their properties mentioned in the design drawing. Mass is taken distributed over each and every member. To consider the mass of non-structural components, equivalent point mass and mass moment of inertia are distributed at joints in the diaphragm.

The most important structural components that are considered for post-retrofit modeling are suspended truss system, deck shear connectors, cable bent cross-sections,

suspenders and dampers installed. Figure 2.9 shows detailed model of one panel and construction drawing.

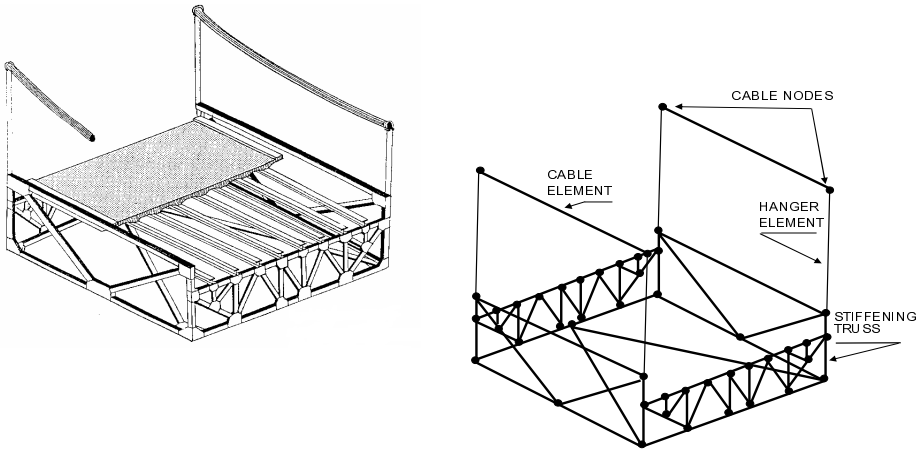

Figure 2.9 The detailed model of one panel

2.5.1 Cable Bent

Four feet of stiffening truss in the cable bent was removed to allow free oscillations of the side spans of the bridge. Also, the cable bent cross section was changed. This change in the cross section is considered in the post-retrofit modeling of the bridge. Cross sectional properties of the modified sections are calculated and used in the post-retrofit analysis.

2.5.2 Deck Shear Connector

Deck shear connectors were replaced with new types. Deck shear connectors of the original structure were removed and then a new set was introduced. Figures 2.10 and 2.11 (taken from Design Drawing) shows the comparison between the shapes of the deck shear connectors before and after retrofit. The FE modeling is done according to this design drawing.

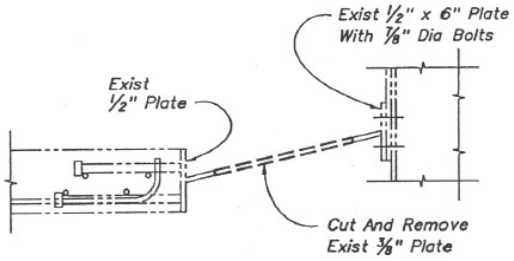

Figure 2.10 Deck shear connector (before retrofit)

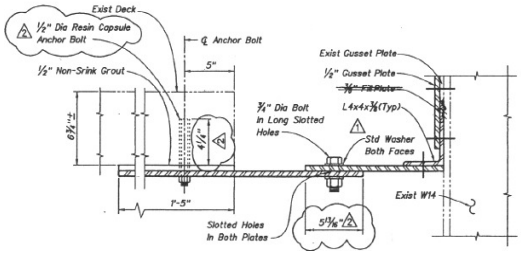

Figure 2.11 Deck shear connector (after retrofit)

2.5.3 Dampers

Total of 48 dampers were installed in the bridge as a retrofit measure with 16 dampers installed in each tower, at the junction between tower and girder connection. In each cable bent, 4 dampers were installed. In the middle of each side span a new diaphragm was inserted. At the location of the inserted diaphragm, 4 more dampers were installed in each side span. These 8 dampers in the side spans were non-linear dampers having the form of $F = cv^n$ where n = 0.5. For all other dampers, n = 1.0 is used.

2.5.4 Suspended Truss

The suspended truss structure was modified by inserting new members and also replacing some members in the K-truss in the middle span as well as in the side spans. Figure 2.12 (taken from Design Drawing) shows the modifications made in the K-truss.

2.5.5 Suspenders

Some suspenders in the middle span were replaced with new suspenders. Figure 2.13 (taken from Design Drawing) describes the modified suspenders in the middle span.

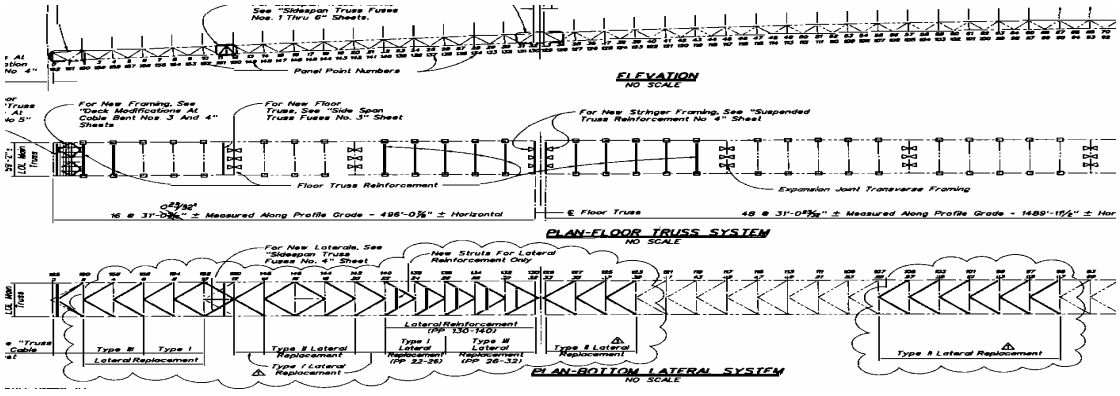

Figure 2.12 K-truss modifications after retrofit

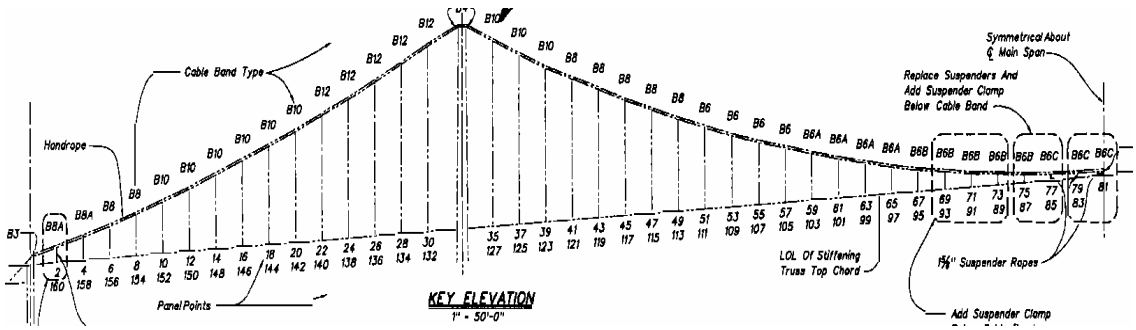

Figure 2.13 Suspender modifications after retrofit

2.6 Eigen Value Analysis

First 100 eigen vectors were calculated with a convergence tolerance of 1.0×10^{-5}. Table 2.6 shows the comparison of modal frequencies obtained from before retrofit panel-based simple model and member-based detailed model with analytical eigen properties of the bridge obtained by previous researchers. Table 2.7 shows the aforementioned comparison of results obtained from after retrofit model of the bridge, In the tables the computed modal frequencies were obtained from the FE models by using SUCOT (Kim, 1993) and

SAP 2000 V 10 (Computers and Structures, 2002). It can be seen from the results that the computed modal frequencies obtained from the SUCOT and the SAP 2000 panel based model are having a good match with the calculated frequencies from finite element models developed by previous researchers. First three modes obtained from the SAP 2000 model are shown in Figure 2.14.

Figure 2.14 First three mode shapes of the simple model

Table 2.6 Comparison of modal frequencies in Hz (before retrofit)

Dominant Motion	Abdel-Ghaffar, 1976	Niazy et al., 1991	Present study		
			Panel-based simple		Member-based detailed
			SUCOT	SAP 2000	SAP 2000
L*-S*	0.173	0.169	0.159	0.152	0.161
V*-AS*	0.197	0.201	0.210	0.223	0.221
V-S	0.221	0.224	0.232	0.239	0.226
V-S	0.348	0.336	0.460	0.384	0.363
V-AS	0.346	0.344	0.456	0.495	0.369
L-AS	0.565	0.432	0.472	0.448	0.503
T*-S	0.449	0.438	0.483	0.482	0.477
V-S	0.459	0.442	0.500	0.538	0.479

* L: Lateral, S: Symmetric, V: Vertical, AS: Asymmetric and T: Torsional

Table 2.7 Comparison of modal frequencies in Hz (after retrofit)

Dominant motion	Ingham et al., 1997 (ADINA)		Fraser, 2003 (ADINA)	Present Study		
				Panel-based Simple		Member-based Detailed
	Simple	Detailed	Detailed	SUCOT	SAP 2000	SAP 2000
L-S	0.162	0.135	0.130	0.161	0.152	0.160
V-AS	0.197	0.171	0.182	0.210	0.218	0.220
V-S	0.232	0.229	0.226	0.232	0.235	0.226
V-S	-	-	-	0.360	0.369	0.362
V-AS	-	-	-	0.453	0.469	0.372
L-AS	0.535	0.420	0.409	0.473	0.447	0.494
T-S	0.588	0.510	0.511	0.490	0.484	0.482
V-S	-	-	-	0.498	0.513	0.486

* L: Lateral, S: Symmetric, V: Vertical, AS: Asymmetric and T: Torsional

2.7 Closure

In this chapter numerical modeling has been achieved for Vincent Thomas Bridge. A member-based detailed three-dimensional Finite Element (FE) as well as a panel-based simplified model of the Vincent Thomas Bridge have been developed for the bridge before and after retrofit. First eight modal frequencies obtained from FE models developed using different commercially available softwares have been compared. The results obtained from this study are also compared with previous results obtained for the bridge. It has been observed that the first lateral modal frequency for the member-based detailed model is 20% higher than those presented in previous studies. It is also found

that results of panel-based simple models are in good agreement with those obtained from the detailed model and those reported in previous similar studies.

CHAPTER 3

SYSTEM IDENTIFICATION AND MODEL VERIFICATION

3.1 Background

To ensure the validity of the analytical finite element model of a massive structure like a suspension bridge, the eigenproperties obtained from the analytical model should be compared with the identified modal frequencies. Modal identification can be done by using measured ambient vibration response or strong motion earthquake response of the bridge. The response of the bridge, under external excitations, is measured with the help of acceleration measuring sensors installed at different locations of the bridge.

3.2 Evaluation of Eigenproperties using Ambient Vibration Data

Experimental modal analysis has drawn significant attention from structural engineers for updating the analysis model and estimating the present state of structural integrity. Forced vibration tests such as impact tests can be carried out to this end. However, it is usually restricted to small-size structures or to their components. For large structures such as dams, and long-span bridges, ambient vibration tests under wind, wave, or traffic loadings are the effective alternatives. In this study, modal parameters were obtained using the frequency domain decomposition technique (Otte et al, 1990 and Brincker et al., 2000) which is one of the frequency domain methods without using input information.

It is very difficult, if not impossible, to identify closely spaced modes using the

peak-picking (PP) method. In this case, the frequency domain decomposition (FDD) method that utilizes the singular value decomposition of the PSD matrix may be used to separate close modes (Brincker et al., 2000). The method was originally used to extract the operational deflection shapes in mechanical vibrating systems (Otte et al, 1990). The natural frequencies are estimated from the peaks of the PSD functions in the PP method. On the other hand, they are evaluated from singular value (SV) functions of the PSD matrix in the FDD method.

$$S_{yy}(\omega) = U(\omega) s(\omega) V(\omega)^T \tag{3.1}$$

where $S_{yy}(\omega) \in R^{N_m \times N_m}$ is the PSD matrix for output responses $y(t) \in R^{N_m}$, $s(\omega) \in R^{N_m \times N_m}$ is a diagonal matrix containing the singular values of its PSD matrix, and, $U(\omega)$, $V(\omega) \in R^{N_m \times N_m}$ are corresponding unitary matrices. N_m is the number of measuring points. The general multi-DOF system can be transformed to the single DOF system nearby its natural frequencies by singular value decomposition. The mode shape can be estimated as the first column vector of the unitary matrix of *U* since the first singular value may include the structural mode nearby its natural frequencies. However in the closely spaced modes, the peak of largest singular values at one natural frequency indicates the structural mode and adjacent second singular value may indicate the close mode.

Figure 3.1 shows the layout of the acceleration sensors installed in the bridge site. Table 3.1 describes the location and direction of all the accelerometers present in the bridge site. Figure 3.2 shows the vertical accelerometers and Figure 3.3 shows the lateral

accelerometers used in the modal identification of the bridge structure. Figure 3.4 shows the plot of SV vs. frequency for the acceleration data obtained from vertical channels.

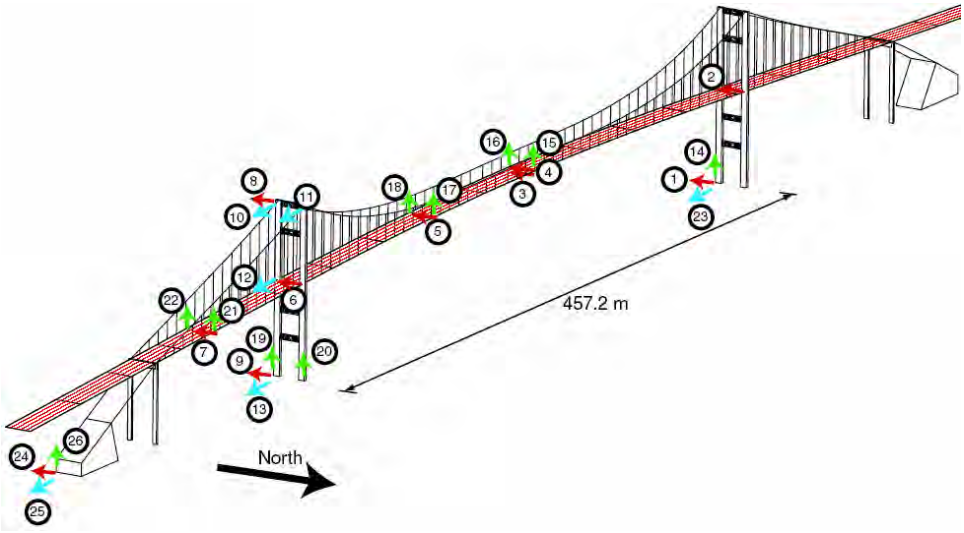

Figure 3.1 Location and direction of sensors installed in the bridge

Table 3.1 Location and direction of accelerometers

Sensor Number	Sensor Location	Sensor Direction
22, 15, 16, 17, 18, 21	Truss top/Deck	Vertical
2, 4, 5, 6, 7	Truss top/Deck	Lateral
12	Truss top/Deck	Longitudinal
3	Truss bottom	Lateral
8	Tower	Lateral
10, 11	Tower	Longitudinal
14, 19, 20	Tower base	Vertical
1, 9	Tower base	Lateral
13, 23	Tower base	Longitudinal
26	Anchorage	Vertical
24	Anchorage	Lateral
25	Anchorage	Longitudinal

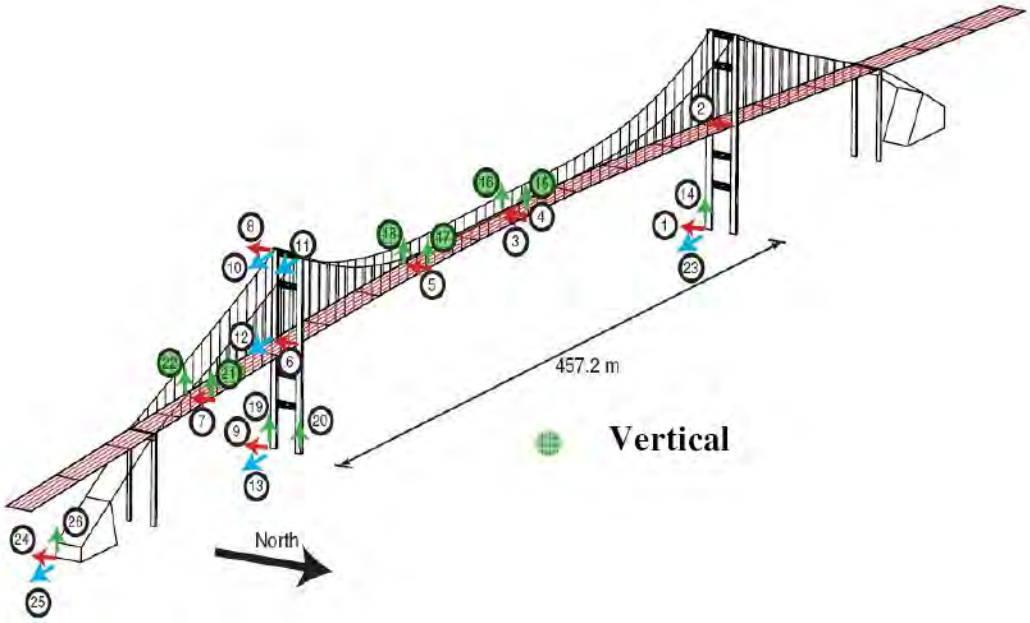

Figure 3.2 Vertical accelerometer data used in the study

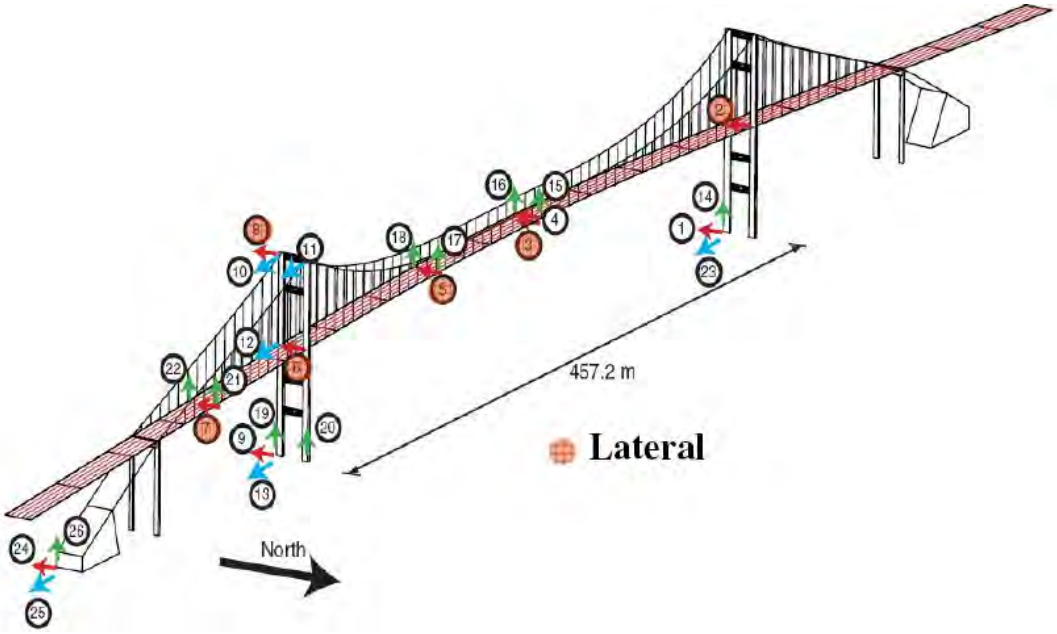

Figure 3.3 Lateral accelerometer data used in the study

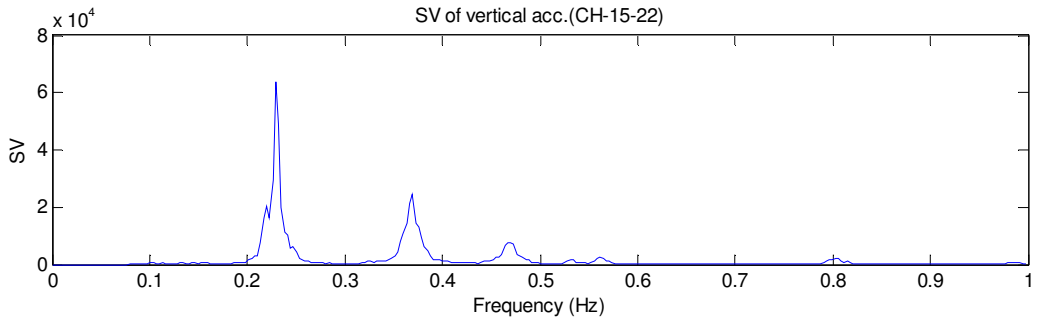

Figure 3.4 Plot of SV vs. Frequency

3.3 Comparison of System ID Result with Analytical Eigen Properties

In this study, modal parameters have been obtained using the frequency domain decomposition (FDD) technique (Brincker et al. 2000) which is one of the frequency domain methods without using in-put information. The method utilizes the singular value decomposition of the PSD matrix and may be used to separate close modes. Total 15 ambient vibration recording has been used for this purpose from the installed sensors. The data were recorded from April, 2003 to October, 2004, over 1 year 6 months record has been considered for system identification analysis. Average identified modal frequencies obtained from 15 data-set are considered as final identified modal frequencies from the ambient vibration data. Figure 1 shows previously installed sensor locations on the bridge. For system ID from ambient vibration data, vertical sensors 15, 16, 17, 18, 21, 22 and lateral sensors 4, 5, 6, 7 are used. Sensor # 3 in the lateral direction is excluded because it provided some noisy data.

Table 3.2 and 3.3 below shows the comparison of modal frequencies before and after retrofitting of the bridge. Modal identification results from ambient vibration data are also tabulated in Table 3.3. It can be seen from Table 3.3 that in the first mode of

vibration, the structure is a little bit stiffer in the simple model rather than detailed model. In case of first mode of vibration the system ID result matches with the frequency obtained from the detailed model. Also, from the second mode and above both the analytical and system ID results shows pretty good match. On an average sense, it can be seen from Table 3.3 that system ID results show pretty good match with detailed model.

3.4 Modal Parameter Identification from Chino Hills Earthquake Response

Chino Hills earthquake data recorded at the bridge site are also used in the modal identification. Chino Hills earthquake occurred on July 29, 2008, in Southern California. The epicenter of the magnitude 5.4 earthquake was in Chino Hills, approximately 45 km east-southeast of downtown Los Angeles. Table 3.4 compares the modal frequencies of the bridge obtained from ambient vibration and Chino Hills earthquake data. These two identified frequencies matches very well. Note also that the two other previous studies (Ingham et al. 1997 and Fraser 2003) involving detailed models under predict modal frequencies significantly for the first two modes. Results from these two studies are also tabulated in Table 3.4.

Table 3.2 Comparison of modal frequencies in Hz (before retrofit)

Dominant Motion	Identified (System ID)			Computed				
	Abdel-Ghaffar and Housner, 1977 (Ambient)	Niazy et al., 1991 (Whittier)	Ingham et al., 1997 (Northridge)	Abdel-Ghaffar, 1976	Niazy et al., 1991	Present Study		
						Panel-based Simple		Member-based Detailed
						SUCOT	SAP 2000	SAP 2000
L*-S*	0.168	0.149	0.145	0.173	0.169	0.159	0.152	0.161
V*-AS*	0.216	0.209	-	0.197	0.201	0.210	0.223	0.221
V-S	0.234	0.224	0.222	0.221	0.224	0.232	0.239	0.226
V-S	0.366	0.363	0.370	0.348	0.336	0.460	0.384	0.363
V-AS	-	0.373	-	0.346	0.344	0.456	0.495	0.369
L-AS	0.623	0.459	0.417	0.565	0.432	0.472	0.448	0.503
T*-S	0.494	0.513	0.556	0.449	0.438	0.483	0.482	0.477
V-S	0.487	0.448	-	0.459	0.442	0.500	0.538	0.479

* L: Lateral, S: Symmetric, V: Vertical, AS: Anti-Symmetric, T: Torsional

Table 3.3 Comparison of modal frequencies in Hz (after retrofit)

Dominant Motion	Identified (System ID)			Computed					
	Fraser, 2003	He et al., 2008	Present Study (Ambient)			Fraser, 2003 (ADINA)	Present Study		
							Panel-based Simple		Member-based Detailed
				Simple	Detailed	Detailed	SUCOT	SAP 2000	SAP 2000
L-S	0.150	-	0.162	0.162	0.135	0.130	0.161	0.152	0.160
V-AS	-	0.168	0.219	0.197	0.171	0.182	0.210	0.218	0.220
V-S	0.233	0.224	0.229	0.232	0.229	0.226	0.232	0.235	0.226
V-S	0.367	0.356	0.369	-	-	-	0.360	0.369	0.362
V-AS	-	-	-	-	-	-	0.453	0.469	0.372
L-AS	-	-	0.534	0.535	0.420	0.409	0.473	0.447	0.494
T-S	-	0.483	0.471	0.588	0.510	0.511	0.490	0.484	0.482
V-S	-	-	-	-	-	-	0.498	0.513	0.486

* L: Lateral, S: Symmetric, V: Vertical, AS: Anti-Symmetric, T: Torsional

Table 3.4 Comparison of modal frequencies (in Hz) of the Vincent Thomas Bridge

Mode Number	Dominant Motion	Identified (System ID)		Computed		
		Ambient Vibration	Chino Hills Earthquake	SAP 2000 (Present Study)	Ingham et al., 1997	Fraser, 2003
1	L*-S*1	0.162	0.168	0.160	0.135	0.130
2	V*-AS*1	0.219	-	0.220	0.171	0.182
3	V-S1	0.229	0.228	0.222	0.229	0.226
4	V-S2	0.369	0.362	0.362	-	-
5	V-AS2	-	0.467	0.372	-	-
6	T*-S1	0.471	0.491	0.478	0.510	0.511
7	V-S3	-	-	0.483	-	-
8	L-AS1	0.534	-	0.491	0.420	0.409

* L: Lateral, S: Symmetric, V: Vertical, AS: Anti-Symmetric, T: Torsional

3.5 Effect of Parameter Uncertainty on Modal Frequency

3.5.1 Soil Spring Modeling

To consider the effect of soil structure interaction kinematic three translational and three rotational soil springs with their coupling effects are considered at the foundations of east tower, west tower, east cable bent, west cable bent, east anchorage and west anchorage. The stiffness of the soil springs are calculated from the equivalent pile group stiffness at the foundations discussed earlier. Table 3.5 gives the number of piles at different foundations considered for the FE model of the bridge. Figure 3.5 shows the finite element model of the bridge with foundation springs.

Table 3.5 Location and number of piles considered

Location	Number of piles
East tower	167
West tower	167
East cable bent	48
Wast cable bent	48
East anchorage	188
West anchorage	188

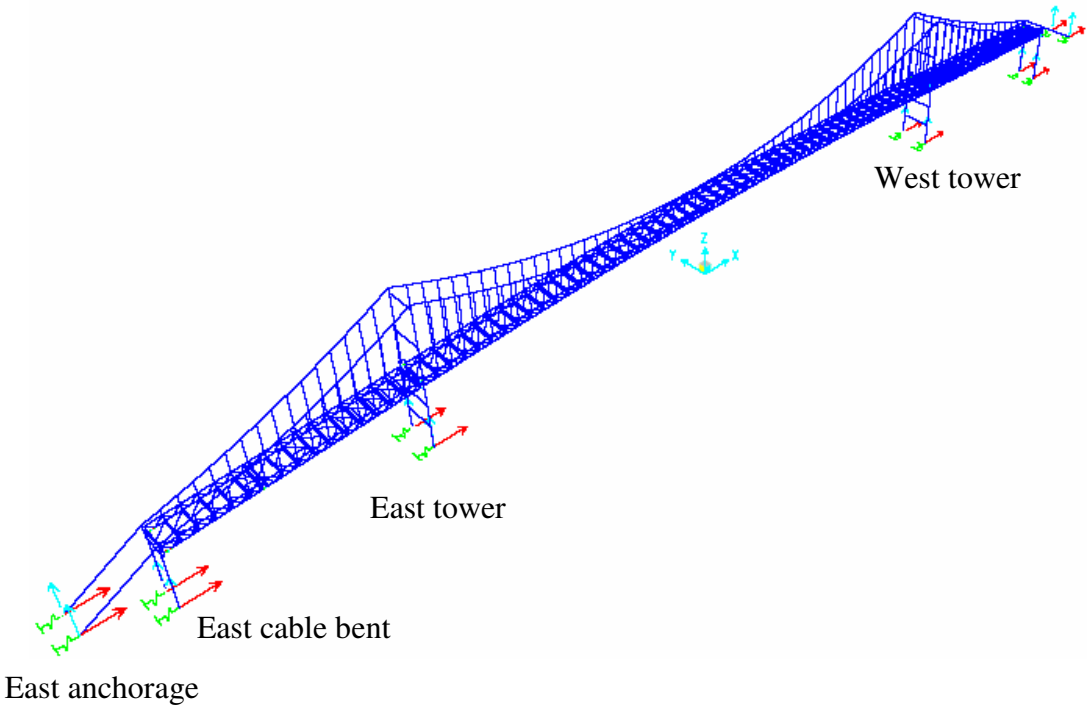

Figure 3.5 Detailed model in SAP 2000 with foundation springs

3.5.2 Uncertain Parameters Considered

For model updating purpose, in ideal case, all parameters related to elastic, inertial properties and boundary conditions should be considered. However, if too many parameters are considered for model updating then chances of obtaining unreliable model increases (Zhang et al., 2001). For this reason, parameter selection is a very important

task in model updating process. Practically if the parameters considered do not have much effect on the modal frequencies and mode shapes, then they should be excluded from the list. Therefore a comprehensive eigenvalue sensitivity study is performed to figure out the most sensitive parameters to be considered for suspension bridge finite element model calibration.

Total 19 parameters are considered for the sensitivity analysis. The selection of these parameters is based on the outcome of previous research (Zhang et al., 2001) and engineering judgments. Elastic modulus and mass density of different set of structural members, boundary conditions (deck and tower connection and deck and cable bent connection) and stiffness of the soil springs are considered as variable parameters. However the cable and the concrete deck have homogeneous properties, but due to corrosion the structural strength may get decreased over the service life of the bridge. To capture that effect, elastic modulus and mass density of cable and concrete deck is considered as variable parameters in the analysis. Also, for the generality of the analysis kinematic spring stiffnesses (soil spring stiffness) are also considered as variable parameters in the analysis. Since there was no tower dominant mode in the considered first 8 mode shapes, therefore, the stiffness and inertial properties of the tower is not considered as a variable parameter in the present study.

For evaluating the effect of uncertainty in the modal parameters of Vincent Thomas Bridge, uncertainty associated with elastic and inertial property of different members is represented by assigning a mean and standard deviation in terms of coefficient of variation for each parameter. The mean values considered here are calculated based on the design drawing of the bridge. Table 3.6 lists these parameters with their mean values.

To asses the sensitivity, coefficients of variation (COV) of all the parameters are considered as 10%. In the analysis, all the 36 values of the spring stiffness matrices are varied by 10% for the case of east tower, west tower, east cable bent and west cable bent. For the first-order second-moment (FOSM) analysis only lateral translational stiffness of each foundation spring is considered.

Table 3.6 Parameters considered for sensitivity analysis

Serial Number	Parameters	Mean Value
1	Side link elastic modulus	2.00×10^8 kPa
2	Cable bent and girder connection elastic modulus	2.00×10^8 kPa
3	Top Chord Elastic Modulus	2.00×10^8 kPa
4	Top Chord Mass Density	7.85 kg/m^3
5	Bottom Chord Elastic Modulus	2.00×10^8 kPa
6	Bottom Chord Mass Density	7.85 kg/m^3
7	Stringer Elastic Modulus	2.00×10^8 kPa
8	Stringer Mass Density	7.85 kg/m^3
9	Deck Slab Elastic Modulus	2.48×10^7 kPa
10	Deck Slab Mass Density	1.48 kg/m^3
11	Main Cable Elastic Modulus	1.66×10^8 kPa
12	Main Cable Mass Density	8.37 kg/m^3
13	Suspender Elastic Modulus	1.38×10^8 kPa
14	Suspender Mass Density	7.85 kg/m^3
15	Wind Shoe Elastic Modulus	2.00×10^8 kPa
16	East Tower Spring	1.30×10^6 kPa
17	East Cable Bent Spring	7.35×10^6 kPa
18	West Tower Spring	1.19×10^6 kPa
19	West Cable Bent Spring	4.65×10^6 kPa

3.5.3 Analysis methods

Reduction of the number of uncertain parameters cuts down the computational effort and cost. One way of doing this is to identify those parameters with associated ranges of uncertainty that lead to relatively insignificant variability in response and then treating these as deterministic parameters by fixing their values at their best estimate, such as the mean. For ranking uncertain parameters according to their sensitivity to desired response

parameters, there are various methods such as tornado diagram analysis, first order second moment (FOSM) analysis, and Monte Carlo simulation (Porter et al. 2002, Lee and Mosalam 2006). Monte Carlo simulation, which is computationally demanding due to the requirement of a large number of simulations, especially for a model consisting of a large number of degrees of freedom as in the case here, is not used in this study because of these practical considerations. Instead, the tornado diagram analysis and the FOSM analysis have been used here due to their simplicity and efficiency to identify sensitivity of uncertain parameters.

For the tornado diagram analysis, all uncertain parameters are assumed as random variables, and for each of these random variables, two extreme values the 84^{th} percentile and 16^{th} percentile corresponding to assumed upper and lower bounds, respectively, of its probability distribution have been selected. One can observe that these extreme values come from the normal distribution assumption, mean + standard deviation and mean – standard deviation, respectively representing their upper and lower bounds. Using these two extreme values for a certain selected random variable, the modal frequencies of the model has been evaluated for both cases, while all other random variables have been assumed to be deterministic parameter with values equal to their mean value. The absolute difference of these two modal frequency values corresponding to the two extreme values of that random variable, which is termed as swing of the modal frequency corresponding to the selected random variable, is calculated.

This calculation procedure has then been repeated for all random variables in question. Finally, these swings have been plotted in a figure from the top to the bottom in a descending order according to their size to demonstrate the relative contribution of each

variable to the specific mode under question. It is noteworthy that longer swing implies that the corresponding variable has larger effect on the modal frequency than those with shorter swing.

For the FOSM analysis, the modal frequency has been considered as a random variable Y, which has been expressed as the function of random variables, X_i (for i = 1 to N) denoting uncertain parameters and Y is given by

$$Y = g(X_1, X_2, ..., X_N) \tag{3.2}$$

Let X_i has been characterized by mean μ_X and variance σ_X^2. Now, the derivatives of $g(X)$ with respect to X_i , one can express Y by expanding Eq. (3.2) in Taylor series as

$$Y = g(\mu_{X_1}, \mu_{X_2}, \ldots, \mu_{X_N}) + \frac{1}{1!}\sum_{i=1}^{N}(X_i - \mu_{X_i})\frac{\delta g}{\delta X_i} + \frac{1}{2!}\sum_{i=1}^{N}\sum_{j=1}^{N}(X_i - \mu_{X_i})(X_j - \mu_{X_j})\frac{\delta^2 g}{\delta X_i \delta X_j} + \cdots\cdots \tag{3.3}$$

Considering only the first order terms of Eq. (3.3) and ignoring higher order terms Y can be approximated as

$$Y \approx g(\mu_{X_1}, \mu_{X_2}, \ldots, \mu_{X_N}) + \frac{1}{1!}\sum_{i=1}^{N}(X_i - \mu_{X_i})\frac{\delta g}{\delta X_i} \tag{3.4}$$

Taking expectation of both sides, the mean of Y, μ_Y can be expressed as

$$\mu_Y \approx g(\mu_{X_1}, \mu_{X_2}, \ldots, \mu_{X_N}) \tag{3.5}$$

Utilizing the second moment of Y as expressed in Eq. (3.4) and simplifying, the variance of Y, σ_Y^2 can be derived as

$$\sigma_Y^2 \approx \sum_{i=1}^{N}\sum_{j=1}^{N}\mathrm{cov}(X_i, X_j)\frac{\delta g(X_1, X_2, ..., X_N)}{\delta X_i}\frac{\delta g(X_1, X_2, ..., X_N)}{\delta X_j}$$

$$\approx \sum_{i=1}^{N} \sigma_{X_i}^2 \left(\frac{\delta g(X_1, X_2, ..., X_N)}{\delta X_i} \right)^2 + \sum_{i=1}^{N} \sum_{j \neq i}^{N} \rho_{X_i X_j} \frac{\delta g(X_1, X_2, ..., X_N)}{\delta X_i} \frac{\delta g(X_1, X_2, ..., X_N)}{\delta X_j} \quad (3.6)$$

where $\rho_{X_i X_j}$ denotes correlation coefficient for random values X_i and X_j (i.e., coefficient defining the degree to which one variable is related to another). The partial derivative of $g(X_1, X_2, ..., X_N)$ with respect to X_i has been calculated numerically using the finite difference equation given below

$$\frac{\delta g(X_1, X_2, ..., X_N)}{\delta X_i} = \frac{g(x_1, x_2, ..., \mu_i + \Delta x_i, x_N) - g(x_1, x_2, ..., \mu_i - \Delta x_i, x_N)}{2\Delta x_i} \quad (3.7)$$

In this case, a large number of simulations were performed varying each input parameter individually to approximate the partial derivatives as given in Eq. (3.7). For these calculations, the mean and the standard deviation values given in Table 3.6 are used.

For these sensitivity analyses, at first, the reference model with mean parameters of each 19 random variable considered in this study is analyzed. Then the analyses have been carried out using their lower and then upper bounds. Altogether 39 cases of modal analysis are performed for each set of parameters, modal frequencies expressed as $Y = g(X_1, X_2, ..., X_N)$ is observed.

3.5.4 Sensitivity of Modal Frequencies

For tornado diagram analysis, all the 19 parameters shown in Table 3.6 are used for total 8 mode shapes. Figures 3.6 (a-h) show tornado diagrams for 8 modes developed according to the procedure in section 3.5.3. The vertical line in the middle of tornado

diagrams indicates modal frequency value calculated for a certain mode considering only the mean values of all random variables and the length of each swing (horizontal bar) represents the variation in the modal frequency due to the variation in the respective random variable.

It is clear from Figures 3.6 (a-e) that, up to mode # 5 deck slab mass density and bottom chord elastic modulus have almost the largest contribution in response variability. In mode numbers 2, 3, 6, and 7, mostly vertical and torsional modes, main cable elastic modulus is significant contributor of the response variability. One can also notice from Figures 3.6 (a-h) that couple of swings are asymmetric about the vertical line. This skew of the modal frequency distributions implies that the problem is highly nonlinear. In other words, the same amount of a positive and a negative change in these parameters does not produce the same amount of variation in modal frequency. This skewness is very clear for 2^{nd} mode in case of main cable elastic modulus variation. Since the 2^{nd} mode is vertical antisymmetric, increase is main cable elastic modulus does not have much effect on increase in frequency but decrease in the stiffness of main cable decreases the frequency by 8% from the base model frequency.

Interestingly, deck slab stiffness has most contribution in the 1^{st} mode, but it does not have any contribution in rest of the modes except the 8^{th} mode. Most of the boundary condition (P1, P2, and P15) and soil spring (P16, P17, P18, and P19) related parameters have very insignificant effect on response variability.

For FOSM method, analyses have been carried out to determine the sensitivity of modal frequencies to the uncertainty in each random variable. Focus has been placed on the variance of modal frequency when considering uncertainties of 19 input parameters.

Figures 3.7 (a-h) show relative variance contributions of each parameter to the modal frequency when the correlation, as given in the second term of Eq. (3.6), is neglected. From this figure, it can be observed that the uncertainties in the deck slab mass density and bottom chord elastic modulus contribute mostly to the variance of modal frequencies. This is the same trend as observed from the tornado diagram analysis for all the 8 modes considered.

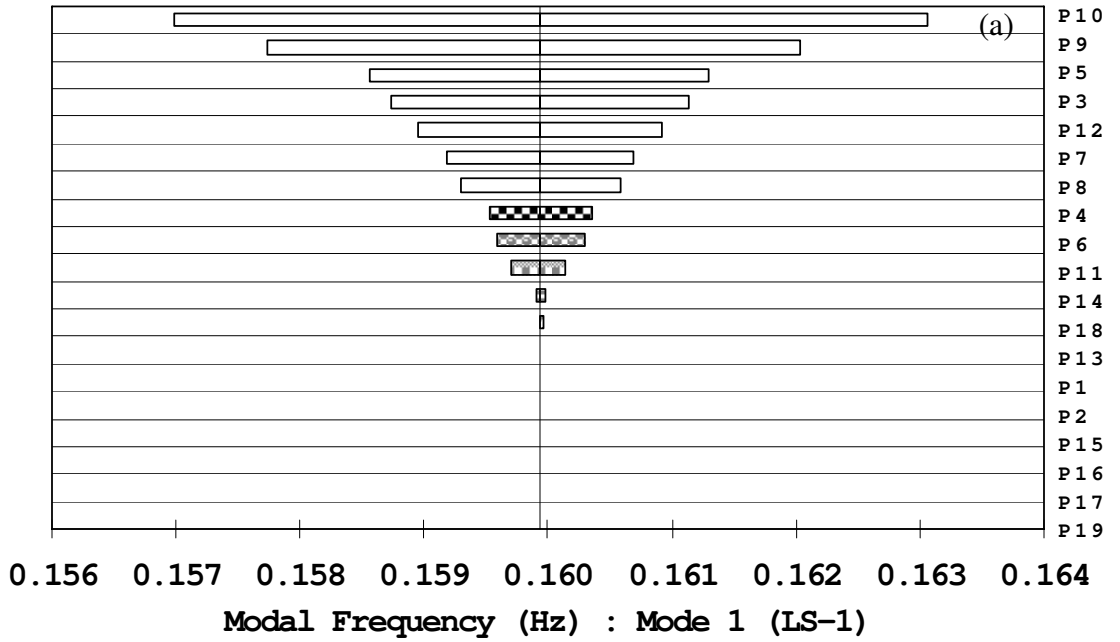
(a)
P10
P9
P5
P3
P12
P7
P8
P4
P6
P11
P14
P18
P13
P1
P2
P15
P16
P17
P19
0.156 0.157 0.158 0.159 0.160 0.161 0.162 0.163 0.164
Modal Frequency (Hz) : Mode 1 (LS-1)

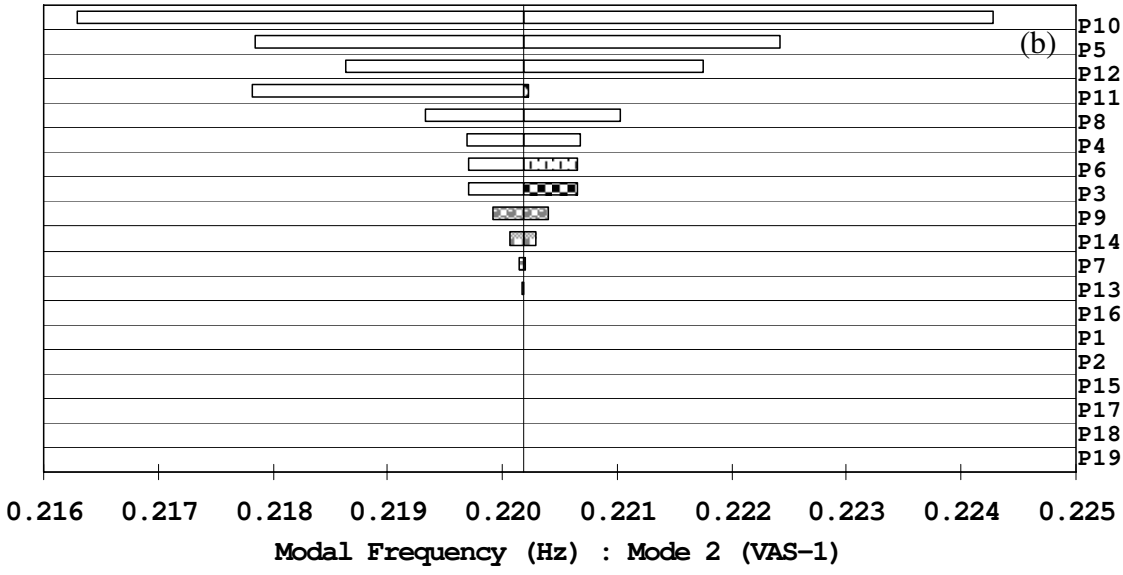
(b)
P10
P5
P12
P11
P8
P4
P6
P3
P9
P14
P7
P13
P16
P1
P2
P15
P17
P18
P19
0.216 0.217 0.218 0.219 0.220 0.221 0.222 0.223 0.224 0.225
Modal Frequency (Hz) : Mode 2 (VAS-1)

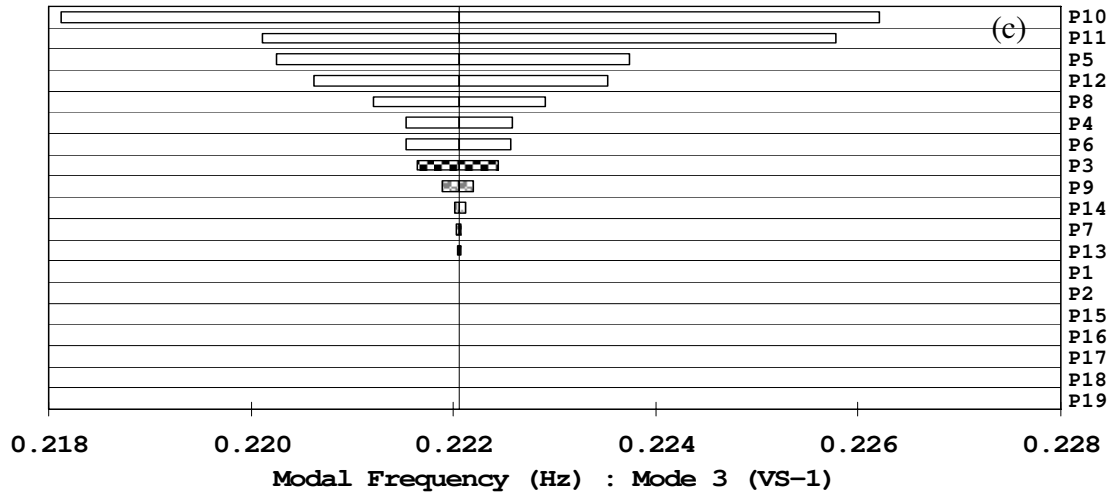
(c)
P10
P11
P5
P12
P8
P4
P6
P3
P9
P14
P7
P13
P1
P2
P15
P16
P17
P18
P19
0.218
0.220
0.222
0.224
0.226
0.228
Modal Frequency (Hz) : Mode 3 (VS-1)

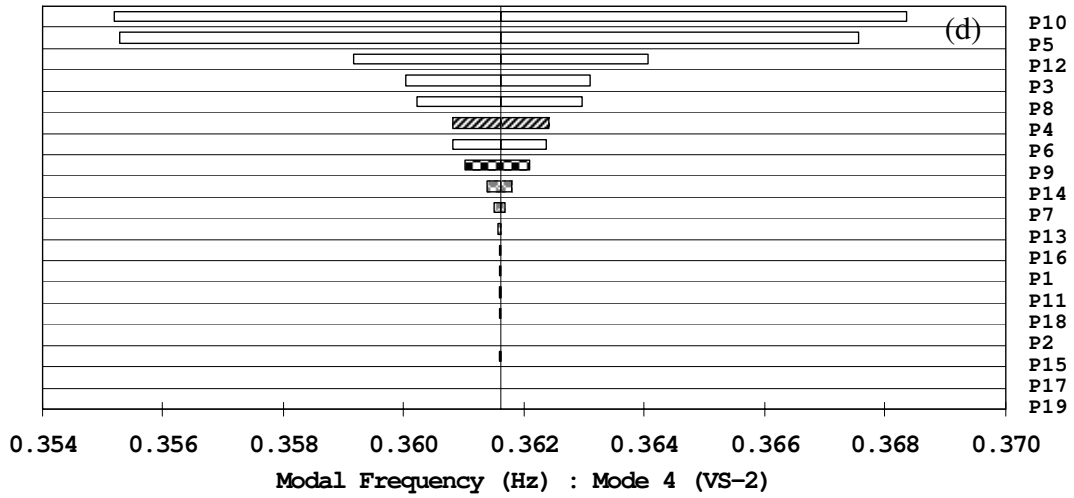
(d)
P10
P5
P12
P3
P8
P4
P6
P9
P14
P7
P13
P16
P1
P11
P18
P2
P15
P17
P19
0.354
0.356
0.358
0.360
0.362
0.364
0.366
0.368
0.370
Modal Frequency (Hz) : Mode 4 (VS-2)

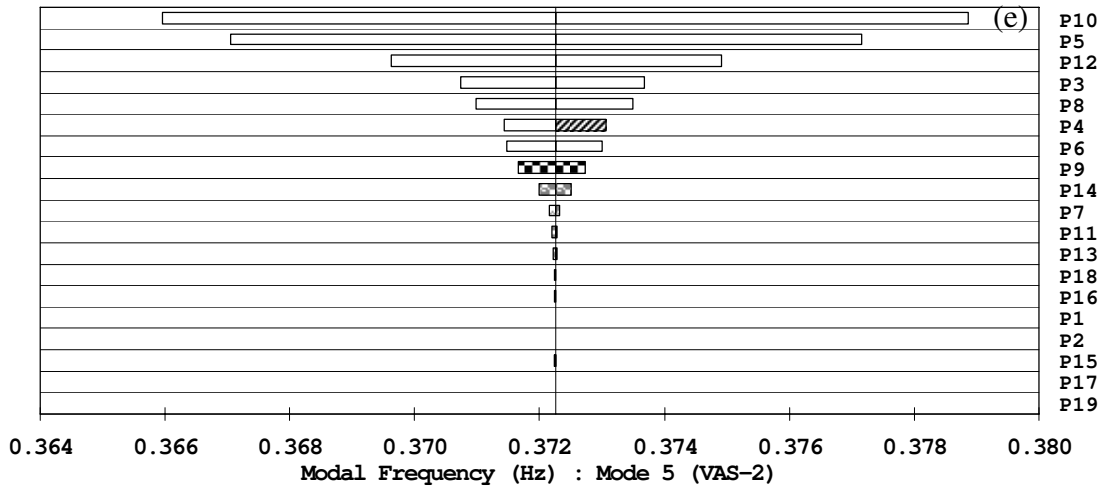
(e)
P10
P5
P12
P3
P8
P4
P6
P9
P14
P7
P11
P13
P18
P16
P1
P2
P15
P17
P19
0.364
0.366
0.368
0.370
0.372
0.374
0.376
0.378
0.380
Modal Frequency (Hz) : Mode 5 (VAS-2)

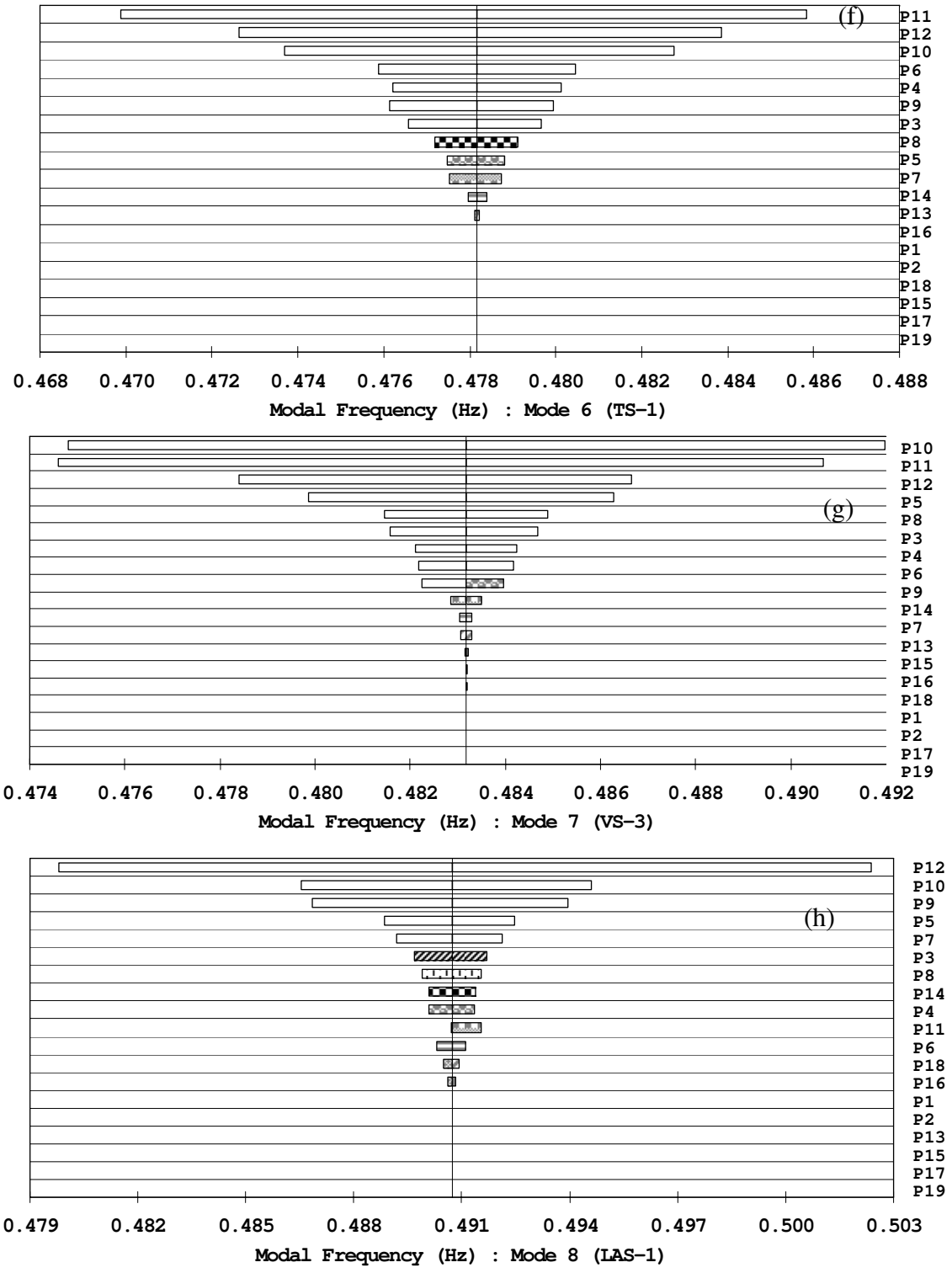

Figure 3.6 Tornado diagram considering 19 parameters

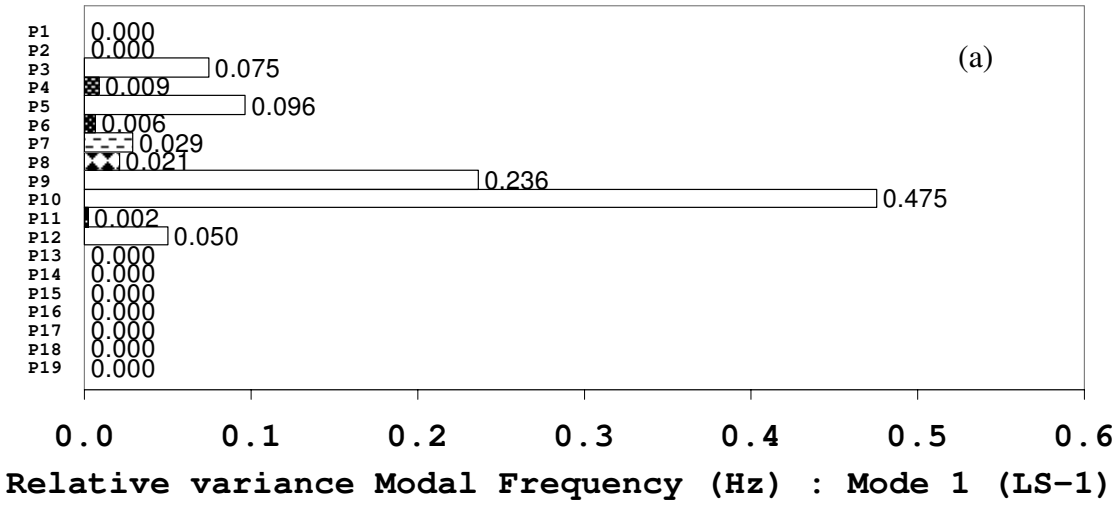
P1 0.000
P2 0.000
P3 0.075
P4 0.009
P5 0.096
P6 0.006
P7 0.029
P8 0.021
P9 0.236
P10 0.475
P11 0.002
P12 0.050
P13 0.000
P14 0.000
P15 0.000
P16 0.000
P17 0.000
P18 0.000
P19 0.000
(a)
0.0 0.1 0.2 0.3 0.4 0.5 0.6
Relative variance Modal Frequency (Hz) : Mode 1 (LS-1)

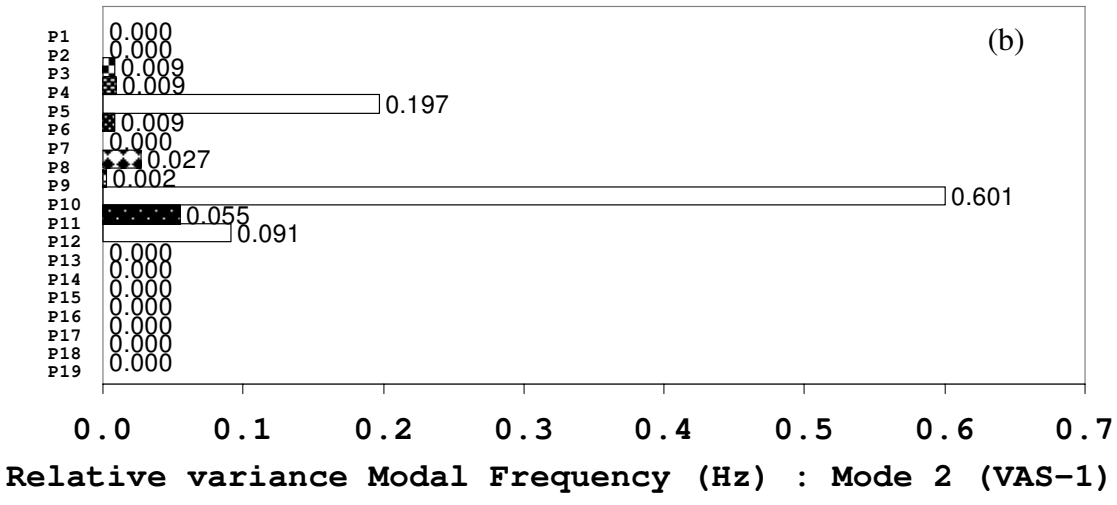
P1 0.000
P2 0.000
P3 0.009
P4 0.009
P5 0.197
P6 0.009
P7 0.000
P8 0.027
P9 0.002
P10 0.601
P11 0.055
P12 0.091
P13 0.000
P14 0.000
P15 0.000
P16 0.000
P17 0.000
P18 0.000
P19 0.000
(b)
0.0 0.1 0.2 0.3 0.4 0.5 0.6 0.7
Relative variance Modal Frequency (Hz) : Mode 2 (VAS-1)

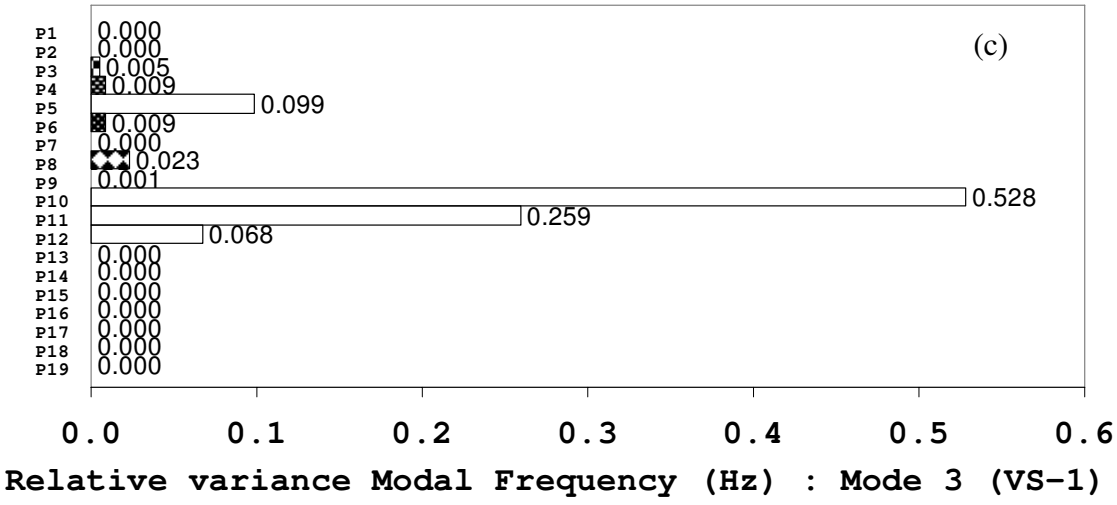
P1 0.000
P2 0.000
P3 0.005
P4 0.009
P5 0.099
P6 0.009
P7 0.000
P8 0.023
P9 0.001
P10 0.528
P11 0.259
P12 0.068
P13 0.000
P14 0.000
P15 0.000
P16 0.000
P17 0.000
P18 0.000
P19 0.000
(c)
0.0 0.1 0.2 0.3 0.4 0.5 0.6
Relative variance Modal Frequency (Hz) : Mode 3 (VS-1)

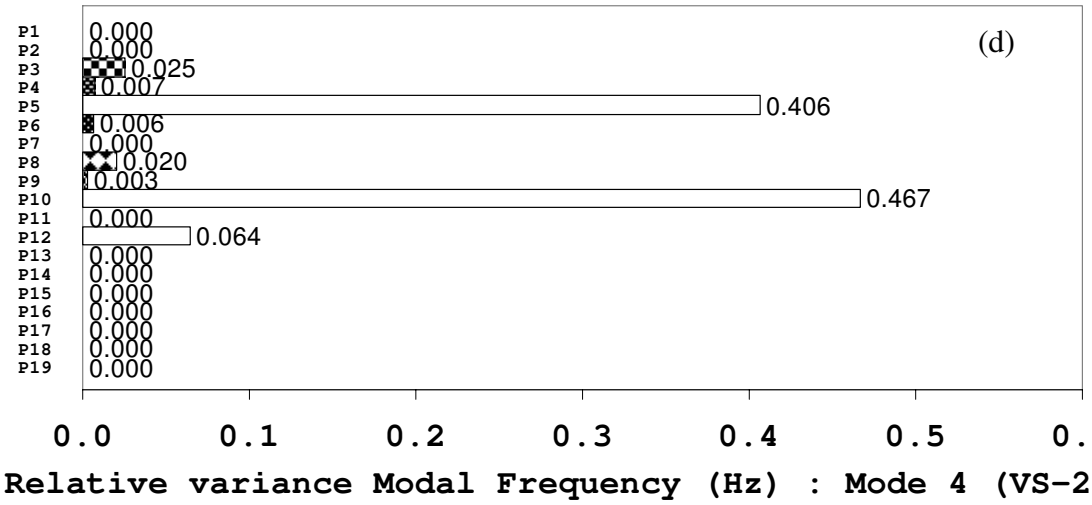
P1 0.000
P2 0.000
P3 0.025
P4 0.007
P5 0.406
P6 0.006
P7 0.000
P8 0.020
P9 0.003
P10 0.467
P11 0.000
P12 0.064
P13 0.000
P14 0.000
P15 0.000
P16 0.000
P17 0.000
P18 0.000
P19 0.000
(d)
0.0 0.1 0.2 0.3 0.4 0.5 0.6
Relative variance Modal Frequency (Hz) : Mode 4 (VS-2)

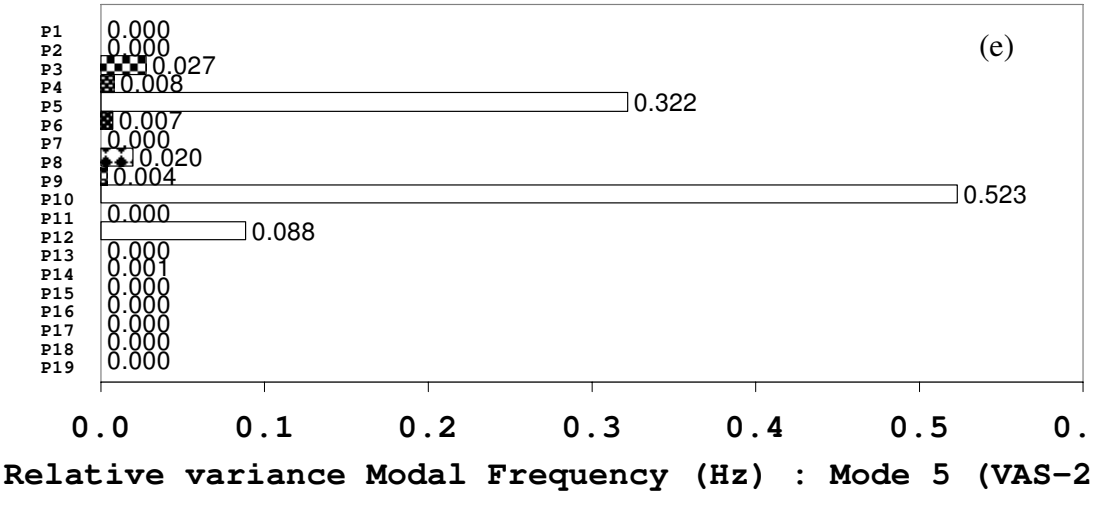
P1 0.000
P2 0.000
P3 0.027
P4 0.008
P5 0.322
P6 0.007
P7 0.000
P8 0.020
P9 0.004
P10 0.523
P11 0.000
P12 0.088
P13 0.000
P14 0.001
P15 0.000
P16 0.000
P17 0.000
P18 0.000
P19 0.000
(e)
0.0 0.1 0.2 0.3 0.4 0.5 0.6
Relative variance Modal Frequency (Hz) : Mode 5 (VAS-2)

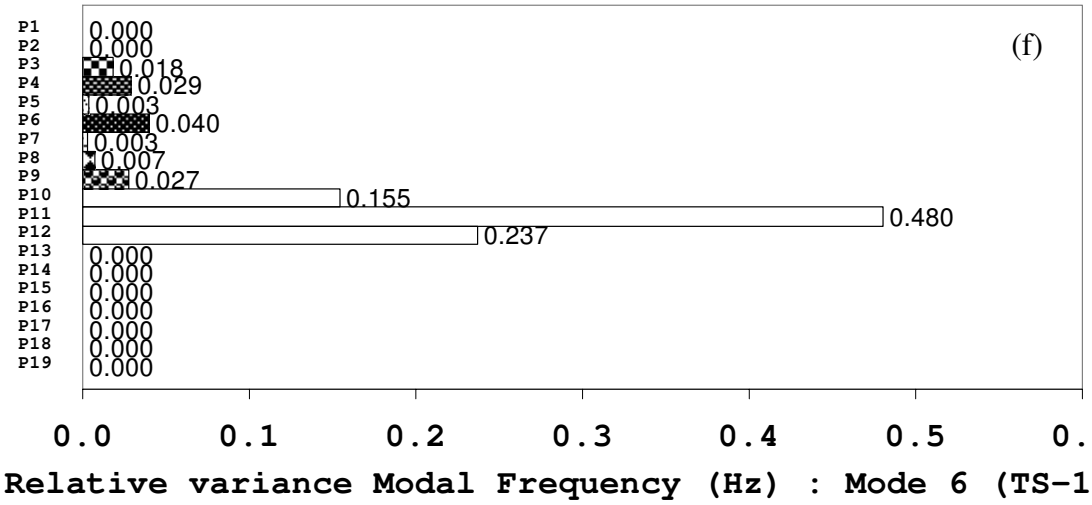
P1 0.000
P2 0.000
P3 0.018
P4 0.029
P5 0.003
P6 0.040
P7 0.003
P8 0.007
P9 0.027
P10 0.155
P11 0.480
P12 0.237
P13 0.000
P14 0.000
P15 0.000
P16 0.000
P17 0.000
P18 0.000
P19 0.000
(f)
0.0 0.1 0.2 0.3 0.4 0.5 0.6
Relative variance Modal Frequency (Hz) : Mode 6 (TS-1)

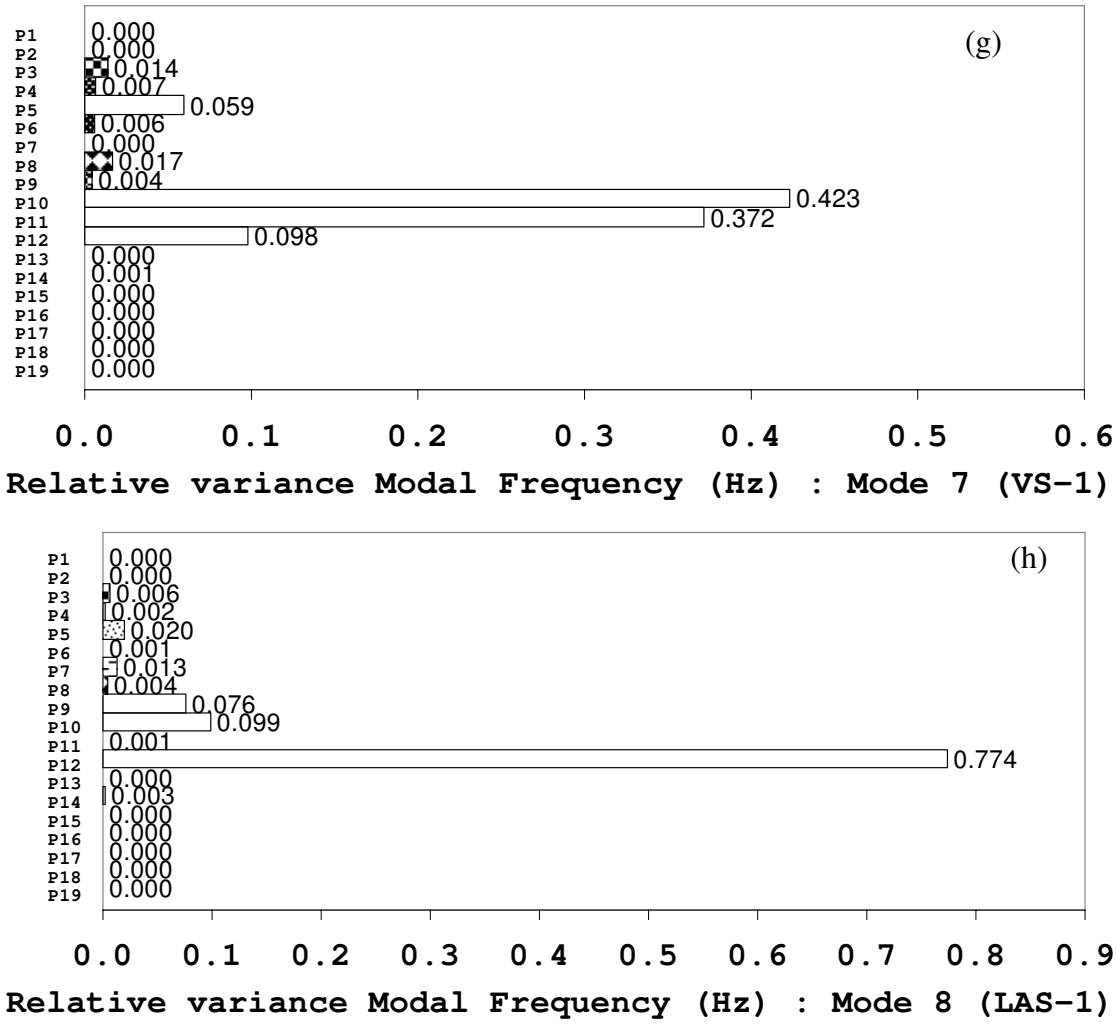

Figure 3.7 Relative variance contribution (neglecting correlation terms) from FOSM analysis

3.6 Finite Element Model Updating

A detailed three-dimensional finite element (FE) model of Vincent Thomas Bridge was developed using the finite element analysis code ADINA 8.3. This finite element model is composed of 3D elastic truss elements to represent the main cables and suspenders, 2D shell elements to model the bridge deck and beam elements to model the stiffening trusses and tower shafts. The ADINA bridge model is shown in Figure 3.8.

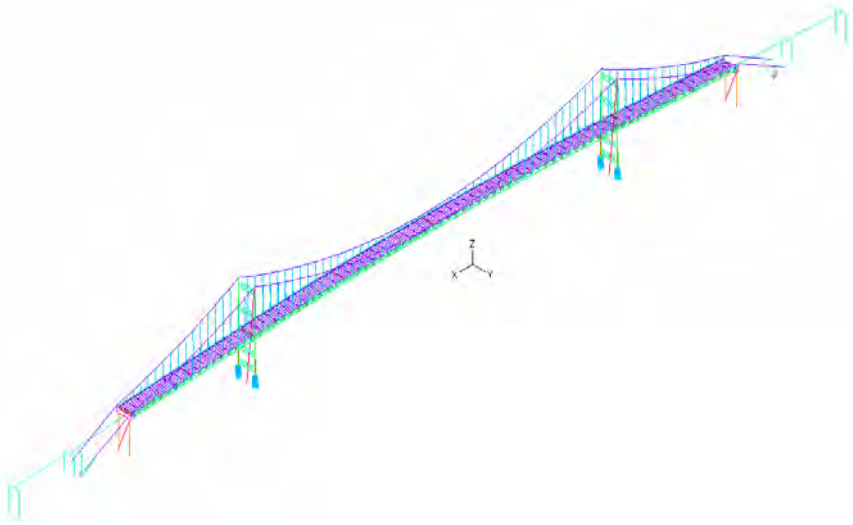

Figure 3.8 Three-dimensional finite element model of Vincent Thomas Bridge

For updating the original ADINA model an improved sensitivity-based parameter updating method is employed (Zhang et al., 2001). The method is based on the eigen value sensitivity to some selected structural parameters that are assumed to be bounded within some prescribed regions according to the degrees of uncertainty and variation existing in the parameters, together with engineering judgment. The changes of these parameters are found by solving a quadratic programming problem.

3.6.1 Sensitivity Based Model Updating

The structural parameters affecting the natural frequencies are selected to construct the design parameter vector P_a. The eigenvalue vector based on the designed parameters is denoted as λ_a, while the measured eigenvalue vector as λ_m. The error vector is defined as $\delta\lambda = \lambda_m - \lambda_a$. The updating process minimizes the error vector by changing the design parameter vector P_a. The variation of design parameter vector δp can be determined by

$$\delta\lambda = S\delta p \tag{3.8}$$

where S is the sensitivity matrix that represents the variation of natural frequencies of the model due to the variation of design parameter vector.

The solution of Eq. (3.8) can be solved by the following iterative updating procedures.

$$p^{k+1} = p^k + \delta p \tag{3.9}$$

$$\lambda_a^{k+1} = \lambda_a^k + \delta\lambda \tag{3.10}$$

where p^k, λ_a^k are the parameter vector and eigenvalue vector of FE model, respectively, at the k-th updating step. The iterative updating is repeated until the updated eigenvalue vector λ_a^k converges to the measured eigenvalue vector λ_m.

The criteria of convergence are used as

$$\max_i \left| \frac{f_{a,i}^k - f_{m,i}}{f_{m,i}} \right| \le tolerance \tag{3.11}$$

$$\max_i \left| \frac{\lambda_{a,i}^k - \lambda_{a,i}^{k-1}}{\lambda_{a,i}^{k-1}} \right| \le tolerance \tag{3.12}$$

where $f_{a,i}^k$ and $\lambda_{a,i}^k$ are the i-th natural frequency and corresponding eigenvalue at k-th update, and $f_{m,i}$ the measured i-th natural frequency. The following optimization problem is applied to determine δp in Eq. (3.8) (Friswell and Mottershead, 1994).

$$\min_{\Phi} J_1 + J_2 = \frac{1}{2}(\delta\lambda - S\delta p)^T W_e (\delta\lambda - S\delta p) + \frac{1}{2}\delta p^T W_p \delta p \tag{3.13}$$

subject to $b_l \le \delta p \le b_u$

The first term in right hand side of Eq. (3.13) represents the objective function to minimize the error vector, while the second term to minimize the variation of design parameter vector. W_e and W_p are weighting functions. The constrained optimization solutions as outlined in Eq. (3.13) are incorporated into an iterative procedure as shown in Figure 3.9 for the model updating Vincent Thomas Bridge.

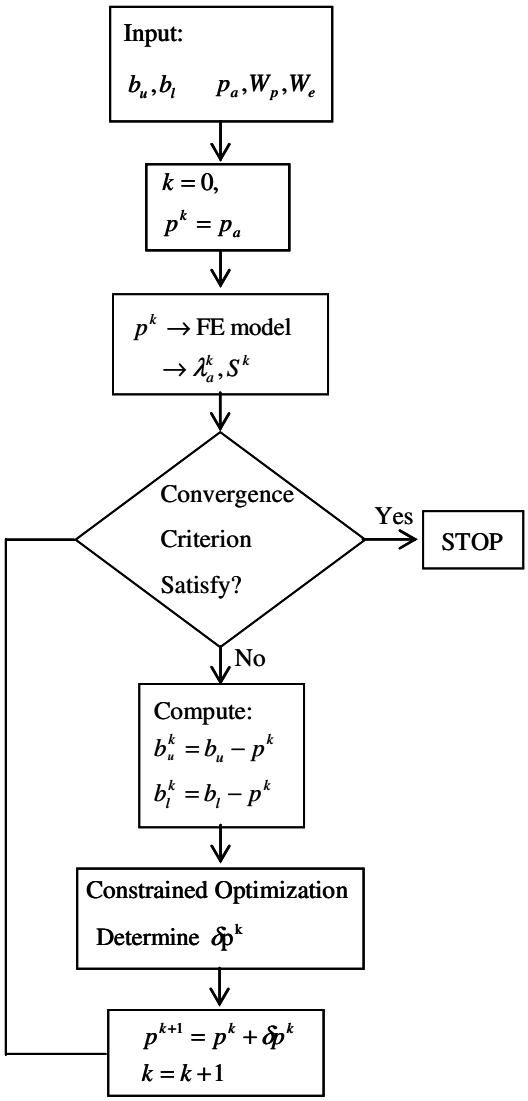

Figure 3.9 Procedure for the sensitivity-based model updating

3.6.2 Selection of Modes and Parameters

3.6.2.1 Selection of Modes

Average values of the identified modal frequencies obtained from 14 different ambient vibration data recorded at the bridge site are considered as target frequencies for further ADINA model updating. Those 14 ambient vibration data were recorded from April, 2003 to October 2004. In the study, it is decided to select 8 modes to be matched between the updated FE analysis and the measured results. These include five vertical-dominant; two lateral-dominant; one torsional-dominant modes of the deck. Table 3.7 shows the modal frequencies and percentage error in modal frequencies of Initial (original) and Baseline ADINA model results with respect to identified frequencies obtained from the ambient vibration measurement data.

Table 3.7 Comparison of natural frequencies

Mode no.	Mode Type	Measured frequency (Hz)	Finite element analyzed frequencies		err.(%)	
			Initial	Baseline	Initial	Baseline
1	L-S	0.161	0.131	0.148	-18.63	-7.83
2	V-AS1	0.221	0.206	0.210	-6.79	-5.02
3	V-S1	0.233	0.226	0.227	-3.00	-2.66
4	V-S2	0.374	0.363	0.371	-2.94	-0.86
5	V-S3	0.474	0.460	0.470	-2.95	-0.78
6	L-AS	0.476	0.411	0.462	-13.66	-2.90
7	T-S	0.538	0.500	0.506	-7.06	-6.02
8	V-AS2	0.568	0.568	0.583	0.00	2.66

3.6.2.2 Selection of Parameters

All possible parameters relating to the geometric, structural properties as well as the boundary conditions should be considered for adjustment in the updating procedure. However, if the parameters are found to have little or no effect on the targeted vibration modes, then they can be excluded from parameters list. After removing those parameters with very small sensitivities, total 17 different parameters are considered for this analysis. For this purpose, a sensitivity study is done and is explained in Section 3.5. They are summarized in Table 3.8 together with their initial estimates.

Table 3.8 Parameters selected for adjustment

Structure		parameters	Initial estimation	Variations in %
Stiffening truss	Top chord	Elastic modulus	29000 kip/in^2	± 15
		Mass density	8.71E-07 kip/in^3	± 15
	Bottom chord	Elastic modulus	29000 kip/in^2	± 20
		Mass density	8.71E-07 kip/in^3	± 15
	Diagonal	Mass density	8.71E-07 kip/in^3	± 20
	lateral brace (k-truss)	Elastic modulus	29000 kip/in^2	± 10
		Mass density	1.35E-06 kip/in^3	± 20
	Stringers	Elastic modulus	29000 kip/in^2	± 20
		Mass density	9.02E-07 kip/in^3	± 10
Deck	Slab	Elastic modulus	2825 kip/in^2	± 30
		Mass density	2.01E-07 kip/in^3	± 5
Cable	Main cable	Initial strain	1	± 20
		Elastic modulus	29000 kip/in^2	± 20
		Mass density	7.71E-07 kip/in^3	± 15
	Suspender	Mass density	7.65E-07 kip/in^3	± 15
Tower		Elastic modulus	29000 kip/in^2	± 15
		Mass density	7.62E-07 kip/in^3	± 15

3.6.3 Updated Results

The allowable errors permitted for the check of natural frequency convergence was applied 6% for the general modes, while 3% for the first and second modes. If the ratio of variation for the eigenvalue is lower than 0.1%, then the iteration is also ended. For the cable supported bridge of which modes are closely spaced, the disorder between adjacent modes should be critically checked. The following MAC (Modal Assurance Criteria) is applied to the each set of two updated natural modes (Friswell and Mottershead, 1994).

$$MAC = \frac{\left|\sum_{l=l}^{p} \phi_{l,i}^{e} \phi_{l,j}^{a}\right|^{2}}{\left(\sum_{l=1}^{p} \phi_{l,i}^{e} \phi_{l,i}^{e}\right)\left(\sum_{l=1}^{p} \phi_{l,j}^{a} \phi_{l,j}^{a}\right)} \qquad 0 \le MAC \le 1 \tag{3.14}$$

If the two shape vectors ϕ^a, ϕ^e to be compared are identical, then MAC becomes 1, while if the two shape vectors are orthogonal, MAC becomes 0. Therefore, MAC can be utilized to prevent disorder between the calculated and measured frequency. MAC also provides the criteria for the reliability of the developed model after model updating. The MACs are listed in Table 3.9. The differences between the measured and the calculated frequencies for the initial and the final updated FE modes are showed in Figure 3.10. Table 3.10 shows the natural frequencies of the baseline model and updated model. For most of the modes, the discrepancies between measured frequencies and updated frequencies decreased less than 3%, while a few modes such as the first lateral frequency shows about 4% discrepancy. However, the discrepancy between measured and baseline model was about 19% and the current updating decreases the error in amount of 4%.

Table 3.9 MAC matrix of updated FE model

#	1	2	3	4	5	6	7	8
1	0.542	0.015	0.007	0.000	0.000	0.000	0.000	0.000
2	0.001	0.531	0.000	0.000	0.000	0.000	0.000	0.000
3	0.003	0.009	0.490	0.000	0.000	0.000	0.000	0.000
4	0.000	0.000	0.000	0.500	0.000	0.000	0.000	0.000
5	0.000	0.000	0.000	0.000	0.500	0.000	0.000	0.000
6	0.000	0.000	0.000	0.000	0.000	0.538	0.000	0.000
7	0.090	0.005	0.001	0.003	0.006	0.094	0.541	0.000
8	0.001	0.003	0.008	0.113	0.002	0.000	0.000	0.486

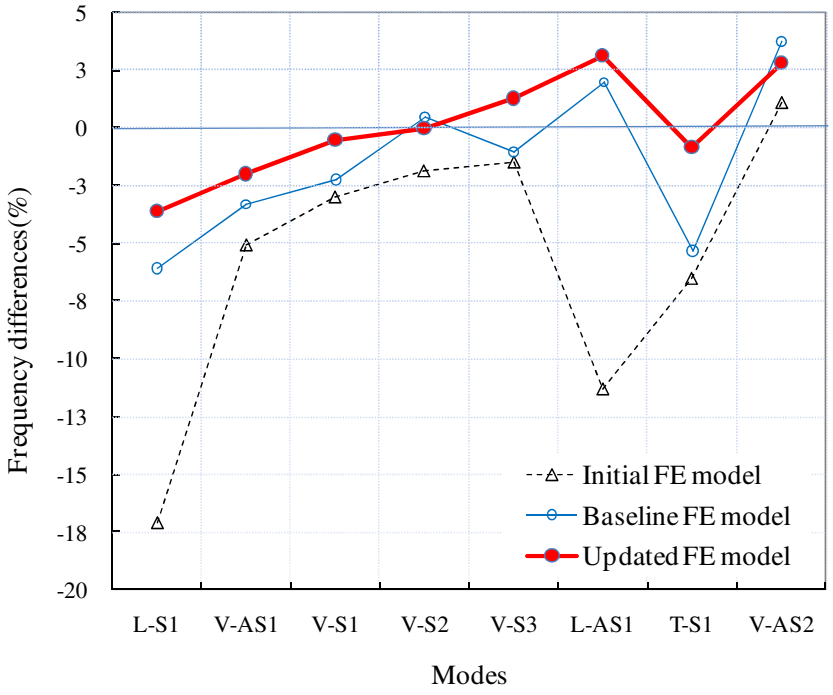

Figure 3.10 Comparison of frequency differences using the initial and updated FE models

Table 3.10 Comparison of natural frequencies between baseline and updated FE model

Mode no.	Mode Type	Identified	Finite element analyzed frequencies					
			Initial		Baseline		Updated	
		Frequency (Hz)	Frequency (Hz)	Err.(%)	Frequency (Hz)	Err.(%)	Frequency (Hz)	Err.(%)
1	L-S	0.161	0.131	-18.63	0.148	-7.83	0.155	-4.04
2	V-AS1	0.221	0.206	-6.79	0.210	-5.02	0.215	-2.90
3	V-S1	0.233	0.226	-3.00	0.227	-2.66	0.233	-0.09
4	V-S2	0.374	0.363	-2.94	0.371	-0.86	0.373	-0.19
5	V-S3	0.474	0.460	-2.95	0.470	-0.78	0.478	0.80
6	L-AS	0.476	0.411	-13.66	0.462	-2.90	0.487	2.25
7	T-S	0.538	0.500	-7.06	0.506	-6.02	0.538	-0.04
8	V-AS2	0.568	0.568	0.00	0.583	2.66	0.587	3.31

The variations of design parameters are also important to estimate reliability and effectiveness of updating results. The variations of design parameters are well limited in permitted arrange that can be regarded as reasonable as shown in Table 3.11.

Table 3.11 Updated design parameters

Structure		parameters	Initial estimation	Updated value	Percent changes
Stiffening truss	Top chord	Elastic modulus(kip/in^2)	29000	30815	6.3
		Mass density(kip/in^3)	8.71E-07	7.85E-07	-9.8
	Bottom chord	Elastic modulus(kip/in^2)	29000	33350	15.0
		Mass density(kip/in^3)	8.71E-07	7.58E-07	-13.0
	Diagonal	Mass density(kip/in^3)	8.71E-07	7.49E-07	-14.0
	lateral brace (k-truss)	Elastic modulus(kip/in^2)	29000	29442	1.5
		Mass density(kip/in^3)	1.35E-06	1.14E-06	-15.0
	Stringers	Elastic modulus(kip/in^2)	29000	24650	-15.0
		Mass density(kip/in^3)	9.02E-07	8.16E-07	-9.5
Deck	Slab	Elastic modulus(kip/in^2)	2825	3390	20.0
		Mass density(kip/in^3)	2.01E-07	1.82E-07	-9.2
Cable	Main cable	Initial strain	1.00	1.15	15.0
		Elastic modulus(kip/in^2)	29000	24650	-15.0
		Mass density(kip/in^3)	7.71E-07	7.45E-07	-3.3
	Suspender	Mass density(kip/in3)	7.65E-07	8.41E-07	10.0
Tower		Elastic modulus(kip/in^2)	29000	27931	-3.7
		Mass density(kip/in^3)	7.62454E-07	7.87E-07	3.3

3.7 Closure

To demonstrate the appropriateness of the bridge models developed in the previous chapter, eigen properties of the models are evaluated in this chapter and compared with those of the system identification results obtained using frequency domain decomposition technique on ambient vibration and recorded earthquake response data. After that, a comprehensive sensitivity analysis is performed considering 19 different structural and soil spring parameters. First eight modal frequencies are considered for the sensitivity study. Tornado diagram and FOSM methods are applied for the sensitivity study. It is observed that the mass density of deck slab and elastic modulus of bottom chord contributes most to the modal frequencies of the bridge. This kind of study will be very helpful in selecting parameters and their variability ranges for FE model updating of suspension bridges.

In this study, a sensitivity based automatic model updating procedure is presented, which solves an optimization problem for model error minimization. Four vertical vibration modes, two lateral modes, one torsional mode and 17 design parameters are selected for the problem. Updated results show that the model error could be reduced from 0~18% to 0~4% in terms of modal frequency ratio. During the optimization procedure, the target error bounds were 3% for the lower vertical modes and 6% for the horizontal modes. In order to prevent mode interchange due to the closely spaced frequencies of the three dimensional FE model, MACs are introduced to verify the updated results through the optimization procedure.

CHAPTER 4

SEISMIC ANALYSIS

4.1 Background

The Vincent Thomas Bridge, connecting Terminal Island with San Pedro, serves both Los Angeles and Long Beach ports, two of the busiest ports in the west coast of USA. Thus, the bridge carries an overwhelming number of traffic with an Annual Average Daily Traffic (AADT) volume of 100,000, many of which are cargo trucks. Based on the recent finding that the main span of the Vincent Thomas Bridge crosses directly over the Palos Verdes fault, which has the capacity to produce a devastating earthquake, in spring 2000, the bridge underwent a major retrofit using visco-elastic dampers. This study focuses on seismic vulnerability of the retrofitted bridge. A member-based detailed three-dimensional Finite Element (FE) as well as panel-based simplified models of the bridge are developed. In order to show the appropriateness of these models, eigenproperties of the bridge models are evaluated and compared with the system identification results obtained using ambient vibration. In addition, model validation is also performed by simulating the dynamic response during the 1994 Northridge earthquake and 2008 Chino Hills earthquake and comparing with the measured response. Finally, considering a set of strong ground motions in the Los Angeles area, nonlinear time history analyses are performed and the ductility demands of critical sections are presented in terms of fragility curves. The study shows that a ground motion with PGA of 0.9g or greater will result in plastic hinge formation at one or more locations with a probability of exceedance of 50%.

Also, it is found that the effect of damper is minimal for low to moderate earthquakes and high for strong earthquakes.

The spatial variation of earthquake ground motions may have significant effect on the response of long span suspension bridges. Abdel-Ghaffar and Rubin (1982) and Abdel-Ghaffar and Nazmy (1988) studied response of suspension and cable-stayed bridges under multiple support excitations. Zerva (1990) and Harichandran and Wang (1990) examined the effect of spatial variable ground motions on different types of bridge models. Harichandran et al. (1996) studied the response of long-span bridges to spatially varying ground motion. Deodatis et al. (2000) and Kim and Feng (2003) investigated the effect of spatial variability of ground motions on fragility curves for bridges. Lou and Zerva (2005) analyzed the effects of spatially variable ground motions on the seismic response of a skewed, multi-span, RC highway bridge. Most of the aforementioned studies dealt with simple FE models of the bridge, as a result response of critical members could not be evaluated. In the present analysis a panel based detailed 3D FE model of a long span suspension bridge is utilized.

For design purpose of important structures in a site, U.S. Geological Survey (USGS) provides a set of scenario earthquakes specified for a site. To consider spatial variability of ground motions one needs to know the ground excitations at different supports of a long span suspension bridge. For generating spatial variable ground motions from a scenario earthquake compatible to different design spectra for different supports (as the local soil conditions will be different for different supports) a new algorithm is proposed using evolutionary power spectral density function (PSDF) of the scenario earthquake specified for the site. Evolutionary PSDF of LA21 scenario earthquake is

estimated by using short-time Fourier transform (STFT) and wavelet transform (WT) methods. Two evolutionary PSDFs thus developed maintain the same total energy possessed by the time history data. Using the evolutionary 20 sets of simulated ground motions for six different spatially correlated supports are generated. Ensemble average of 5% damped spectral acceleration response spectra obtained from simulated earthquake time histories are compared with the design response spectra for all the support locations. Good match has been found with the target design acceleration response spectra with the simulated one.

Simulated spatially variable ground motions are used in calculating the response of the bridge. In addition to spatial variable seismic ground motions, two uniform ground motions are also considered for comparison purpose. The seismic responses of the bridge deck and the east tower are calculated using those three different cases and compared in both seismic displacement demand and seismic force demand.

4.2 Scope

FE model validation of the bridge is also performed by simulating the dynamic response during the 1994 Northridge earthquake and 2008 Chino Hills earthquake and comparing with the measured response from installed acceleration sensors. Considering a set of strong ground motions in the Los Angeles area, nonlinear time history analyses are performed and ductility demands of critical tower section are presented in terms of seismic fragility curves. Effect of spatial variability of ground motions on seismic displacement demand and seismic force demand is investigated. To generate spatially

correlated spectrum compatible nonstationary acceleration time histories, a newly developed algorithm using evolutionary PSDF and spectral representation method is used.

4.3 Response Analysis under Northridge Earthquake

To validate the developed numerical models (discussed in Chapter 2), time history analysis is performed using the 1994 Northridge earthquake (M_w = 6.7) ground motions recorded at the bridge sites. Newmark-Beta method is used with $\gamma = 0.5$ and $\beta = 0.25$ for this purpose. The ground motions and the bridge response during the Northridge earthquake are collected from the sensors installed at the bridge site (California Strong Motion Instrumentation Program (CSMIP) [http://www.strongmotioncenter.org/]). Since the earthquake occurred before the retrofit, detailed model before the retrofit is used here.

To consider the effect of spatial variation, different ground motions are considered at different support locations, wherever possible. In some cases, due to the unavailability of recorded support motions, ground motions recorded at the nearest support is considered. Figure 4.1 shows the location of sensors and Table 4.1 illustrates the list of supports on which ground motions are applied for this analysis. Figure 4.2 shows comparison of measured and calculated longitudinal displacement at the top of the east tower location (channel # 10) of the bridge. The plot shows good match between the calculated and field measured responses.

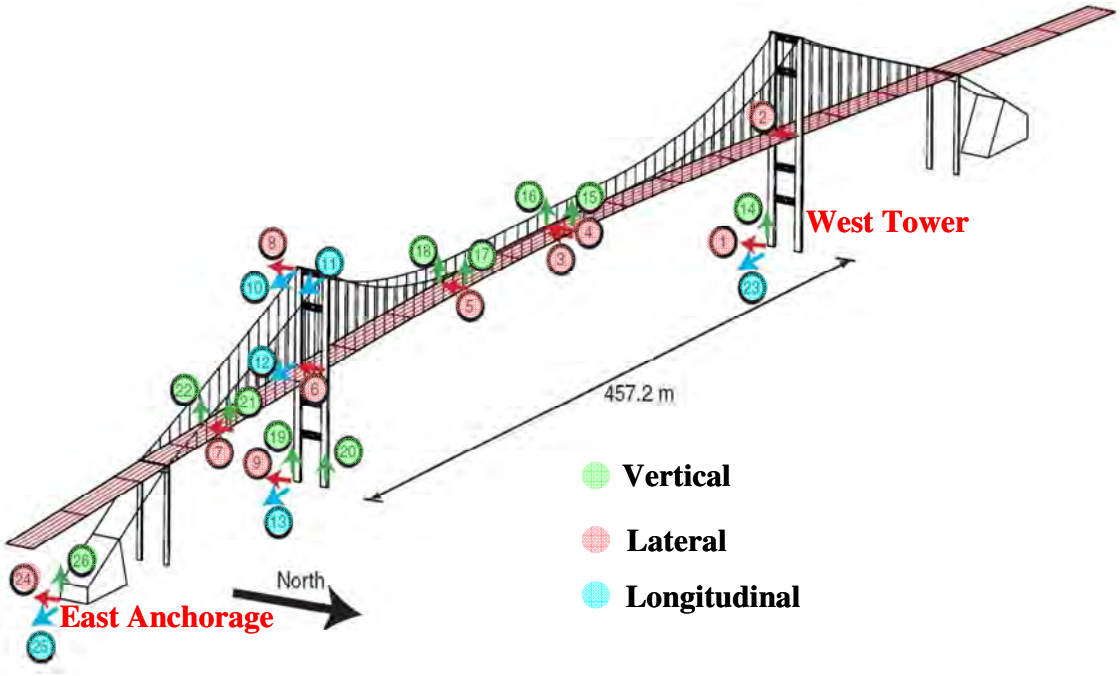

Figure 4.1 Location and direction of sensors

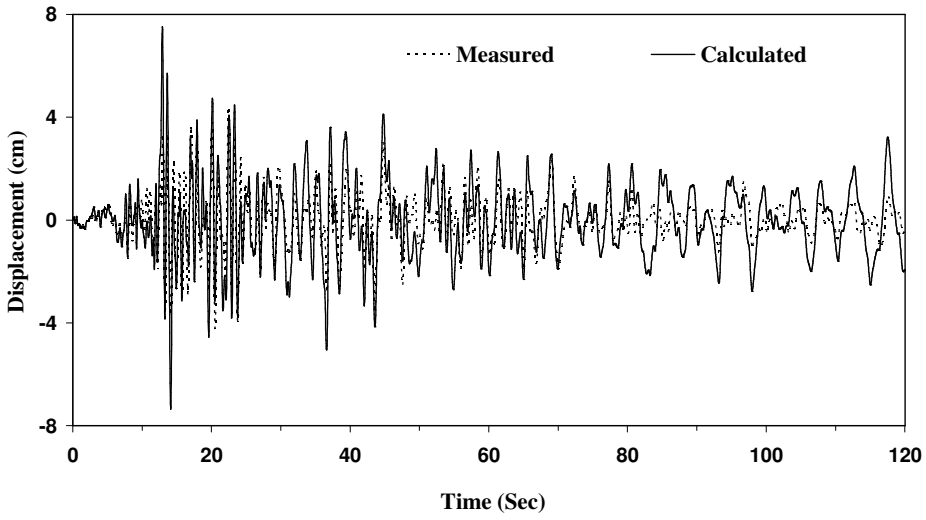

Figure 4.2 Comparison of measured and calculated longitudinal displacement at channel # 10 location

Table 4.1 Different support motions considered with channel numbers

Location	Longitudinal	Lateral	Vertical
East Anchorage	Ch. 25	Ch. 24	Ch. 26
East Cable Bent*	Ch. 13	Ch. 9	Ch. 19
East Tower	Ch. 13	Ch. 9	Ch. 19
West Anchorage*	Ch. 23	Ch. 1	Ch. 14
West Cable Bent*	Ch. 23	Ch. 1	Ch. 14
West Tower	Ch. 23	Ch. 1	Ch. 14

* No recording at these locations

4.4 Response Analysis under Chino Hills Earthquake

To study the developed numerical model, time history analysis is performed using the 2008 Chino Hills earthquake (M_w = 5.4) ground motions recorded at the bridge sites. Newmark-Beta method is used with γ = 0.5 and β = 0.25 for this purpose with time step equal to 0.01 sec. The ground motions and the bridge response during the Chino Hills earthquake are collected from the sensors installed at the bridge site (California Strong Motion Instrumentation Program (CSMIP) [http://www.strongmotioncenter.org/]). Figure 1 shows the location of sensors already installed in the bridge. Since the earthquake occurred after the retrofit, detailed model after the retrofit is used here. Three directional components of ground motions recorded at east anchorage, east tower and west tower are applied uniformly over all the supports to study which set of ground motions will give much more accurate results. Figure 4.3 shows the comparison of analytical lateral response at channel 5 due to ground motions at east anchorage, east tower, west tower and considering spatial variation in ground motion with field measured response. It can be seen from figure 4.3 that the analytical response due the ground motion recorded at east tower matches well with the measured response. Figures 4.4, 4.5 and 4.6 show

comparison of analytical lateral, vertical and longitudinal responses at different channels due to ground motions at east tower with field measured response. These plots shows good match between the analytical and field measured responses.

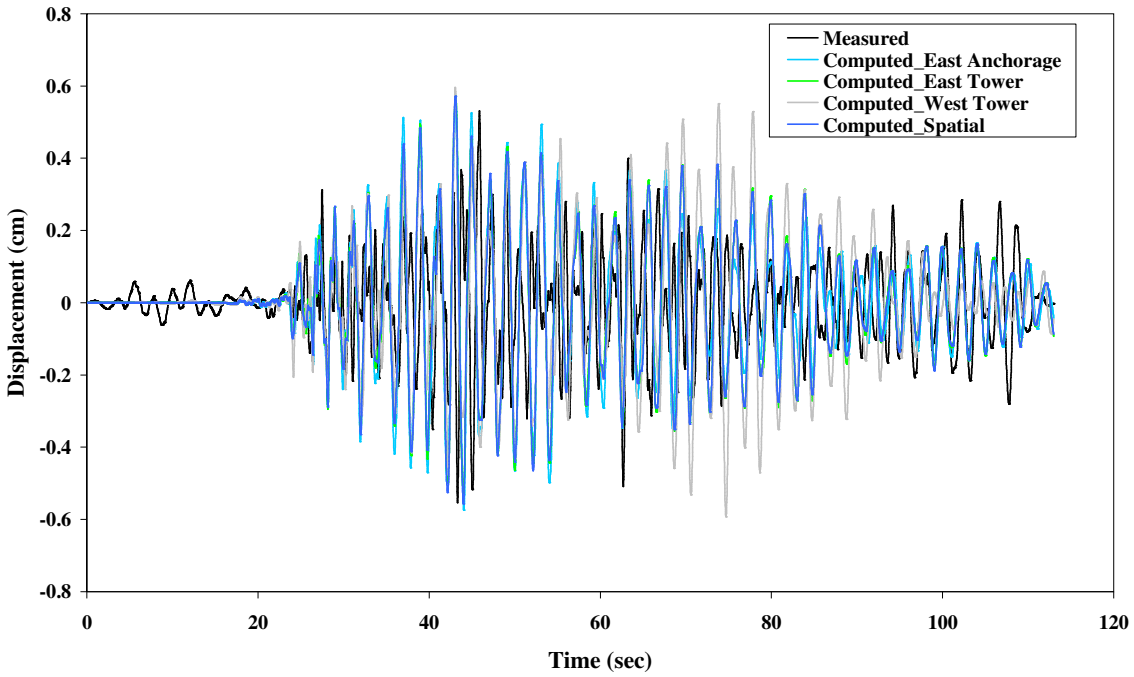

Figure 4.3 Comparison of analytical lateral response at channel 5 due to ground motions at east anchorage, east tower and west tower with field measured response

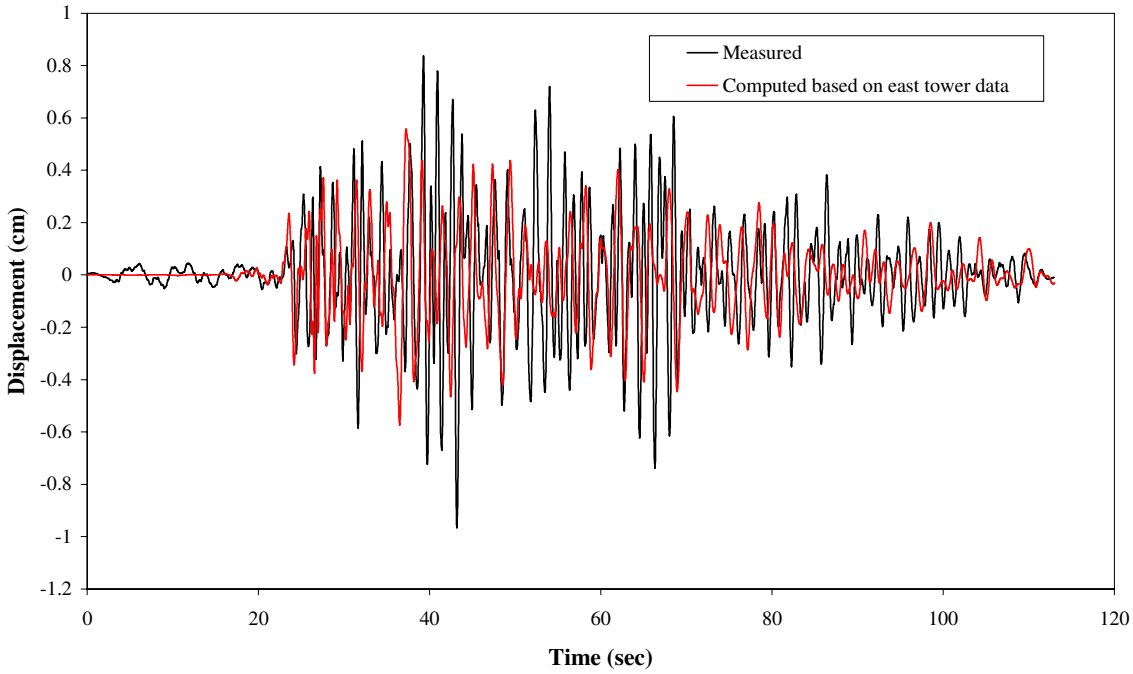

Figure 4.4 Comparison of analytical lateral response at channel 3 due to ground motions at east tower with field measured response

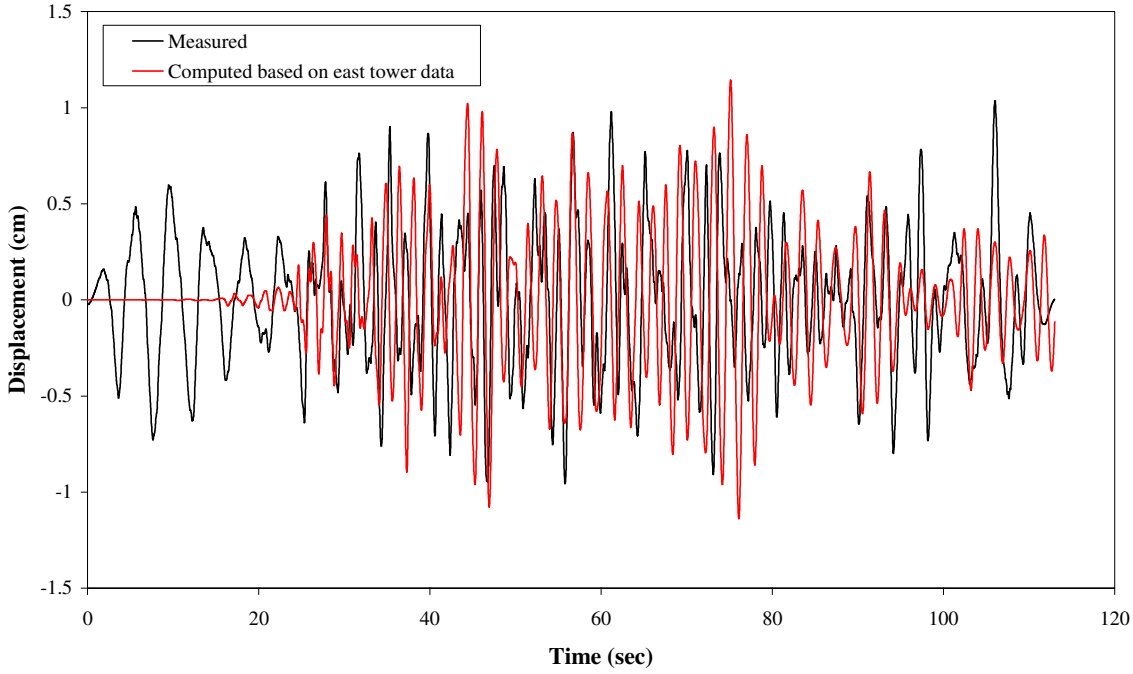

Figure 4.5 Comparison of analytical vertical response at channel 17 due to ground motions at east tower with field measured response

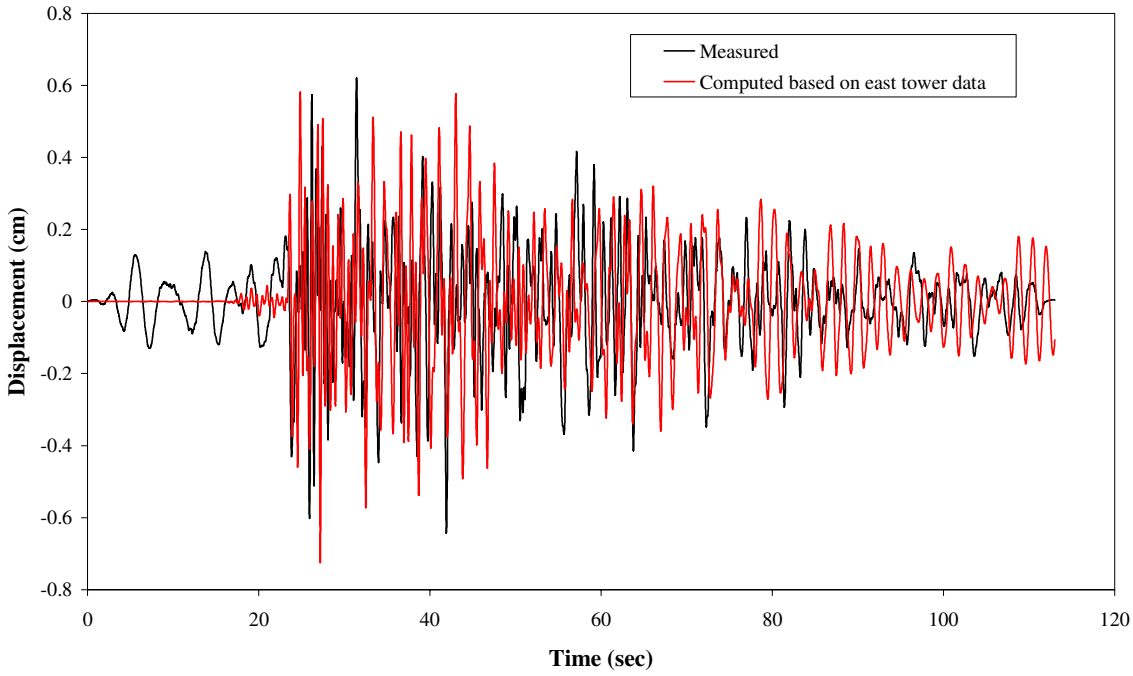

Figure 4.6 Comparison of analytical longitudinal response at channel 10 due to ground motions at east tower with field measured response

4.5 Generation of Fragility Curves

It is clear from the previous literature, especially those studies in the aftermath of 1995 Kobe (Hyogo-ken Nanbu) earthquake at Japan that the bridge deck and cables of suspension bridges are less vulnerable under strong earthquake ground motion (remain elastic) while the tower is the most vulnerable part. In order to simplify analysis, in this study, only the towers are modeled as nonlinear elements. Remaining elements of the bridge are considered as linear. Each tower leg is constructed with members of 5 different cross sections. A total of 40 plastic hinges are introduced at all four tower legs. An elasto-plastic behavior with 3% strain hardening is considered for the material models of these plastic hinges. 2% Raleigh damping is used for the first and tenth modes. Forty ground motions representing 2% in 50 years and 10% in 50 years of hazard level as specified by

FEMA/SAC are used for evaluating seismic vulnerability of the retrofitted bridge. The motions cover wide range peak characteristics with Peak Ground Acceleration (PGA) ranging from 0.42 to 1.30g. Note also that these motions include expected motions from Palos Verdes fault, the fault crossing the main span of this bridge. For nonlinear time history analysis, direct time integration is used in the framework of SAP 2000. Motions are applied in the lateral direction of the bridge and no spatial variation is considered. After performing the nonlinear time history analysis, the ductility demands of all the critical sections are evaluated and the maximum ductility demand is noted for each motion. Considering all these motions, the maximum ductility demand is found to be 6.23, which is from LA 36 motion (with a PGA of 1.1g) and for the plastic hinge at the base of the tower.

In this study, fragility curves corresponding to different damage states are developed following Shinozuka et al., 2000. For a given damage state, the fragility curves are expressed in terms of lognormal distribution. PGA is considered as Ground motion intensity. Two fragility parameters, median (c) and log-standard deviation (ζ) are estimated through a maximum likelihood method such that fragility curves at different damage levels do not intersect each other. Therefore, a common ζ is needed to satisfy this criterion. Although this method can be used for any number of damage states, for the ease of demonstration of analytical procedure it is assumed here that there are three states of bridge damage. Therefore, a family of three fragility curves exists in this case for damage states of 'Level-I', 'Level-II', and 'Level-III' identified by k = 1, 2, and 3. Under this lognormal assumption, the analytical form of the fragility function F(•) for the state of damage k is,

$$F(a_i, c_k, \zeta) = \Phi\left[\frac{\ln(a_i / c_k)}{\zeta}\right] \tag{4.1}$$

where c_k is median of the fragility function associated with damage state k, ζ is the common log-standard deviation, a_i is the PGA value to which the bridge is subjected and $\Phi[\bullet]$ is the standardized normal distribution function. The fragility parameters are computed by maximizing the likelihood function, L which is given by Eq. (4.2),

$$L(c_1, c_2, c_3, \zeta) = \prod_{k=1}^{3}\prod_{i=1}^{n}[P_{ik}]^{x_{ik}} \tag{4.2}$$

where x_{ik} is 1 or 0, depending on whether or not the bridge sustains damage state k under a_i, and n is the total number of ground motions under which the analysis is performed. P_{ik} is the probability that the example bridge will suffer from a damage state k when subjected to a_i and is expressed as

$$P_{i0} = 1 - F(a_i, c_1, \zeta) \tag{4.3}$$

$$P_{i1} = F(a_i, c_1, \zeta) - F(a_i, c_2, \zeta) \tag{4.4}$$

$$P_{i2} = F(a_i, c_2, \zeta) - F(a_i, c_3, \zeta) \tag{4.5}$$

$$P_{i3} = F(a_i, c_3, \zeta) \tag{4.6}$$

Fragility parameters are obtained by solving the Eq. (4.7), by implementing a straightforward optimization algorithm.

$$\frac{\partial \ln L(c_1, c_2, c_3, \zeta)}{\partial c_k} = \frac{\partial \ln L(c_1, c_2, c_3, \zeta)}{\partial \zeta} = 0 \quad \text{for} \quad k = 1,2,3 \qquad (4.7)$$

For the fragility curves, this study proposes performance levels in terms of ductility demands of critical tower sections, since the damage states related to expected performance level of suspension bridge is not clearly defined in the literature. Three different damage states are considered in this study in terms of the maximum ductility demands of all the critical tower sections. They are (1) Level-I (plastic hinge formation, ductility > 1) (2) Level-II (ductility ≥ 2) and (3) Level-III (ductility ≥ 4). Figure 4.5 shows the fragility curves considering these damage states and for before and after retrofitting of the bridge. One can observe from this figure that for a PGA of 0.9g, the probability of exceedance corresponding to damage Level-I (i.e., plastic hinge formation at one or more locations) is 50%. Similarly, for the same probability of exceedance, a ground motion with PGA of 1.05g or greater will cause a damage of Level-II. PGA of 1.82g was recorded at the Tarzana Station during the main shock of the 1994 Northridge earthquake. For that PGA the probability of exceedance to damage Level-II is 90%. The bridge was retrofitted with total 48 dampers and from the fragility curves it is clear that the effect of dampers are minimal for low to moderate earthquake and high for strong earthquake.

Table 4.2 Details of the motions considered in this study for fragility development

SAC Name	Record	Earthquake Magnitude	Distance (km)	Scale Factor	dt (sec)	Duration (sec)	PGA (g)	PGV (cm/sec)	PGD (cm)
LA21	1995 Kobe	6.9	3.4	1.15	0.02	59.98	1.28	142.70	37.81
LA22	1995 Kobe	6.9	3.4	1.15	0.02	59.98	0.92	123.16	34.22
LA23	1989 Loma Prieta	7	3.5	0.82	0.01	24.99	0.42	73.75	23.07
LA24	1989 Loma Prieta	7	3.5	0.82	0.01	24.99	0.47	136.88	58.85
LA25	1994 Northridge	6.7	7.5	1.29	0.005	14.945	0.87	160.42	29.31
LA26	1994 Northridge	6.7	7.5	1.29	0.005	14.945	0.94	163.72	42.93
LA27	1994 Northridge	6.7	6.4	1.61	0.02	59.98	0.93	130.46	28.27
LA28	1994 Northridge	6.7	6.4	1.61	0.02	59.98	1.33	193.52	43.72
LA29	1974 Tabas	7.4	1.2	1.08	0.02	49.98	0.81	71.20	34.58
LA30	1974 Tabas	7.4	1.2	1.08	0.02	49.98	0.99	138.68	93.43
LA31	Elysian Park (simulated)	7.1	17.5	1.43	0.01	29.99	1.30	119.97	36.17
LA32	Elysian Park (simulated)	7.1	17.5	1.43	0.01	29.99	1.19	141.12	45.80
LA33	Elysian Park (simulated)	7.1	10.7	0.97	0.01	29.99	0.78	111.03	50.61
LA34	Elysian Park (simulated)	7.1	10.7	0.97	0.01	29.99	0.68	108.44	50.12
LA35	Elysian Park (simulated)	7.1	11.2	1.1	0.01	29.99	0.99	222.78	89.88
LA36	Elysian Park (simulated)	7.1	11.2	1.1	0.01	29.99	1.10	245.41	82.94
LA37	Palos Verdes (simulated)	7.1	1.5	0.9	0.02	59.98	0.71	177.47	77.38
LA38	Palos Verdes (simulated)	7.1	1.5	0.9	0.02	59.98	0.78	194.07	92.56
LA39	Palos Verdes (simulated)	7.1	1.5	0.88	0.02	59.98	0.50	85.50	22.64
LA40	Palos Verdes (simulated)	7.1	1.5	0.88	0.02	59.98	0.63	169.30	67.84

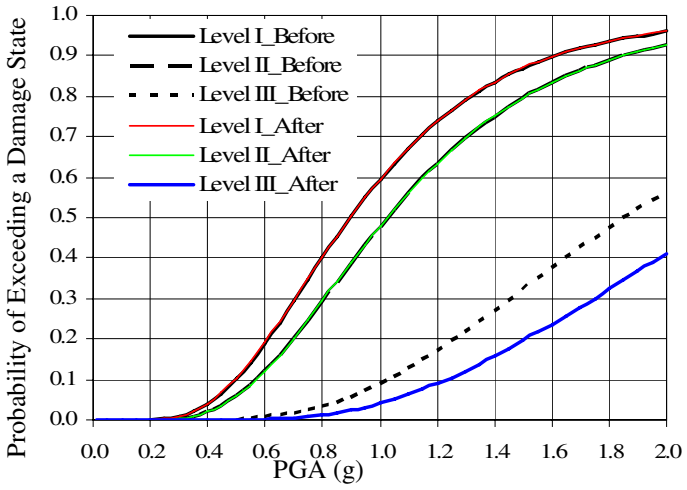

Figure 4.7 Before and after retrofit Fragility curves for different damage levels

4.6 Simulation of Ground Motion Considering Spatial Variability

4.6.1 Generation of Evolutionary PSDF from Given Ground Motion using STFT

This section briefly reviews the work done by Liang et al. (2007). The STFT $F(t,\omega)$ of a function $f(t)$ is expressed by the convolution integral in the following form:

$$F(t,\omega)=\int_{-\infty}^{\infty} f(\tau)h(t-\tau)e^{-i\omega\tau}d\tau \qquad (4.8)$$

where $h(t)$ is an appropriate time window. The evolutionary PSDF $S_{f_0f_0}(t,w)$ can be written as

$$\left|F(t,\omega)\right|^2=\int_{-\infty}^{\infty}\int_{-\infty}^{\infty} f(\tau_1)f(\tau_2)h(t-\tau_1)h(t-\tau_2)e^{-i\omega\tau_1}e^{-i\omega\tau_2}d\tau_1 d\tau_2 \qquad (4.9)$$

The total energy of $f(t)$ can be estimated as

$$\begin{aligned}&\int_{-\infty}^{\infty}\int_{-\infty}^{\infty}\left|F(t,\omega)\right|^2 dtd\omega\\&=\int_{-\infty}^{\infty}\int_{-\infty}^{\infty}\int_{-\infty}^{\infty}\int_{-\infty}^{\infty} f(\tau_1)f(\tau_2)h(t-\tau_1)h(t-\tau_2)e^{-i\omega(\tau_1-\tau_2)}d\tau_1 d\tau_2 dtd\omega\\&=\int_{-\infty}^{\infty}\int_{-\infty}^{\infty} f^2(\tau)h^2(t-\tau)d\tau dt\end{aligned} \qquad (4.10)$$

For the derivation of Eq. (4.10), the following equation is used:

$$\int_{-\infty}^{\infty} e^{-i\omega(\tau_1-\tau_2)}d\omega=\delta(\tau_1-\tau_2) \qquad (4.11)$$

If $h^2(t)=\delta(t)$, the total energy in Eq. (xx) is

$$\int_{-\infty}^{\infty}\int_{-\infty}^{\infty}\left|F(t,\omega)\right|^2 dtd\omega=\int_{-\infty}^{\infty} f^2(t)dt \qquad (4.12)$$

This implies that the time window should be chosen such that it satisfies the following condition

$$\int_{-\infty}^{\infty} h^2(t)dt = 1 \qquad (4.13)$$

The total energy can be kept identical (Perseval's identity) in estimating evolutionary PSDF. Here a Gaussian time window squared with standard deviation $\sigma = 0.25$ s, is used. It satisfies the condition in Eq. (4.13). The time window function has the following form,

$$h^2(t) = \frac{1}{\sigma\sqrt{2\pi}} e^{-t^2/2\sigma^2} \quad (\sigma = 0.25) \qquad (4.14)$$

Figure 4.8 shows the evolutionary PSDF of LA21 scenario earthquake record estimated using STFT (Gaussian window).

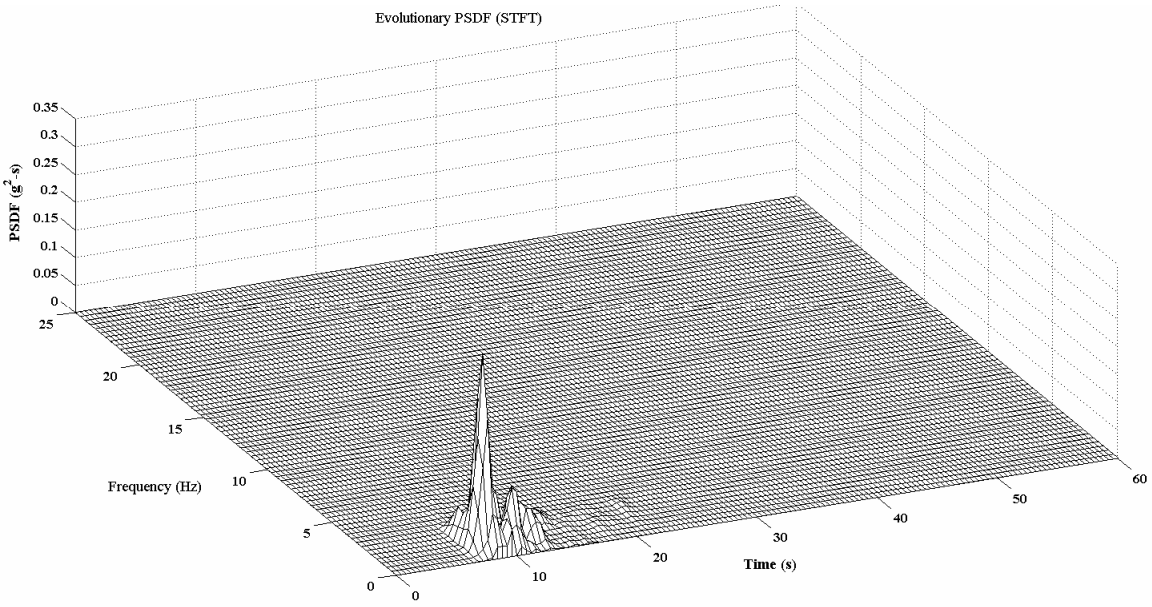

Figure 4.8 Evolutionary PSDF of LA21 earthquake record using STFT method

4.6.2 Generation of Evolutionary PSDF from Given Ground Motion using Wavelet Transform

This section briefly reviews the work done by Liang et al. (2007). The wavelet transform (WT) of a function $f \in \mathbf{L}^2(R)$ (finite energy function $\int |f(t)|^2 dt < +\infty$) at time u and scale s, and the corresponding inverse relationship are given by Daubechies (1992)

$$W_\psi f(u,s) = \frac{1}{\sqrt{s}} \int_{-\infty}^{\infty} f(t) \psi^* \left(\frac{t-u}{s} \right) dt, \quad u, s \in R \tag{4.15}$$

and

$$f(t) = \frac{1}{2\pi C_\psi} \int_{-\infty}^{\infty} \int_{-\infty}^{\infty} \frac{1}{s^2} W_\psi f(u,s) f(t) \psi \left(\frac{t-u}{s} \right) du ds, \quad u, s \in R \tag{4.16}$$

where

$$C_\psi = \int_{-\infty}^{\infty} \frac{|\hat{\psi}(\omega)|^2}{|\omega|} d\omega < \infty \tag{4.17}$$

In Equations (4.15) – (4.17), the wavelet function $\psi \in \mathbf{L}^2(R)$ known as 'mother" wavelet with average value equal to zero,

$$\int_{-\infty}^{\infty} \psi(t) dt = 0 \tag{4.18}$$

and is centered in the neighborhood of t = 0, and as normalized $\|\psi\|$ = 1. $\hat{\psi}(\omega)$ denotes the Fourier transform of $\psi(t)$ and is given by

$$\hat{\psi}(\omega) = \frac{1}{\sqrt{2\pi}} \int_{-\infty}^{\infty} \psi(t) e^{-i\omega t} dt \tag{4.19}$$

It may be noted that the WT decomposes signal $f(t)$ over dilated and translated wavelets. As $W_\psi f(u,s)$ is convolution of $f(t)$ with $(1/\sqrt{s})\psi^*(-t/s)$, $W_\psi f(u,s)$

represents the contribution of the function $f(t)$ in the neighborhood of $t=u$ and in the frequency band corresponding to scale s. It can be shown that (Daubechies, 1992)

$$\int_{-\infty}^{\infty}|f(t)|^2 dt=\frac{1}{2\pi C_\psi}\int_{-\infty}^{\infty}\int_{-\infty}^{\infty}\frac{1}{s^2}|W_\psi f(u,s)|^2 duds \tag{4.20}$$

Now, if any wavelet function satisfies the condition

$$\int_{-\infty}^{\infty}|\hat{\psi}_{u,s}(\omega)|^2 d\omega=1 \tag{4.21}$$

Then Equation (4.20) can be written as

$$\int_{-\infty}^{\infty}|f(t)|^2 dt=\int_{-\infty}^{\infty}\left[\frac{1}{2\pi C_\psi}\int_{-\infty}^{\infty}\int_{-\infty}^{\infty}\frac{1}{s^2}|W_\psi f(u,s)|^2 duds\right]\times\int_{-\infty}^{\infty}|\hat{\psi}_{u,s}(\omega)|^2 d\omega \tag{4.22}$$

In Equations (4.21) and (4.22), $\hat{\psi}_{u,s}(\omega)$ represents the Fourier transform of $\psi\left(\frac{t-u}{s}\right)$ and can be expressed as $\hat{\psi}_{u,s}(\omega)=\sqrt{s}\hat{\psi}(s\omega)e^{i\omega u}$. Then, using Perseval's identity, one can write

$$|F(\omega)|^2=\frac{1}{2\pi C_\psi}\int_{-\infty}^{\infty}\int_{-\infty}^{\infty}\frac{1}{s^2}|W_\psi f(u,s)|^2|\hat{\psi}_{u,s}(\omega)|^2 duds \tag{4.23}$$

where $F(\omega)$ = Fourier transform of $f(t)$. As the wavelet coefficient $W_\psi f(u,s)$ provides the localized information of signal $f(t)$ at $t=u$, from Equation (4.23) the Evolutionary PSDF $S_{f_0 f_0}(t,\omega)$ can be expressed as

$$|F(\omega,t)|^2=\frac{1}{2\pi C_\psi}\int_{-\infty}^{\infty}\frac{1}{s^2}|W_\psi f(t,s)|^2|\hat{\psi}_{t,s}(\omega)|^2 ds \tag{4.24}$$

It may be noted that the expression of evolutionary PSDF given in Equation (4.24) obeys total energy equilibrium. Therefore, any wavelet basis can be used which satisfies Equation (4.21), for generation of evolutionary PSDF [e.g., modified Littlewood-Paley basis proposed by Basu and Gupta (1998)] that maintains total energy. Figure 4.9 shows

the evolutionary PSDF of LA21 scenario earthquake record estimated using STFT (Gaussian window).

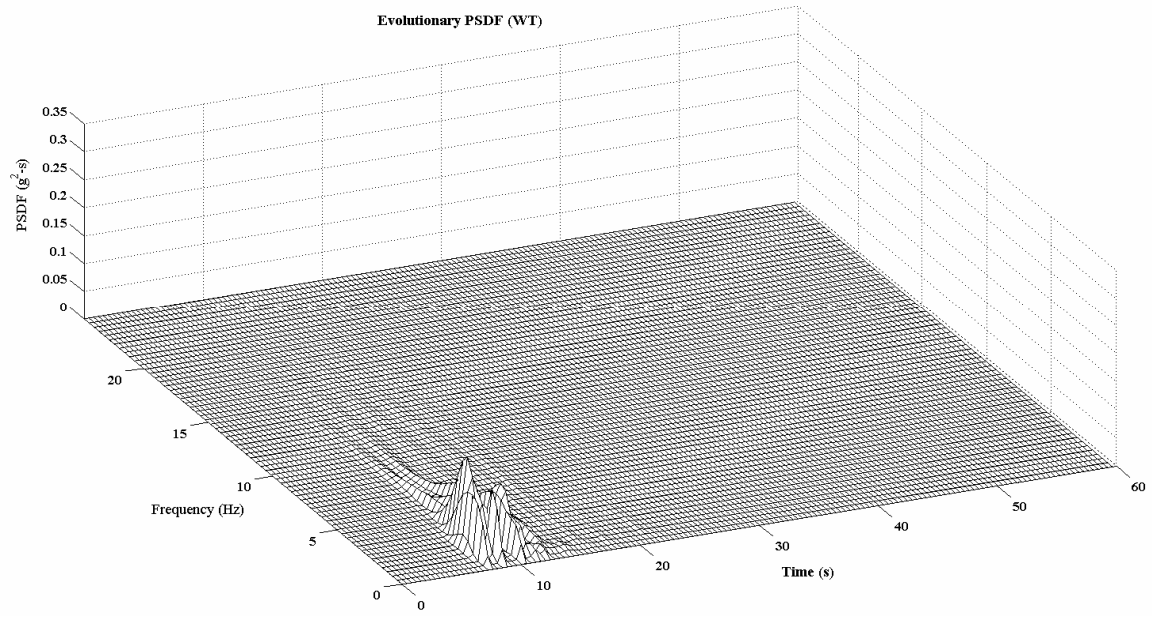

Figure 4.9 Evolutionary PSDF of LA21 earthquake record using wavelet transform

4.6.3 Simulation of One-Dimensional Multi-Variate (1D-mV), Nonstationary Gaussian Stochastic Process

To generate sample functions of stochastic processes, the spectral representation method developed by Shinozuka and Jan (1972) appears to be most versatile and widely used today. Spectral representation based algorithm to simulate one-dimensional multi-variate nonstationary Gaussian stochastic process developed by Deodatis (1996b) is used in this study and described as follows.

Consider a one-dimensional, n-variate (1D-nV) non-stationary stochastic vector process with components $f_1^0(t), f_2^0(t),\ldots\ldots, f_n^0(t)$, having a mean value equal to zero, and the cross-spectra density matrix given by

$$\mathbf{S}^0(\omega,t) = \begin{bmatrix} S_{11}^0(\omega,t) & S_{12}^0(\omega,t) & \cdots & S_{1n}^0(\omega,t) \\ S_{21}^0(\omega,t) & S_{22}^0(\omega,t) & \cdots & S_{2n}^0(\omega,t) \\ \vdots & \vdots & \ddots & \vdots \\ S_{n1}^0(\omega,t) & S_{n2}^0(\omega,t) & \cdots & S_{nn}^0(\omega,t) \end{bmatrix} \tag{4.15}$$

The elements of $\mathbf{S}^0(\omega,t)$ are expressed as

$$S_{jj}^0(\omega,t) = S_j(\omega,t), \qquad j = 1,2,\ldots,n \tag{4.16}$$

$$S_{jk}^0(\omega,t) = \sqrt{S_j(\omega,t)S_k(\omega,t)}\Gamma_{jk}(\omega), \qquad j,k = 1,2,\ldots,n; j \neq k \tag{4.17}$$

where $S_j(\omega,t)$ = Evolutionary power spectral density function of $f_j^0(t)$, and $\Gamma_{jk}(\omega)$ = coherence function between $f_j^0(t)$ and $f_k^0(t)$.

In order to simulate the 1D-mV stochastic vector process $f_j^0(t)$; j = 1, 2,... ,n, its cross-spectral density matrix $S^0(\omega,t)$ must be first decomposed at every time instant t under consideration, into the following product:

$$S^0(\omega,t) = H(\omega,t)H^{T*}(\omega,t) \qquad \text{for every } t \text{ under consideration} \tag{4.18}$$

Where superscript T denotes the transpose of a matrix. Using Cholesky's method or modal decomposition, $H(\omega,t)$ can be evaluated as a lower triangular matrix:

$$H(\omega,t)=\begin{bmatrix} H_{11}(\omega,t) & 0 & 0 & \cdots & 0 \\ H_{21}(\omega,t) & H_{22}(\omega,t) & 0 & \cdots & 0 \\ H_{31}(\omega,t) & H_{32}(\omega,t) & H_{33}(\omega,t) & \cdots & 0 \\ \vdots & \vdots & \vdots & \ddots & \vdots \\ H_{n1}(\omega,t) & H_{n2}(\omega,t) & H_{n3}(\omega,t) & \cdots & H_{nn}(\omega,t) \end{bmatrix} \tag{4.19}$$

The following relations are valid for the elements of matrix $H(\omega,t)$:

$$H_{jj}(\omega,t) = H_{jj}(-\omega,t) \;\; ; \quad j = 1,2,.....,n \tag{4.20}$$

$$H_{jk}(\omega,t) = H^{*}_{jk}(-\omega,t) \;\; ; \quad j = 2,3,.....,n;\; k = 1,2,.....,n-1;\; j > k \tag{4.21}$$

If the off-diagonal elements $H_{jk}(\omega,t)$ are written in polar form as:

$$H_{jk}(\omega,t) = \left|H_{jk}(\omega,t)\right| e^{i\theta_{jk}(\omega,t)} \;\; ; \quad j = 2,3,.....,n;\; k = 1,2,.....,n-1;\; j > k \tag{4.22}$$

where

$$\theta_{jk}(\omega,t) = \tan^{-1}\left(\frac{\mathrm{Im}\left[H_{jk}(\omega,t)\right]}{\mathrm{Re}\left[H_{jk}(\omega,t)\right]}\right) \tag{4.23}$$

with Im and Re denote the imaginary and the real part of a complex number respectively. Then Eq. 10 equivalently can be written as :

$$\left|H_{jk}(\omega,t)\right| = \left|H_{jk}(-\omega,t)\right| \;\; ; \quad j = 2,3,.....,n;\; k = 1,2,.....,n-1;\; j > k \tag{4.24}$$

$$\theta_{jk}(\omega,t) = -\theta_{jk}(-\omega,t) \;\; ; \quad j = 2,3,.....,n;\; k = 1,2,.....,n-1;\; j > k \tag{4.25}$$

Once matrix $S^0(\omega)$ is decomposed using Cheloskey's decomposition Equation 4.18, the stochastic process $f_j^0(t);\ j = 1,2,.....,n$ can be simulated by the following series as $N \to \infty$

$$f_j(t) = 2\sum_{q=1}^{j}\sum_{l=0}^{N-1}\left|H_{jq}(\omega_l,t)\right|\sqrt{\Delta\omega}\cos\left[\omega_l t - \theta_{jq}(\omega_l,t) + \Phi_{ql}\right];\ j = 1,2,3,.....,n \qquad (4.26)$$

where:

$$\Delta\omega = \frac{\omega_u}{N} \qquad (4.27)$$

$$\omega_l = l\Delta\omega,\quad l = 0,1,\cdots,N-1 \qquad (4.28)$$

$$\theta_{jq}(\omega_l,t) = \tan^{-1}\left(\frac{\mathrm{Im}\left[H_{jq}(\omega_l,t)\right]}{\mathrm{Re}\left[H_{jq}(\omega_l,t)\right]}\right) \qquad (4.29)$$

In Eq. (4.27), ω_u represents an upper cut-off frequency beyond which the elements of the cross-spectral density matrix Eq. (4.18) may be assumed to be zero for either mathematical or physical reasons.

4.6.4 Simulation of Seismic Spectrum Compatible Accelerograms

This study presents the influence of spatial variable ground motions on the lateral seismic response of a long span suspension bridge. The spatial variability of ground motions is considered with site-response, incoherence, and wave passage effects. The site-response effect arises from variable soil profiles at different support locations on the ground of the

structure. The incoherency effect comes from the scatterings of seismic wave and change in shape of the propagating waveform due to the inhomogeneous soil medium. When the seismic wave travels through the soil medium in non-vertical direction, the seismic energy arrives at different times at different support locations. The difference in arrival times of seismic waves at different support locations is due to wave passage effect.

Effects of variable soil conditions are considered in the design response spectra considered for 6 different supports of the bridge. Loss of coherency is considered by using the coherency function proposed by Harichandran et al. (1996). Since the ground motions considered for dynamic analysis of the bridge was in lateral direction, i.e. perpendicular to the longitudinal axis of the bridge, wave passage effect is neglected for the present analysis case.

In this study, an iterative algorithm is proposed to generate spatially variable, design spectrum compatible acceleration time histories at different support locations of the bridge. The proposed algorithm is used to generate synthetic ground motions at six different points on the ground surface. For generating non-stationary accelerograms, previously researchers used time dependent envelope function on top of simulated stationary ground motions (Deodatis 1996). In this study by using evolutionary power spectral density function from the mother accelerogram, a new algorithm has been proposed to simulate spatial variable ground motions. In the simulated acceleration time histories the temporal variations of the frequency content are same as the mother accelerogram. Mukherjee and Gupta (2002) proposed a new wavelet based approach to simulate spectrum compatible time histories. But they only considered one design

spectrum and simulated one accelrogram from a single mother acceleration time history. Sarkar and Gupta (2006) developed a wavelet based approach to simulate spatially correlated and spectrum compatible accelerogram. But they failed to consider different design spectra for different support locations. Because of the variability of soil conditions at different support locations, different design spectra should be considered at different supports. In this study different design spectra at different support locations are considered. Another advantage of this method over the previous methods is that, one can generate multiple set of spectrum compatible accelerograms from one mother accelrogram. Every simulation will give different set of simulated accecelerograms because of randomly generated phase angles used in the simulation formula. From USGS one can get only one scenario earthquake for a certain location. But they can not provide engineers with spatially variable ground motions considering aforementioned three different effects, for different supports of a long span bridge. The proposed method will overcome that limitation, as long as the site specific scenario earthquake time history is available for the bridge site.

The proposed algorithm for simulation of earthquake ground motion time histories utilizes the new simulation algorithm proposed here for generating sample functions of a general non-stationary stochastic vector process with evolutionary power, according to a previously defined non-stationary cross-spectral density matrix. In this study six synthetic acceleration time histories are generated at six different support locations. The support locations are anchorage, cable bent, and tower at east and west side of the bridge. An iterative algorithm shown in Figure 4.10 depicts the procedure for generation of spectral compatible accelerograms at six different support locations. In

general, all the six different support locations will have different local soil conditions. The local soil conditions used in this study are taken from the soil report of the bridge site. These soil conditions are tabulated in Table 4.3. Six different target design spectra $RSA_j(\omega);\ j=1,2,3,4,5,6$ are assigned for six different support points (Figure 4.11). These bridge site specific target design spectra are obtained from the ASCE (2006) and are used in this study. The site specific parameters S_s and S_1 are found to be 2.75 and 0.75 respectively for the Vincent Thomas bride site location (33º45′ North, 118º16′ West). The Site coefficient parameters to calculate design spectra at different supports are tabulated in Table 4.3. In addition, complex coherence functions $\Gamma_{jk}(\omega);\ j,k=1,2,3,4,5,6;\ j\neq k$ are prescribed between pairs of points. The initial value of the evolutionary PSDFs at different points are obtained from the mother accelerogram using the STFT and WT techniques as described in Sections 4.6.1 and 4.6.2. A set of non-stationary, six-variate, random vector processes are simulated using the calculated cross-spectral density matrix from the initial PSDFs. The algorithm proposed here is used to generate a sample function according to prescribed evolutionary cross-spectral density matrix. The response spectra calculated from the simulated acceleration time histories are compared with the design spectra at different supports. If the error is more than a tolerance limit, then the evolutionary PSDFs are updated according to Figure 4.10 and are used to generate new set of simulated ground motions. The iteration stops when it satisfies the pre defined convergence criteria.

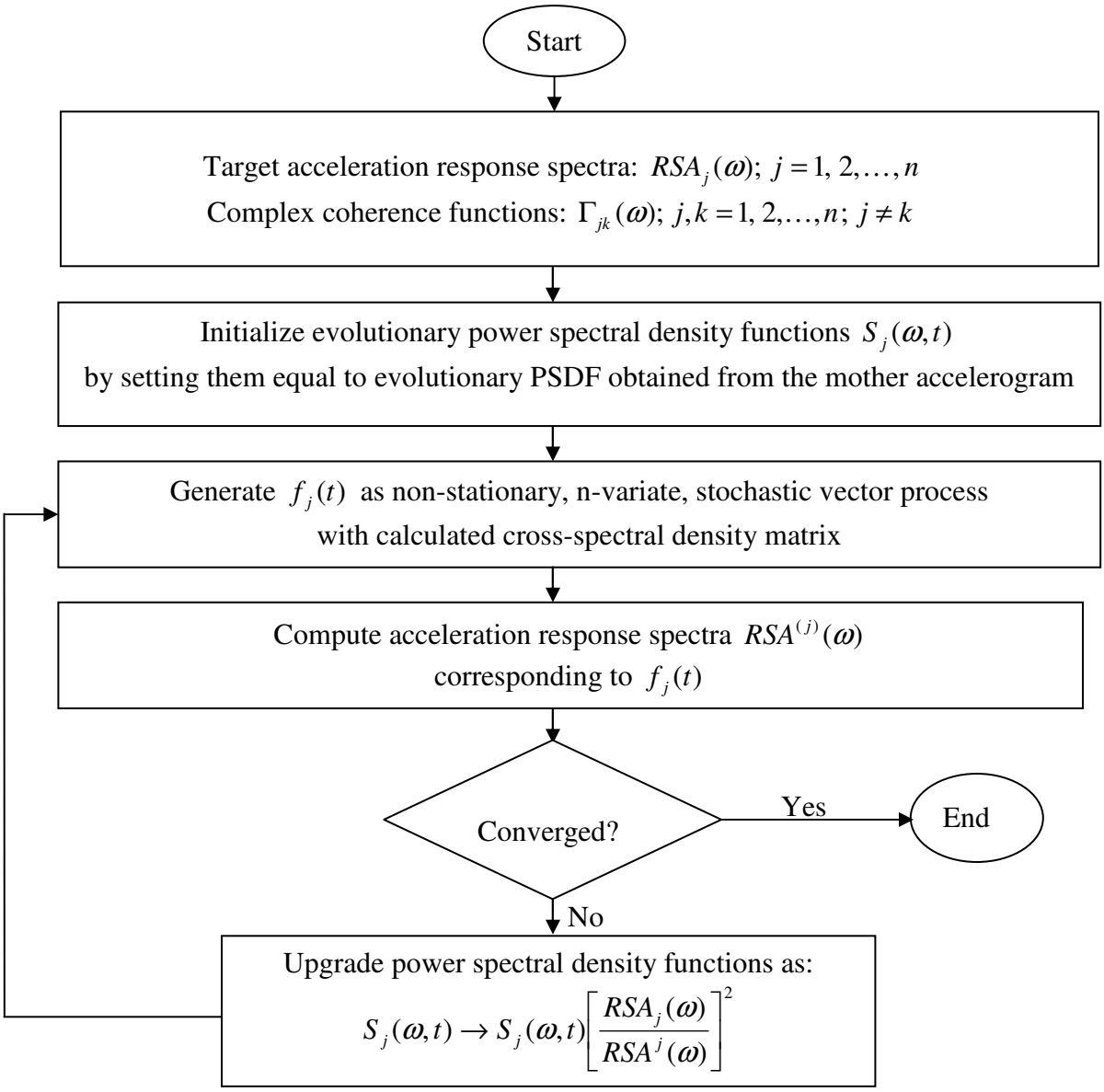

Figure 4.10 Iterative scheme to simulate spectrum compatible acceleration time histories

4.6.5 Examples of Generated Seismic Ground Motion

For the prescribed coherence function, the Harichandran and Vanmarcke model (Harichandran and Vanmarcke 1986) is chosen to describe the target coherence function $\gamma_{jk}(\omega);\ j,k=1,2,.....;\ j\neq k$ between $f_j^0(t)$ and $f_k^0(t)$.

$$\gamma_{jk}(\omega)=A\exp\left[-\frac{2\xi_{jk}}{\alpha\theta(\omega)}(1-A+\alpha A)\right]+(1-A)\exp\left[-\frac{2\xi_{jk}}{\theta(\omega)}(1-A+\alpha A)\right] \tag{4.30}$$

where ξ_{jk} is the distance between points j and k, $\theta(\omega)$ is the frequency dependent correlation distance:

$$\theta(\omega)=k\left[1+\left(\frac{\omega}{2\pi f_0}\right)^b\right]^{-1/2} \tag{4.31}$$

and $A,\alpha,\ k,\omega_0$ and b are the model parameters. In this study the model parameters are obtained from Harichandran et al. (1996). These values are $A=0.626,\ \alpha=0.186,\ k=31200,\ f_0=1.51$ Hz and $b=2.95$. In the simulation formula, $\Gamma_{jk}(\omega)=\gamma_{jk}(\omega)\exp(-i\omega\xi_{jk}/v)$, with $\gamma_{jk}(\omega)$ is the coherence function between two spatially separated points, separated at a distance of ξ_{jk}, and the exponential term in the expression reflects the apparent propagation of motions with shear wave velocity v.

The acceleration time histories $f_j^0(t);\ j = 1,2,3,4,5,and\ 6$ are modeled as a non-stationary stochastic vector process. The LA21 scenario earthquake i.e. the mother accelerogram is shown in Figure 4.12. According to the iterative scheme outlined in Figure 4.10, generated sample six acceleration time histories are plotted in Figures 4.13 – 4.18. The generated sample displacement time histories at six different supports of a bridge are calculated through double integration with respect to time and only two are plotted in Figure 4.19 and Figure 4.20. In order to verify the generated acceleration time histories compatible with prescribed response spectra, the acceleration response spectra computed using the ground motion time histories should be compared with the target response spectra. Ensemble average of 5% damped spectral acceleration response spectra obtained from 20 set of simulations for six different spatially separated supports is compared with the design response spectra for all the support locations. This comparison is shown in Figures 4.7 – 4.9 at locations 1 and 3 by using STFT and Wavelet approach. It shows good match with the target design acceleration response spectra with the simulated one.

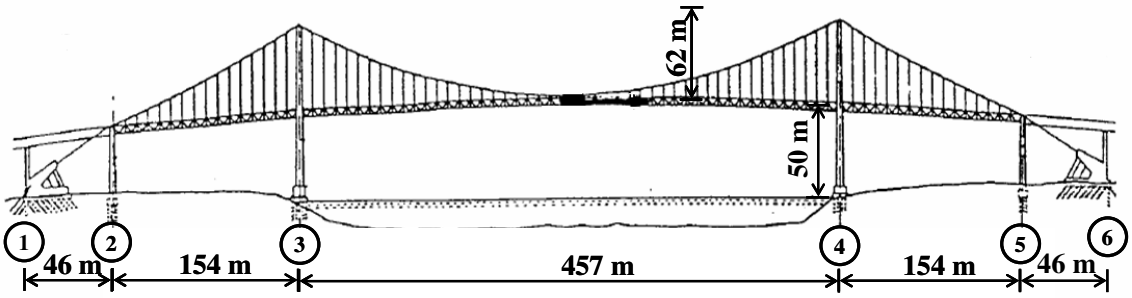

Figure 4.11 Different support locations of the bridge

Table 4.3 Site coefficient parameters to calculate design spectra at different supports

Support No.	Distance (m)	*Fa*	*Fv*	Site Class	Soil Property
1	0	1	1.5	D	Stiff Soil
2	46	1	1.5	D	Stiff Soil
3	200	0.9	2.4	E	Soft Clay Soil
4	657	0.9	2.4	E	Soft Clay Soil
5	811	1	1.5	D	Stiff Soil
6	857	1	1.5	D	Stiff Soil

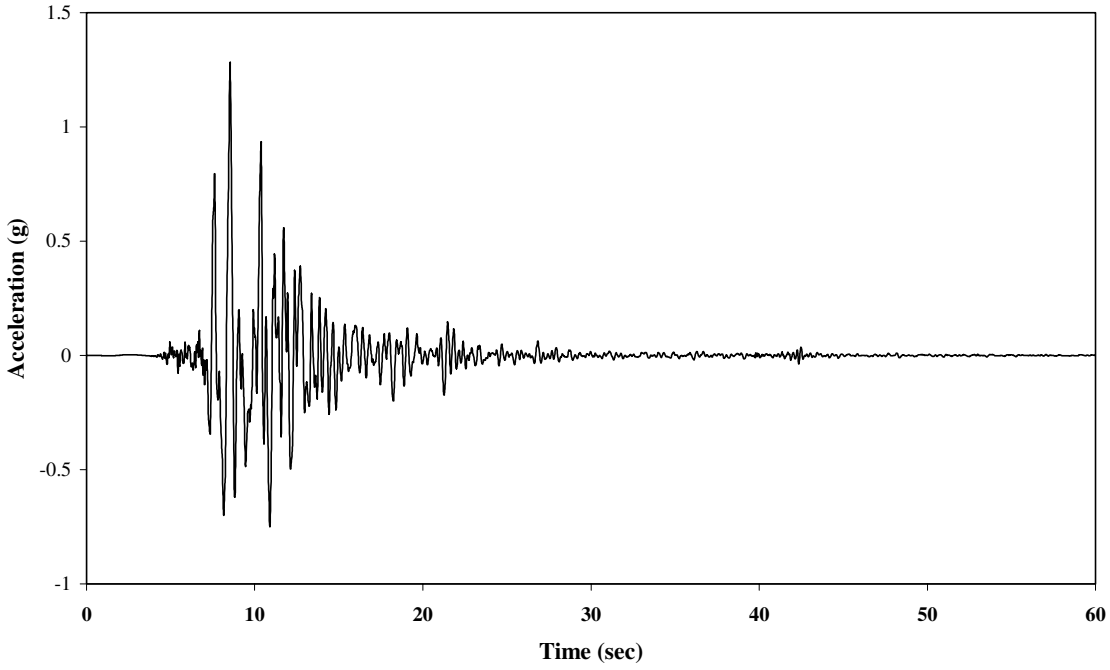

Figure 4.12 Acceleration time history of LA 21 scenario earthquake

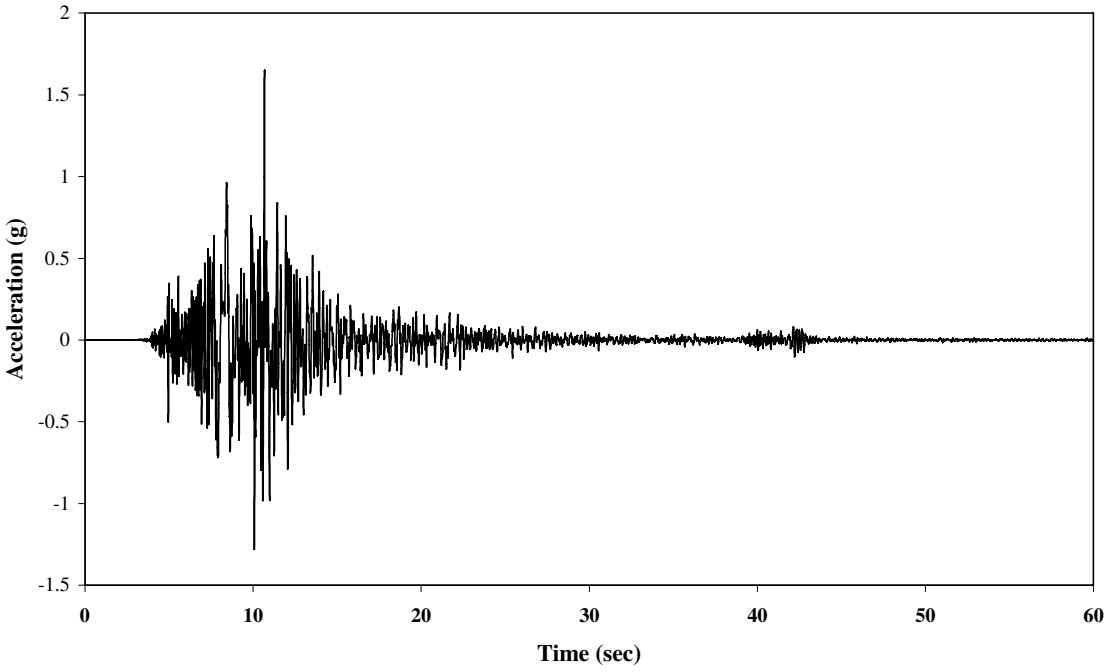

Figure 4.13 Acceleration time history at location 1

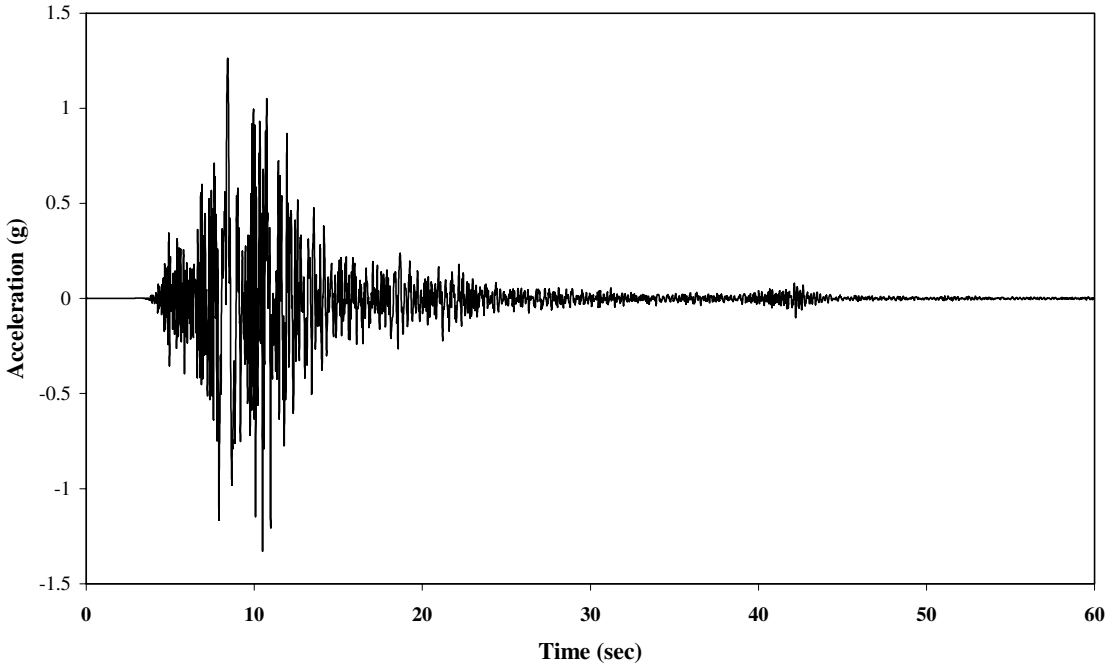

Figure 4.14 Acceleration time history at location 2

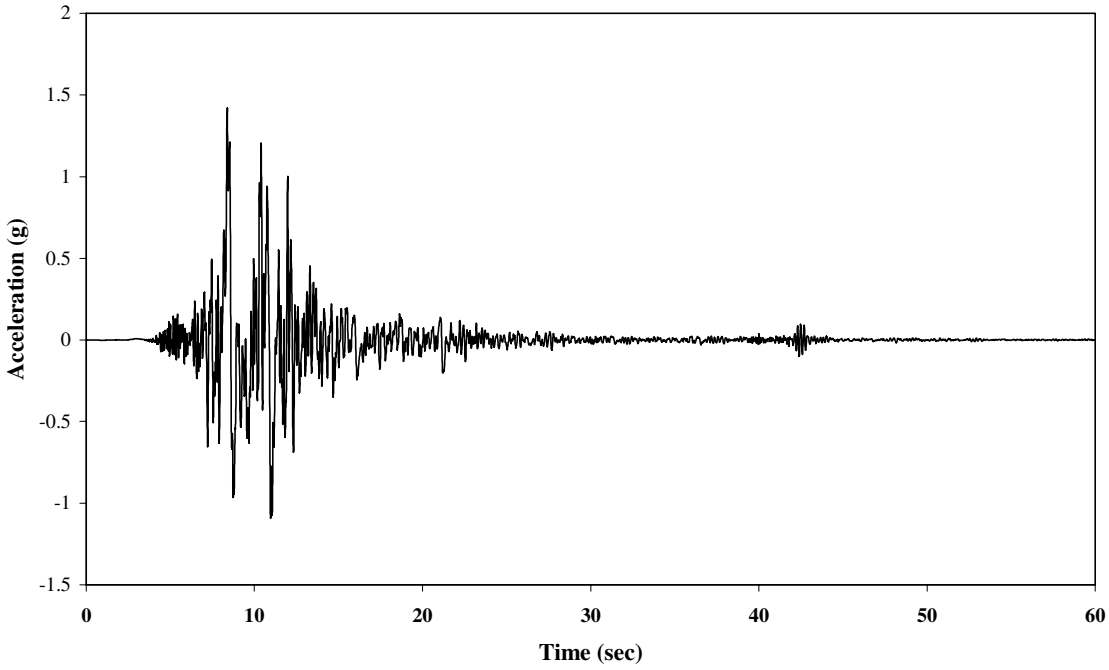

Figure 4.15 Acceleration time history at location 3

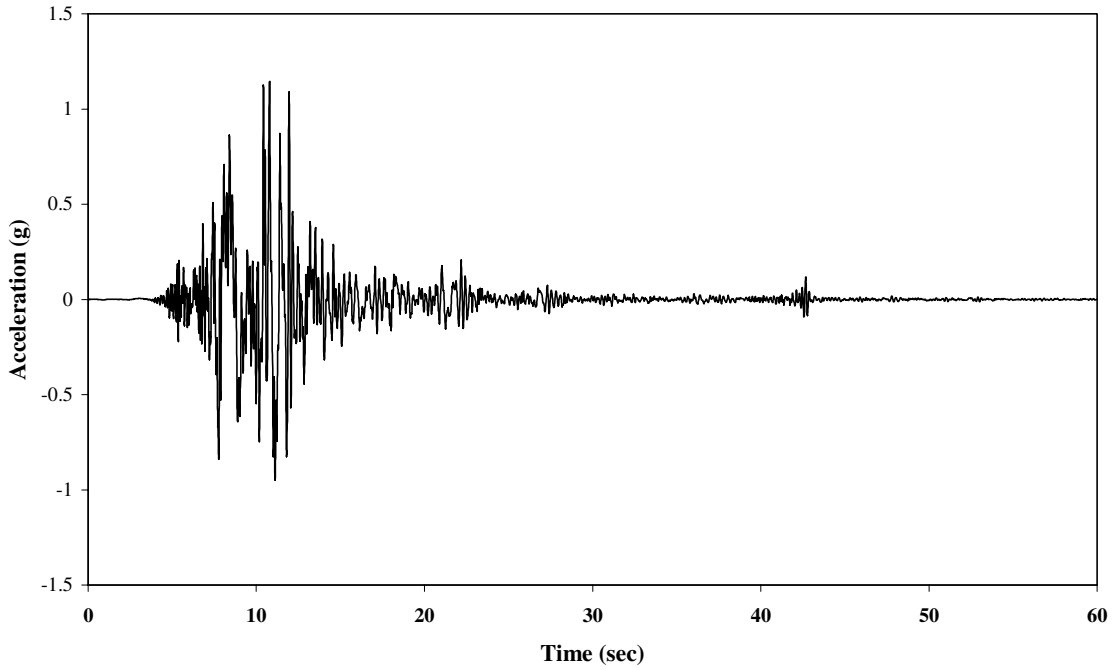

Figure 4.16 Acceleration time history at location 4

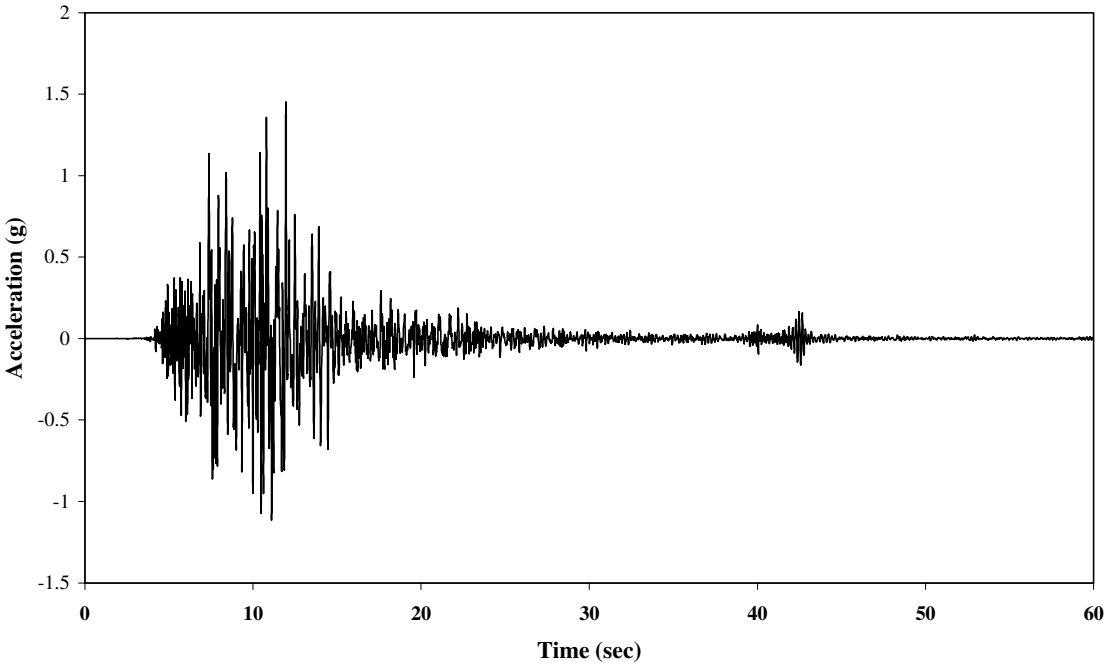

Figure 4.17 Acceleration time history at location 5

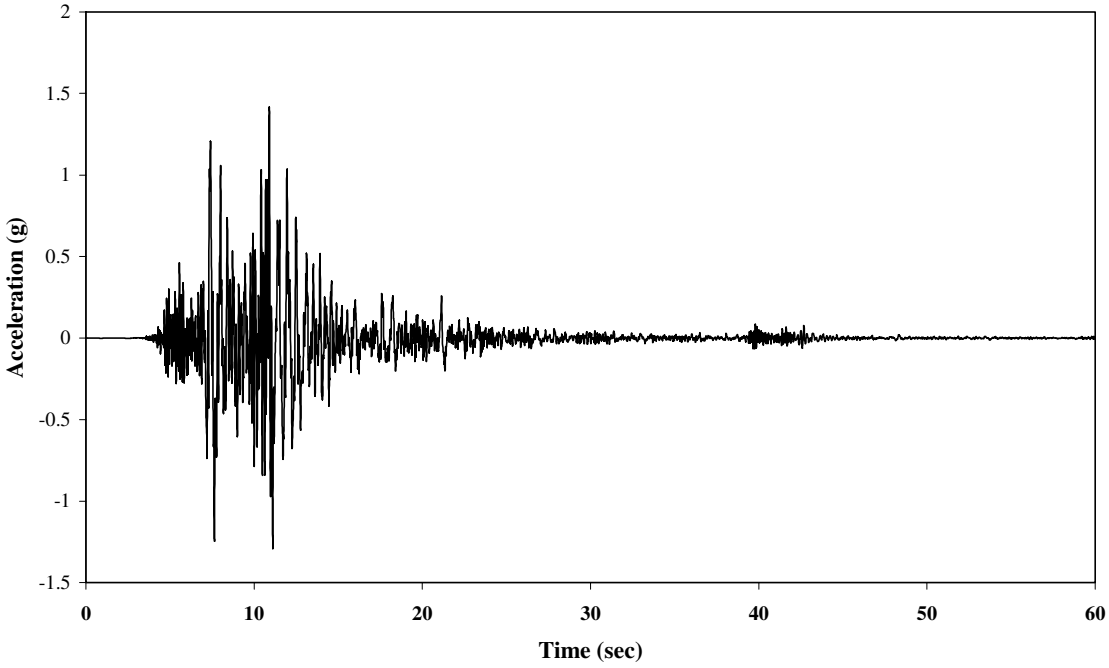

Figure 4.18 Acceleration time history at location 6

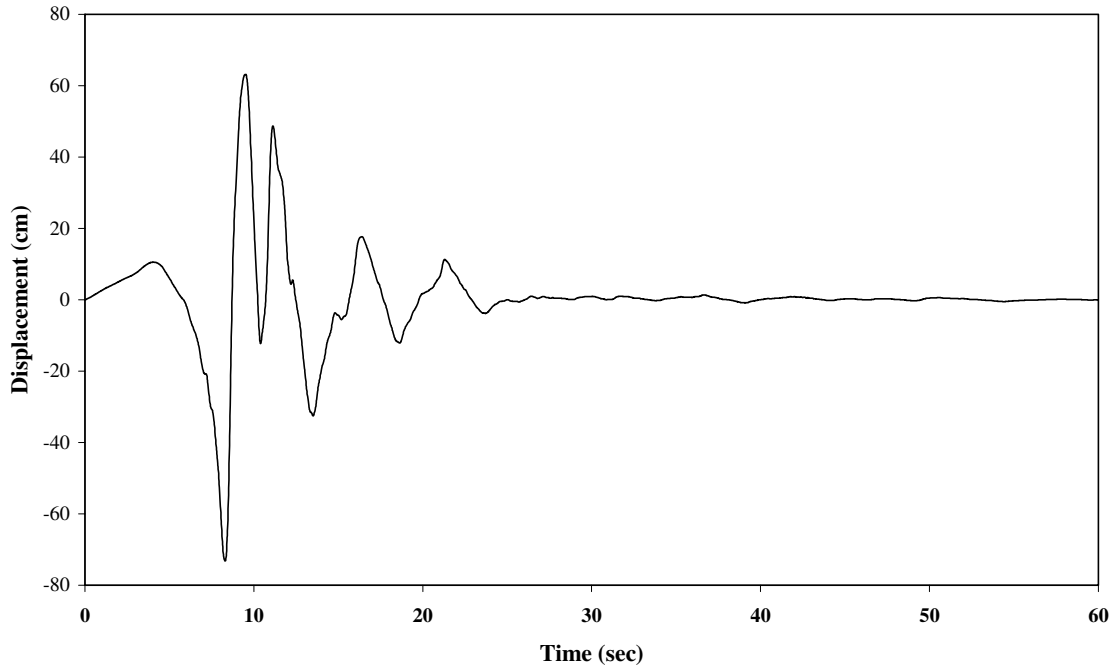

Figure 4.19 Displacement time history at location 3

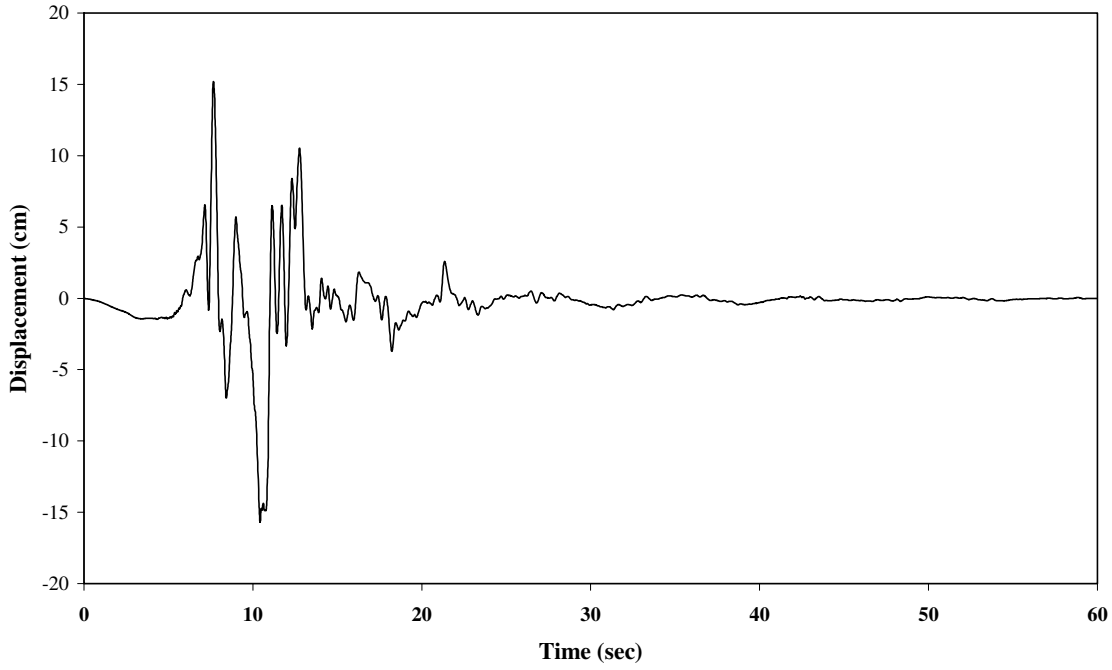

Figure 4.20 Displacement time history at location 6

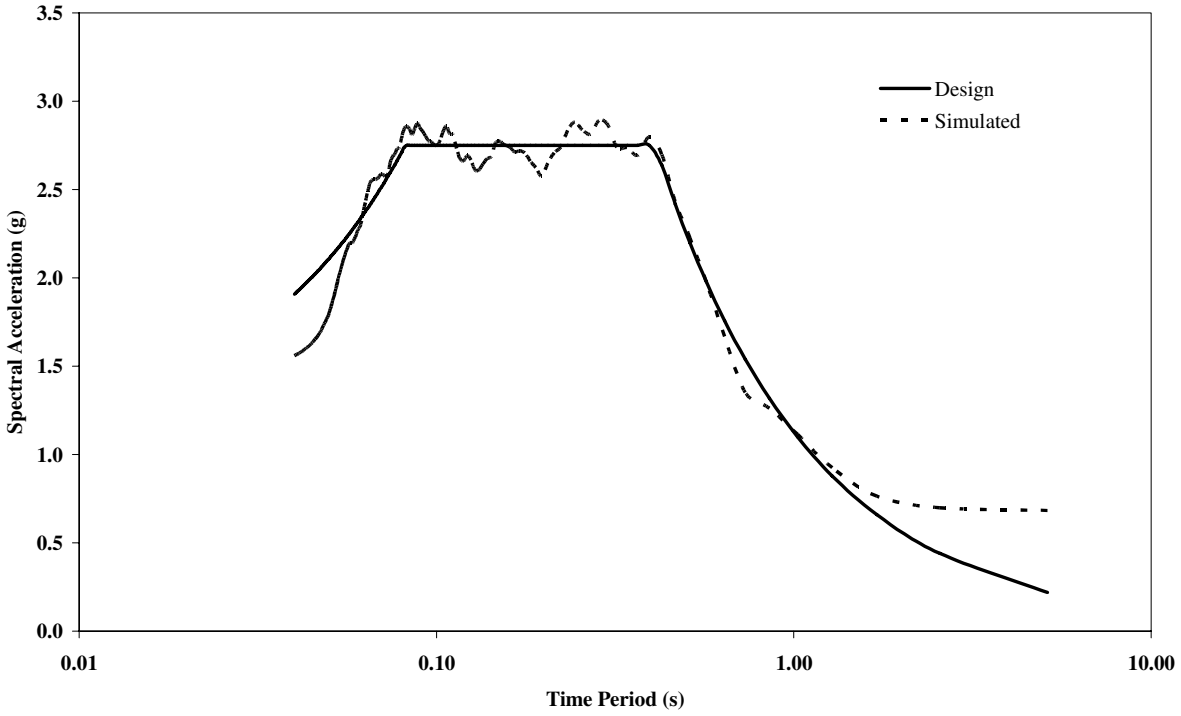

Figure 4.21 Comparison between simulated and design spectra at location 1 using STFT

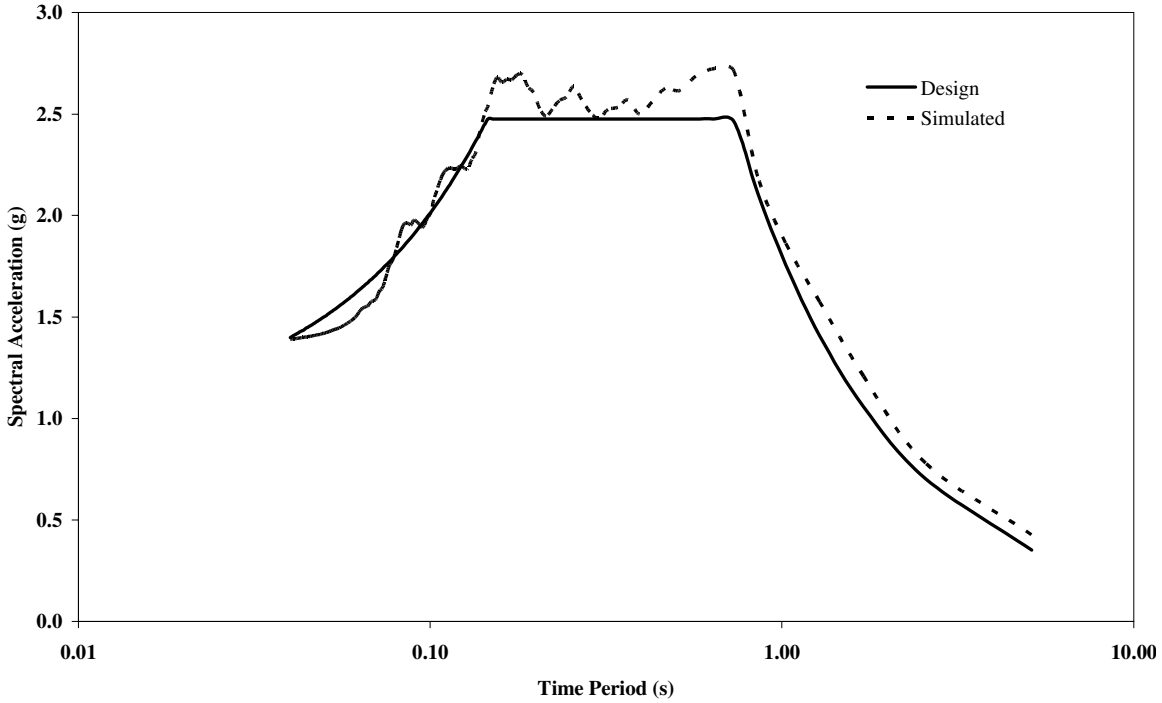

Figure 4.22 Comparison between simulated and design spectra at location 3 using STFT

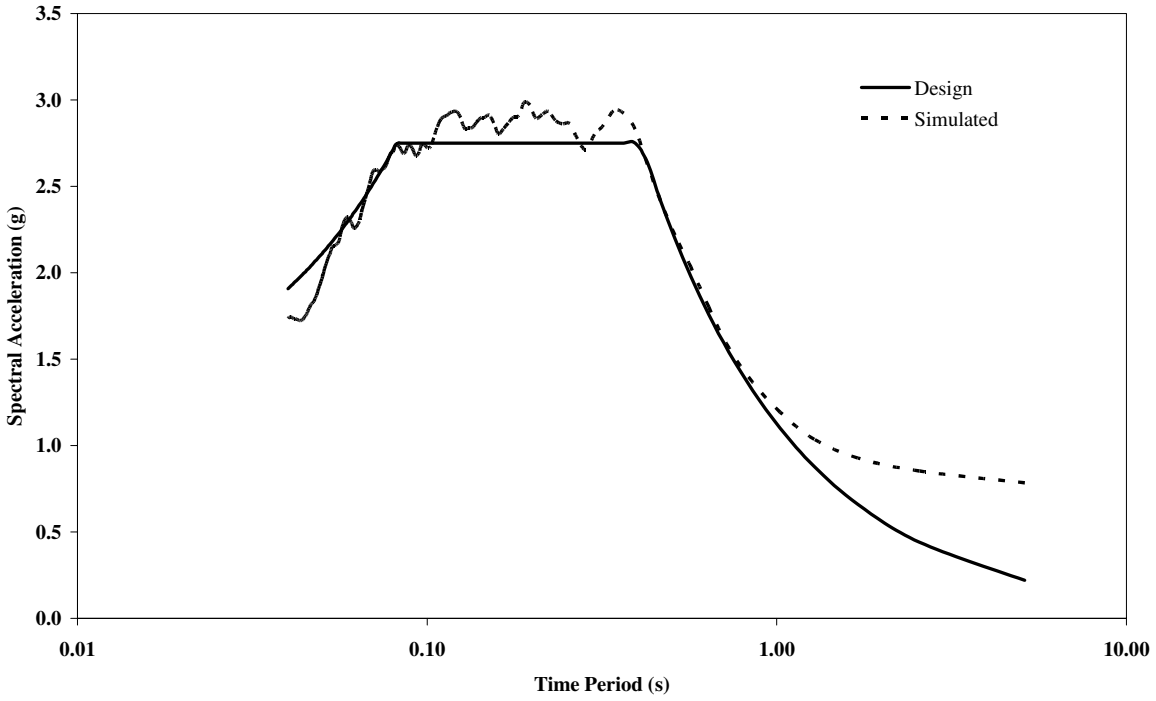

Figure 4.23 Comparison between simulated and design spectra at location 1 using Wavelet

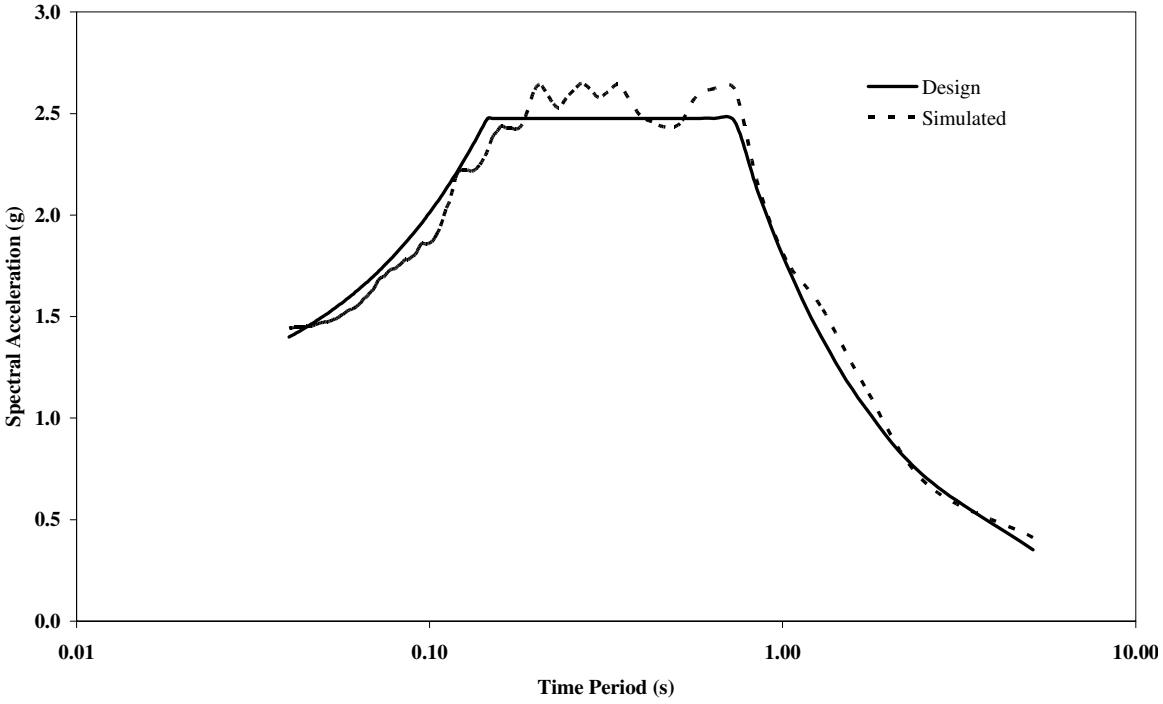

Figure 4.24 Comparison between simulated and design spectra at location 3 using Wavelet

4.7 Results

Spatially variable ground motions simulated in the previous section are used in calculating the response of the bridge. In addition to spatial variable seismic ground motions, two uniform ground motions are also considered for comparison purpose. From the 6 simulated acceleration time histories, one with the largest peak ground displacement (PGD) ('worst-case' scenario) and the other with the smallest PGD ('best-case' scenario) are considered. In this case uniform ground acceleration time history at location 3 (soft clay soil) with PGD 73.20 cm is the 'worst-case' scenario and uniform ground acceleration time history at location 6 (stiff soil) with PGD 15.68 cm is the 'best-case'

scenario. The seismic response of the bridge is calculated using those three different cases and compared in both seismic displacement demand and seismic force demand. The spatial variation, best-case and worst-case scenarios will be denoted by 'SV', 'BEST', and 'WORST' respectively. Table 4.2 shows the displacement demand comparison at the center of the deck and at the top of the east tower for three different cases. The WORST case scenario displacement demand in both deck and tower are larger than SV and BEST cases. Figures 4.25 – 4.28 show the absolute axial force, shear force, moment, and torsional force demand envelopes for the bridge girder for three different scenario cases of analysis. It can be seen from the figures that the WORST case scenario produces more seismic force demand at most locations on the bridge deck except for the shear force demand. In case of shear force demand SV case gives more force along the deck. Also, for other three force demands at the sides of the middle span SV produces more force demand than WORST case scenario. Figures 4.29 – 4.32 show the absolute axial force, shear force, moment, and torsional force demand envelopes for the east tower of the bridge for three different scenario cases of analysis. In all of them, WORST case scenario gives a little bit higher seismic force demand compared to SV case. Axial force, shear force, and moment demand at the middle of the tower decreased drastically because the force is transferred from the bottom section to the top section by the tower link at that location of the tower.

Table 4.4 Displacement demand comparison

Maximum displacement (m)	BEST	WORST	SV
Center of the deck	0.67	2.52	1.97
Top of the east tower	0.39	1.49	1.60

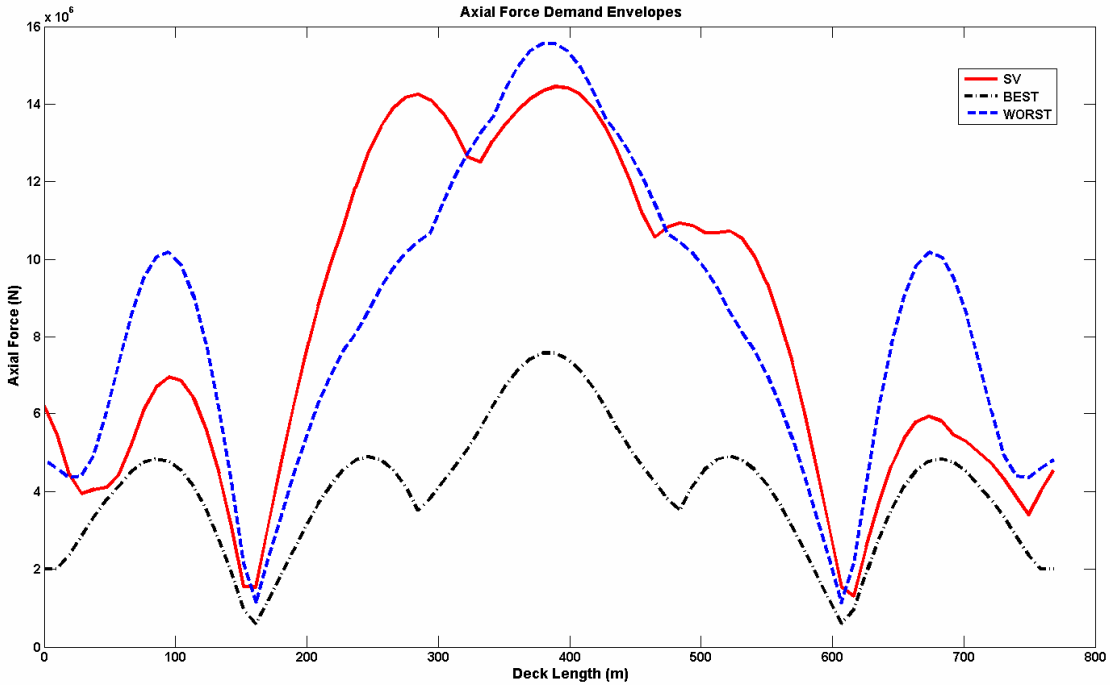

Figure 4.25 Absolute axial force demand envelope for the bridge girder

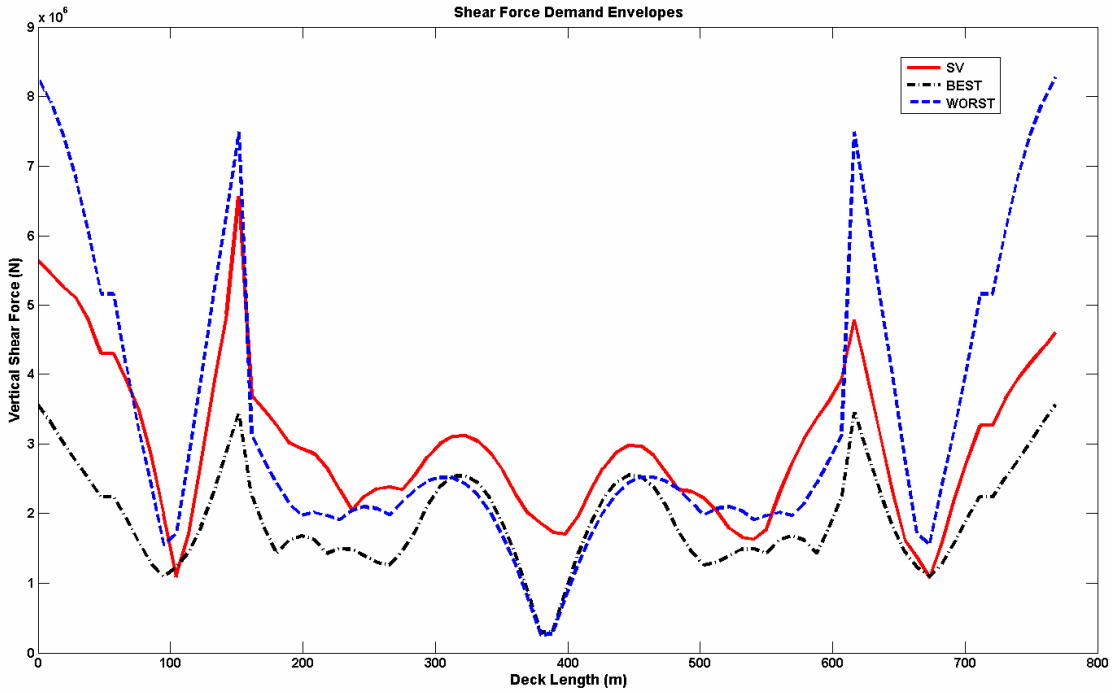

Figure 4.26 Absolute shear force demand envelope for the bridge girder

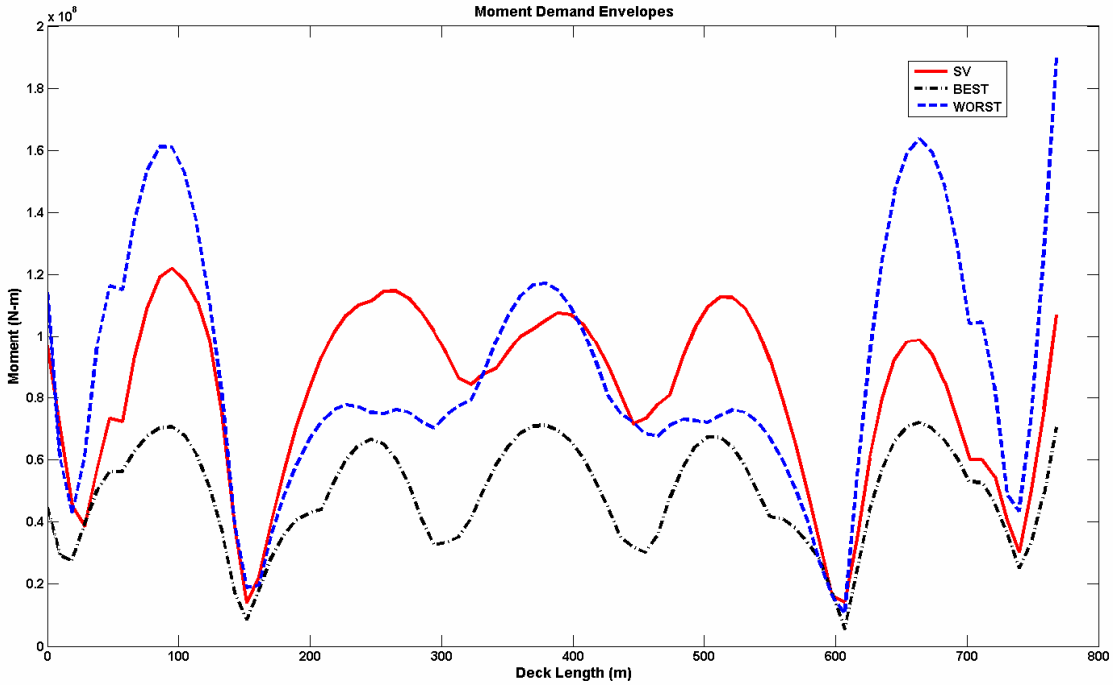

Figure 4.27 Absolute moment demand envelope for the bridge girder

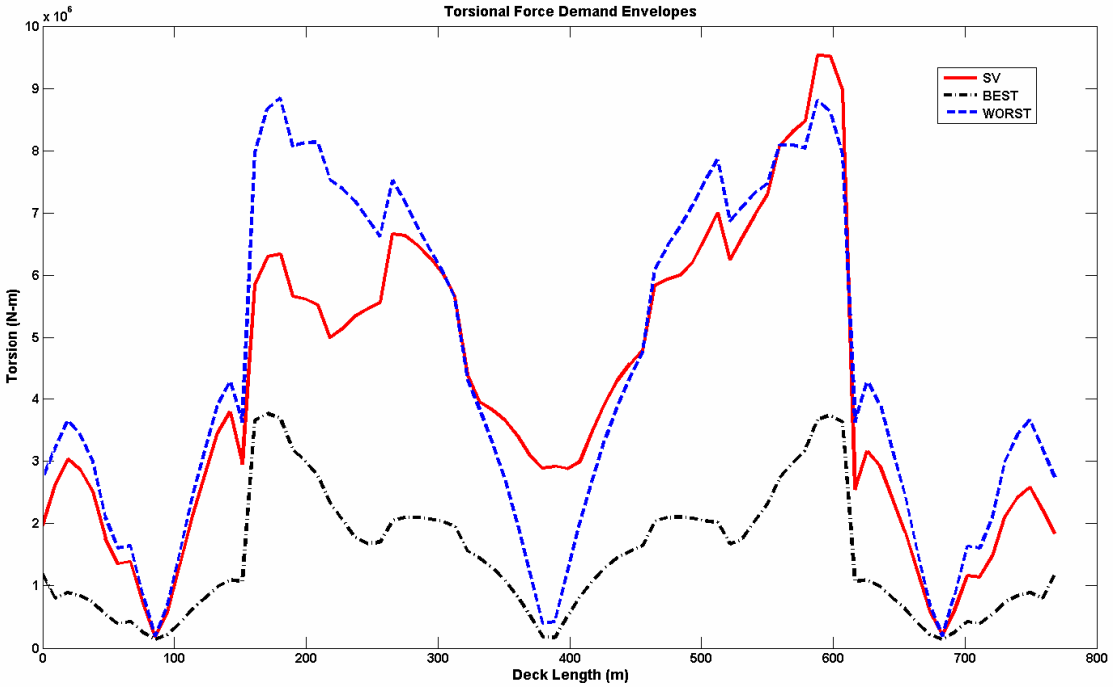

Figure 4.28 Absolute torsional force demand envelope for the bridge girder

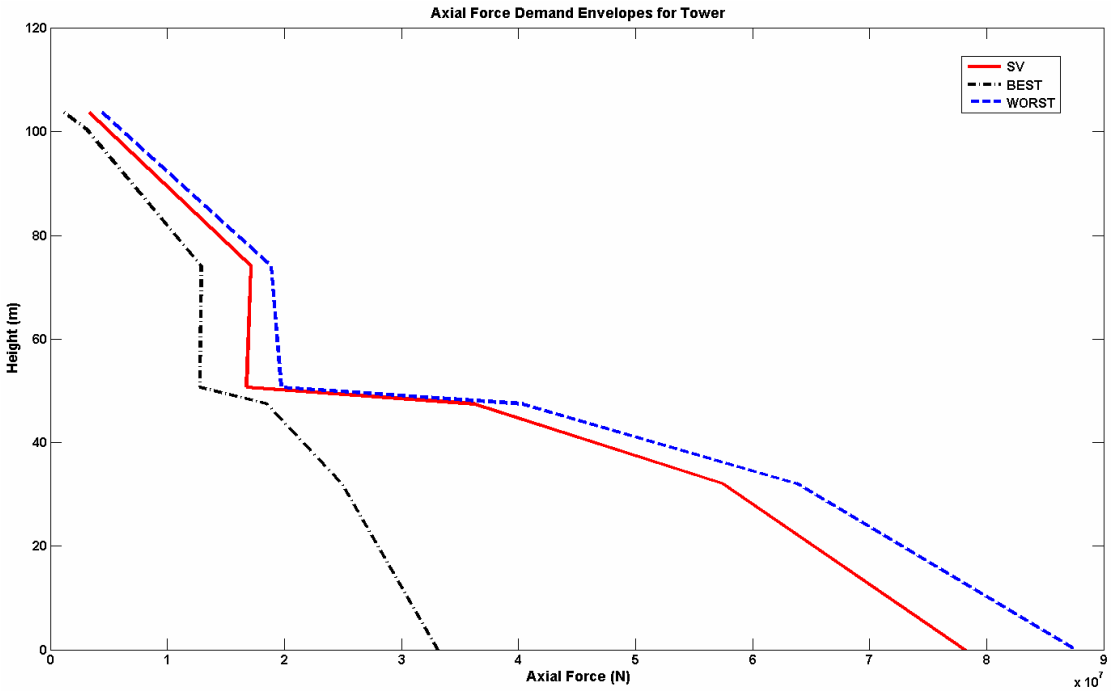

Figure 4.29 Absolute axial force demand envelope for the east tower of the bridge

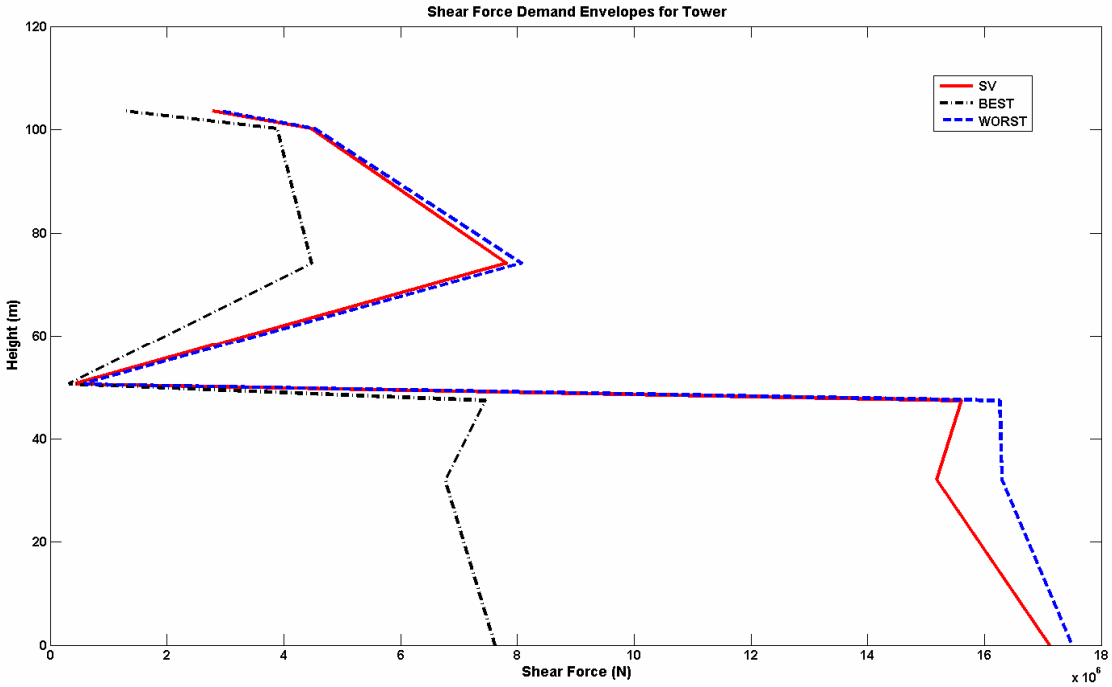

Figure 4.30 Absolute shear force demand envelope for the east tower of the bridge

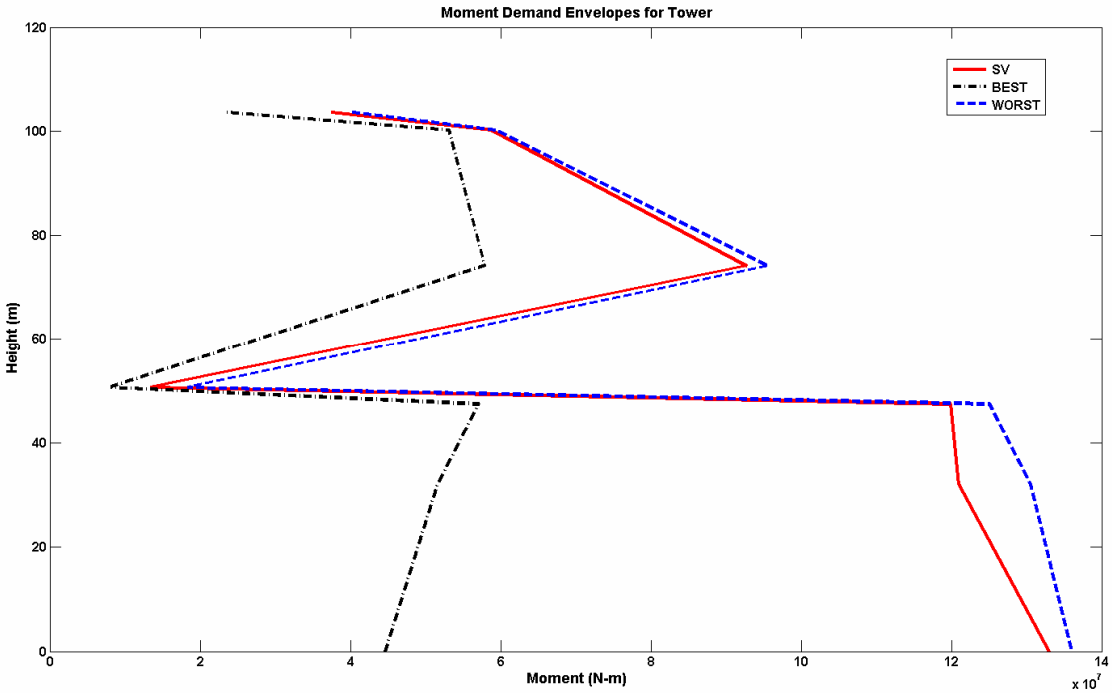

Figure 4.31 Absolute moment demand envelope for the east tower of the bridge

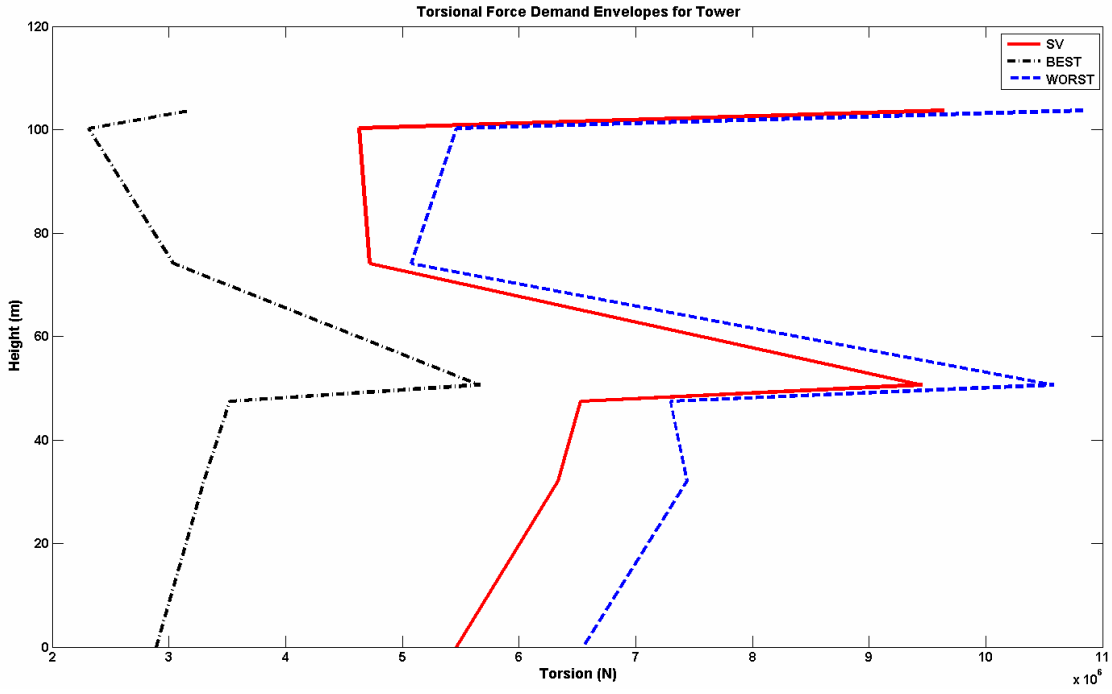

Figure 4.32 Absolute torsional force demand envelope for the east tower of the bridge

4.8 Closure

In this chapter, at first, the FE models developed in Chapter 2 are validated by simulating the dynamic response during the 1994 Northridge earthquake and 2008 Chino Hills earthquake and comparing with the recorded response during these two events. After that considering 40 ground motions representing 2% in 50 years and 10% in 50 years of hazard level in the Los Angeles area, nonlinear time history analyses are performed. Fragility curves are then generated considering ductility demands of critical tower sections. It is observed from this study that a ground motion with PGA of 0.9g or greater will result in plastic hinge formation at one or more locations with a probability of exceedance of 50%. Also, it is found that the effect of damper (used for retrofitting of the bridge) on reducing seismic vulnerability is minimal for low to moderate earthquakes and high for strong earthquakes. Finally, the effect of spatial variability of ground motions on seismic displacement and force demands is investigated. To generate spatially correlated spectrum compatible nonstationary acceleration time histories, a new algorithm is developed involving evolutionary PSDF and spectral representation method. The proposed procedure is more realistic than other existing procedures that utilize envelope function with (time-invariant) Fourier spectrum or stationary PSDF to induce nonstationarity in the simulated time histories. Using spatially variable motions, it is found that the response in some locations on the bridge deck, may be under predicted even if the motion with maximum intensity is uniformly applied at all supports (worst-case scenario).

CHAPTER 5

WIND SENSOR INSTALLATION AND WIND SPEED MEASUREMENT

5.1 Background

Long suspension bridges are flexible to the extent that they vibrate significantly under wind conditions. To identify the structural characteristics of suspension bridges using ambient vibration data, external loading conditions, especially wind loads, should be carefully investigated. The research related to this issue has a long history especially in the areas of buffeting effect of the wind on bridges and aeroelastic stability. In 1960's, random vibration theory and stochastic models of wind flow emerged and has obtained maturity to the point where the response of bridges under these wind conditions can be generated even including geometric nonlinearity of the bridges (Kim et al., 2004). In view of the lack of wind data at the site of the Vincent Thomas Bridge, a number of anemometers will be installed in a vertical plane near and parallel to the bridge to measure the wind speed and estimate its spatial correlation. Anemometers will be installed away from the bridge so that incoming wind flow is not disturbed by the bridge. The field experiment will provide useful reality check for the wind characterization in temporal and spatial variation.

Long suspension bridges are very flexible to vibrate significantly under wind conditions. Therefore, we plan to develop a wind speed monitoring network initially with three anemometers installed along the bridge length with one each located at the center

and the location of tower on the main bridge truss and one at the top of the tower all on the same side of the bridge as shown in (Figure 5.6). This will provide a reality check for the wind characterization in temporal and spatial variation. The anemometer Model # 7911, built by Davis Instruments Corp., is equipped the sensors to measure both wind speed and wind direction.

5.2 Anemometer and Data Acquisition System

The following components were acquired from Davis Instruments.

5.2.1 Anemometer for Vantage Pro2

The Anemometer has both wind speed and wind direction sensors. It can withstand up to hurricane-force winds. It is also sensitive to a light breeze. It was reported that a Davis Anemometer measured wind speeds of 175 miles per hour before its tower collapsed during hurricane Andrew in 1992. Digital filtering with is applied to wind direction measurements. It has an accuracy of $\pm 4^{\circ}$ at the time of measuring wind direction and for wind speed measurement the accuracy is ± 2 mph. Figure 5.1 shows an anemometer with wind cups and wind vane.

5.2.2 Anemometer Transmitter with Solar Power

Anemometer transmitter will transmit the data of wind velocity and direction from anemometer to a repeater or directly to the receiver attached with the personal computer (PC). For longer distance between the anemometer and the data acquisition system one or more wireless repeaters should be added. The transmitter has a range is up to 1000 ft (300

m), line of sight, under optimal conditions. Typical range under most conditions is 200 ft to 400 ft (60 m to 120 m), but this may be reduced by walls, ceilings, trees, or foliage. Radio-frequency interference (RF) can also reduce transmission distance. Cordless phones (900 MHz) and ham radios are common examples of RF interference. Wireless transmission frequency range is 902 MHz to 928 MHz. Primary power input is solar power and secondary (backup) power is from CR-123A 3-volt lithium battery or optional AC power. Figure 5.2 shows an anemometer transmitter with solar power and fixtures.

Figure 5.1 Anemometer

5.2.3 Wireless Repeater with Solar Power

For longer distances or to improve reception in troublesome areas wireless repeaters will be added. Transmitting and receiving range for each repeater is up to 1000 ft (300 m) outdoors, line of sight; typical range through walls under most conditions is 200 ft to 400 ft (60 m to 120 m). Use up to eight repeaters with a single wireless station, or form a network of weather stations by linking eight repeaters to eight different wireless stations. For wireless repeater primary power input is solar power and secondary power is from

lithium battery. The expected service life without any interruption is more than two years with normal solar input. Figure 5.3 shows a wireless repeater with solar power.

Figure 5.2 Anemometer transmitter with solar power

Figure 5.3 Wireless repeater with solar power

5.2.4 Wireless Weather Envoy (Wireless Receiver)

It receives data from the transmitter or from repeater whichever is communicating with it. The data get stored in the data logger inside it. With the help of universal serial bus (USB) cable the data stored in the memory of a PC. Figure 4 shows a wireless weather envoy i.e. wireless receiver.

Figure 5.4 Wireless Weather Envoy (Wireless Receiver)

5.2.5 WeatherLink Software for Data Collection

WeatherLink software helps to collect the data from the data logger of weather envoy i.e. the receiver. It updates the data every 1 min. It also helps to make a weather report over a long period of time.

5.2.6 Data Acquisition Software Developed

The resolution of the data (wind velocity and direction) collected from Davis Instruments anemometer was 1 sample data per min. This resolution is good for getting the steady

part of the wind. To consider the fluctuating part of the wind, high resolution data is needed. Fluctuating part of the wind is the most important component in assessing the buffeting response of long span suspension bridge. In-home data acquisition software was developed to collect the data from the data logger of the receiver at a rate of 1 sample data per 3 sec.

5.2.7 Experimental Setup

Figure 5.5 shows schematically how the wind sensor data will be collected at the bridge site and transferred to UCI server over the internet for real-time data collection.

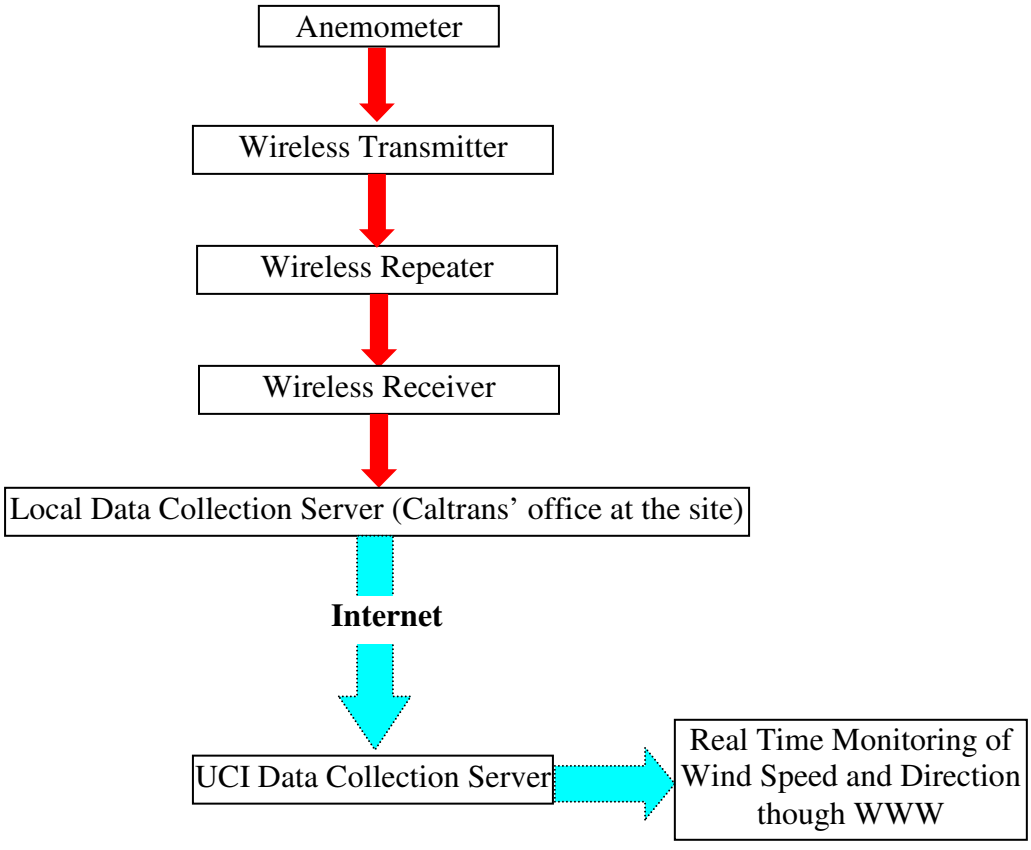

Figure 5.5 Layout of the data acquisition system

5.2.8 Anemometer Installation and Data Acquisition System

Total three anemometers, three transmitters, eight repeaters and three receivers were installed in the bridge site at different locations (Figure 5.6 and Figure 5.7). The anemometers, repeaters and transmitters were installed in durable plastic pipes with L joints. The pipes were connected to the bridge structure with the help of different size hose clamps. Figures 5.8 (a-d) show the installation of anemometers, transmitters and repeaters at different locations of the bridge. Anemometer and transmitter were connected by a data cable so that the data collected by the sensor in the anemometer can be transmitted by transmitter to the receiver. As the receivers were installed in the anchorage house, which is approximately 1500 ft from the center of the mid span, 4 repeaters were installed for the anemometer installed at the center of the mid span. The other two anemometers were installed, one at the top of the east tower and the other at the connection of east tower and deck i.e., at the east tower platform. For each of those two anemometers two repeaters were installed to transmit the data to the receiver at the anchorage house. Because the receivers were installed inside the anchorage house, there was no clear line of sight between the repeaters and the receivers. To transmit the data from the repeaters to receiver, three receivers were installed on the wall of the anchorage house. Note, through walls or around large objects the range of wireless communication is 200 ft – 400 ft (Vantage Pro2^{TM} Wireless Repeater Installation Manual, 2005).

Since the distance from the receiver to the repeater at the anchorage house wall is around 100 ft, there was no problem in wireless communication between the receiver and the repeater. Four repeaters were installed at different locations of the bridge deck. Those repeaters were installed on the vertical posts of bridge deck railing. One repeater was

installed at the east tower platform at the tower and deck connection. To ensure that there will be no problem in wireless communication for the data transfer from the transmitter to the receiver, the locations of the repeaters were chosen such that the distance between transmitter and repeater and between two repeaters will be less than 400 ft. Figure 5.6 shows the locations of anemometers, transmitters, repeaters and receivers installed at the bridge site.

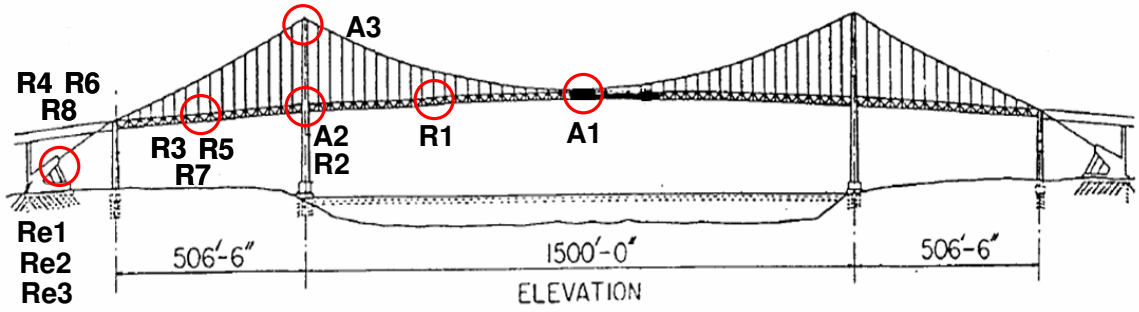

Figure 5.6 Locations of anemometers, transmitters, repeaters and receivers
(A : Anemometer and Transmitter, R : Repeater and Re : Receiver)

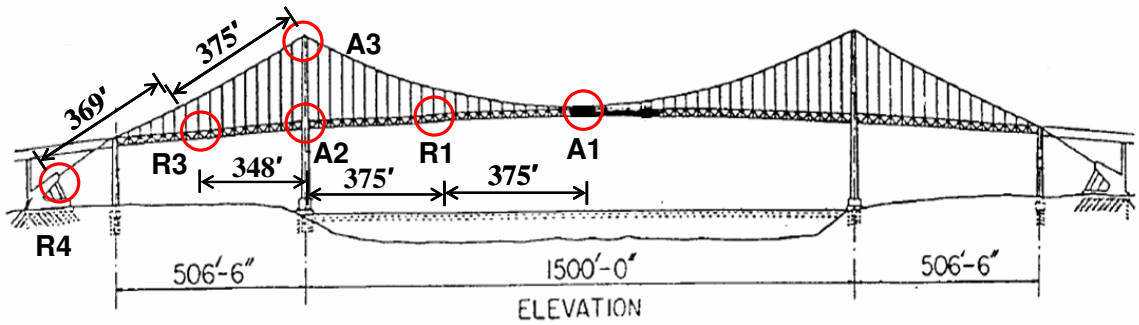

Figure 5.7 Distance between different components

The chain of communication for Anemometer # 1 is A1→R1→R2→R3→R4→Re1, the same for Anemometer # 2 is A2→R5→R6→Re2 and for Anemometer # 3 is A3→R7→R8→Re3. Anemometer and transmitter A1 is located at the panel # 81, repeater R1 is located at the panel # 57/105 and repeaters R3, R5 and R7 are located near

panel # 10/152. Figure 5.7 shows the distances between different components of the wind data collection system. It can be seen from the figure that all the distances are less than 400 ft to ensure uninterrupted wireless communication between different components of the whole system. For anemometers A1, A2 and A3, the transmitters IDs (Vantage Pro2™ Anemometer Transmitter Kit Installation Manual, 2005) are set to 1, 2 and 3 respectively. The different repeater settings are tabulated in Table 5.1. Table 5.2 shows the different receiver settings. As the repeaters and transmitters are solar powered with backup lithium battery, the expected service life of the system without any interruption is more than two years with normal solar input.

Table 5.1 Settings of different repeaters

Repeater #	Repeater Settings		
	Transmitter ID	Repeater ID	Jumper Position
R1	1	A	Default
R2	None	B	Default
R3	None	C	Default
R4	None	D	Default
R5	2	E	First in Chain
R6	None	F	Default
R7	3	G	First in Chain
R8	None	H	Default

Table 5.2 Settings of different receivers

Receiver #	Receiver Settings	
	Transmitter ID	Repeater ID
Re1	1	D
Re2	2	F
Re3	3	H

5.3 WeatherLink Software for Data Collection

WeatherLink software (WeatherLink for Vantage Pro® and Vantage Pro2™) helps to collect the data from the data logger of weather envoy i.e. the receiver. It updates the data

every 1 min. It also helps to make a weather report over a long period of time. Figures 5.9 (a-d) show three different screen shots for three anemometer locations from the WeatherLink software and the data acquisition system.

(a) (b)

(c) (d)

Figure 5.8 Installation of anemometers, transmitters and repeaters :
(a) Top of the east tower, (b) Vertical post on deck, (c) East tower platform and
(d) Anchorage house wall

5.4 Recorded Wind Velocities

Wind data has been collected from the bridge site at a sampling rate of both 1 sample per minute and 1 sample per 3 sec. It can be seen from Figure 5.10 that sometimes the wind velocity comes down to zero, this is because of the data packet loss in wireless communication. Figure 5.10 shows the plot of wind velocity recorded for 24 hrs on April

8, 2009 at 3 different locations at 1 sample per minute. Figure 5.11 shows the plot of wind velocity recorded for 30 minutes on April 15, 2009 at 3 different locations at 1 sample per 3 sec.

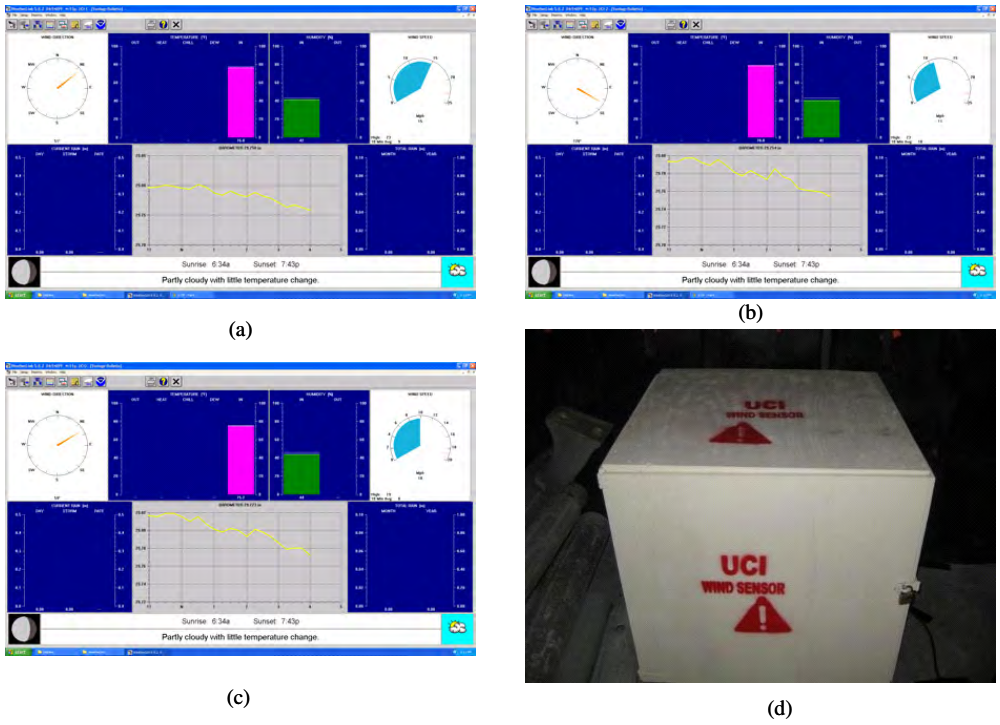

Figure 5.9 Screen shots from Weather Link and data acquisition system: (a) Anemometer # 1, (b) Anemometer # 2, (c) Anemometer # 3 and (d) Data acquisition system

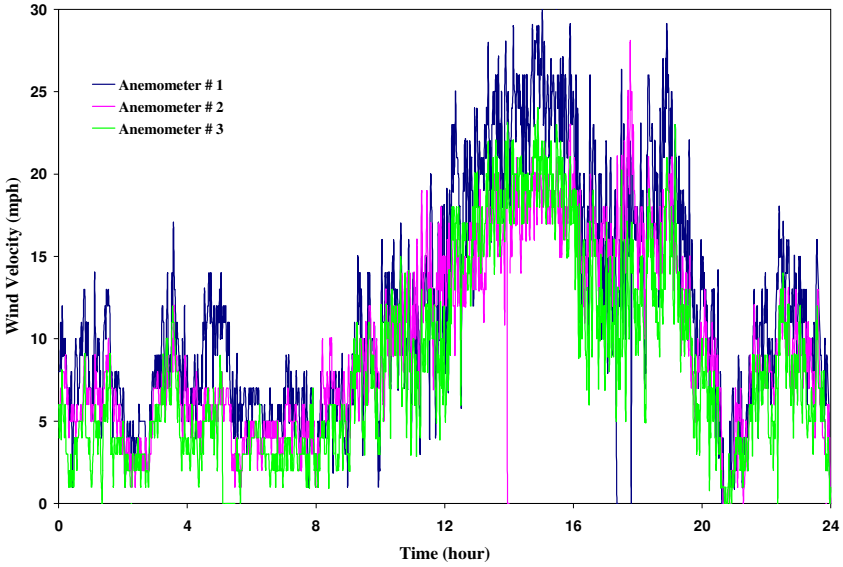

Figure 5.10 Wind velocity recorded for 24 hrs on April 8, 2009 (1 sample/min)

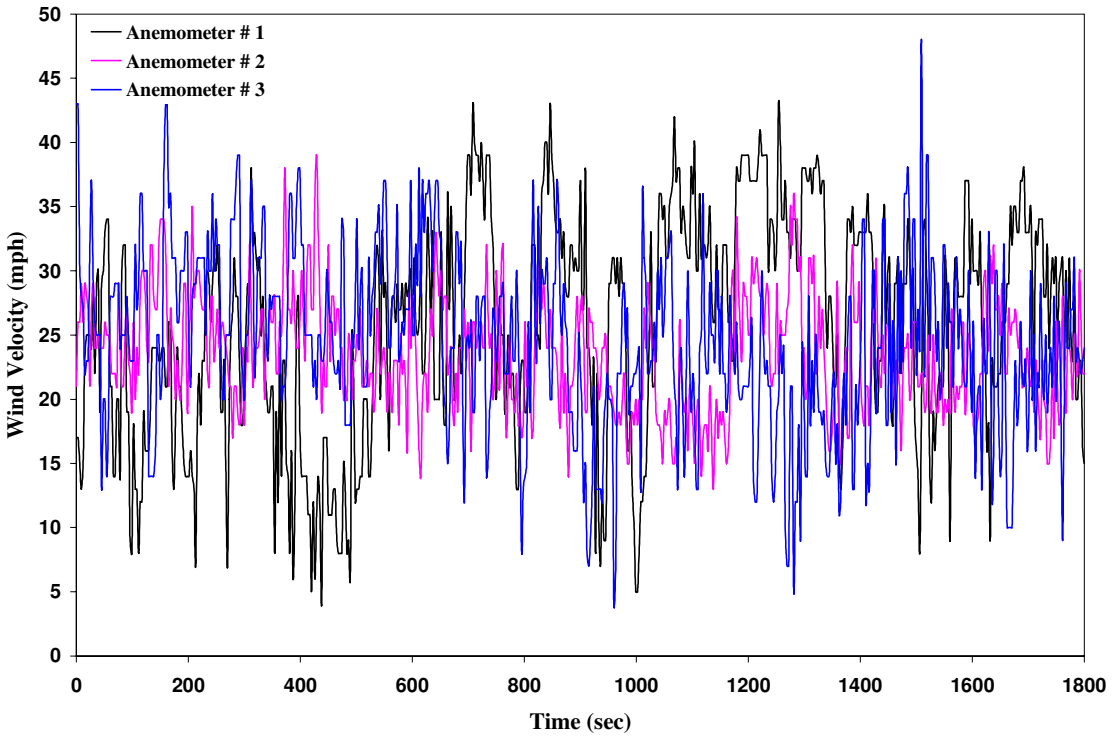

Figure 5.11 Wind velocity recorded for 30 minutes on April 15, 2009 (1 sample/3s)

5.5 Closure

Three anemometers are installed at three locations of the bridge : two at deck level and one at the top of the east tower. Wind data from those anemometers are collected at both 1 sample per minute and at 1 sample per 3 sec sampling interval. For the collection of 1 sample per 3 sec wind data, a new software code has been developed. Collected data show that the wind velocity changes along the length as well as with the height when using 1 sample per 3 sec or 1 sample per minute data.

CHAPTER 6

WIND BUFFETING ANALYSIS

6.1 Background

Simulation of random velocity profiles at unmeasured locations of a structure conditioned to the wind velocity profiles at measured locations is very useful in performing nonlinear time history analysis of any kind of structure like long span cable supported bridge, wind turbine, slender tower etc. If some of the wind measuring sensors do not work properly, then conditional simulation will be useful to simulate wind velocity profiles at those damaged sensor locations. The following study presents a non-Gaussian conditional simulation technique for simulating wind velocity fluctuations.

The proposed method can be used for conditionally simulating time-dependent zero mean one-dimensional multivariate non-Gaussian stationary processes using Yamazaki and Shinozuka's (1988) mapping technique along with the Gaussian conditional simulation algorithm. This method can only be used for generating wind velocity fluctuations at unrecorded locations, provided the velocity fluctuations are available at some specified measured locations. To get the actual information regarding wind velocity at the bridge site, three anemometers have been installed on the bridge. The data form these three anemometers have been used for conditional simulation of the non-Gaussian wind velocity field using the proposed simulation technique. From the simulated wind velocity field, buffeting forces are calculated. Using detailed member-based FE model, the buffeting response of the bridge is calculated.

Simulation of random velocity profiles at unmeasured locations of a structure conditioned to the wind velocity profiles at measured locations is very useful in performing nonlinear time history analysis of any kind of structure like long span cable supported bridge, wind turbine, slender tower etc. If some of the wind measuring sensors do not work properly, then conditional simulation will be useful to simulate wind velocity profiles at those damaged sensor locations.

So far in a broad sense two approaches have been introduced by researchers regarding conditional simulation. The two approaches are based on "kriging" (Krige, 1966) (linear estimation theory applied to random functions) and conditional probability density function. Vanmarcke and Fenton (1991) applied conditional simulation of to simulate Fourier coefficients using kriging technique. Kameda and Morikawa (1992 and 1994), used an analytical framework based on spectral representation method, derived joint probability density functions of Fourier coefficients obtained from the expansion of conditioned random processes into Fourier series. They calculated conditional expectations and variances of the conditioned random processes and considered their first-passage probabilities. Hoshiya (1994) considered a conditional random field as a sum of its kriging estimate and the error. He simulated the kriging estimate and the error separately and combined them to get the Gaussian conditionally simulated field. In all the above studies the investigators considered Gaussian processes and Gaussian random fields.

Sometimes the assumption of Gaussian wind loading is not correct. In those cases, conditional simulation of non-Gaussian wind velocity field should be used. Elishakoff et al. (1994) combined the conditional simulation technique of Gaussian random fields by

Hoshiya (1994) and the iterative procedure for unconditional simulation of non-Gaussian random fields by Yamazaki and Shinozuka (1988), to conditionally simulate time-independent non-Gaussian random fields. Gurley and Kareem (1998) developed a procedure for conditional simulation of multivariate non-Gaussian velocity/pressure fields. For mapping the Gaussian process to non-Gaussian process and vice versa, they used modified Hermite transformation using Hermite polynomial function. This method compares the simulated process with the target one up to fourth order of statistics, as a result it fails to match the whole distribution function.

The present study uses a scheme developed for Gaussian conditional simulation of wind velocity fluctuations in frequency domain, along with the iterative procedure for unconditional simulation of non-Gaussian random fields by Yamazaki and Shinozuka (1988), to conditionally simulate time-dependent multivariate non-Gaussian wind velocity fluctuations.

Throughout the history of suspension bridges, their tendency to vibrate under different dynamic loadings such as wind, earthquake, and traffic loads has been a matter of concern. In particular, after the disastrous failure of Tacoma Narrows Bridge in 1940, wind-induced vibrations of suspension bridges have mostly been studied. For design of long span suspension bridges, correct prediction of wind induced buffeting and flutter instability is very important. Frequency domain analysis is popular in predicting response of suspension bridges due to random wind. Frequency domain approach is applicable for linear structures and subjected to stationary wind loads. But, frequency domain analysis can not be applied for geometrically non-linear structure. Although, structural members of suspension bridge behave linearly, under high speed wind but it shows geometric

nonlinearity. To overcome this problem, time domain approach is more appropriate to apply for flutter and buffeting response. Most of the researchers used multimodal analysis. But to consider the effect of geometric non-linearity it is very important to consider the time domain analysis. Chen (2001), Kim (2004) used time domain analysis to consider the effect of non-linearity in the structure. Also they only considered the wind forces on the deck only. They neglected the coupling effect of wind forces on tower and cable. Sun (1999) considered the coupling effect of the aeroelastic forces on the bridge deck, towers and cables. But they did not consider a 3D detailed finite element (FE) model of the bridge. Recently, He (2008) considered a detailed 3D model for buffeting analysis. But, they failed to consider aeroelastic forces on towers and cables.

This study considers the aeroelastic forces on bridge deck only. To simulate the wind velocity field conditional simulation technique will be used using the recorded wind velocity data from the installed anemometer on the bridge.

6.2 Scope

In this study, a new algorithm for conditional simulation of non-Gaussian wind velocity fluctuation field is proposed. Also, to compare the velocity fluctuations obtained from proposed simulation technique, Gaussian unconditional and Gaussian conditional simulation techniques are also used to get the wind velocity fluctuations. Velocity fluctuations obtained from all these three cases i.e. Gaussian unconditional, Gaussian conditional and non-Gaussian conditional simulation, are used for coupled geometrically

nonlinear buffeting analysis of the suspension bridge i.e. VTB considered in this study. A member based detailed three-dimensional Finite Element (FE) model of the bridge have been developed and used in this study.

6.3 Conditional Simulation of Gaussian Random Processes

The algorithm for conditional simulation of Gaussian processes is first discussed. The method of simulating non-Gaussian process conditioned to some measured data at some points is developed using transformation from Gaussian to non-Gaussian process proposed by Yamazaki and Shinozuka (1988) for unconditional simulation of non-Gaussian random fields.

Following Borgman's (1990) work, Murlidharan and Kareem (1993), Hoshiya (1995) have developed the following scheme for conditional simulation of Gaussian wind fields utilizing both frequency and time domain conditioning. Consider two Gaussian random vectors V_r and V_u are correlated. Also, the bi-variate Gaussian distribution of those can be expressed as

$$p(V) = p\begin{pmatrix} V_r \\ V_u \end{pmatrix} = N\left(\begin{bmatrix} \mu_r \\ \mu_u \end{bmatrix}, \begin{bmatrix} C_{rr} & C_{ru} \\ C_{ur} & C_{uu} \end{bmatrix}\right) \tag{6.1}$$

where μ_m is the mean value of variable m and C_{mn} is the auto or cross co-variance between variables m and n. Lets assume, a set of realizations of random variable V_r is

recorded at locations $x_r\,(r=1,2,\cdots,N)$ are given as v_r . Then one can simulate realizations of random variable V_u at unrecorded locations $x_u\,(u=1,2,\cdots,M)$, conditioned on the measured data v_r . Many researchers have done this conditional simulation [Venmarke, Hoshiya, 9-12 from kareem's paper]. The conditional probability density function (PDF) of V_u can be written as

$$p(V_u \mid V_r = v_r) = N\left(\mu_u + C_{ru}^T C_{rr}^{-1}(v_r - \mu_r), C_{uu} - C_{ru}^T C_{rr}^{-1} C_{ru}\right) \tag{6.2}$$

So, conditionally simulated realizations of variable V_u can be expressed as,

$$(v_u \mid V_r = v_r) = C_{ru}^T C_{rr}^{-1}\left(v_r - V_r^*\right) + V_u^* \tag{6.3}$$

where V_r^* and V_u^* are unconditionally simulated variates, which can be simulated from standard algorithms for simulating Gaussian multivariate processes (Shinozuka, 1971 and Deodatis, 1996) and v_r are the known variates measured at *N* locations. For conditional simulation of multivariate Gaussian process one needs to know the covariance matrices C_{rr} and C_{ru} .

6.3.1 Conditional Simulation in Frequency Domain

Frequency domain conditional simulation is applied for generation of realizations of conditionally simulated variates at unrecorded locations $x_u\,(u=1,2,\cdots,M)$ based on

recorded data at locations $x_r\left(r=1,2,\cdots,N\right)$. The spectral density matrix between recorded and unrecorded locations should be known beforehand. The spectral density matrix between the measured locations can be calculated from the actual data recorded. In frequency domain the covariance matrices C_{rr} and C_{ru} can be expressed as

$$C_{rr}=\begin{bmatrix} S_{11} & S_{12} & \cdots & S_{1N} \\ S_{21} & S_{22} & \cdots & S_{2N} \\ \vdots & \vdots & \ddots & \vdots \\ S_{N1} & S_{N2} & \cdots & S_{NN} \end{bmatrix}, \tag{6.4}$$

$$C_{ru}=\begin{bmatrix} S_{11} & S_{12} & \cdots & S_{1M} \\ S_{21} & S_{22} & \cdots & S_{2M} \\ \vdots & \vdots & \ddots & \vdots \\ S_{N1} & S_{N2} & \cdots & S_{NM} \end{bmatrix} \tag{6.5}$$

where S_{mn} is the cross-spectral density function between locations *m* and *n*.

6.4 Conditional Simulation of Non-Gaussian Random Processes

A method for conditional simulation of one-dimensional multivariate non-Gaussian stationary processes is developed. Non-Gaussian random processes $v_u^N\left(t\right)$at unrecorded locations $x_u\left(u=1,2,\cdots,M\right)$ will be simulated under the condition that the non-Gaussian data $v_r^N\left(t\right)$ at recorded locations $x_r\left(r=1,2,\cdots,N\right)$ are given. The flowchart of this proposed method is shown in Figure 6.1. First, the target power spectra $S_{NN}^{(T)}(\omega)$ and the

one-dimensional probability distribution function $F_N(n)$ of non-Gaussian stochastic processes are specified. In this process of simulation $F_N(n)$ represents one-dimensional distribution function of a non-Gaussian random variable n with zero mean and variance σ_n^2. One can easily find the equivalent Gaussian probability distribution function $F_G(g)$ with zero mean and variance $\sigma_g^2 = \sigma_n^2$. The first step will be to assume the initial power spectra of Gaussian processes to be

$$S_{GG}^{(i)}(\omega) = S_{NN}^{(T)}(\omega), \tag{6.6}$$

which will be used for simulation of multi-variate Gaussian processes $V_r^G(t)$ and $V_u^G(t)$ at N recorded locations $x_r\,(r = 1, 2, \cdots, N)$ and M unrecorded locations $x_u\,(u = 1, 2, \cdots, M)$. To use the conditional simulation technique for Gaussian process, the recorded non-Gaussian realizations $v_r^N(t)$ are mapped back into a set a Gaussian realizations $v_r^G(t)$ using a backward mapping technique. Using the nonlinear backward transformation proposed by Yamazaki and Shinozuka (1988) for unconditional simulation of non-Gaussian stochastic fields,

$$v_r^G(t) = F_G^{-1}\left\{F_N\left[v_r^N(t)\right]\right\} \tag{6.7}$$

a set of Gaussian realizations $v_r^G(t)$ can be generated. The conditional simulation process shown in Eq. (6.3) require v_r, V_r^*, and V_u^* to be Gaussian. For this reason, conditionally

simulated v_u will be Gaussian too. Now Eq. (6.3) is used to conditionally simulate Gaussian realizations of $v_u^G(t)$ at unrecorded locations $x_u\,(u=1,2,\cdots,M)$. These conditionally simulated Gaussian realizations will be mapped into non-Gaussian realizations $v_u^N(t)$ using a forward mapping technique, as shown in the following equation,

$$v_u^N(t)=F_N^{-1}\left\{F_G\left[v_u^G(t)\right]\right\} \tag{6.8}$$

Because of the nonlinearity of the mapping technique used here, the power spectra calculated from the conditionally simulated non-Gaussian processes $S_{NN}^{(i)}(\omega)$ will not match the target spectra $S_{NN}^{(T)}(\omega)$ assumed at the beginning of the simulation process. Therefore an iterative algorithm is used to update the power spectra, so that the power spectra generated from simulated non-Gaussian processes will match the target spectra of the non-Gaussian process assumed at the first place. The power spectra to be used for generating Gaussian stochastic processes in the $(i+1)^{\text{th}}$ iteration are obtained using the following updating formula,

$$S_{GG}^{(i+1)}(\omega)=\frac{S_{GG}^{(i)}(\omega)}{S_{NN}^{(i)}(\omega)}S_{NN}^{(T)}(\omega) \tag{6.9}$$

where $S_{GG}^{(i)}(\omega)$ is power spectra calculated from the unconditionally simulated Gaussian processes $V^G(t)$ at $(N+M)$ recorded as well as unrecorded locations. Iteration continues until the error converges to a constant value.

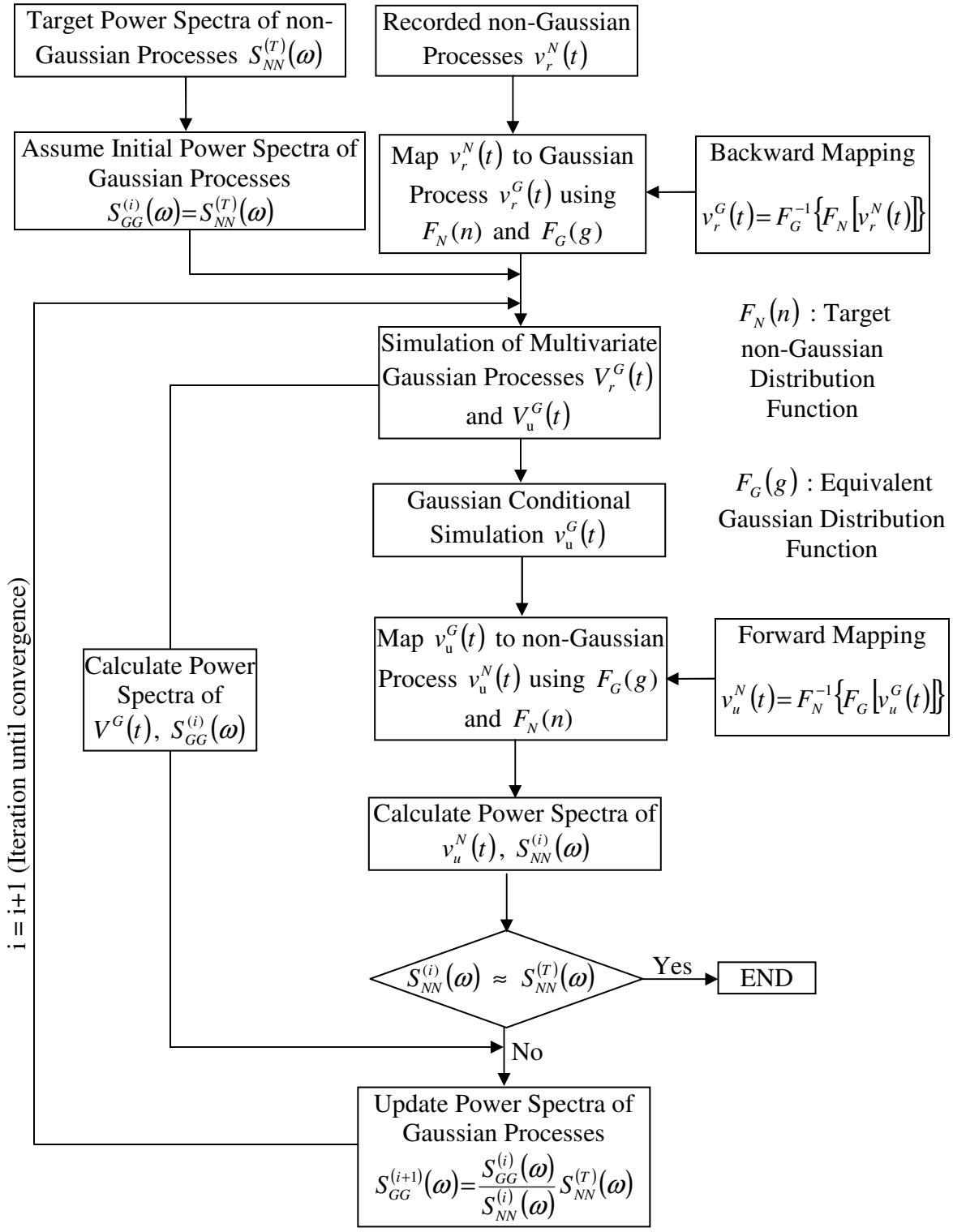

Figure 6.1 Flow chart of conditional simulation of non-Gaussian random processes

6.5 Simulation of Spatially Correlated Gaussian Wind Velocity Fluctuations

To generate sample functions of stochastic processes, the spectral representation method developed by Shinozuka and Jan (1972) appears to be most versatile and widely used today. Spectral representation based algorithm to simulate one-dimensional multi-variate stationary Gaussian stochastic process developed by Deodatis (1996a) is used in this study and described as follows. Consider a one-dimensional, m-variate (1D-mV) stationary stochastic vector process with components $f_1^0(t), f_2^0(t), \ldots\ldots\ldots, f_m^0(t)$, having a mean value equal to zero, and the cross-spectral density matrix given by

$$\mathbf{S}^0(\omega) = \begin{bmatrix} S_{11}^0(\omega) & S_{12}^0(\omega) & \cdots & S_{1m}^0(\omega) \\ S_{21}^0(\omega) & S_{22}^0(\omega) & \cdots & S_{2m}^0(\omega) \\ \vdots & \vdots & \ddots & \vdots \\ S_{m1}^0(\omega) & S_{m2}^0(\omega) & \cdots & S_{mm}^0(\omega) \end{bmatrix} \tag{6.10}$$

The elements of $\mathbf{S}^0(\omega)$ are expressed as

$$S_{jj}^0(\omega) = S_j(\omega), \qquad j = 1,2,\ldots,m \tag{6.11}$$

$$S_{jk}^0(\omega) = \sqrt{S_j(\omega) S_k(\omega)}\,\gamma_{jk}(\omega), \qquad j,k = 1,2,\ldots,m,\ j \neq k \tag{6.12}$$

Where $S_j(\omega)$ = power spectral density function of $f_j^0(t)$, and $\gamma_{jk}(\omega)$ = coherence function between $f_j^0(t)$ and $f_k^0(t)$. The auto-/cross-correlation is defined by

$$R_{jk}^0(\tau) = \int_{-\infty}^{\infty} S_{jk}^0(\omega) e^{i\omega\tau} d\omega, \qquad j,k = 1,2,\ldots,m \tag{6.13}$$

The following form, proposed by Kaimal et al. (1972), was selected to model the two-sided power spectral density function of the horizontal wind velocity fluctuation:

$$S_u(\omega) = \frac{1}{2}\frac{1}{2\pi} 200 u_*^2 \frac{z}{U(z)} \frac{1}{\left(1 + 50\frac{|\omega| z}{2\pi U(z)}\right)^{5/3}} \tag{6.14}$$

Where z = height of the superstructure in meters; ω = frequency in rad/s; u_* = shear velocity of the flow in m/s; and $U(z)$= mean wind speed at height z in m/s.

The model proposed by Davenport (1968) was chosen for the coherence function between the velocity fluctuations at two separated points x_1 and x_2 along the bridge deck

$$\gamma_{jk}(\xi, \omega) = \exp\left[-\frac{|\omega|}{2\pi}\frac{C_x \xi}{U(z)}\right] \tag{6.15}$$

where $\xi = |x_1 - x_2|$ and C_x = constant that can be set to 10 for horizontal wind velocity fluctuations.

For two-sided power spectral density function for the vertical wind velocity fluctuation, Lumley and Panofsky (1964) proposed the following model:

$$S_u(\omega) = \frac{1}{2}\frac{1}{2\pi} 3.36 u_*^2 \frac{z}{U(z)} \frac{1}{1 + 10\left(\frac{|\omega| z}{2\pi U(z)}\right)^{5/3}} \tag{6.16}$$

And the coherence function is defined in the form of Eq. (6.15) again with $C_x = 8$.

Where $\boldsymbol{u_*} = \dfrac{\boldsymbol{kU(z)}}{\ln\left(\dfrac{\boldsymbol{z}}{\boldsymbol{z_0}}\right)}$ is the shear velocity of the wind field in m/s,

z_0 = roughness length in m

$\boldsymbol{U(z)}$= mean velocity in m/s at height z m above the ground

In this case height is the bridge deck above the ground is taken as $z = 60$ m, $z_0 = 0.07$ m and the constant $k \approx 0.04$. The mean wind velocity $U(z)$ is taken as 10 m/s.

By decomposing $\mathbf{S}^0(\omega)$, the 1D-mV stationary stochastic process $f_j^0(t),\ j = 1,2,\ldots,m$ can be simulated via the application of fast Fourier transform techniques (Shinozuka and Jan 1972 and Deodatis 1996).

In order to simulate the 1D-mV stochastic vector process $f_j^0(t);\ j = 1, 2,\ldots, m$, its cross-spectral density matrix $S^0(\omega)$ must be first decomposed into the following product:

$$S^0(\omega) = H(\omega) H^{T*}(\omega) \tag{6.17}$$

Where superscript T denotes the transpose of a matrix. Using Cholesky's method or modal decomposition, $H(\omega)$ can be evaluated as a lower triangular matrix:

$$\boldsymbol{H}(\omega) = \begin{bmatrix} \boldsymbol{H}_{11}(\omega) & 0 & 0 & \cdots & 0 \\ \boldsymbol{H}_{21}(\omega) & \boldsymbol{H}_{22}(\omega) & 0 & \cdots & 0 \\ \boldsymbol{H}_{31}(\omega) & \boldsymbol{H}_{32}(\omega) & \boldsymbol{H}_{33}(\omega) & \cdots & 0 \\ \vdots & \vdots & \vdots & \ddots & \vdots \\ \boldsymbol{H}_{m1}(\omega) & \boldsymbol{H}_{m2}(\omega) & \boldsymbol{H}_{m3}(\omega) & \cdots & \boldsymbol{H}_{mm}(\omega) \end{bmatrix} \tag{6.18}$$

The following relations are valid for the elements of matrix $\boldsymbol{H}(\omega)$:

$$\boldsymbol{H}_{jj}(\omega) = \boldsymbol{H}_{jj}(-\omega) \ ; \quad \boldsymbol{j} = 1,2,\ldots\ldots,\boldsymbol{m} \tag{6.19}$$

$$\boldsymbol{H}_{jk}(\omega) = \boldsymbol{H}_{jk}^{*}(-\omega) \ ; \quad \boldsymbol{j} = 2,3,\ldots\ldots,\boldsymbol{m};\ \boldsymbol{k} = 1,2,\ldots\ldots,\boldsymbol{m}-1;\ \boldsymbol{j} > \boldsymbol{k} \tag{6.20}$$

If the off-diagonal elements $\boldsymbol{H}_{jk}(\omega)$ are written in polar form as:

$$\boldsymbol{H}_{jk}(\omega) = \left|\boldsymbol{H}_{jk}(\omega)\right| \boldsymbol{e}^{i\theta_{jk}(\omega)} \ ; \quad \boldsymbol{j} = 2,3,\ldots\ldots,\boldsymbol{m};\ \boldsymbol{k} = 1,2,\ldots\ldots,\boldsymbol{m}-1;\ \boldsymbol{j} > \boldsymbol{k} \tag{6.21}$$

where

$$\theta_{jk}(\omega) = \tan^{-1}\left(\frac{\mathrm{Im}\left[\boldsymbol{H}_{jk}(\omega)\right]}{\mathrm{Re}\left[\boldsymbol{H}_{jk}(\omega)\right]}\right) \tag{6.22}$$

with Im and Re denote the imaginary and the real part of a complex number respectively. Then Eq. 10 equivalently can be written as :

$$\left|\boldsymbol{H}_{jk}(\omega)\right| = \left|\boldsymbol{H}_{jk}(-\omega)\right| \;\; ; \;\; \boldsymbol{j} = 2,3,.....,\boldsymbol{m};\ \boldsymbol{k} = 1,2,.....,\boldsymbol{m}-1;\ \boldsymbol{j} > \boldsymbol{k} \tag{6.23}$$

$$\theta_{jk}(\omega) = -\theta_{jk}(-\omega) \;\; ; \;\; \boldsymbol{j} = 2,3,.....,\boldsymbol{m};\ \boldsymbol{k} = 1,2,.....,\boldsymbol{m}-1;\ \boldsymbol{j} > \boldsymbol{k} \tag{6.24}$$

Once matrix $\boldsymbol{S}^{0}(\omega)$ is decomposed using Cheloskey's decomposition Eq.s (6.18-6.24), the stochastic process $\boldsymbol{f}_{j}^{0}(\boldsymbol{t});\ \boldsymbol{j} = 1,2,.....,\boldsymbol{m}$ can be simulated by the following series as $\boldsymbol{N} \to \infty$

$$\boldsymbol{f}_{j}(\boldsymbol{t}) = 2\sum_{\boldsymbol{q}=1}^{\boldsymbol{j}}\sum_{\boldsymbol{l}=0}^{\boldsymbol{N}-1}\left|\boldsymbol{H}_{\boldsymbol{jq}}(\omega_{\boldsymbol{l}})\right|\sqrt{\Delta\omega}\cos\left[\omega_{\boldsymbol{l}}\boldsymbol{t} - \theta_{\boldsymbol{jq}}(\omega_{\boldsymbol{l}}) + \Phi_{\boldsymbol{ql}}\right];\ \boldsymbol{j} = 1,2,3,.....,\boldsymbol{m} \tag{6.25}$$

where

$$\Delta\omega = \frac{\omega_{u}}{\boldsymbol{N}} \tag{6.26}$$

$$\theta_{jq}(\omega_{l}) = \tan^{-1}\left(\frac{\mathrm{Im}\left[\boldsymbol{H}_{jq}(\omega_{l})\right]}{\mathrm{Re}\left[\boldsymbol{H}_{jq}(\omega_{l})\right]}\right) \tag{6.27}$$

In Eq. (6.16), ω_{u} [Eq. 6.26] represents an upper cut-off frequency beyond which the elements of the cross-spectral density matrix may be assumed to be zero for either mathematical or physical reasons.

The cost of digitally generating sample functions of the simulated stochastic vector process can be drastically reduced by using the FFT technique (e.g. Brigham (1988)). In

order to take advantage of the FFT technique, Eq. (6.25) is rewritten explicitly in the following form:

$$f_j^{(i)}(p\Delta t) = \mathrm{Re}\left\{\sum_{q=1}^{j}\sum_{l=0}^{M-1} B_{jql}\exp\left[i\left(l\Delta\omega\right)\left(p\Delta t\right)\right]\right\};\ j = 1,2,3;\quad p = 0,1,.....,M-1 \tag{6.28}$$

where

$$\boldsymbol{B}_{jql} = 2\left|\boldsymbol{H}_{jq}\left(l\Delta\omega\right)\right|\sqrt{\Delta\omega}\exp\left[-\boldsymbol{i}\,\theta_{jq}\left(l\Delta\omega\right)\right]\exp\left[\boldsymbol{i}\,\phi_{ql}^{(i)}\right] \tag{6.29}$$

$\Delta\omega$ is defined as

$$\Delta\omega = \frac{\omega_u}{N} \tag{6.30}$$

Note that sample function $\boldsymbol{f}_j^{\,i}(\boldsymbol{p}\Delta\boldsymbol{t});\ \boldsymbol{j} = 1,2,3$ is periodic with period $\boldsymbol{T}_0$

$$\boldsymbol{T}_0 = \frac{2\pi}{\Delta\omega} \tag{6.31}$$

Hence, Δt and $\Delta\omega$ are related in the following way:

$$\boldsymbol{M}\,\Delta\boldsymbol{t} = \boldsymbol{T}_0 = \frac{2\pi}{\Delta\omega} \tag{6.32}$$

$$\Delta\boldsymbol{t} = \frac{2\pi}{\boldsymbol{M}\,\Delta\omega} \tag{6.33}$$

$$\Delta\boldsymbol{t}\,\Delta\omega = \frac{2\pi}{\boldsymbol{M}} \tag{6.34}$$

Eq. (6.28) can be written as:

$$\boldsymbol{f}_j^{(i)}(\boldsymbol{p}\Delta\boldsymbol{t}) = \mathrm{Re}\left\{\sum_{\boldsymbol{q}=1}^{\boldsymbol{j}}\sum_{\boldsymbol{l}=0}^{\boldsymbol{M}-1}\boldsymbol{B}_{jql}\exp\left[\boldsymbol{i}\,\boldsymbol{l}\,\boldsymbol{p}\,\frac{2\pi}{\boldsymbol{M}}\right]\right\};\boldsymbol{j} = 1,2,3;\quad \boldsymbol{p} = 0,1,.....,\boldsymbol{M}-1 \tag{6.35}$$

For calculation of wind velocity fluctuations, total 41 locations are considered along the deck of the bridge and total 8 locations along the tower. Every other hanger and deck connections are considered as locations for simulation of wind velocity fluctuations along

the deck. In case of tower, the connection between tower strut and tower legs are considered as locations for simulation of wind velocity fluctuations along the tower. 512 sec long wind velocity fluctuation records are with a time step of 0.25 sec. For simulation purpose different values of parameters considered are as follows: N = 1024, M = 2048, and $\omega_u = 4\pi$ rad/sec. For wind velocity monitoring at the bridge site total 3 anemometers have been installed at the bridge. Figure 6.2 shows the locations of the installed anemometers at the bridge site. Figure 6.3 shows 16 out of total 41 "aerodynamic" nodes considered along the bridge deck. Figures 6.4 and 6.5 show the horizontal wind velocity fluctuations simulated with Gaussian unconditional simulation technique at six different locations around anemometer # 2 and anemometer # 1 along the bridge deck. The wind velocity fluctuation plotted using red line denotes respective anemometer locations. Figure 6.6 depicts horizontal wind velocity fluctuations at two different locations from Gaussian unconditional simulation.

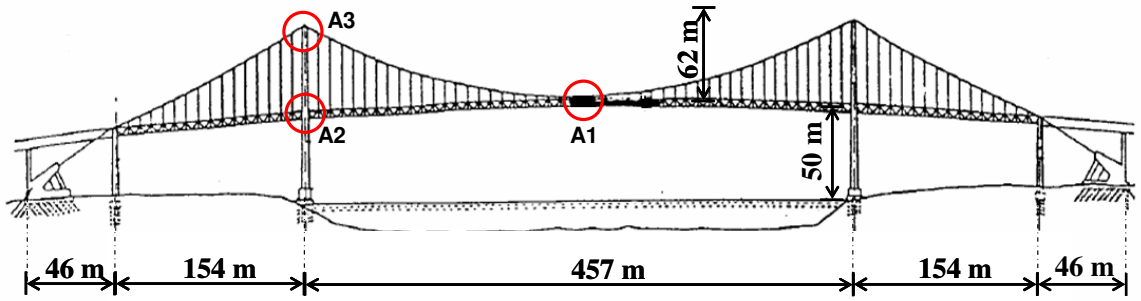

Figure 6.2 Installed anemometer locations on VTB
(A : Anemometer)

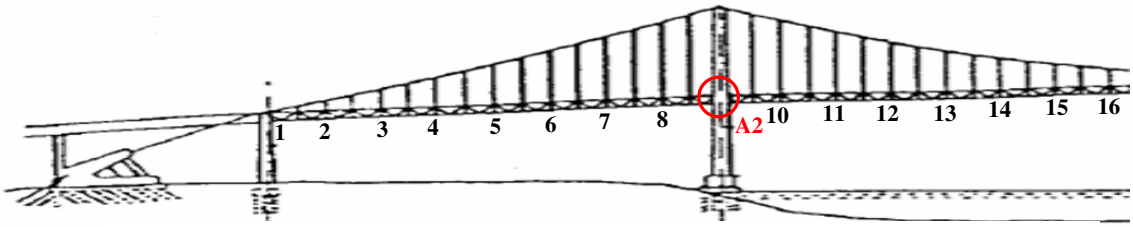

Figure 6.3 Locations of “aerodynamic” nodes along the bridge deck
(A : Anemometer)

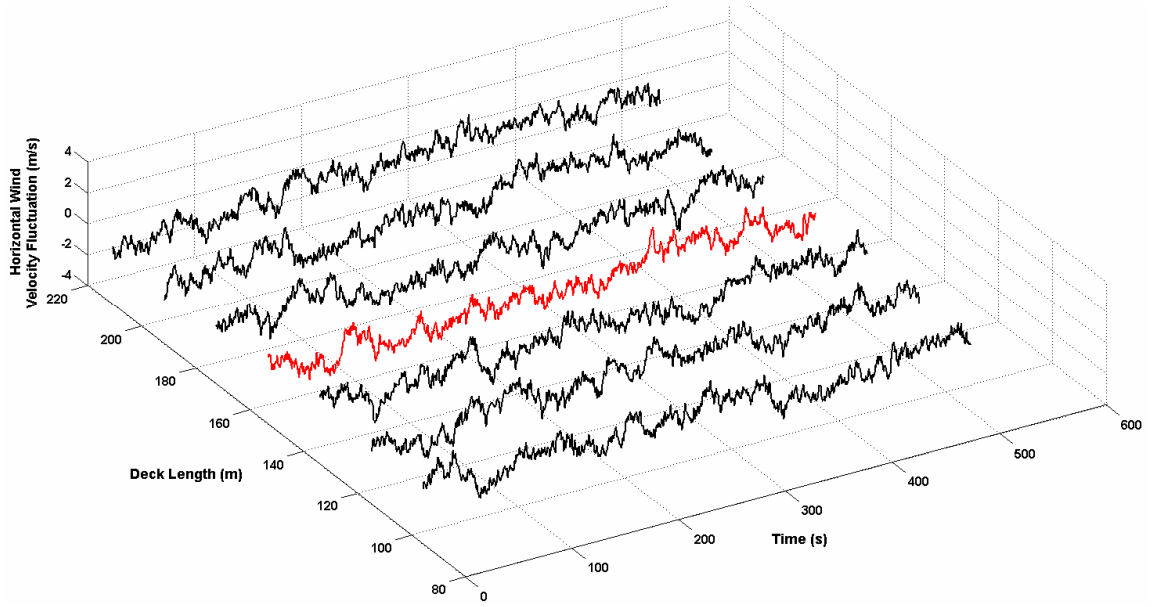

Fig. 6.4 Horizontal wind velocity fluctuations at different locations along the deck (around anemometer # 2) in m/s from Gaussian unconditional simulation

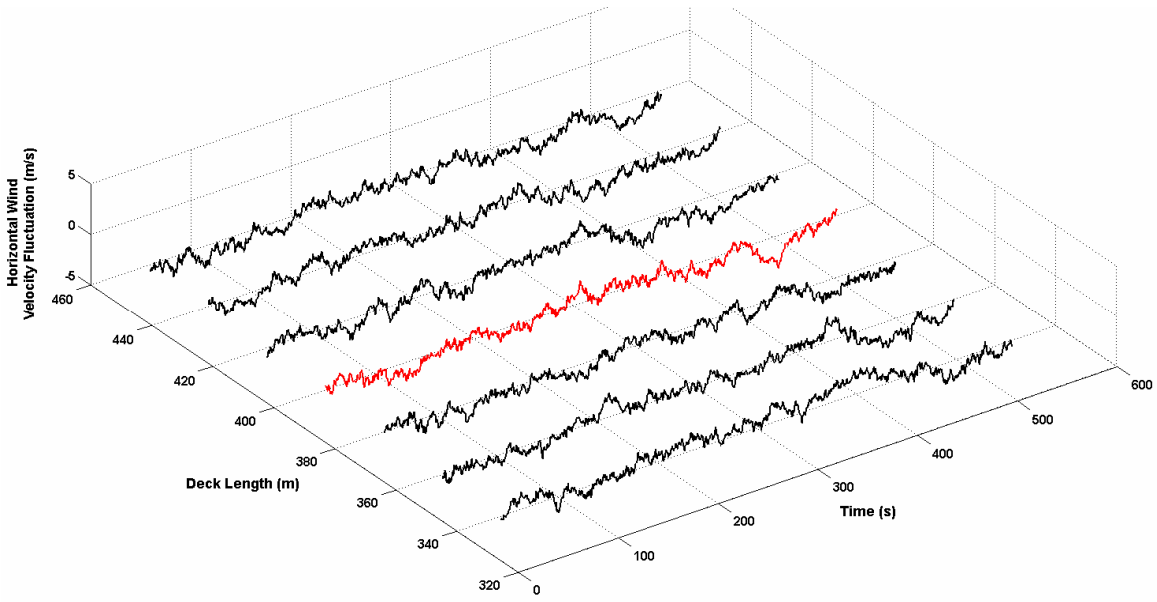

Fig. 6.5 Horizontal wind velocity fluctuations at different locations along the deck (around anemometer # 1) in m/s from Gaussian unconditional simulation

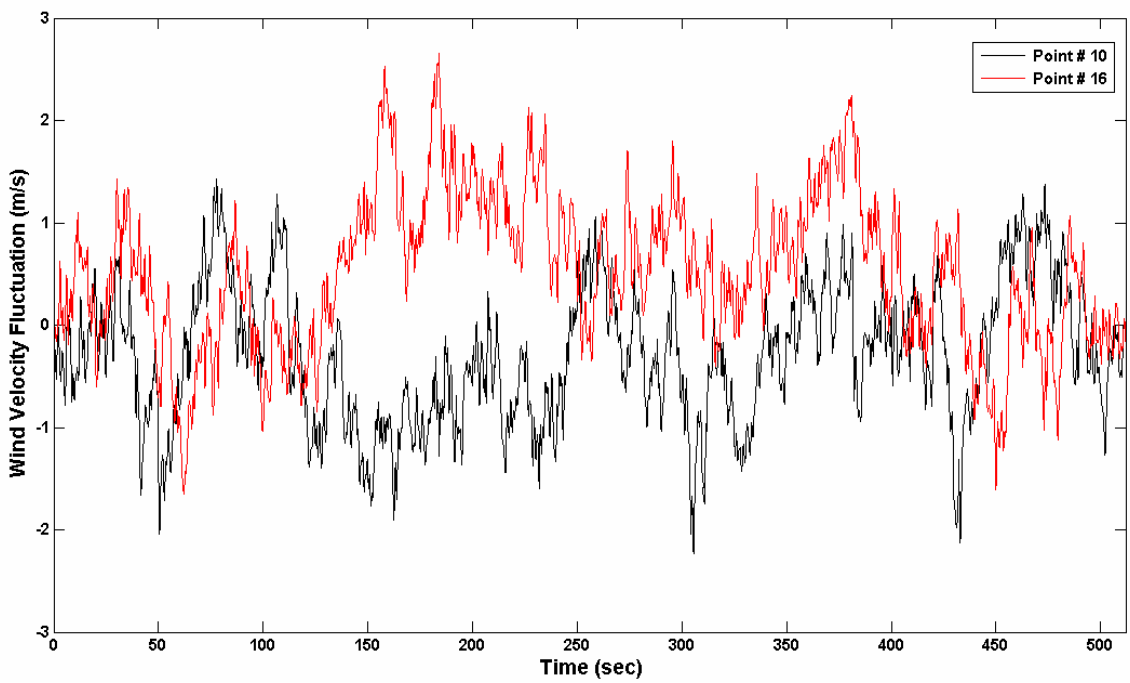

Figure 6.6 Horizontal wind velocity fluctuations at two different locations from Gaussian conditional simulation

6.6 Conditional Simulation of Gaussian Wind Velocity Fluctuations

Assuming the measured wind velocity fluctuation is Gaussian, Gaussian conditional simulation of wind velocity fluctuation is achieved using the methodology proposed in Section 6.3. Figures 6.7, 6.8, and 6.9 show the measured mean deducted wind velocity profiles at anemometer # 1, anemometer # 2, and anemometer # 2 locations respectively. For the simulation mean wind velocity is taken as the average mean wind measured between anemometer # 1 and anemometer # 2. Figures 6.10 and 6.11 show the horizontal wind velocity fluctuations simulated with Gaussian conditional simulation technique at six different locations around anemometer # 2 and anemometer # 1 along the bridge deck. The wind velocity fluctuation plotted using red line denotes respective anemometer

locations. It can be seen from the wind velocity fluctuation profiles that around the measured data the profile has similar trend but it differs with the increase in distance from the measured location. Figure 6.12 depicts horizontal wind velocity fluctuations at two different locations from Gaussian conditional simulation.

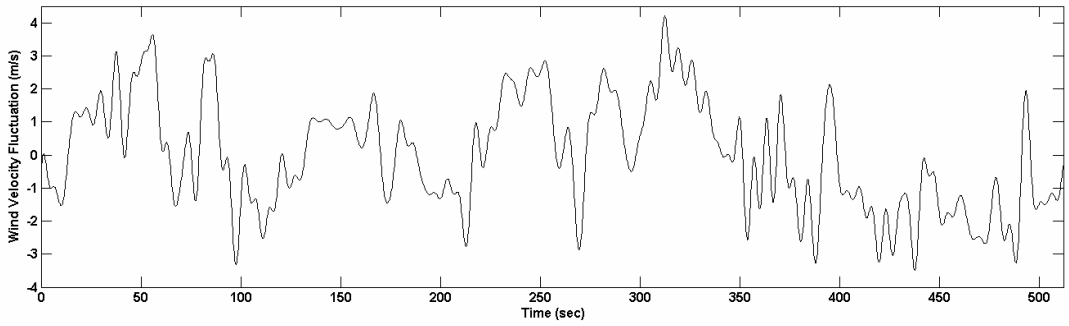

Figure 6.7 Measured wind velocity fluctuation at anemometer # 1 location

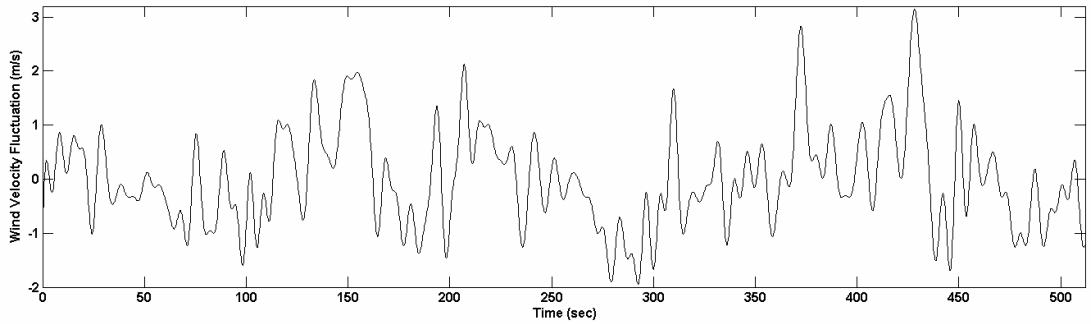

Figure 6.8 Measured wind velocity fluctuation at anemometer # 2 location

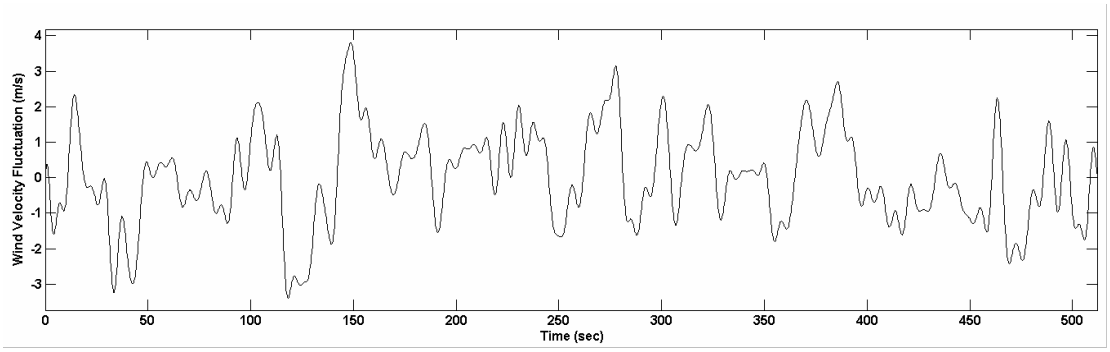

Figure 6.9 Measured wind velocity fluctuation at anemometer # 3 location

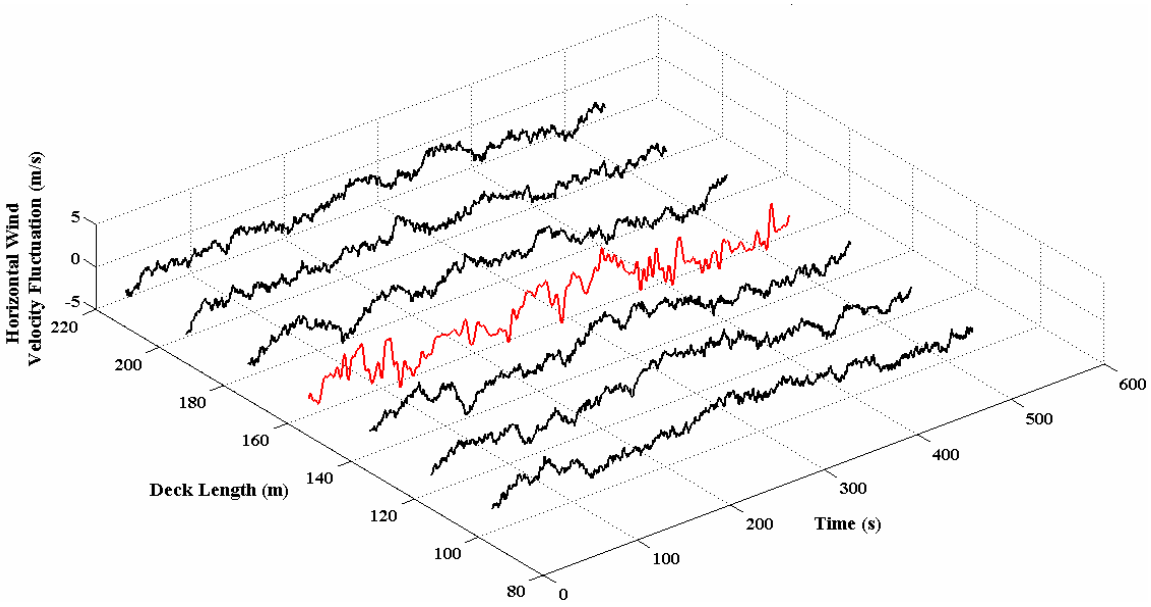

Figure 6.10 Horizontal wind velocity fluctuations at different locations along the deck (around anemometer # 2) in m/s from Gaussian conditional simulation

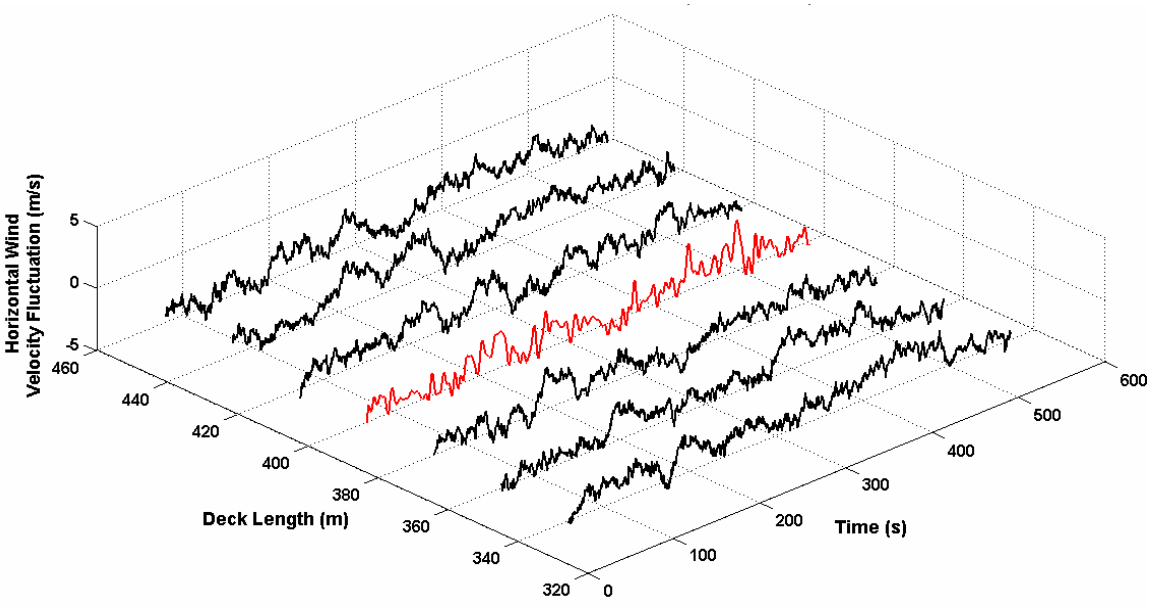

Figure 6.11 Horizontal wind velocity fluctuations at different locations along the deck (around anemometer # 1) in m/s from Gaussian conditional simulation

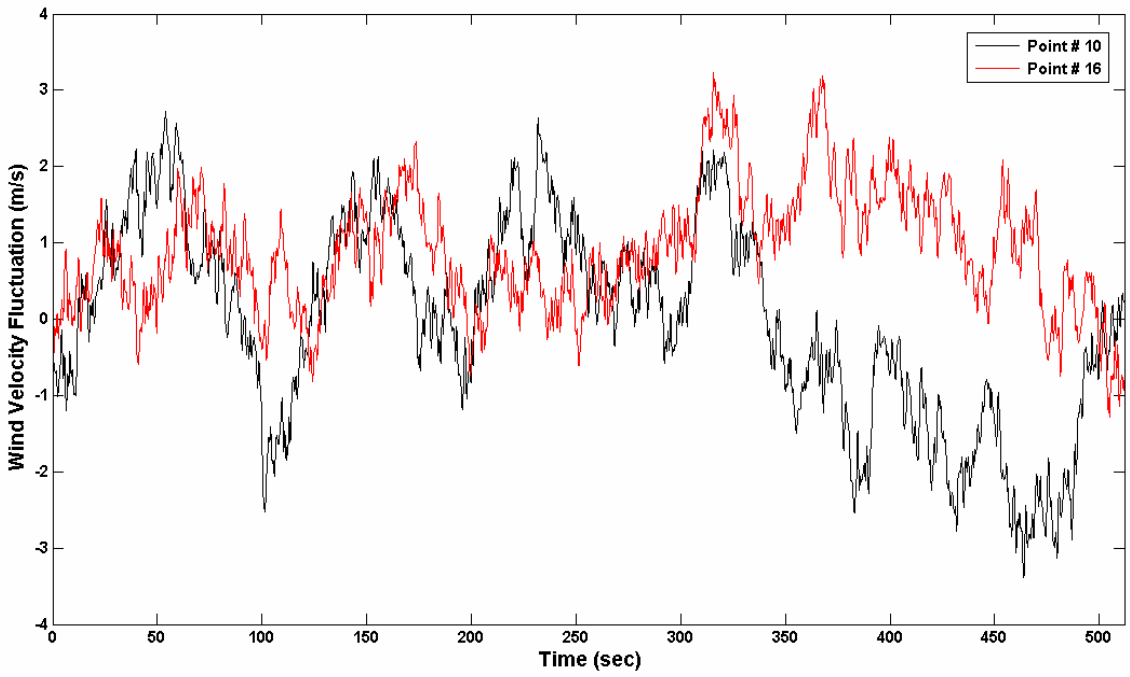

Figure 6.12 Horizontal wind velocity fluctuations at two different locations from Gaussian unconditional simulation

6.7 Conditional Simulation of non-Gaussian Wind Velocity Fluctuations

It was examined whether the assumption of non-Gaussian distribution of wind velocity fluctuation is correct or not. For this purpose Probability Density Functions (PDFs) were plotted for three measured data. Figures 6.13, 6.14, and 6.15 show the comparison between actual and analytical PDF of wind velocity fluctuation measured at anemometer # 1, 2, and 3 locations. Generalized extreme value distribution function is assumed, and the parameters are tabulated in Table 6.1. The PDF for the generalized extreme value distribution with location parameter μ, scale parameter σ, and shape parameter $\kappa \neq 0$ is

$$f(x \mid \kappa,\mu,\sigma)=\left(\frac{1}{\sigma}\right)\exp\left(-\left(1+\kappa\frac{(x-\mu)}{\sigma}\right)^{-\frac{1}{\kappa}}\right)\left(1+\kappa\frac{(x-\mu)}{\sigma}\right)^{-1-\frac{1}{\kappa}} \tag{6.36}$$

for $1+\kappa\frac{(x-\mu)}{\sigma}>0$, $\kappa>0$ corresponds to the Type II case, while $\kappa>0$ corresponds to the Type III case. In the limit for $\kappa=0$, corresponding to the Type I case, the PDF is

$$f(x \mid 0,\mu,\sigma)=\left(\frac{1}{\sigma}\right)\exp\left(-\exp\left(-\frac{(x-\mu)}{\sigma}\right)-\frac{(x-\mu)}{\sigma}\right) \tag{6.37}$$

Figures 6.16, 6.17, and 6.18 show the comparison between actual and analytical Cumulative Distribution Functions (CDFs) of wind velocity fluctuation measured at anemometer # 1, 2, and 3 locations. It can be seen from the figures that the analytical PDFs and CDFs match the actual distributions very well. So the assumption of non-Gaussian distribution is validated here.

The non-Gaussian distribution function used in the simulation is calculated from the measured velocity fluctuations from three anemometer locations at the bridge site. The non-Gaussian distribution functions fitted to the actual wind velocity fluctuations at three different locations were different. For the conditional simulation purpose the distribution function for wind velocity fluctuation at different points along the deck is considered same. This distribution function is calculated in an average sense between the fitted distribution obtained from the measured wind velocity at anemometer # 1 and anemometer # 2. At the time of calculating distribution function for wind velocity fluctuation along the tower, the measured wind velocity fluctuations at anemometer # 2 and anemometer # 3 are considered. Also the roughness length z_0 and shear wave

velocity of the flow u_* are calculated from the measured mean wind velocity $U(z)$ at height z along the tower.

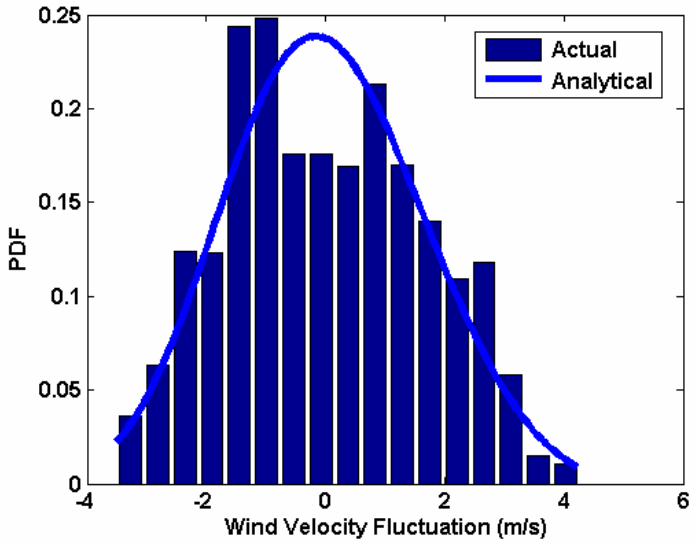

Figure 6.13 Actual and analytical PDF of wind velocity fluctuation measured at anemometer # 1 location

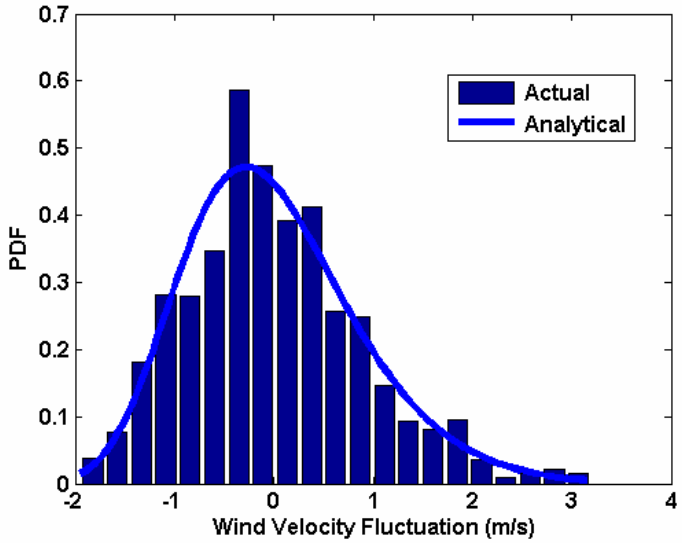

Figure 6.14 Actual and analytical PDF of wind velocity fluctuation measured at anemometer # 2 location

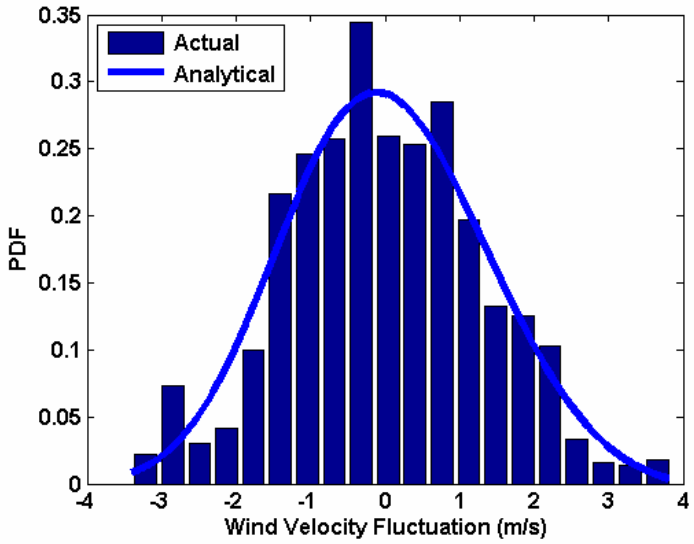

Figure 6.15 Actual and analytical PDF of wind velocity fluctuation measured at anemometer # 3 location

Table 6.1 Properties for assumed generalized extreme value distribution

Parameter	Anemometer # 1	Anemometer # 2	Anemometer # 3
Shape Parameter (κ)	-0.1123	-0.2512	-0.2543
Scale Parameter (σ)	0.7858	1.5971	1.3058
Location Parameter (μ)	-0.3740	-0.6094	-0.4820

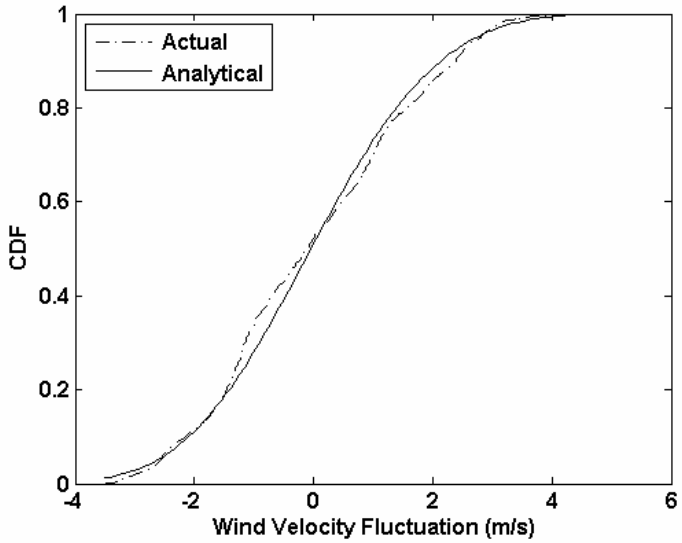

Figure 6.16 Actual and analytical CDF of wind velocity fluctuation measured at anemometer # 1 location

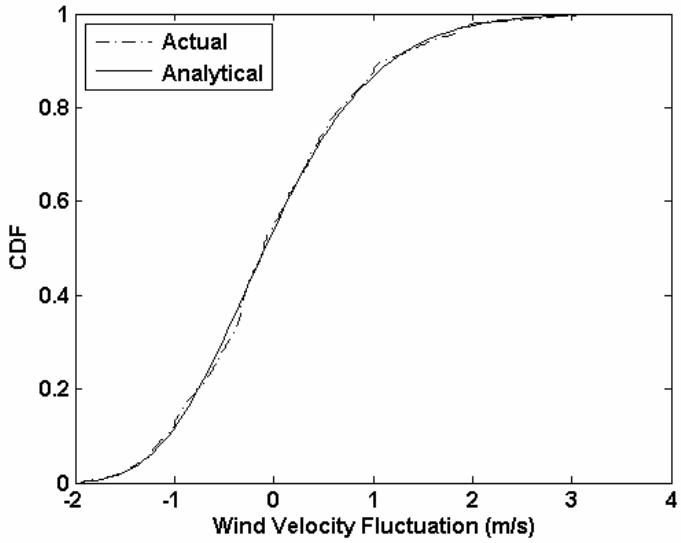

Figure 6.17 Actual and analytical CDF of wind velocity fluctuation measured at anemometer # 2 location

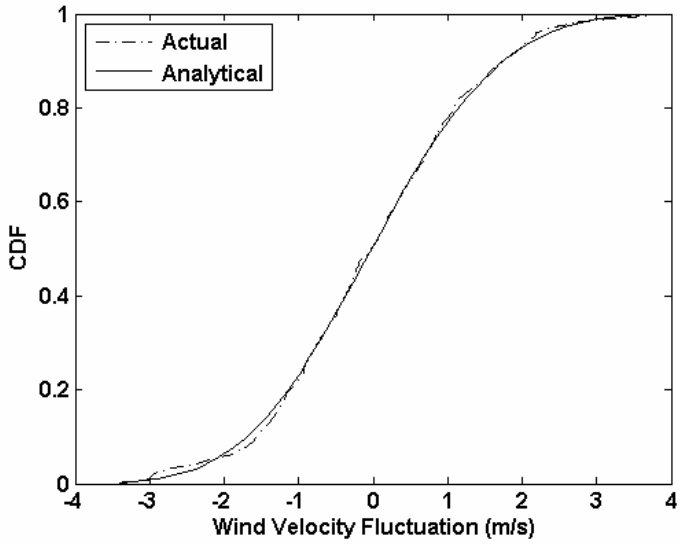

Figure 6.18 Actual and analytical CDF of wind velocity fluctuation measured at anemometer # 3 location

Since, only the horizontal velocity fluctuation was obtained from the site, for the conditional simulation non-Gaussian wind velocity fluctuation only the horizontal velocity fluctuation will be considered. Figure 6.19 shows horizontal wind velocity fluctuations at two different locations from non-Gaussian conditional simulation. Figure 6.20 and 6.21 show simulated and target CDF of wind velocity fluctuation at point # 10 and 16. The simulated and target CDFs match very well. It also can be seen from Figures 6.22 and 6.23 that the target and simulated PSDF also match very well in an average sense. The analytical PSDF with the actual PSDF obtained from the field measured data re also compared in Figures 6.24-6.26. Figures 6.27 and 6.28 show the horizontal wind velocity fluctuations simulated with non-Gaussian conditional simulation technique at six different locations around anemometer # 2 and anemometer # 1 along the bridge deck. The wind velocity fluctuation plotted using red line denotes respective anemometer locations. It can be seen from the wind velocity fluctuation profiles that around the measured data the profile has similar trend but it differs with the increase in distance from the measured location. Figure 6.29 and 6.30 show simulated wind velocity fluctuations at point # 10 and 16 with three different simulation techniques. Also, along the tower the horizontal wind velocity fluctuations are simulated at eight different nodal points along the vertical height of the tower. From mean sea level (MSL) these heights are 7.62 m, 23.65 m, 39.68 m, 55.04 m (location of anemometer # 2), 58.27 m, 81.76 m, 107.87 m, and 111.33 m (anemometer # 3 location). Figures 6.31, 6.32, and 6.33 shows the simulated horizontal velocity fluctuation at four different locations along the tower height around anemometer # 2 using Gaussian unconditional, Gaussian conditional, and

non-Gaussian conditional simulation techniques respectively. The wind velocity fluctuation plotted using red line denotes anemometer # 2 location.

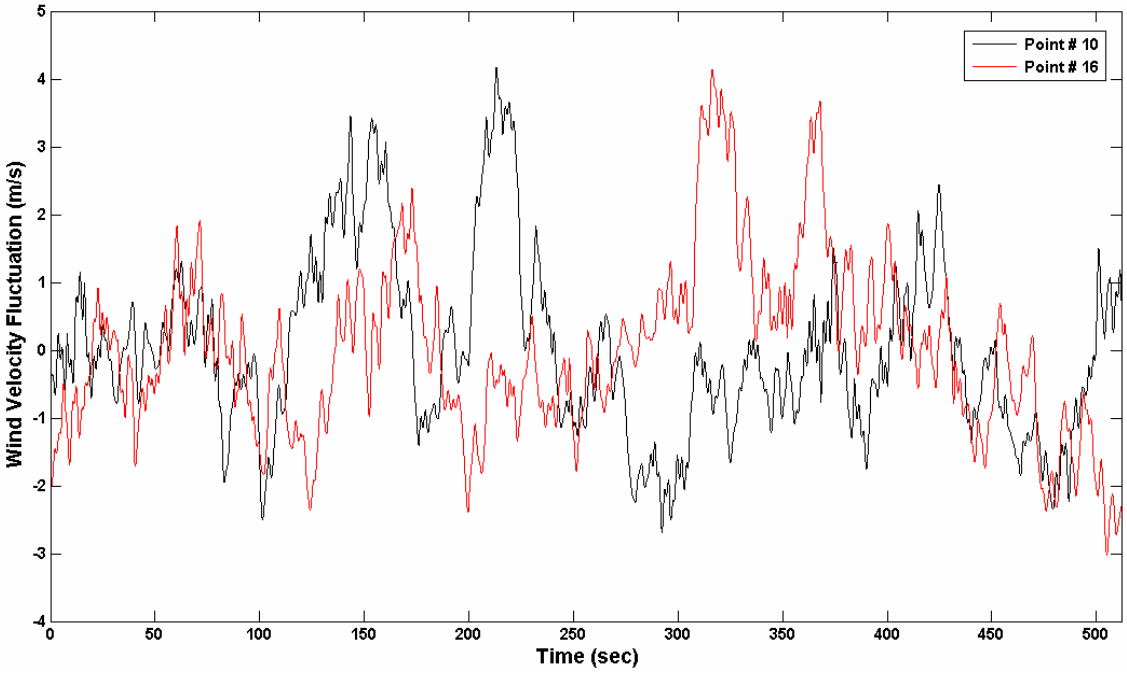

Figure 6.19 Horizontal wind velocity fluctuations at two different locations from non-Gaussian conditional simulation

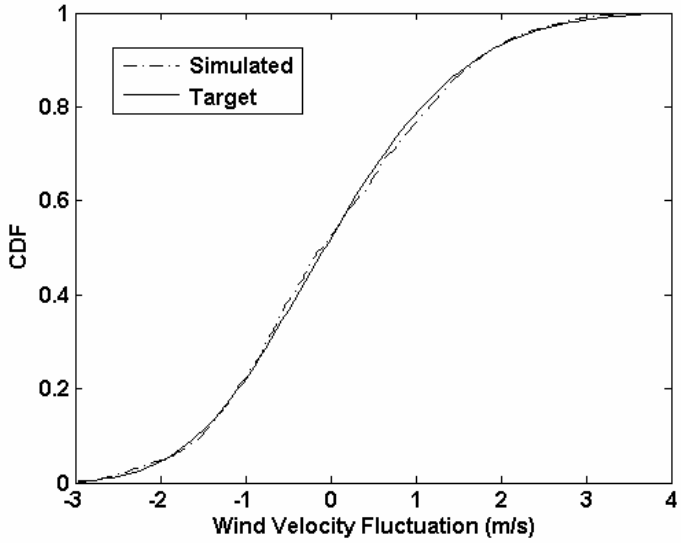

Figure 6.20 Simulated and target CDF of wind velocity fluctuation at point # 10

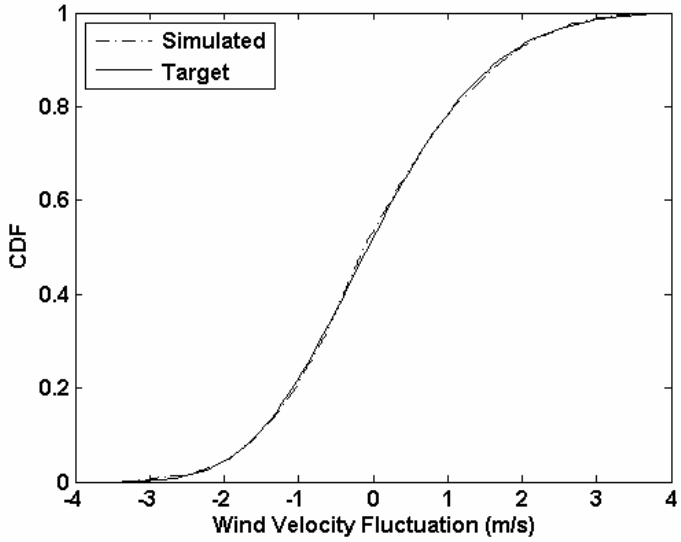

Figure 6.21 Simulated and target CDF of wind velocity fluctuation at point # 16

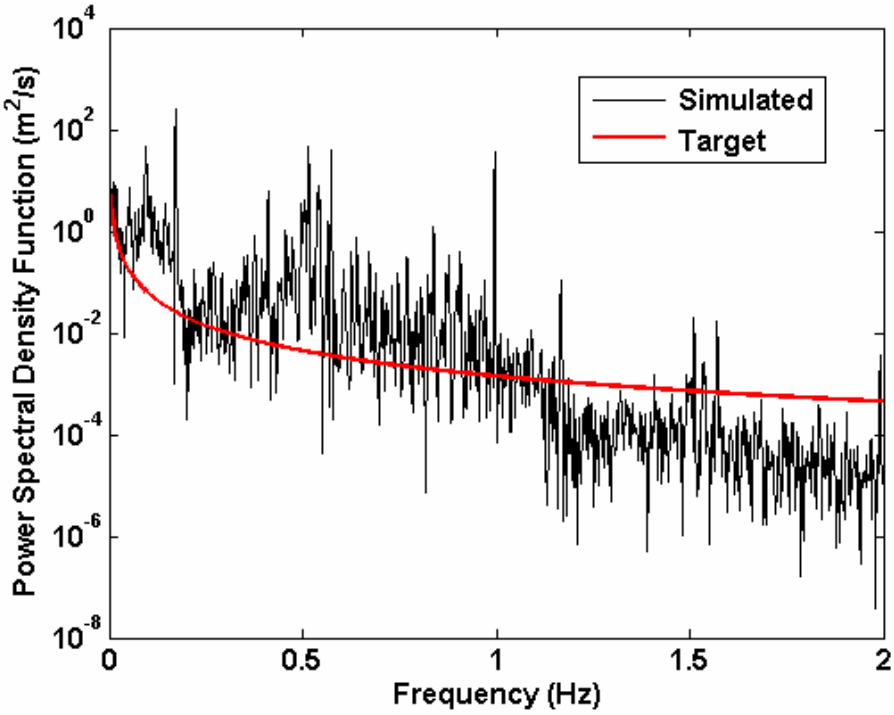

Figure 6.22 Comparison of PSDF from simulated wind velocity fluctuation and target PSDF at point # 10

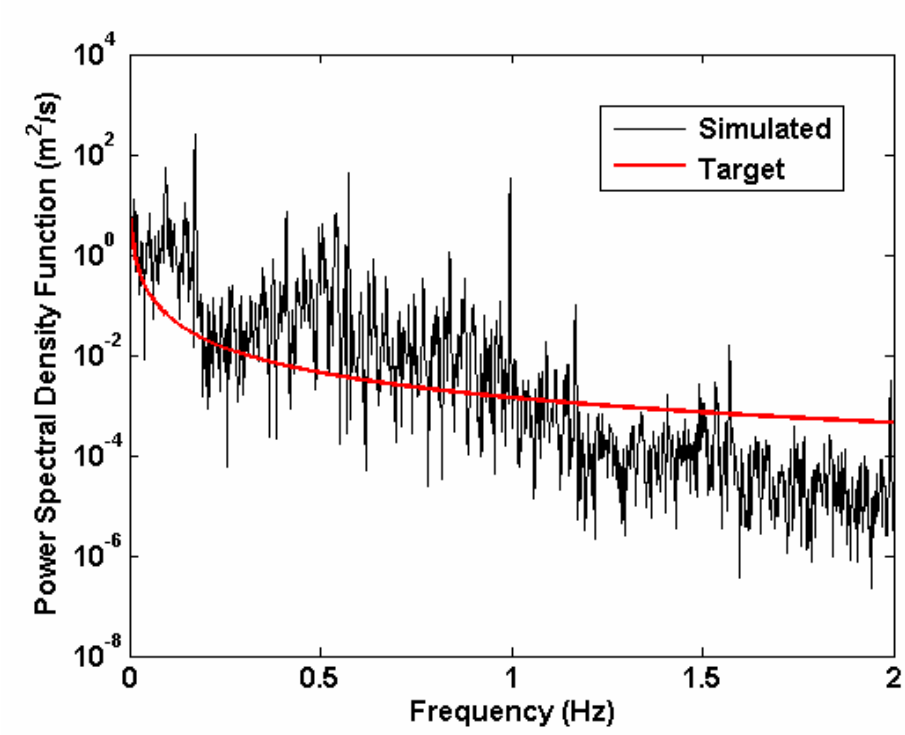

Figure 6.23 Comparison of PSDF from simulated wind velocity fluctuation and target PSDF at point # 16

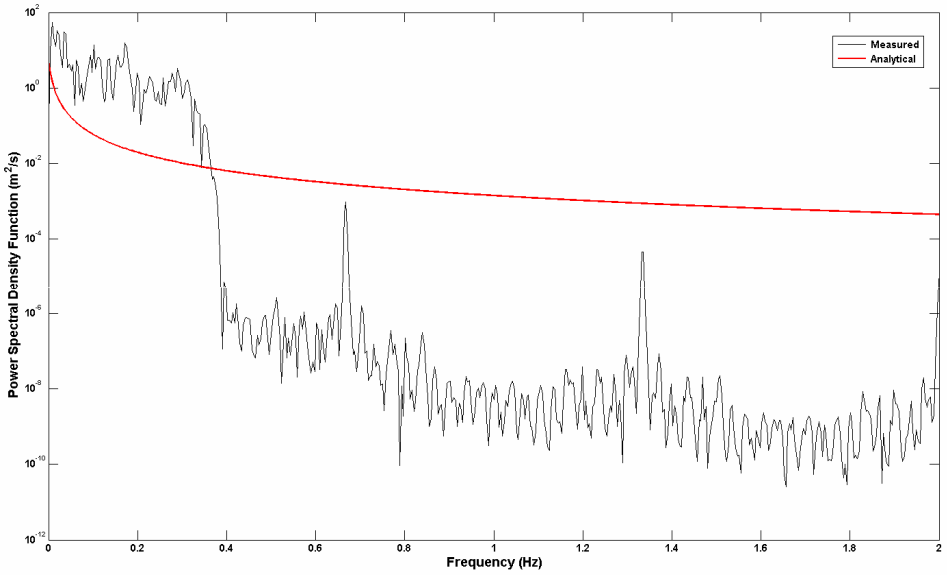

Figure 6.24 Comparison of PSDF from measured velocity fluctuation at anemometer # 1 and assumed analytical PSDF

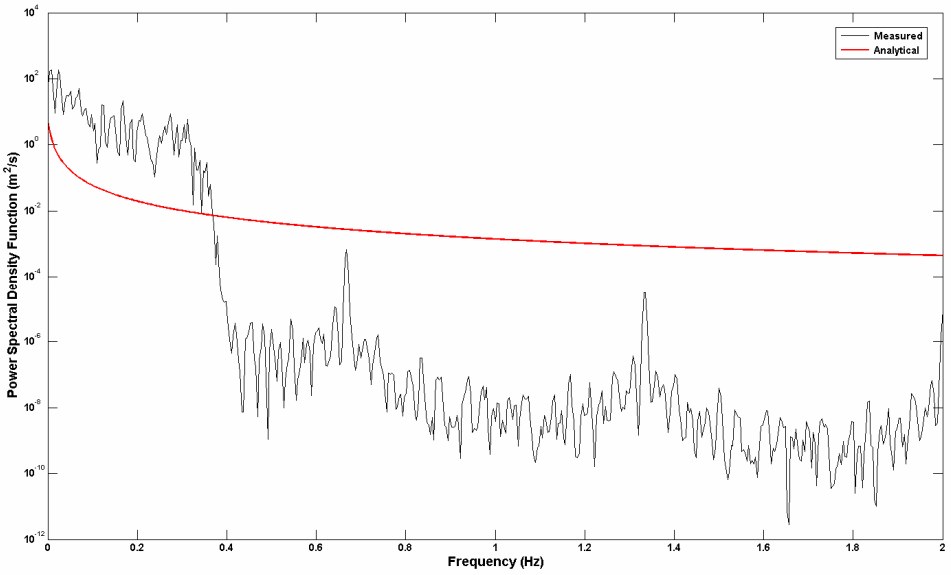

Figure 6.25 Comparison of PSDF from measured velocity fluctuation at anemometer # 2 and assumed analytical PSDF

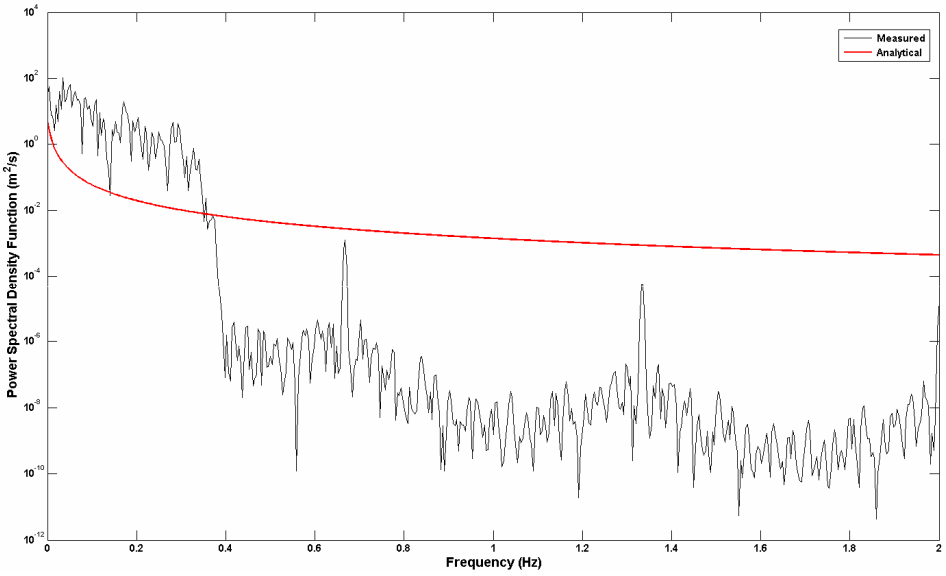

Figure 6.26 Comparison of PSDF from measured velocity fluctuation at anemometer # 3 and assumed analytical PSDF

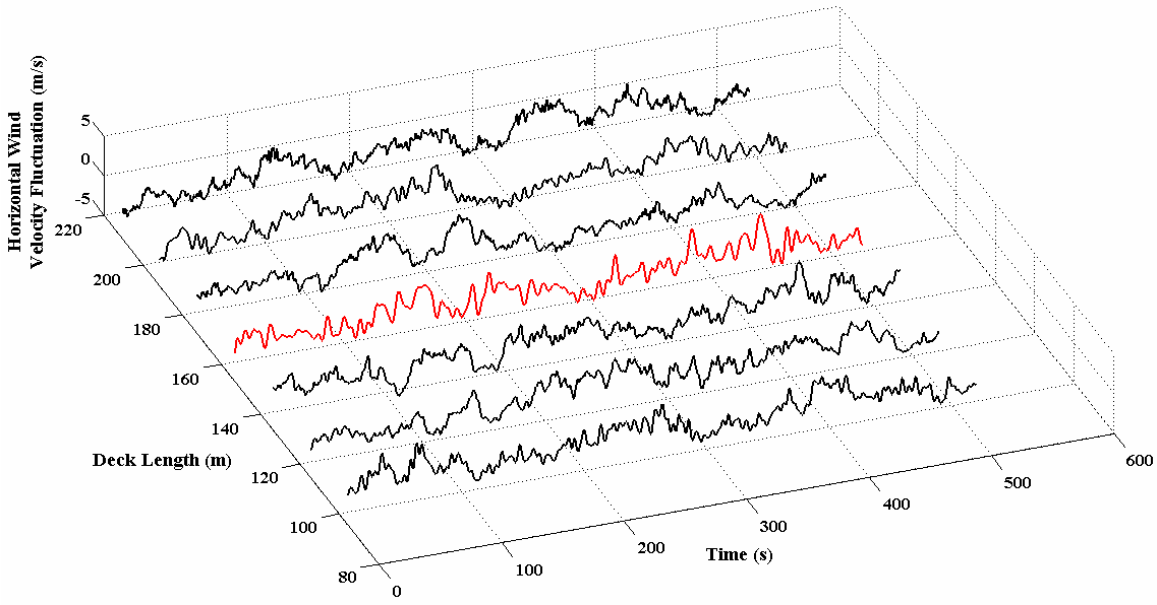

Figure 6.27 Horizontal wind velocity fluctuations at different locations along the deck (around anemometer # 2) in m/s from non-Gaussian conditional simulation

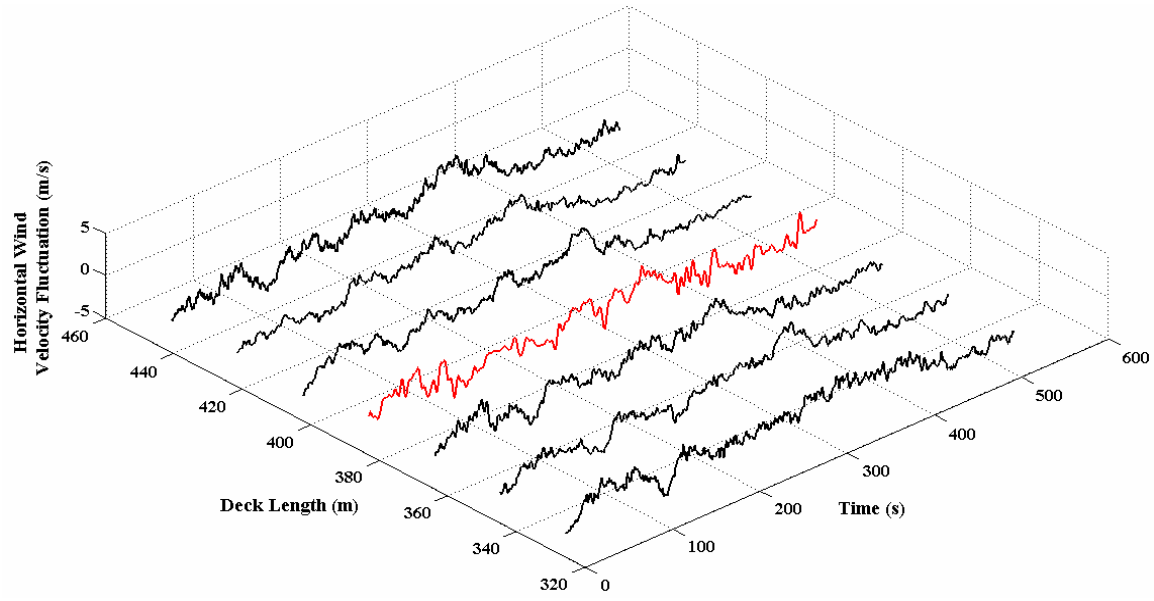

Figure 6.28 Horizontal wind velocity fluctuations at different locations along the deck (around anemometer # 1) in m/s from non-Gaussian conditional simulation

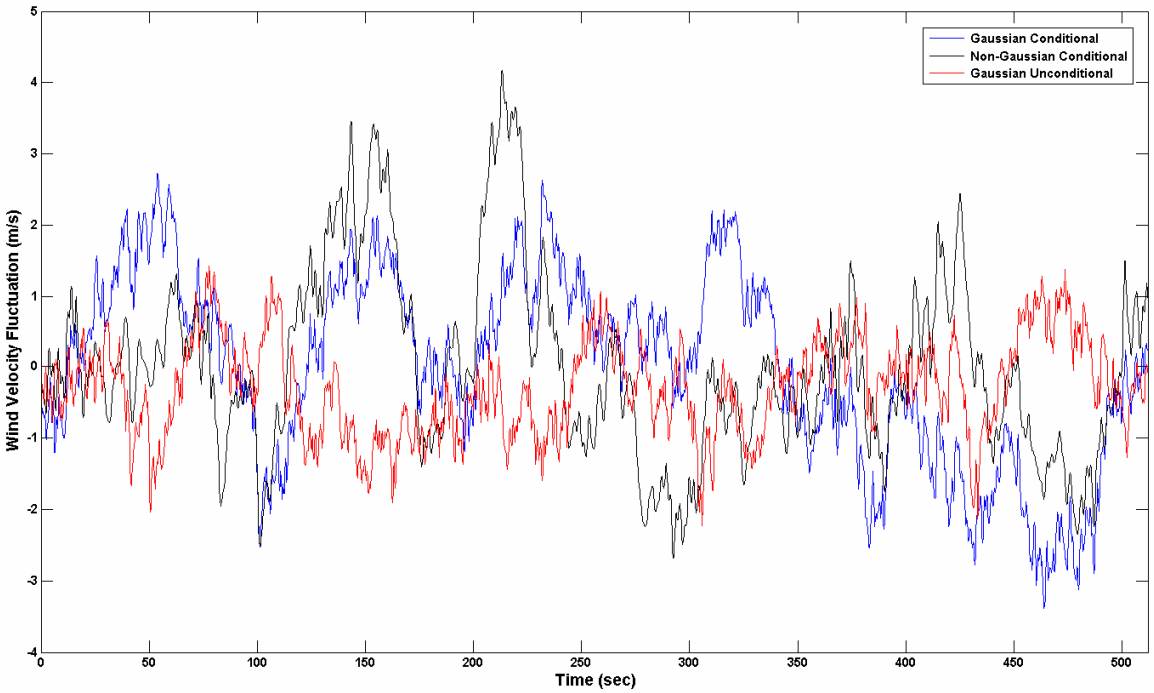

Figure 6.29 Simulated wind velocity fluctuations at location # 10 with three different simulation techniques

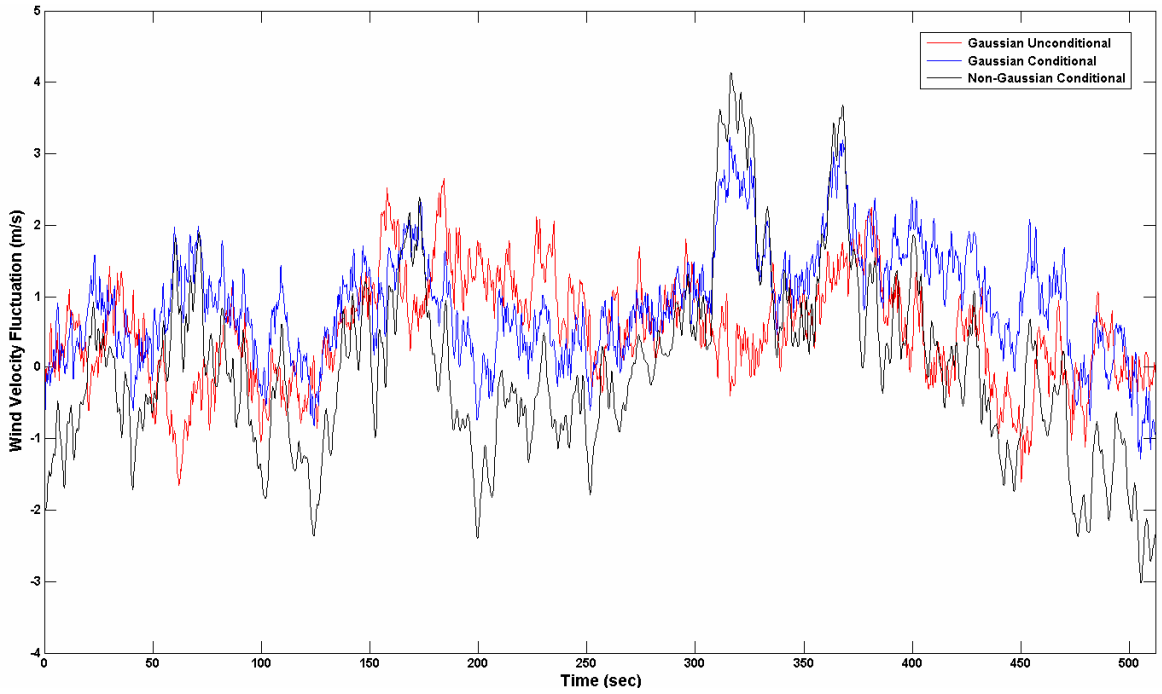

Figure 6.30 Simulated wind velocity fluctuations at location # 16 with three different simulation techniques

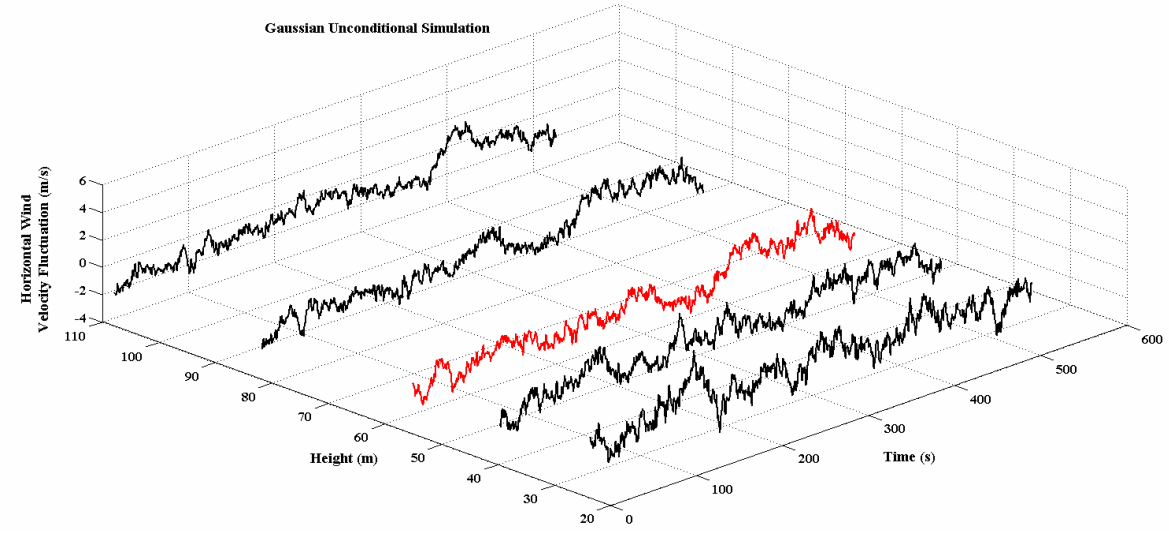

Figure 6.31 Horizontal wind velocity fluctuations at different locations along the tower (around anemometer # 2) in m/s from Gaussian unconditional simulation

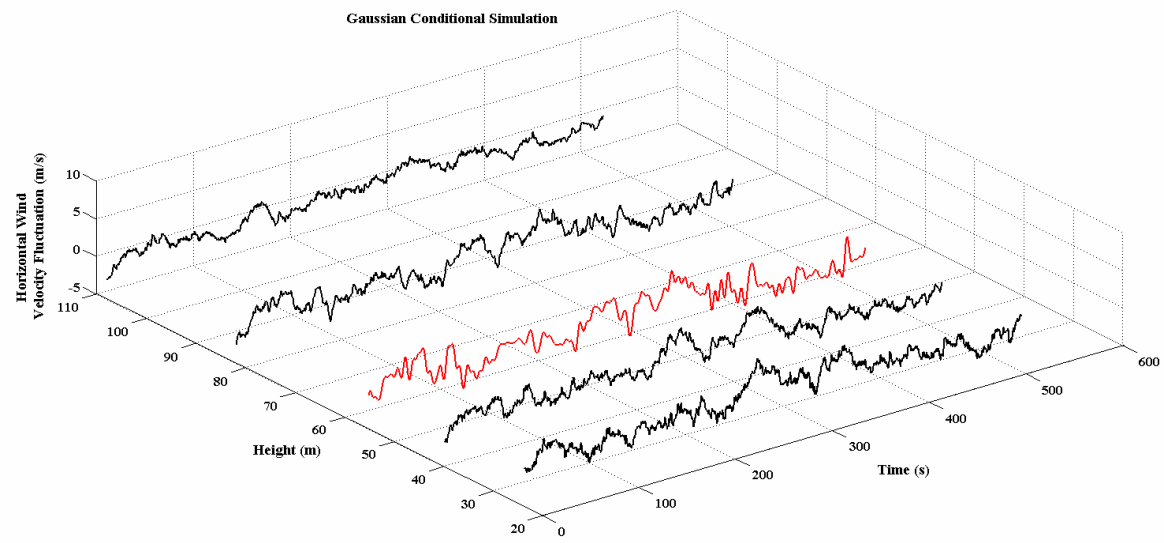

Figure 6.32 Horizontal wind velocity fluctuations at different locations along the tower (around anemometer # 2) in m/s from Gaussian conditional simulation

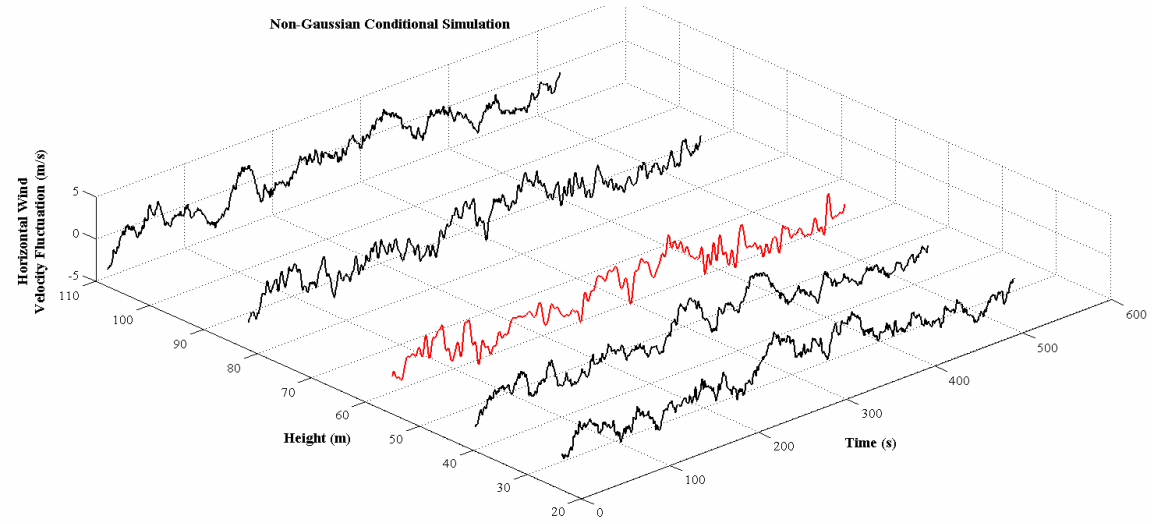

Figure 6.33 Horizontal wind velocity fluctuations at different locations along the tower (around anemometer # 2) in m/s from non=Gaussian conditional simulation

6.8 Buffeting Force Calculation

Wind loads acting on a bridge deck can be divided into self-excited aerodynamic loads due to bridge motion and turbulent loads independent of bridge motion. Buffeting loads due to turbulence are assumed to be linearly added to the self-excited part of the load as (Scanlan, 1978a,b).

$$\begin{aligned} L(t) &= L_{se}(t) + L_b(t) \\ D(t) &= D_{se}(t) + D_b(t) \\ M(t) &= M_{se}(t) + M_b(t) \end{aligned} \tag{6.38}$$

where L_{se}, D_{se} and M_{se} represent lift, drag and moment due to self-excited motions and L_b, L_b and L_b represent lift, drag and moment due to buffeting effects. Self-excited and buffeting forces are shown schematically in Figure 6.34.

For purely sinusoidal motions of the bridge deck the lift, drag and moment of the self-excited part of the force per unit length of the deck can be expressed with the help of flutter derivatives (Scanlan and Tomko, 1971) as follows:

$$\begin{aligned} L_{se}(t) &= \frac{1}{2}\rho \overline{U}^2 B\left[KH_1^* \frac{\dot{h}}{\overline{U}} + KH_2^* \frac{B\dot{\alpha}}{\overline{U}} + K^2 H_3^* \alpha \right] \\ D_{se}(t) &= \frac{1}{2}\rho \overline{U}^2 B\left[KP_1^* \frac{\dot{h}}{\overline{U}} + KP_2^* \frac{B\dot{\alpha}}{\overline{U}} + K^2 P_3^* \alpha \right] \\ M_{se}(t) &= \frac{1}{2}\rho \overline{U}^2 B\left[KA_1^* \frac{\dot{h}}{\overline{U}} + KA_2^* \frac{B\dot{\alpha}}{\overline{U}} + K^2 A_3^* \alpha \right] \end{aligned} \tag{6.39}$$

where ρ = density of air; B = full width of the bridge deck; $K\left(=B\omega/U\right)$ = reduced frequency, ω = circular frequency of the bridge motion; H_i^*, P_i^*, and A_i^*; (i = 1, 2, 3) are aerodynamic coefficients representing influences on the bridge motion; $\overline{U}$ = horizontal mean wind velocity; h and α = vertical and rotational displacement of the bridge deck while $\dot{h}$ and $\dot{\alpha}$ = velocities of each component.

Buffeting loads per unit span length are expressed as

$$
\begin{aligned}
L_b(t) &= \frac{1}{2}\rho\overline{U}^2 B\left\{C_L(0)\left[1+\frac{2u(t)}{\overline{U}}\right]+\left[\frac{dC_L(0)}{d\alpha}+C_D(0)\right]\frac{w(t)}{\overline{U}}\right\} \\
D_b(t) &= \frac{1}{2}\rho\overline{U}^2 B\left\{C_D(0)\left[1+\frac{2u(t)}{\overline{U}}\right]\right\} \\
M_b(t) &= \frac{1}{2}\rho\overline{U}^2 B\left\{C_M(0)\left[1+\frac{2u(t)}{\overline{U}}\right]+\frac{dC_M(0)}{d\alpha}\frac{w(t)}{\overline{U}}\right\}
\end{aligned}
\tag{6.40}
$$

where $C_L(0)$, $C_D(0)$ and $C_M(0)$ = dimensionless lift, drag and moment coefficients at a wind angle of 0° ; $u(t)$ and $w(t)$ are wind velocity fluctuations in the horizontal and vertical directions.

6.9 Buffeting Response of Vincent Thomas Bridge

The statistical correlation between horizontal and vertical wind velocity fluctuations is ignored. As a result, the spatially separated wind velocity field is simulated as combination of two independent stochastic vector processes. Since only the horizontal

wind velocity fluctuation was measured at the bridge site with the help of anemometers, so, three different methods were used to simulate the horizontal velocity fluctuation. These methods are Gaussian unconditional simulation, Gaussian conditional simulation, and non-Gaussian conditional simulation. For vertical wind velocity fluctuation only Gaussian unconditional simulation technique was used in this study. Horizontal and vertical wind velocity fluctuations are simulated at 41 locations (Figure 6.2) along the bridge deck. The aerodynamic buffeting forces are calculated and applied at those 41 locations. Every other hanger and deck connection is chosen as the nodal point for application of buffeting force along the bridge deck. Wind velocity fluctuation time history is simulated for 512 sec with a sampling duration of $\Delta t = 0.25$ sec. Since the flutter derivatives used to calculate self excited forces are frequency dependent, only buffeting forces are considered for this analysis. The dimensionless aerodynamic coefficients (taken from He et al. 2008) required for calculating the buffeting force are considered as : $C_L = 0, C_M = 0, C_D = 0.162, C_L' = 1.415, C_M' = 0.238, and\ C_D' = 0.$

The buffeting response of the bridge is calculated using the buffeting forces as described in Eq. (6.40). Figure 6.35 shows the lateral displacement at the center of the mid span due to buffeting force calculated from three different simulation techniques. It has been found out that the response from using non-Gaussian simulation technique is higher than other two techniques. The peak lateral displacement is 0.86 cm for non-Gaussian conditional case, on the other hand for Gaussian conditional and Gaussian unconditional cases the peak lateral displacements are 0.59 cm and 0.67 cm respectively. So, consideration of non-Gaussian conditional simulation technique will produce conservative response. Figure 6.36 Simulated vertical deck displacement at the center of

the mid span due to buffeting force calculated from non-Gaussian conditional simulation technique. Since no vertical wind velocity fluctuation was measured at the bridge site, for vertical wind velocity fluctuation simulation only Gaussian unconditional simulation technique is used. As a result the vertical displacement at the middle of the center span deck from three different buffeting forces was not very different from each other. The peak vertical deck displacement is 1.44 cm. The mean wind velocity considered here is 10 m/s. Since the magnitude of wind load is very small the deck displacement is also very small compared to the length of the bridge.

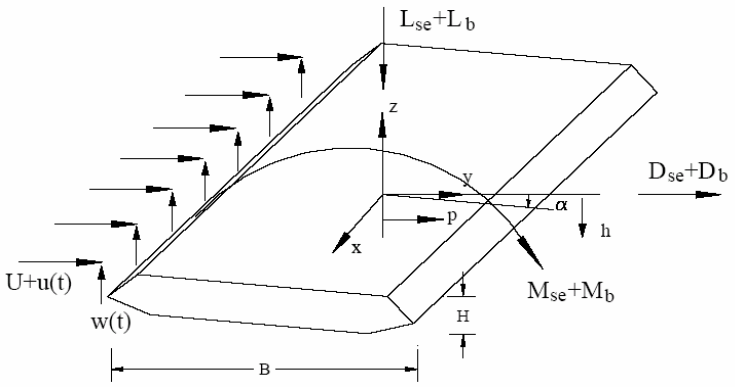

Figure 6.34 Schematic diagram for aerodynamic forces on bridge deck

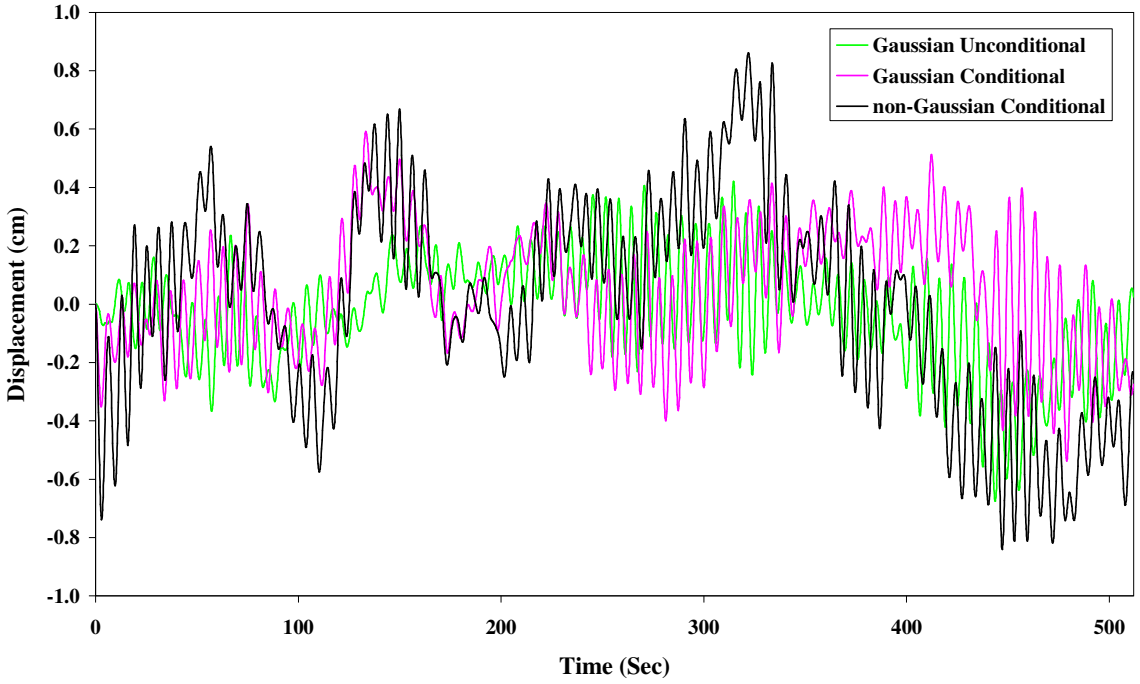

Figure 6.35 Simulated lateral deck displacements at the center of the mid span

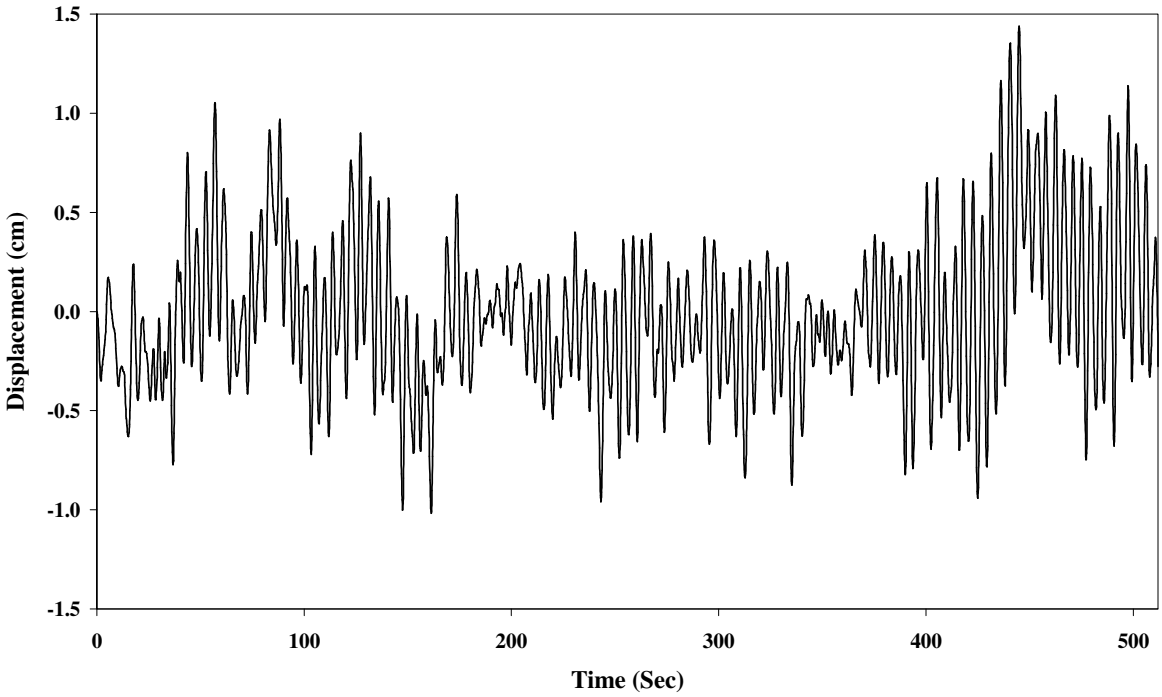

Figure 6.36 Simulated vertical deck displacement at the center of the mid span

6.10 Closure

Response of Vincent Thomas Bridge under conditionally simulated non-Gaussian wind velocity field is presented in this chapter. Wind velocity fluctuations are simulated along the deck as well as along the tower. A new conditional simulation technique for simulation of the wind velocity fluctuation field is developed. The applicability of the method is shown with a simulation example. Further, under wind loading simulated using three different simulation techniques, namely, Gaussian unconditional, Gaussian conditional, and non-Gaussian conditional, response evaluated using the detailed member-based three dimensional FE model (Chapter 2) is compared. For this comparison, lateral and vertical displacements at the center of the mid span due to buffeting force are calculated. It is observed that the response using the non-Gaussian simulation technique is higher than the other two techniques. The simulation techniques presented herein can be used for the wind-induced fatigue analysis of critical members of the bridge.

CHAPTER 7

TRAFFIC LOAD ANALYSIS

7.1 Background

The main purpose of this study is to examine the deck shear connectors in detail. After retrofitting of the bridge some the bolts in the deck shear connector were coming off. Maybe the shear force generated in the bolts was large enough to shear off the bolts of the deck shear connector. Also some blots were sheared off from shear keys. The reason has also been investigated. Damper displacements under normal traffic loading are also computed. Investigation is done for the reason of humming sound from suspenders in the middle span.

7.2 Moving Load Analysis

Analysis of Moving Load for Shear Force and Axial Force in the Deck Shear Connector is done. In the Figure 7.1 below the partial plan of deck shear connector removal and partial plan of deck shear connector retrofit is shown. Also, a picture was taken from the bridge site is shown below (Figure 7.2). This is a type A deck shear connector after retrofit. Caltrans' maintenance engineers noticed that there is some problem with the Type B and Type C deck shear connectors after retrofit. A typical cross-sectional elevation view of those two types of deck shear connectors is shown below (Figure 7.3). It has been found that many bolts, a typical one of which is marked with red circle, are coming off from the deck.

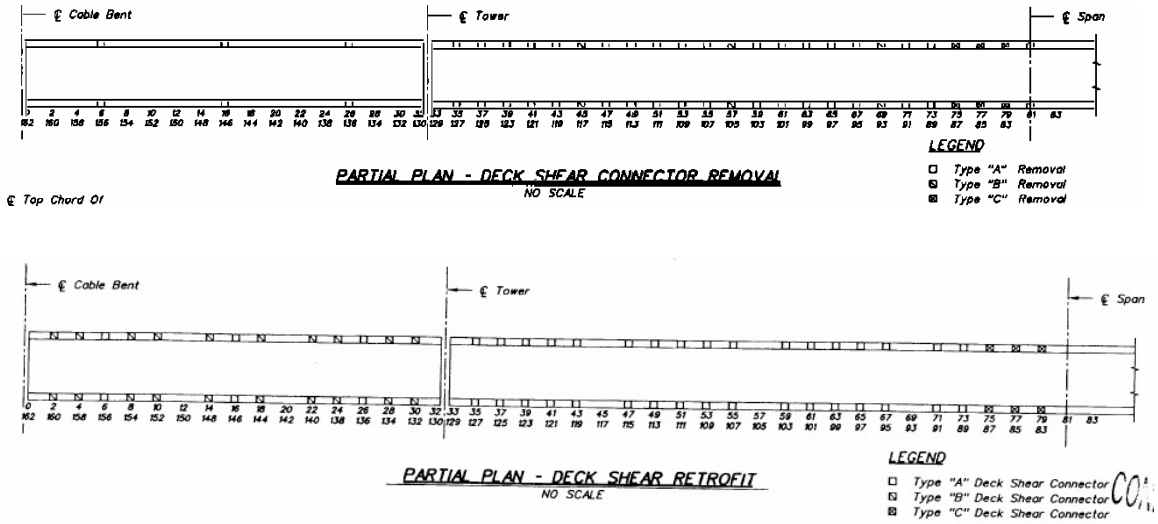

Figure 7.1 Plan view of deck shear connectors before and after retrofit

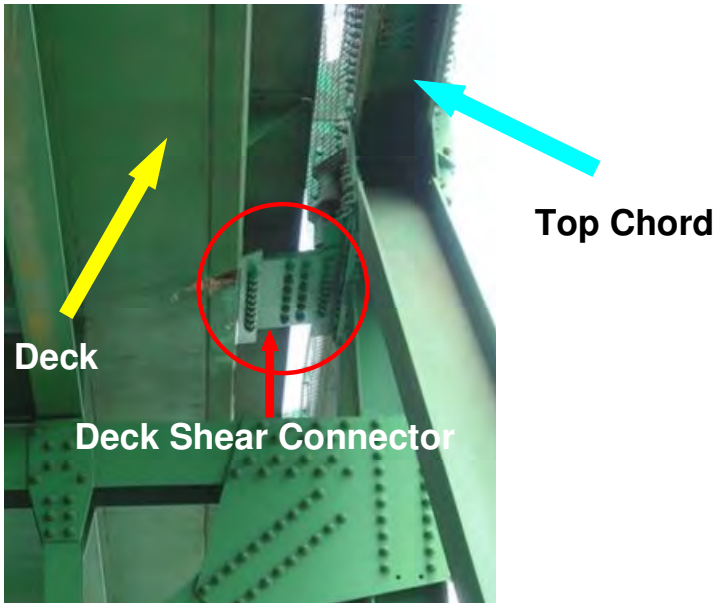

Figure 7.2 Deck shear connector

So, to investigate the reason for this type of failure, axial force, longitudinal and transverse shear forces acted on the shear connectors are calculated for moving truck load under quasi-static conditions. Then the stresses developed in the bolts were also calculated by SAP2000 Nonlinear computer code. For the moving truck load analysis, the

truck is considered is HS 20-44, a 3 axel truck (Figure 7.4). The axel loads are of 8 kips, 32 kips and 32 kips.

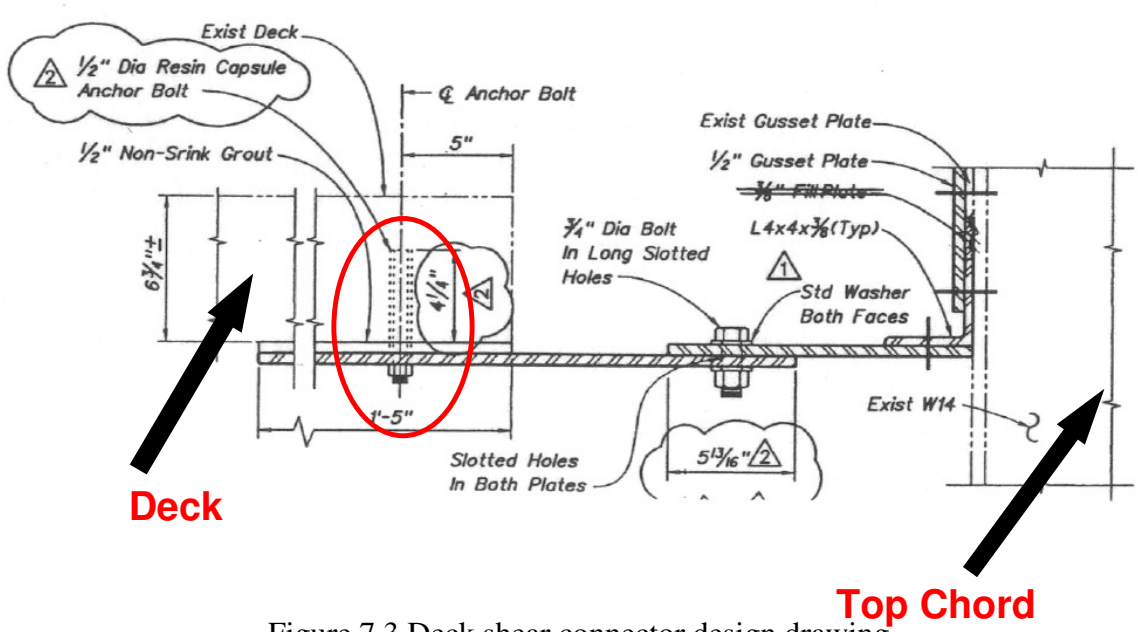

Figure 7.3 Deck shear connector design drawing

For this analysis four different cases were considered which are explained in the following figure (Figure 7.5). The maximum value of axial force, longitudinal and transverse shear forces are plotted along the length of the bridge for different deck shear connectors for before and after retrofit cases (Figures 7.6 – 7.8). Trucks were considered moving in the same direction in four lanes. As case four gives maximum forces, the force distribution is shown for case four only i.e., when the traffic is on all 4 lanes. It was found out that the longitudinal shear force and axial force were increased 15% from before retrofit and the vertical shear force was increased as high as 72%. Shear stress developed in the type B and type C deck shear connector is computed. Shear stress in the bolts embedded in the deck in type C shear connector as shown in Figure 3 is estimated as 4.04

kips/in^2. Shear stress of the bolts in type B shear connector = 16.6 kips/in^2. Allowable shear stress of the bolts = 10 kips/in^2, and therefore, bolts in the type B deck shear connectors may fail in shear. Vertical stress along the shaft of the bolt is also calculated for those two types of shear connectors. Maximum stress developed for vertical shear in the bolts of Type C shear connectors = 8.96 psi and in bolts of Type B shear connectors = 21.13 psi. Allowable rupture strength of concrete is 400 psi, and hence, those bolts are safe from the vertical pulling load. However, Caltrans' engineers found that the bolts came off indicating that epoxy used is not well bonded to the concrete. Further investigation may be required to reveal the failure mechanisms.

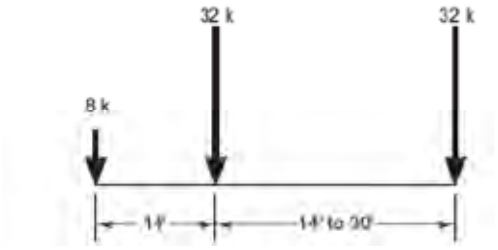

Figure 7.4 HS20-44 AASTHO traffic loading

The torsional rotation of the deck due to moving load is calculated. It has been found out that torsional rotation of the deck does not change much after retrofit. The stress developed in the bolts of the shear key, damper deformation and the cause for development of humming and popping sound in the main cable and suspenders have also been examined. The shear key is shown in Figure 7.9 also calculated and shear stresses developed in the bolts are shown in Table 7.1. The bolts in the member # 1 and # 3 may

fail in shear. Also the maximum damper deformation was 1.125 in. That is comparable with the observation which showed the deformation in the range of 1-4 inch. Audible sound frequency range is between 20 Hz - 20000 Hz, and therefore, it may be possible that the suspender vibrated in its first natural frequency under wind and it is in the audible range. Two suspenders in the center of the middle span are considered for this study. The natural frequencies of the two middle suspenders after retrofitting of the bridge are 35 Hz and 37 Hz.

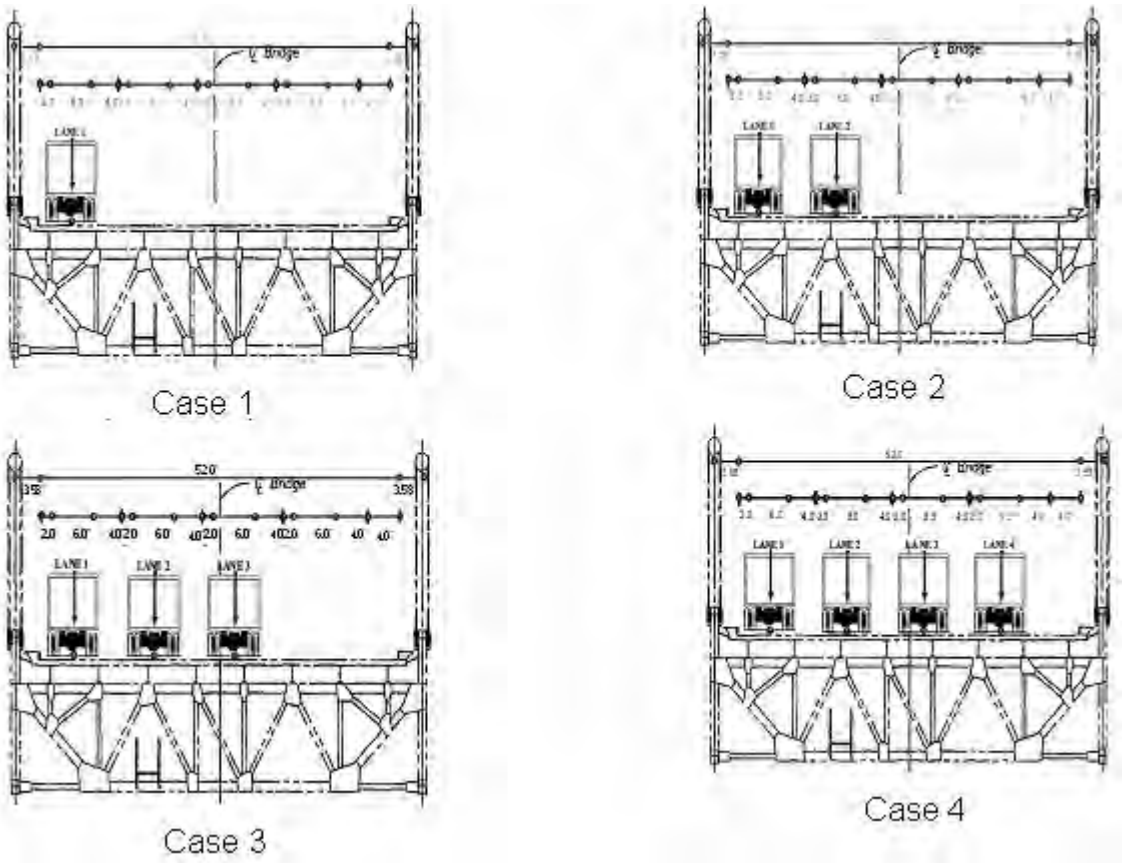

Figure 7.5 Different traffic load cases

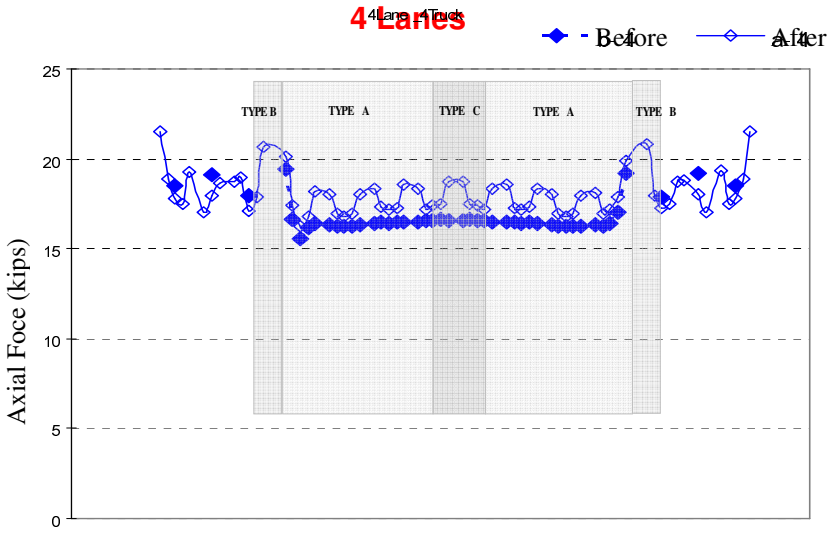

Figure 7.6 Axial force in shear connector due to traffic load (before and after retrofit)

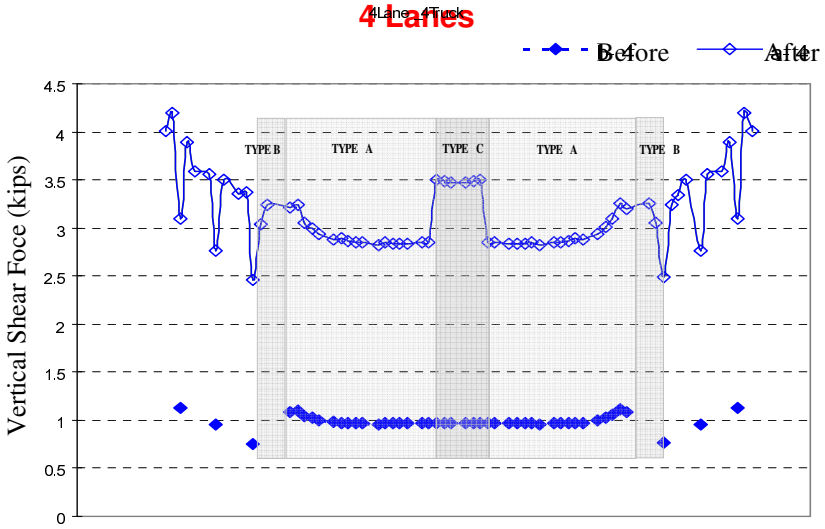

Figure 7.7 Vertical shear force in shear connector due to traffic load (before and after retrofit)

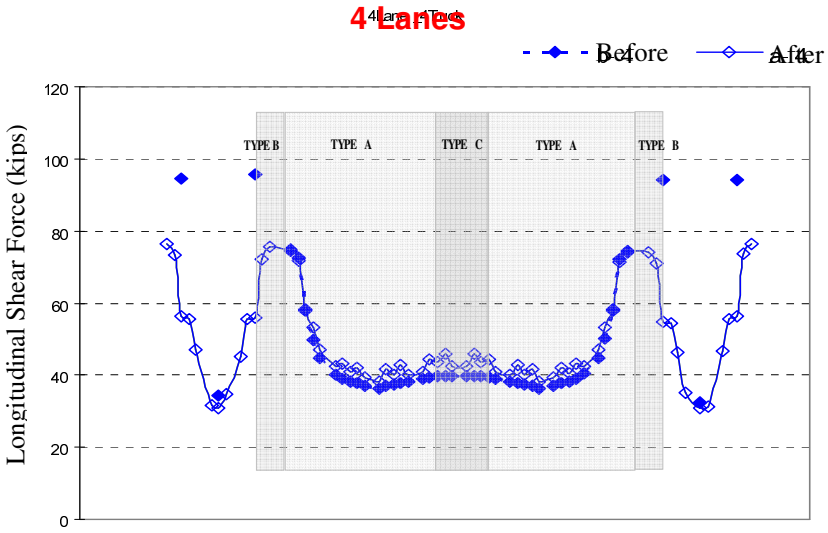

Figure 7.8 Longitudinal shear force in shear connector due to traffic load (before and after retrofit)

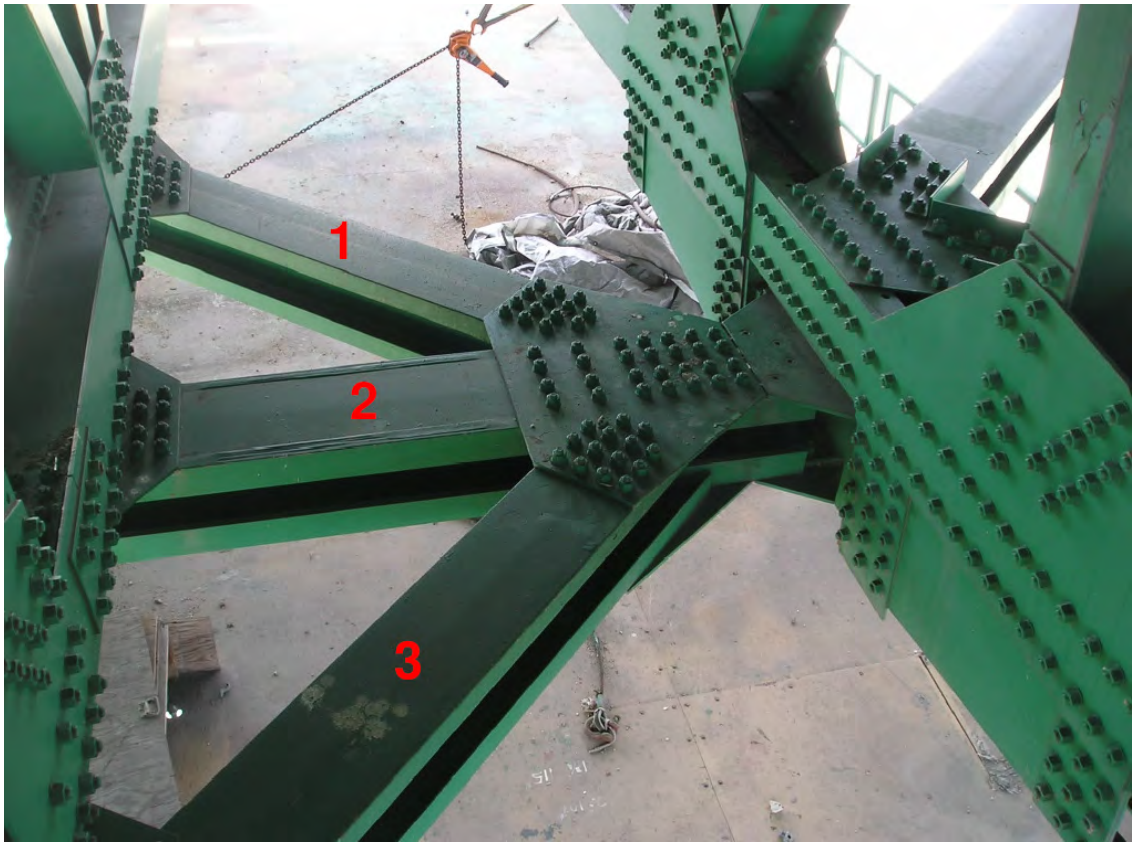

Figure 7.9 Shear key in east side span

Table 7.1 Shear stress developed in shear key bolts

East side span Allowable stress = 10 ksi

Member No.	Shear Stress (ksi)	Comment
1	17.63	Fail
2	2.23	OK
3	15.86	Fail

* 1 ksi = 6.8948 MPa

7.3 Closure

The analysis of force concentration on deck shear connectors due to traffic load is carried out in this chapter. Shearing off of the deck shear connector bolts are examined in terms of shear force generated in these bolts. It is found, while some bolts sheared off from the shear keys due to excessive shear force generated in these bolts, others sheared off bolts from deck shear connectors. Further investigation may be required to reveal the failure mechanisms. This study can be further extended for the investigation of traffic-induced response of other critical members/components.

According to a VTB inspection site engineer, “Standing on VTB, you can observe the bridge deck continue to swing with respect to the towers following its natural frequency, the force is huge and independent to the traffic loads. The retrofitting may have somehow changed its natural frequency (by adding the damping system). It seems this is a large component of lateral force acting on the shear connectors. Considering 10% of total truck load and calculating some traffic statistics, it appears attributing the failure force to traffic loads may be a weak argument.” Further investigation is required to resolve this issue.

CHAPTER 8

CONCLUSIONS AND FUTURE WORK

8.1 Summary and Conclusions

This study deals with performance evaluation of the Vincent Thomas Bridge under earthquake, wind, and traffic loads. The Vincent Thomas Bridge, located in the city of San Pedro, serves both Los Angeles and Long Beach Ports. The bridge carries an overwhelming number of traffic many of which are cargo trucks with an Annual Average Daily Traffic (AADT) volume of 45,500. The bridge was constructed in 1963 and is subjected to frequent high wind and heavy port traffic loads. As a result, the bridge is prone to fatigue damage. Based on the recent finding that the main span of the Vincent Thomas Bridge crosses directly over the Palos Verdes Fault, which has the capacity to produce an earthquake with a magnitude (M_w) of 7.25 with a return period of 1000 years, in spring 2000, the bridge underwent a major retrofit, using visco-elastic dampers.

In this study, a panel based simplified model as well as a member based detailed three-dimensional Finite Element (FE) model of the Vincent Thomas Bridge have been developed using a commercial software so that the models can be used by Caltrans' engineers for their future evaluation purpose. To demonstrate the appropriateness of these models, eigenproperties of the models are evaluated and compared with those of system identification results obtained using ambient vibration data and two earthquake records, the 1994 Northridge earthquake (M_w 6.4) and the 2008 Chino Hills earthquake (M_w 5.5).

The models are also validated by simulating the dynamic response during these two earthquakes and comparing with the measured response. After that a comprehensive sensitivity analysis is performed considering 19 different structural and soil spring parameters. First eight modal frequencies are considered for the purpose of sensitivity study. Tornado diagram and FOSM methods are used for the sensitivity analysis. It is found that the mass density of deck slab and the elastic modulus of bottom chord are most sensitive to the modal frequencies of the bridge. FE model is also updated using a sensitivity-based parameter updating method.

For development of seismic fragility curves, considering an ensemble of a large number of ground motions representing 2% in 50 years hazard level in the Los Angeles area, nonlinear time history analyses are performed using the detailed model of the bridge. In order to simplify the analysis procedure, only the towers are modeled as nonlinear elements while remaining elements of the bridge are modeled as linear. Fragility curves are then generated considering ductility demands of the critical tower sections. It is observed from this study that a ground motion with PGA of 0.9g or greater will result in plastic hinge formation at one or more locations with a probability of exceedance of 50%. Also, it is found that the effect of damper on reducing the seismic vulnerability of the bridge is minimal for low to moderate earthquakes and high for strong earthquakes.

Effect of spatial variability of ground motions on seismic displacement and force demands is then investigated. To generate spatially correlated spectrum compatible nonstationary acceleration time histories, a new algorithm using evolutionary PSDF and spectral representation method is proposed. The proposed procedure is more realistic than

other previous procedures based on utilization of the envelope function with (time-invariant) Fourier spectrum or stationary PSDF to induce nonstationarity in the simulated time histories. Simulated spatially variable ground motions are used in calculating the response of the bridge. In addition to spatial variable seismic ground motions, two uniform ground motions (one with the highest and the other with the lowest ground displacement) are also considered for comparison purpose. It has been found that, in some locations on the bridge deck, the spatial variable case gives higher response than the uniform ground motion having the highest ground displacement scenario.

It is well-known that long suspension bridges are highly vulnerable to rough wind conditions and thus, measurement of wind velocity under such conditions is crucial for proper response prediction. In this study, a wind speed monitoring network is developed with three anemometers being installed along the bridge: two at deck level and one at the top of the east tower. The wind data has been collected at both 1 sample per minute and at 1 sample per 3 sec sampling interval. For the collection of 1 sample per 3 sec wind data, special software has been developed. Collected data show that the wind velocity changes along the length as well as with the height when using 1 sample per 3 sec or 1 sample per minute data. It is also envisioned that the measured data will provide a reality check for the wind characterization in temporal and spatial variation.

Further, measured wind data have been used to conditionally simulate the wind velocity fluctuation field at the bridge site as an input for evaluating the response of the bridge under wind load. Wind velocity fluctuations are simulated along the deck and tower. A new conditional simulation technique for simulation of wind velocity fluctuation field is proposed. The applicability of the method is shown with a simulation

example. Further, under wind loading simulated using three different simulation techniques, namely, Gaussian unconditional, Gaussian conditional, and non-Gaussian conditional, response evaluated using the detailed member-based three dimensional FE model is compared. For this comparison, lateral and vertical displacements at the center of the mid span due to buffeting force are calculated. It is observed that the response using the non-Gaussian simulation technique is higher than the other two techniques. The simulation techniques presented herein can be used for the wind-induced fatigue analysis of critical members of the bridge.

The response of the bridge under different types of traffic loads is also investigated using influence line diagram approach. Under traffic load, the analysis of force concentration on deck shear connectors has been achieved in detail. The reason for shearing off the bolts in the deck shear connector is examined in terms of shear force generated in the beck shear connector bolts. It is found, while some bolts sheared off from the shear keys due to excessive shear force generated in these bolts, others sheared off bolts from deck shear connectors are believed to be damaged due to poor workmanship.

8.2 Future Work

This research can be extended through additional work including the following:

1) Sensitivity study for the dynamic response of the suspension bridge should be carried out considering additional parameters such as, damping coefficients of dampers

and soil springs.

2) Generation of spatial variable ground motions should be carried out using evolutionary PSDF generated by other technique such as Hilbert Huang transform.

3) Fragility analysis should be carried out under spatial variable ground motion to consider the effect of spatial variability of ground motions in fragility curves.

(4) Wind tunnel testing should be carried out for experimental determination of aerodynamic coefficients (flutter derivatives) for the bridge deck and the tower sections.

(5) Wind load should be considered on deck, tower, and cables so that the coupling effect of wind forces in different components of the bridge can be taken into account.

(6) This study should be extended to determine the fatigue crack inspection schedule for critical members of the bridge under traffic and wind loading.

REFERENCES

Aas-Jakobsen, K., and Strømmen, E. (1998). ‘‘Time domain calculations of buffeting response for wind-sensitive structures.’’ Journal of Wind Engineering and Industrial Aerodynamics, 74–76, pp. 687–695.

Aas-Jakobsen, K., and Strømmen, E. (2001). ‘‘Time domain buffeting response calculations of slender structures.’’ Journal of Wind Engineering and Industrial Aerodynamics, 89, pp. 341–364.

Abdel-Ghaffar, A.M. (1976). “Dynamic analysis of suspension bridge structures.” Technical Report 76-01, California Institute of Technology, Earthquake Engineering Research Laboratory, College of Engineering, Passadena, CA.

Abdel-Ghaffar, A.M. (1977). “Studies on the effect of differential motions of two foundations upon the response of the superstructure of a bridge.” Technical Report 77-02, California Institute of Technology, Earthquake Engineering Research Laboratory, College of Engineering, Passadena, CA.

Abdel-Ghaffar, A.M. (1978a). “Free lateral vibrations of suspension bridges.” Journal of the Structural Division, ASCE, 104(ST3), pp. 503-525.

Abdel-Ghaffar, A.M. (1978b). “Vibration studies and tests of a suspension bridge.” Journal of Earthquake Engineering and Structural Dynamics, 6(5), pp. 473-496.

Abdel-Ghaffar, A.M. (1979). “Free torsional vibrations of suspension bridges.” Journal of the Structural Division, ASCE, 105(ST4), pp. 767-788.

Abdel-Ghaffar, A.M. (1980). “Vertical vibration analysis of suspension bridges.” Journal of the Structural Division, ASCE, 106(ST10), pp. 2053-2075.

Abdel-Ghaffar, A.M. (1982). “Suspension bridge vibration: Continuum formulation.” Journal of Engineering Mechanics, ASCE, 108(EM6), pp. 1215-1232.

Abdel-Ghaffar, A.M., and Housner, G.W. (1977). “An analysis of the dynamic characteristics of a suspension bridge by ambient vibration measurements.” Technical Report 77-01, California Institute of Technology, Earthquake Engineering Research Laboratory, College of Engineering, Passadena, CA.

Abdel-Ghaffar, A.M. and Nazmy, A.S. (1988). “3D nonlinear seismic behavior cable-stayed bridges.” Journal of Structural Engineering, ASCE, 117, pp. 3456-3477.

Abdel-Ghaffar, A.M., and Rubin, L.I. (1982). “Suspension bridge response to multiple-support excitations.” Journal of Engineering Mechanics, ASCE, 108(EM2), pp. 419-435.

Abdel-Ghaffar, A.M., and Rubin, L.I. (1983a). "Nonlinear free coupled vibrations of suspension bridges: Application." Journal of Engineering Mechanics, ASCE, 109(EM1), pp. 330-345.

Abdel-Ghaffar, A.M., and Rubin, L.I. (1983b). "Nonlinear free coupled vibrations of suspension bridges: Theory." Journal of Engineering Mechanics, ASCE, 109(EM1), pp. 319-329.

Abdel-Ghaffar, A.M., and Rubin, L.I. (1983c). "Vertical seismic behavior of suspension bridges." International Journal of Earthquake Engineering and Structural Dynamics, 11, pp. 1-19.

Abdel-Ghaffar, A.M., Scanlan, R.H., and Rubin, L.I. (1983). "Earthquake response of long-span suspension bridges." Technical Report 83-SM-13, Princeton University, Civil Engineering Department, Princeton, NJ.

Abdel-Ghaffar, A.M., and Scanlan, R.H. (1985a). "Ambient vibration studies of the Golden Gate Bridge:I. suspended structure." Journal of Engineering Mechanics, ASCE, 111, pp. 463-482.

Abdel-Ghaffar, A.M., and Scanlan, R.H. (1985b). "Ambient vibration studies of the Golden Gate Bridge:II. pier-tower structure." Journal of Engineering Mechanics, ASCE, 111, pp. 483-499.

ADINA R&D, Inc. (1987-2002) (2002). "Theory and modeling Guide Vol. 1: ADINA", Report ARD 02-7.

ASCE Standard (2006), Minimum design loads for buildings and other structures, American Society of Civil Engineers, ASCE/SEI 7-05, www.pubs.asce.org

Arzoumanidis, S. G. (1980). ''Finite-element analysis of suspension bridges.'' Doctoral dissertation, Columbia Univ., New York, USA.

Basu, B., and Gupta, V. K. (1998). Seismic response of SDOF systems by wavelet modeling of nonstationary processes, Journal of Engineering Mechanics, Vol. 124, No. 10, pp. 1142–1150.

Beliveau, J.-G., Vaicaitis, R., and Shinozuka, M. (1977). "Motion of Suspension Bridge Subject to Wind Loads." Journal of the Structural Division, ASCE, 103(ST6), pp. 1189-1205.

Bleich, F.M., McCullough C.B., Rosecrans, R., and Vincent, G.S. (1950). "The Mathematical Theory of Suspension Bridges." U.S. Bureau of Public Roads, Government Printing Office, Washington, D.C., USA.

Borgman, L. E. (1990). Irregular ocean waves: kinematics and forces. The Sea Prentice Hall, Englewood Cliffs, NJ, USA.

Brincker, R., Zhang, L. and Andersen, P. (2000). "Modal identification from ambient response using frequency domain decomposition." Proceedings of 18th International Modal Analysis Conference, 625-630, San Antonio, TX, USA.

Brigham, E. O. (1988). "The fast Fourier transform and its applications". Prentice-Hall, Englewood Cliffs, NJ, USA.

Chen, X., and Kareem, A. (2001). ''Nonlinear response analysis of long-span bridges under turbulent winds.'' Journal of Wind Engineering and Industrial Aerodynamics, 89, pp. 1335–1350.

Chen, X., Matsumoto, M., and Kareem, A. (2000). ''Time domain flutter and buffeting response analysis of bridges.'' Journal of Engineering Mechanics, 126(1), pp. 7–16.

Computer and Structures, Inc. (2002). SAP 2000 Nonlinear users manual, V. 10, Berkeley, CA. (www.csiberkeley.com)

Davenport, A. G. (1968). ''The dependence of wind load upon meteorological parameters.'' Proceedings of International Research Seminar on Wind Effects on Building and Structure, University of Toronto Press, Toronto, pp. 19–82.

Deodatis, G. (1996a). ''Simulation of ergodic multivariate stochastic processes.'' Journal of Engineering Mechanics, 122(8), pp. 778–787.

Deodatis, G. (1996b). "Non-stationary stochastic vector processes: Seismic ground motion applications." Probabilistic Engineering Mechanics, 11(3), pp. 149-167.

Deodatis G, Saxena, V., and Shinozuka, M. (2000). "Effect of spatial variability of ground motion on bridge fragility curves." In the Proceedings of the 8th ASCE specialty conference on probabilistic mechanics and structural reliability, University of Notre Dame, IN, USA.

Ding, Q., and Lee, P. K. K. (2000). ''Computer simulation of buffeting actions of suspension bridges under turbulent wind.'' Computers and Structures, 76, pp. 787–797.

Dumanoglu, A.A., and Severn, R.T. (1990). "Stochastic response of suspension bridges to earthquake forces." Journal of Earthquake Engineering and Structural Dynamics, 19(11), pp. 133–152.

Elishakoff, I, Ren, Y.J., and Shinozuka, M. (1994). "Conditional simulation of non-Gaussian random fields." Engineering Structures, 16 (7), pp. 558-563.

Facchini, L. (1996). ‘‘The numerical simulation of Gaussian cross-correlated wind velocity fluctuations by means of a hybrid model.’’ Journal of Wind Engineering and Industrial Aerodynamics, 64, pp. 187–202.

FEMA/SAC : http://nisee.berkeley.edu/data/strong_motion/sacsteel/ground_motions.html

Feng, M. Q., Kim, D. K., Yi, J. H., and Chen, Y.B., (2004). “Baseline Models for Bridge Performance Monitoring.” Journal of Engineering Mechanics, ASCE, 130(5), pp. 562-569.

Fraser, M. (2003) Exploration of Sensor Network Field Deployment on a Large Highway Bridge and Condition Assessment. ITR Report http://healthmonitoring.ucsd.edu/publicti on_materials.jps

Gurley, K. and Kareem, A. (1998). “A conditional simulation of non-normal velocity-pressure fields.” Journal of Wind Engineering and Industrial Aerodynamics, 77&78, pp. 39-51.

Harichandran, R. S., Hawwari, A., and Sweidan, B. N. (1996). “Response of Long-span Bridges to Spatially Varying Ground Motion,” Journal of Earthquake Engineering, ASCE, 122, pp. 476-484.

Harichandran, R. S. and Wang W. (1990). “Response of indeterminate two-span beam to spatially varying earthquake excitation.” Journal of Earthquake Engineering and Structural Dynamics, 19, pp. 173-187.

He, X., Moaveni, B., Conte, J.P., and Elgamal, A., (2008). “Modal identification study of Vincent Thomas Bridge using simulated wind-induced ambient vibration data.” Computer Aided Civil and Infrastructure Engineering, 23, pp. 373–388.

Hoshiya, M. (1995). “Kriging and conditional simulation of a Gaussian field.” Journal of Engineering Mechanics, ASCE, 121(2), pp. 181-186.

Hoshiya, M. and Maruyama, O. (1994). “Stochastic interpolation of earthquake wave propagation.” Structural Safety and Reliability, edited by G. I. Schueller, M. Shinozuka and J. T. P. Yao, Vol. 3, pp. 2119-2124, Balkema, Rotterdam.

Ingham, T.J., Rodriguez, S., amd Nader, M. (1997). “Nonlinear analysis of the Vincent Thomas Bridge for seismic retrofit.” Computers and Structures, 64(5/6), pp. 1221-1238.

Kaimal, J. C., Wyngaard, J. C., Izumi, Y., and Coté, O. R. (1972). “Spectral characteristics of surface layer turbulence.” Q. J. R. Meteorol. Soc., 98, pp. 563–589.

Kameda, H. and Morikawa, H. (1992). “Interpolating stochastic process for simulation of conditional random fields.” Probabilistic Engineering Mechanics, 7(4), pp. 242-254.

Kameda, H. and Morikawa, H. (1994). "Conditioned stochastic processes for conditional random fields." Journal of Engineering Mechanics, ASCE, 120(4), pp. 855-875.

Ketchum, M.A., and Heledermon, A. (1991). "Probing the Golden Gate." Civil Engineering, ASCE.

Ketchum, M.A., and Seim, C. (1991). "Golden Gate Bridge seismic retrofit studies." Technical report, T.Y. Lin International, Golden Gate Bridge, Highway and Transportation District, San Francisco, California, USA.

Kim, H.-K. (1993). ''Three dimensional analyses of suspension bridges considering construction stages.'' PhD dissertation, Department of Civil Engineering., Seoul National University, Seoul, Korea.

Kim, H.-K., Lee, M.J., and Chang, S.P. (2002). ''Non-linear shape-finding analysis of a self-anchored suspension bridge.'' Engineering Structures, 24, pp. 1547–1559.

Kim, H.K., Shinozuka, M., and Chang, S.P. (2004). "Geometrically Nonlinear Buffeting Response of a Cable-Stayed Bridge." Journal of Engineering Mechanics, ASCE, 130(7), 848-57.

Kim, S-H. and Feng, M. Q. (2003). "Fragility analysis of bridges under ground motion with spatial variation." International Journal of Non-Linear Mechanics, 38(5), pp. 705-721.

Konishi, I., Yamada, Y., and Takaoka, N. (1965). "Earthquake response and earthquake resistant design of long span suspension bridges." In the Proceedings of 3rd World Conference on Earthquake Engineering, Volume III.

Konishi, I., and Yamada, Y. (1969). "Studies on the earthquake resistant design of suspension bridge tower and pier systems." In Proceedings of 4th WCEE, Volume I.

Krige, D. G. (1966). "Two-dimensional weighted moving average trend surfaces for ore evaluation." Journal of South African Institute of Mining and Metallurgy, Proceedings of Symposium on Mathematical Statistics and Computer Applications for Ore Evaluation, Johannesburg, South Africa, pp. 13-38.

Lee T.H. and Mosalam K.M. (2006). "Probabilistic seismic evaluation of reinforced concrete structural components and systems." Report 2006/04, Pacific Earthquake Engineering Research Center, University of California, Berkeley, USA.

Li, Y. and Kareem, A. (1993). ''Simulation of multivariate random processes: Hybrid DFT and digital filtering approach.'' Journal of Engineering Mechanics, ASCE, 119(5), pp. 1078–1098.

Liang, J., Ray Chaudhuri, S. and Shinozuka, M. (2007). "Simulation of Nonstationary Stochastic Processes by Spectral Representation." Journal of Engineering Mechanics, 133(6), pp. 616-627.

Lin, W.D., and Imbsen, R.A. (1990). "Seismic evaluation of Golden Gate Bridge and tower structure." Technical report, T.Y. Lin International, Golden Gate Bridge, Highway and Transportation District, San Francisco, California, USA.

Lin, Y.-Y., Cheng, C.-M., and Lu, Y.-L. (2001). ''Buffeting analysis of cable-stayed bridges with geometrical nonlinearities.'' Proceedings of 5th Asia-Pacific Conference on Wind Engineering, Kyoto, Japan, pp. 269–272.

Lou, L. and Zerva, A. (2005). "Effects of spatially variable ground motions on the seismic response of a skewed, multi-span, RC highway bridge." Soil Dynamics and Earthquake Engineering, 25(7-10), pp. 729-740.

Lumley, J. L., and Panofsky, H.A. (1964). The structure of atmospheric turbulence, Wiley, New York, USA.

Minh, N. N., Miyata, T., Yamada, H., and Sanada, Y. (1999). ''Numerical simulation of wind turbulence and buffeting analysis of long-span bridges.'' Journal of Wind Engineering and Industrial Aerodynamics, 83, pp. 301–315.

Mukherjee, S. and Gupta, V.K. (2002). "Wavelet-based generation of spectrum-compatible time-histories." Soil Dynamics and Earthquake Engineering, 22(9-12), pp. 799-804.

Murlidharan, T. and Kareem, A. (1993). "Conditional simulation of Gaussian velocity field." Technical Report no. CEGEOS-93-1, Department of Civil Engineering and Geological Sciences, University of Notre Dame, Indiana, USA.

Niazy, A-S.M. , Abdel-Ghaffer, A.M., and Masri, S.F. (1991). "Performance of the Vincent-Thomas Suspensin on Bridge During the Whittier, California Earthquake of Ocober 1, 1987." Report No. CRECE 91-05, Bepartment of Civil Engineering, University of Southern California, Los Angeles, California, USA.

Otte, D., Leuridan, J., Grangier, H., and Aquilina, R. (1990). "Coupling of structures using measured FRF's by means of SVD based data reduction techniques." Proceedings of the eighth International Modal Analysis Conference, pp. 213–220.

Paola, M. D. (1998). ''Digital simulation of wind field velocity.'' Journal of Wind Engineering and Industrial Aerodynamics, 74–76, pp. 91–109.

Paola, M. D., and Gullo, I. (2001). ''Digital generation of multivariate wind field processes.'' Pobabilistic Engineering Mechanics, 16, pp. 1–10.

Porter, K.A., Beck, J.L., and Shaikhutdinov, R.V. (2002). “Sensitivity of building loss estimates to major uncertain variables.” Earthquake Spectra, 18(4), pp. 719–743.

Rannie, W.D. (1941). “The Failure of the Tacoma Narrows Bridge.” Board of Engineers, O.H. Amman, T. von Karman, G.B. Woodruff, eds., Federal Works Agency, Appendix VI, March 28.

Sarkar, K. and V.K. Gupta (2005). “Wavelet-based simulation of spatially correlated and spectrum-compatible accelerograms.” Proceedings of National Symposium on Structural Dynamics, Random Vibrations & Earthquake Engineering (NSSD-2005), Department of Civil Engineering, Indian Institute of Science, Bangalore, India, pp. 69-78.

Shinozuka, M. (1971). “Simulation of multivariate and multidimensional random processes.” Journal of the Acoustical Society of America, 49, pp. 357-368.

Shinozuka, M., and Deodatis, G. (1996). ‘‘Simulation of multidimensional Gaussian stochastic fields by spectral representation.’’ Applied Mechanics Review, 49(1), pp. 29–53.

Shinozuka, M., and Jan, C. M. (1972). ‘‘Digital simulation of random processes and its applications.’’ Journal of Sound and Vibration, 25(1), pp. 111–128.

Shinozuka, M., Feng, M. Q., Lee, J. and Naganuma, T. (2000). “Statistical analysis of fragility curves.” Journal of Engineering Mechanics, ASCE, 126(12), pp. 1224-1231.

Shinozuka, M., and Jan, C. M. (1972). ‘‘Digital simulation of random processes and its applications.’’ Journal of Sound Vibration, 25(1), pp. 111–128.

Simiu, E., and Scanlan, R. H. (1996). Wind effects on structures, John Wiley and Sons, Inc., New York, USA.

Smith, S.W., and Bettie, C. (1991). “Secant Method Adjustment for Structural Models.” AIAA Journal, 29(1), pp. 119-126.

Steinman, D.B. (1959). “Modes and natural frequencies of suspension bridge oscillations.” Journal of the Franklin Institute, 268 (3), pp. 148–174.

Sun, D. K., Xu, Y. L., and Ko, J. M. (1999). “Fully coupled buffeting analysis of long span cable-supported bridges : Formulation.” Journal of Sound and Vibration, 228(3), pp. 569-588.

Tezcan, S.S., and Cherry, S. (1969). “Earthquake analysis of suspension bridges.” Proceedings of the 4th World Conference on Earthquake Engineering, II-A3.

Vanmarcke, E.H. and Fenton, G.A. (1991). “Conditioned simulation of local fields of earthquake ground motion.” Structural Safety, 10, pp. 247-274.

Vantage Pro2™ Wireless Repeater Installation Manual, Rev. C, October 18, 2005, Davis Instruments, www. davisnet.com

Vantage Pro2™ Anemometer Transmitter Kit Installation Manual, Rev. C, October 18, 2005, Davis Instruments, www. davisnet.com

WeatherLink for Vantage Pro® and Vantage Pro2™, Getting Started Guide, Davis Instruments, www. davisnet.com

Yamada, Y., and Takemiya, H. (1969). "Studies on the responses of multi-degree-offreedom systems subjected to random excitation with applications to the tower and pier systems of long span suspension bridges." Transactions of the JSCE, 1(part 1).

Yamada, Y., and Takemiya, H. (1970). "Earthquake response analysis and earthquake-resistant design of multi-degree-of-freedom systems." In Proceedings of the JEES, pp. 413-420.

Yamada, Y., and Goto, Y. (1972). "Some studies on the vibration and earthquake response analysis of the tower-pier system of long span suspension bridges." Transactions of the JSCE, 4.

Yamada, Y., Takemiya, H., and Kawano, K. (1979). "Random response analysis of a non-linear soil-suspension bridge pier." Journal of Earthquake Engineering and Structural Dynamics, 7, pp. 31-47.

Yamazaki, F. and Shinozuka, M. (1988). "Digital generation of non-Gaussian stochastic fields." Journal of Engineering Mechanics, ASCE, 114(7), pp. 1183-1197.

Yang, W. W., Chang, T. Y. P., and Chang, C. C. (1997). ''An efficient wind field simulation technique for bridges.'' Journal of Wind Engineering and Industrial Aerodynamics, 67&68, pp. 697–708.

Zhang, Q. W., Y. P. Chang, and C. C. Chang (2001). "Finite-element model updating for the Kap Shui Mun cable-stayed bridge", Journal of Bridge Engineering, 6(4), pp. 285-293.

Zerva, A. (1990). "Response of multi-span beams to spatially incoherent seismic ground motions." Journal of Earthquake Engineering and Structural Dynamics, 19, pp. 819-832.